



**HAL**  
open science

## Study and optimization of high carbon steel flat wires

Thomas Massé

► **To cite this version:**

Thomas Massé. Study and optimization of high carbon steel flat wires. Mechanics [physics.med-ph].  
École Nationale Supérieure des Mines de Paris, 2010. English. NNT : . tel-00457046

**HAL Id: tel-00457046**

**<https://pastel.hal.science/tel-00457046>**

Submitted on 16 Feb 2010

**HAL** is a multi-disciplinary open access archive for the deposit and dissemination of scientific research documents, whether they are published or not. The documents may come from teaching and research institutions in France or abroad, or from public or private research centers.

L'archive ouverte pluridisciplinaire **HAL**, est destinée au dépôt et à la diffusion de documents scientifiques de niveau recherche, publiés ou non, émanant des établissements d'enseignement et de recherche français ou étrangers, des laboratoires publics ou privés.

Ecole doctorale n° 364 : Sciences Fondamentales et Appliquées

## **Doctorat ParisTech**

### **T H È S E**

**pour obtenir le grade de docteur délivré par**

**l'École nationale supérieure des mines de Paris**

**Spécialité “ Mécanique Numérique”**

*présentée et soutenue publiquement par*

**Thomas MASSÉ**

le 7 janvier 2010

## **Study and optimization of high carbon steel flat wires**

Directeur de thèse : **Pierre MONTMITONNET**  
Co-encadrement de la thèse : **Lionel FOURMENT**

### **Jury**

**M. Tudor BALAN**, Docteur, LPMM, ENSAM Metz  
**M. Emin BAYRAKTAR**, Professeur des universités, LISMMA, Supmeca Paris  
**Mme Anne-Marie HABRAKEN**, Directeur de Recherches, MS<sup>2</sup>F – ArGenCo, Université de Liège  
**M. Lionel FOURMENT**, Docteur ingénieur, CEMEF, Mines ParisTech  
**M. Pierre MONTMITONNET**, Docteur ingénieur, CEMEF, Mines ParisTech  
**M. Christian BOBADILLA**, Ingénieur, ArcelorMittal Research and Development, Gandrange  
**M. Sylvain FOISSEY**, Ingénieur, ArcelorMittal Wire Solutions, Bourg-en-Bresse

Rapporteur  
Rapporteur  
Examineur  
Examineur  
Examineur  
Invité

# Acknowledgments

I would like to thank M. LEGAIT, director of Mines Paristech, as well as M. CHENOT, who was at the beginning of my thesis director of CEMEF, for giving me the opportunity to study in this laboratory. I am deeply thankful to Christian BOBADILLA and Sylvain FOISSEY, from ArcelorMittal Gandrange and Bourg-en-Bresse, for trusting me.

I wish to express my sincere gratefulness to the members of my jury for taking time out of their busy schedules to assess my work. It is a great honour to have you on my thesis committee.

I would like to express my warm appreciation to my supervisor, Pierre MONTMITONNET, for his aid, support and advice during these three years at CEMEF. This research would not have been possible without Yvan CHASTEL and Lionel FOURMENT, whose expertise was inspiring to me. It has been a fulfilling experience from a personal as well as a professional perspective and it has been also a great pleasure to work with them.

After spending three years at CEMEF and ArcelorMittal, there are many people I wish to thank. First of all, I am deeply indebted to Gilbert, Eric and Francis for their guidance and advice in the workshop. I wish to thank the people I worked with on the SEM and TEM, Monique, Michel – Yves and Suzanne who have widely contributed to the success of this project. I must also acknowledge Sylvain FOISSEY's team in Bourg-en-Bresse, Anne, Christophe and the newcomers, for passing their knowledge on metal forming and for being brave enough to attend all my presentations. I obviously do not forget all the technicians, engineers, researchers and interns from the Gandrange research centre who have enabled me to acquire a rigorous crystallographic preparation method. In particular, André LEFORT for his expertise in forming and steel industry field; Randolpho Villegas for his incredible competences in pearlitic steel microstructural analysis; and Nicolas PERSEM, for his constant support in the use of the FORGE2005® software. Finally, many thanks to Stéphane MARIE for his availability and his help in optimization field.

I wish to express my most sincere and friendly thanks to my colleagues from CEMEF with whom I shared offices (in particular the 2006 MATMEF students who have welcomed me and with whom I have spent enjoyable times), coffee and lunch breaks, nights outs and MSV evenings. Many thanks to the 2006 PhD students and the VSM for MSV team I was a member of. Strong ties have emerged and I will not forget any of you. Thanks to David for having introduced me to the Riviera Rugby Club, in which I spent great moments. My passion

for rugby has not vanished! I cannot thank Emile Roux enough for his availability and his support in the final straight of my PhD. And finally, many thanks to Damien and Benoît, my rugby, evenings and card partners (and roommates), for their enduring friendship and who have strongly contributed to make these three years an exceptional life experience.

It is now time to thank the people who are the dearest to me.

My first thought goes to my family. My parents, my brothers, my grand-father, thank you all for being a real support to me during all these years. Thank you for always being here.

Last but not least, thank you, Myriam, for remaining by my side through thick and thin. You have always been here to cheer me up and to boost me in the hardest moments. You are the most important person to me. This thesis is dedicated to you and I am sure that yours will also be a great success.

# Résumé français

Les aciers laminés à plat sont utilisés par exemple dans l'industrie automobile. Comme des géométries de plus en plus complexes, ainsi que des caractéristiques mécaniques de plus en plus hautes sont sans cesse requises, les limites du procédé de mise en forme risquent d'être atteintes. En outre, l'endommagement est un point critique du cahier des charges afin d'éviter le risque de rupture lors de la production et en service. C'est pourquoi, la prédiction de l'endommagement apparaît comme un point essentiel pour optimiser ces procédés.

Tout d'abord, l'acier haut carbone a été caractérisé expérimentalement par une large campagne d'essais : essais de traction, compression, torsion, cisaillement tout au long de la gamme de mise en forme à froid. Par ailleurs, les essais de compression ont mis en évidence une ovalisation dans le sens transverse des éprouvettes au cours et en fin de tréfilage qui est la traduction d'une anisotropie mécanique évolutive. C'est pourquoi un critère anisotrope de type Hill quadratique a été choisi pour simuler le comportement du matériau et ses paramètres ont été identifiés à partir de l'équation de contour des éprouvettes de compression. De plus, les paramètres de frottement en tréfilage et en laminage ont été calés, par la mesure de la force de tréfilage avec un axe dynamométrique dans un cas et par des essais de bi poinçonnement dans l'autre cas. Enfin, les paramètres du critère d'endommagement de Lemaître ont été identifiés avant tréfilage afin de pouvoir prédire l'évolution de l'endommagement au cours de la mise en forme.

Ensuite, une fois cette caractérisation effectuée, la simulation du tréfilage et du laminage a été réalisée au moyen d'un logiciel d'éléments finis, FORGE2005®. Une modélisation avec un comportement isotrope a permis d'enrichir les connaissances de ces deux procédés en terme de déformation, taux de déformation, contraintes, prédiction de la géométrie finale... Plusieurs études de sensibilité ont été conduites afin d'apporter des informations supplémentaires. Elles ont concerné le transfert des contraintes résiduelles du tréfilage au laminage, l'influence du transport de la cartographie exacte des déformations du tréfilage au laminage. Un résultat majeur de la modélisation isotrope a été la sous estimation de 10% de la largeur du plat en fin de laminage. Enfin, le laminage a été simulé avec une loi de comportement anisotrope, précédemment identifiée. Cette simulation a mis en évidence un fort impact de l'anisotropie mécanique dans la prédiction de l'élargissement des plats puisque que la sous estimation est alors de 5%. Deux études : une sur le frottement et une sur les paramètres de Hill, n'ont pu expliquer ce sous élargissement restant.

Ensuite, une étude microstructurale couplée à une analyse des mécanismes d'endommagement a été effectuée sur les aciers perlitiques à haut carbone au cours du tréfilage et du laminage. L'anisotropie mécanique est issue de l'orientation progressive des colonies perlitiques au tréfilage et de l'apparition d'une texture cristallographique préférentielle. Cette étude a aussi mis en évidence la nature anisotrope de l'endommagement en relation avec l'évolution microstructurale. Trois mécanismes d'endommagement ont pu être identifiés au cours du tréfilage : l'amorçage de cavités au voisinage d'une inclusion dont les mécanismes diffèrent en fonction du type d'inclusion ; l'amorçage de cavités comme une conséquence de rupture transverse des colonies perlitiques défavorablement alignés par rapport à l'axe de tréfilage ; la nucléation de cavités aux joints de colonies fortement désorientées. Au cours du laminage, l'anisotropie mécanique est stoppée. Ce procédé qui se caractérise par une hétérogénéité de déformation entraîne une microstructure différente entre le cœur et les bords du plat, alors que le tréfilage est un procédé de traction avec des déformations homogènes dues à la symétrie de révolution. Cette déformation hétérogène affecte fortement l'évolution de l'endommagement, notamment avec une densité de cavités plus importante à cœur qui est la zone la plus déformée. Le facteur de forme des cavités est aussi fortement lié à cette hétérogénéité. Les décohésions et les cavités qui se développaient selon l'axe de fil au cours du tréfilage sont élargies dans la direction transverse pendant le laminage. Au voisinage des inclusions, les cinétiques de propagation / transport des décohésions sont également modifiées.

L'utilisation de l'outil numérique a apporté des informations supplémentaires. L'évolution morphologique des cavités a été numériquement vérifiée ; elle est en un bon accord avec le champ de déformation. De plus, l'utilisation d'un critère d'endommagement a permis de vérifier la localisation de l'endommagement à cœur, ainsi que d'exhiber un endommagement surfacique pas forcément visible d'un point de vue microstructural et de correctement prédire le risque de rupture.

Enfin, des calculs d'optimisation ont été effectués. Une stratégie d'évolution assistée par méta modèle a été adoptée. Cette méthode a déjà démontré sa robustesse et son efficacité pour des applications complexes de mise en forme. Cette stratégie consiste en une approximation de la simulation numérique afin d'estimer la réponse de la fonction coût. Seules les meilleures solutions probables sont effectivement simulées ce qui permet d'économiser 80% du temps de calcul. L'optimisation du tréfilage a porté sur la géométrie des filières : le demi angle d'entrée de filière, la longueur de portée et la réduction avec des optimisations mono et multi objectifs : la force de tréfilage et l'endommagement. Les calculs ont montré que quelle que soit la fonction coût, la longueur de portée a une influence mineure sur l'optimum par rapport au demi-angle de filière. Par ailleurs, la minimisation de la force de tréfilage a permis de retrouver la notion d'angle optimal, mise en évidence expérimentalement il y a plusieurs

décennies. Par contre, la minimisation de l'endommagement donne un optimum totalement différent avec un angle minimal qui se cale donc sur la borne inférieure. Enfin, l'optimisation mono objectif pondéré des deux fonctions coûts et l'optimisation multi objectif a mis en évidence la possibilité de diminuer fortement l'endommagement sans trop augmenter la force de tréfilage et le risque de rupture.

# Table of Content

<b>Chapter I</b>	<b>Introduction</b>	<b>10</b>
<b>I.1</b>	<b>Industrial Context</b>	<b>10</b>
<b>I.2</b>	<b>High carbon steel forming processes</b>	<b>10</b>
I.2.1	Four-stepped wire drawing	12
I.2.2	Cold rolling	13
I.2.3	Results	14
I.2.3.1	Process understanding by means of the triaxiality evolution	14
I.2.3.2	Damage prediction	15
I.2.3.3	Final geometry and widening prediction	17
<b>I.3</b>	<b>Objectives of the thesis</b>	<b>19</b>
<b>I.4</b>	<b>Organisation of the thesis</b>	<b>19</b>
<b>Chapter II</b>	<b>Bibliography Review</b>	<b>22</b>
<b>II.1</b>	<b>Lamellar microstructure</b>	<b>23</b>
II.1.1	Influence of patenting on microstructure and mechanical properties	23
II.1.2	Micro - Mesoscopic scale	24
II.1.2.1	Drawn wire	24
II.1.2.2	Cold rolled sheets	26
II.1.3	Macroscopic scale	28
II.1.3.1	Drawn wire	28
II.1.3.2	Cold rolled sheet	28
II.1.4	Summary	29
<b>II.2</b>	<b>Yield functions</b>	<b>29</b>
II.2.1	Isotropic yield functions	30
II.2.1.1	Tresca criterion	30
II.2.1.2	Von Mises criterion	30
II.2.1.3	General quadratic and non-quadratic isotropic criterion	31
II.2.2	Anisotropic yield functions	33
II.2.2.1	Hill quadratic criterion	33
II.2.2.2	Hill non quadratic criterion	33
II.2.2.3	Hosford non quadratic criterion	33
II.2.2.4	Other anisotropic functions	34
II.2.3	Choice of a yield function	35
<b>II.3</b>	<b>Damage mechanisms and models</b>	<b>36</b>
II.3.1	Ductile damage	36
II.3.1.1	Ductile damage characterization	36
II.3.1.2	Ductile damage mechanisms	36
II.3.1.2.1	Nucleation	37
II.3.1.2.2	Growth	38
II.3.1.2.3	Coalescence	38
II.3.2	Ductile damage models	39
II.3.2.1	Introduction	39
II.3.2.2	Non-coupled damage models	40
II.3.2.2.1	Models based on a microscopic analysis	40
II.3.2.2.2	Models based on a macroscopic analysis	43
II.3.2.3	Coupled damage models	43
II.3.2.3.1	Damage variable and effective stress concept	44
II.3.2.3.2	Isotropic Lemaître's model	45
II.3.2.3.2.1	General framework of thermodynamics of damage	45
II.3.2.3.2.2	State potential for isotropic damage	46
II.3.2.3.2.3	Formulation of the isotropic unified damage law	47

II.3.2.3.2.4	Uniaxial behaviour	48
II.3.2.3.3	Tension / compression damage asymmetry, crack closure effects and cut-off value of stress triaxiality	49
II.3.2.3.4	Framework of porous media plasticity	50
II.3.2.4	Microscopic numerical modelling	50
II.3.2.5	Microscopic experimental modelling	51
II.3.3	Choice of a relevant damage model	52
<b>II.4</b>	<b>Summary</b>	<b>54</b>
<b>II.5</b>	<b>Résumé français</b>	<b>56</b>
<b>Chapter III</b>	<b>Experimental mechanical characterisation</b>	<b>58</b>
<b>III.1</b>	<b>Identification of a numerical behaviour law</b>	<b>58</b>
III.1.1	Experimental tests	58
III.1.2	Identification method	59
<b>III.2</b>	<b>Identification of friction parameters</b>	<b>61</b>
III.2.1	Identification of the friction parameter during wire drawing	61
III.2.2	Identification of the friction parameter during rolling	62
<b>III.3</b>	<b>Highlighting the anisotropy phenomenon</b>	<b>63</b>
III.3.1	Compression tests during wire drawing	63
III.3.1.1	Longitudinal compression tests	63
III.3.1.2	Transverse compression tests	64
III.3.2	Comparison of the stress-strain curves	65
<b>III.4</b>	<b>Further mechanical tests</b>	<b>66</b>
III.4.1	Torsion test	66
III.4.1.1	Advantages	66
III.4.1.2	Results	67
III.4.1.3	Fields and Backofen method for the stress-strain curve	68
III.4.2	Ultimate drawing	68
III.4.3	Complete mechanical behaviour	70
<b>III.5</b>	<b>Identification of Hill's parameters</b>	<b>71</b>
III.5.1	Anisotropic constitutive model	71
III.5.2	Coefficients measurement	72
III.5.2.1	At the end of drawing	72
III.5.2.2	At the end of rolling	74
<b>III.6</b>	<b>Identification of Lemaître's parameters</b>	<b>77</b>
III.6.1	Inverse analysis method	77
III.6.2	Hardening law identification	78
III.6.3	Damage parameters identification	80
<b>III.7</b>	<b>Summary</b>	<b>82</b>
<b>III.8</b>	<b>Résumé français</b>	<b>83</b>
<b>Chapter IV</b>	<b>Process Modelling</b>	<b>84</b>
<b>IV.1</b>	<b>The mechanical problem</b>	<b>84</b>
IV.1.1	Continuous problem formulation	84
IV.1.1.1	Conservation equations	84
IV.1.1.2	Boundary conditions	85
IV.1.1.3	Strong formulation of the continuous problem	86
IV.1.1.4	Weak formulation of the continuous problem	86
IV.1.2	Discretized problem formulation	87
IV.1.2.1	Time discretization	87
IV.1.2.2	Spatial discretization	88
IV.1.2.3	Contact management	88
IV.1.3	Problem resolution	89

<b>IV.2</b>	<b>Cold forming processes simulation</b>	<b>90</b>
IV.2.1	Isotropic behaviour	91
IV.2.1.1	Strain rate and strain evolution	91
IV.2.1.2	Stress evolution during wire drawing	93
IV.2.1.2.1	Equivalent stress (according to Von Mises)	93
IV.2.1.2.2	$\sigma_{RR}$ radial stress evolution	93
IV.2.1.2.3	$\sigma_{\theta\theta}$ orthoradial stress evolution	94
IV.2.1.2.4	$\sigma_{xx}$ longitudinal stress evolution	95
IV.2.1.2.5	$\sigma_{xx}$ residual longitudinal stress evolution	96
IV.2.1.3	Stress evolution during rolling	97
IV.2.1.3.1	Equivalent stress (according to Von Mises)	97
IV.2.1.3.2	Longitudinal stress	97
IV.2.1.3.3	Transverse stress	99
IV.2.1.3.4	Vertical stress	99
IV.2.1.3.5	Danger zones	100
IV.2.1.4	Widening prediction	100
IV.2.2	Sensitivity studies	101
IV.2.2.1	Influence of strain map transfer from drawing to rolling	101
IV.2.2.2	Influence of residual stresses transfer from drawing to rolling	102
IV.2.3	Influence of anisotropy	104
IV.2.3.1	On strain – stress evolution	104
IV.2.3.2	On widening prediction	105
IV.2.3.2.1	Sensitivity study on anisotropic coefficients	105
IV.2.3.2.2	Sensitivity study on friction	106
<b>IV.3</b>	<b>Conclusions</b>	<b>107</b>
<b>IV.4</b>	<b>Summary</b>	<b>108</b>
<b>IV.5</b>	<b>Résumé français</b>	<b>109</b>
<b>Chapter V</b>	<b>Microstructure and Damage</b>	<b>110</b>
<b>V.1</b>	<b>Experimental procedure and devices</b>	<b>110</b>
V.1.1	Experimental devices for micro and nanoscopic analysis	110
V.1.2	Experimental procedure of sample preparation	111
V.1.2.1	For SEM pictures	111
V.1.2.2	For TEM pictures	111
<b>V.2</b>	<b>Analysis of the first damage steps during ultimate drawing</b>	<b>112</b>
V.2.1	Ultimate drawing characteristics	112
V.2.2	Microstructural evolution during ultimate drawing: pearlite orientation	113
V.2.2.1	Before drawing	113
V.2.2.2	After 4 passes (equivalent to the end of drawing in the real process): $\epsilon=0.77$	114
V.2.2.3	After 10 passes: $\epsilon=2.1$	115
V.2.2.4	After 16 passes: $\epsilon=3.4$	116
V.2.3	Damage initiation and growth during ultimate drawing	118
V.2.3.1	After 4 passes (equivalent to the end of drawing in the real process): $\epsilon=0.77$	118
V.2.3.2	After 10 passes: $\epsilon=2.1$	119
V.2.3.3	After 16 passes: $\epsilon=3.4$	121
V.2.3.4	Synthesis	122
<b>V.3</b>	<b>Analysis of damage evolution during wire drawing + rolling</b>	<b>123</b>
V.3.1	Process characteristics	123
V.3.2	Microstructural evolution during rolling	123
V.3.3	Damage evolution during rolling	125
V.3.3.1	Transverse cutting plane	125
V.3.3.2	Longitudinal cutting plane	128
<b>V.4</b>	<b>Schematic representation of damage at the end of rolling</b>	<b>130</b>
V.4.1	From experimental observations	130
V.4.2	From process numerical simulation by using spherical markers	132

V.4.3	Comparison between the two representations _____	135
<b>V.5</b>	<b>Damage prediction with finite element modelling _____</b>	<b>137</b>
<b>V.6</b>	<b>Summary _____</b>	<b>139</b>
<b>V.7</b>	<b>Résumé français _____</b>	<b>142</b>
<b>Chapter VI Optimization _____</b>		<b>145</b>
<b>VI.1</b>	<b>Optimization strategy _____</b>	<b>145</b>
VI.1.1	Modelling _____	145
VI.1.1.1	Choice of the optimization situation / reference configuration _____	146
VI.1.1.2	Choice of optimization parameters and their mathematical translations _____	146
VI.1.1.3	Choice of objective functions and constraints and their mathematical translations _____	147
VI.1.1.4	Definition of parameters limits _____	147
VI.1.2	Selection _____	148
VI.1.3	Resolution _____	148
<b>VI.2</b>	<b>Optimization methods and their applications to metal forming processes _____</b>	<b>148</b>
VI.2.1	Gradient-based algorithms _____	148
VI.2.2	Global algorithms _____	149
VI.2.3	Approximate algorithms _____	151
VI.2.4	Hybrid algorithms _____	153
<b>VI.3</b>	<b>Choice of an optimization algorithm _____</b>	<b>153</b>
VI.3.1	MAES algorithm _____	154
VI.3.2	Parallel calculations _____	155
<b>VI.4</b>	<b>Wire drawing optimization _____</b>	<b>155</b>
VI.4.1	Use of the optimization strategy (see VI.1) _____	155
VI.4.1.1	Choice of the optimization case _____	155
VI.4.1.2	Choice of optimization parameters and their mathematical translations _____	156
VI.4.1.3	Choice of objective function and its mathematical translation _____	156
VI.4.1.4	Definition of parameters variation range _____	157
VI.4.2	Parameters sensitivity study: optimization of a single drawing pass _____	157
VI.4.2.1	Mono-objective optimization _____	157
VI.4.2.1.1	Optimization of the drawing force _____	157
VI.4.2.1.2	Optimization of damage _____	162
VI.4.2.1.3	Optimization of damage and force _____	166
VI.4.2.2	Multi-objective optimization _____	167
VI.4.3	Full wire drawing optimization _____	168
VI.4.4	Toward more objectives _____	170
<b>VI.5</b>	<b>Summary _____</b>	<b>171</b>
<b>VI.6</b>	<b>Résumé français _____</b>	<b>172</b>
<b>Chapter VII Conclusions and Perspectives _____</b>		<b>174</b>
<b>ANNEXES _____</b>		<b>177</b>
<b>ANNEX 1: Framework of porous media plasticity _____</b>		<b>177</b>
<b>ANNEX 2: Anisotropic damage models _____</b>		<b>179</b>
<b>ANNEX 3: Fields and Backofen method for the stress-strain curves _____</b>		<b>183</b>
<b>ANNEX 4: Explicative notice of a Focused Ion Beam (FIB) _____</b>		<b>187</b>
<b>References _____</b>		<b>192</b>

# Chapter I Introduction

## I.1 Industrial Context

ArcelorMittal produces flat and shape wires with quite a few different steel grades. For instance, flat-rolled steel wires are used in automotive industries and thus they have to be accurate in terms of final geometry and mechanical properties. Furthermore, flawlessness is a major point of technical specifications in order to avoid break risks in use or during production. Since ever-higher mechanical characteristics and more complex geometries are required, the limits of the current forming processes tend to be reached. Consequently, damage prediction appears as a major point in order to avoid material fracture.

The different damage steps: nucleation, growth and coalescence during forming processes need to be better understood in the case of the high carbon steels involved in this study. Experiments as well as numerical simulation will be used for this purpose. Thanks to this, process optimization will be carried out with adequate algorithms for high strain processes.

## I.2 High carbon steel forming processes

The overall manufacturing process involves seven major steps from continuous casting to final heat treatment as shown in Figure 1. The present work focuses on the two cold processes which are wire drawing on single-pass benches followed by multi-pass tandem rolling (Figure 2), starting from a patented wire rod. Patenting is a thermal treatment in which the hot-rolled wire is:

- Heated to a temperature higher than the austenitizing temperature (about 900°C)
- Cooled down in a lead bath (> 500°C) during a given time.

This results in a very fine wire microstructure (fine pearlite) and in excellent trade-off between high strength and high ductility.

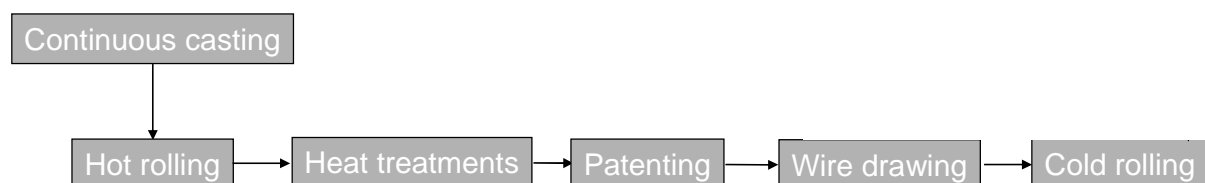


Figure 1: overall diagram of the forming process for high carbon steel

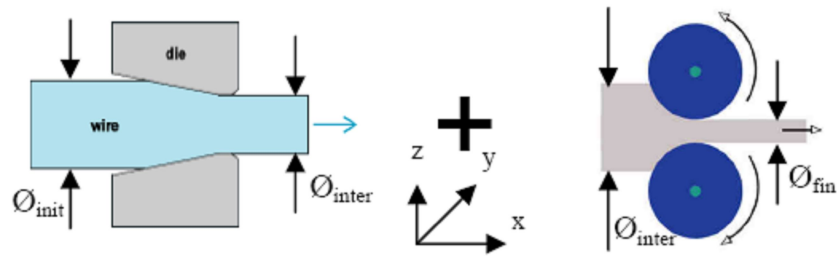


Figure 2: The cold forming processes

The material is a high carbon steel grade C72, i.e. the weight percentage of carbon is near the eutectoid point in the Iron-Iron Carbide phase diagram as shown in Figure 3.

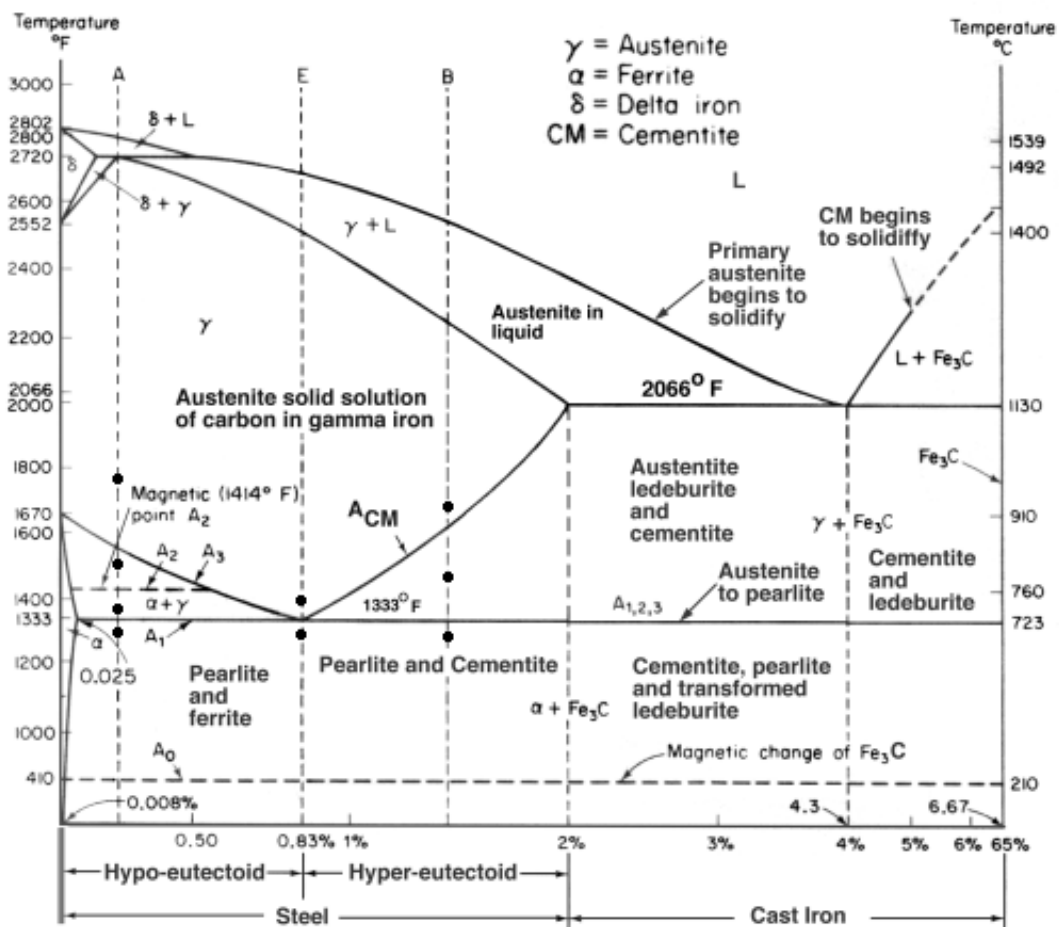
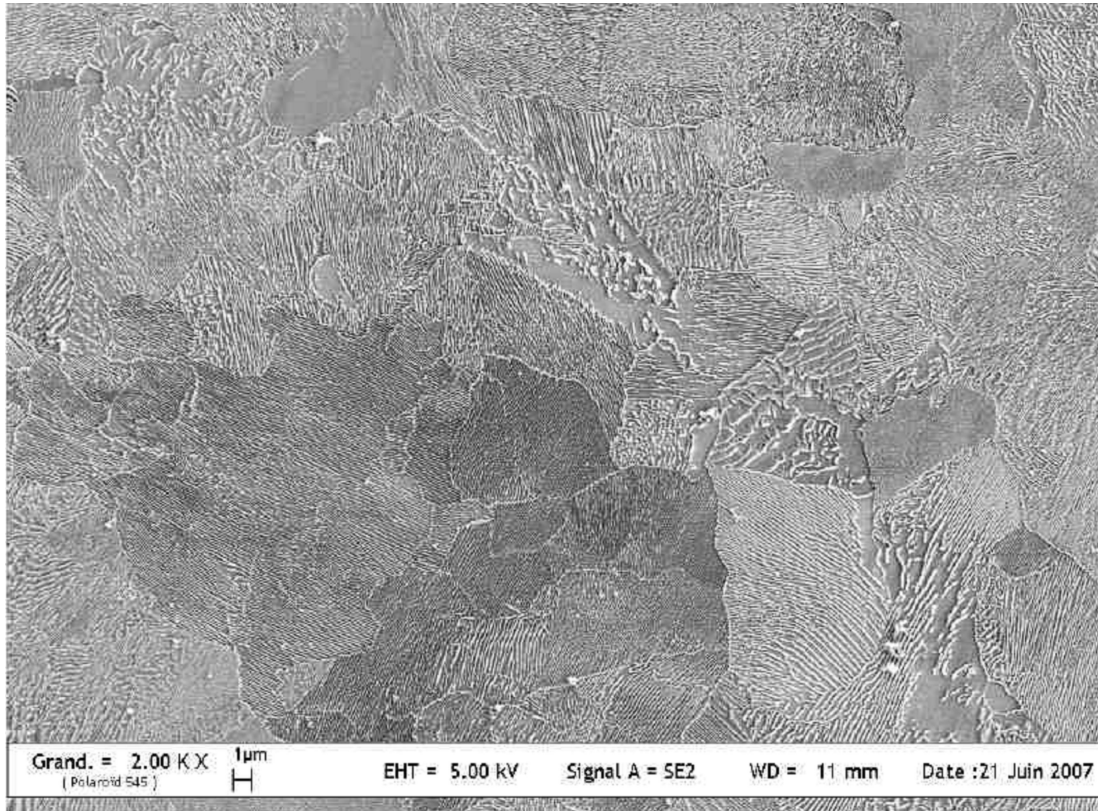


Figure 3: Fe-Fe<sub>3</sub>C Phase Diagram [1]

The microstructure is then pearlitic: ferrite with lamellar cementite. SEM pictures show cementite lamellae in white and ferrite in dark (Figure 4). The microstructure is homogeneous. Grains are equiaxed, with a random crystallographic texture. As there is a crystallographic orientation relationship between  $\alpha$  ferrite and cementite [2], lamellae have the

same orientation within a grain, but the random grain texture gives overall random lamellae and ferrite orientation.



**Figure 4: Initial high carbon steel microstructure (patented wire) [3]**

Following [4] and [5], the industrial drawing and flat-rolling process has been simulated by FEM (Forge2005®). This first attempt at numerical modelling will show some discrepancies with experiments, the correction of which will be addressed in the following chapters.

### **I.2.1 Four-stepped wire drawing**

This forming process consists in reducing product section by pulling the wire through a single or series of drawing dies [6] (Figure 2). To make this operation easier, it needs lubrication at the entrance. This is done by a soap box situated upstream of each drawing die. A high strength level is reached by hardening and will be increased by rolling.

The mechanical analysis of the drawing process is performed with FORGE2005® on a 2D axis-symmetric simulation ( $\epsilon_{r\theta} = 0$ ) (Figure 5). The patented wire rod is isotropic before drawing. All properties acquired during each step are transferred to the next one in order to take into account progressive material hardening. Mesh size is equal to 0.5mm and the total nodes number is about 9600 for pass one and two and about 11500 and 12700 nodes for pass

three and four respectively. The wire is long enough to reach the steady state. A non deformable die is used to set drawing speed.

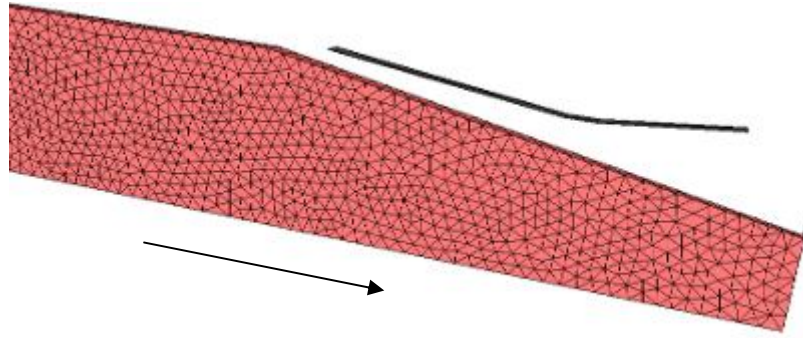


**Figure 5 : Beginning of the wire drawing simulation**

An elasto-plastic behaviour law is used [5] and will be detailed in section III.1:

$$\sigma = \sqrt{3} * 100.64(1 + 7.32\varepsilon^{0.13}) \quad (\text{I.1})$$

Friction law between drawing dies and wire is a Tresca law:

$$\tau_c = \bar{m} \frac{\sigma_0}{\sqrt{3}} \quad \text{with} \quad \bar{m} = 0.02 \quad (\text{I.2})$$

The identification of the friction coefficient will be presented in section III.2.1.

At the end of drawing, strain and stress values are transferred to rolling simulation.

## **I.2.2 Cold rolling**

This is a forming process by plastic deformation (Figure 2), bound to decrease product section thanks to two axisymmetric tools called “cylinders” [7]. Wire is pulled in the roll gap by their rotation. This operation imparts the wire with both the required final geometry and mechanical strength. The rolling mill has three stands which work in tandem, which means the wire is in the three stands simultaneously. Each stand is simulated separately in order to introduce proper interstand tension, which have been measured on the rolling line.

The process geometry calls for a 3D modelling but two symmetry planes are used to reduce computing time (Figure 6). The same workhardening equation is used and the same friction law but with  $\bar{m} = 0.25$  due to a different lubricant (low concentration oil in water emulsion). The identification of the friction coefficient will be introduced in part III.2.2. During 2D – 3D transfer, a manual remeshing took place and mesh size before rolling is 0.5mm leading to a total nodes number of 22000. At the beginning of the simulation a pushing die helps gripping of the wire by the cylinder, and then the cylinders become masters.



Figure 6: Beginning of the rolling simulation

## I.2.3 Results

### I.2.3.1 Process understanding by means of the triaxiality evolution

Triaxiality is the ratio between the hydrostatic pressure and the equivalent stress.

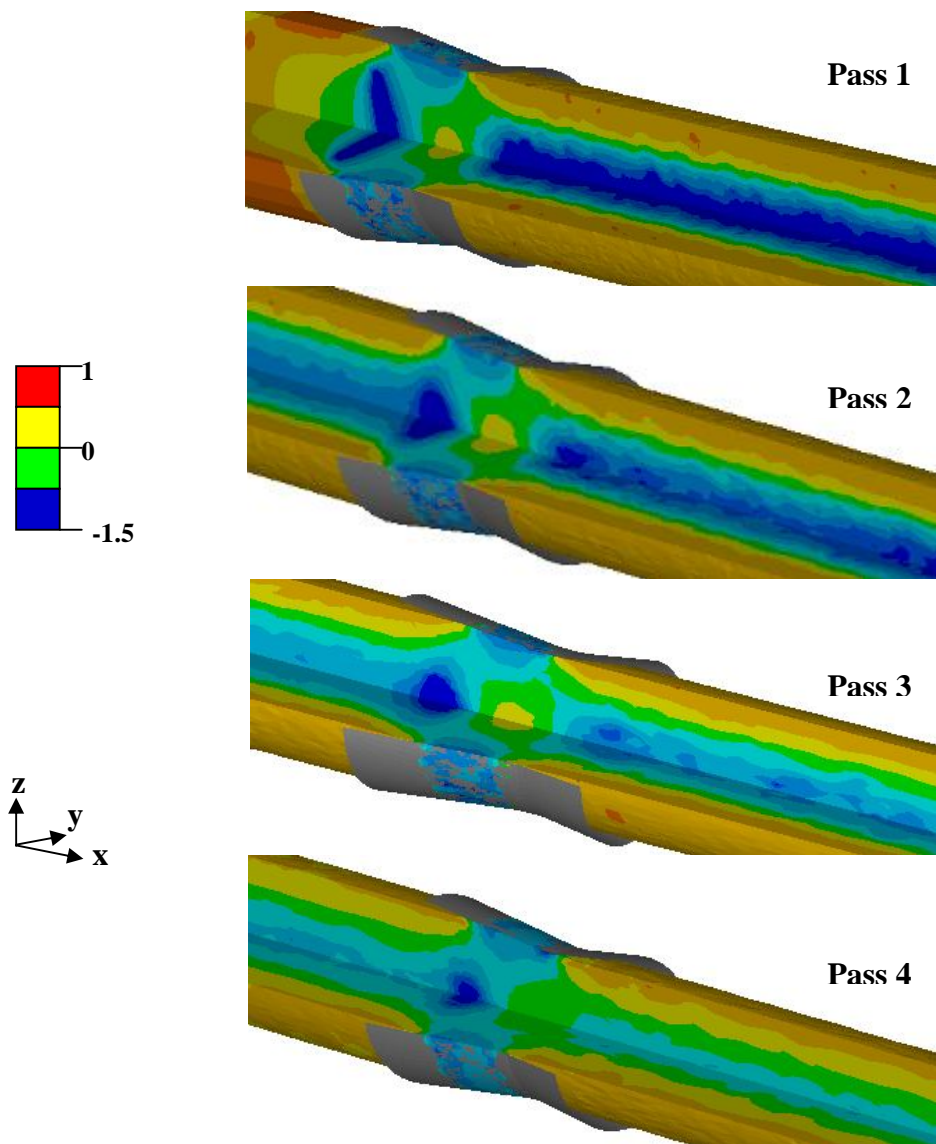


Figure 7: Triaxiality evolution during wire drawing

A triaxiality analysis enables to understand the mechanical behaviour during forming and is presented in Figure 7 and Figure 8. Wire drawing process is mainly compressive in the wire core with local tensile areas. During rolling, the triaxiality is mainly compressive as well in the wire core but also tensile on edges.

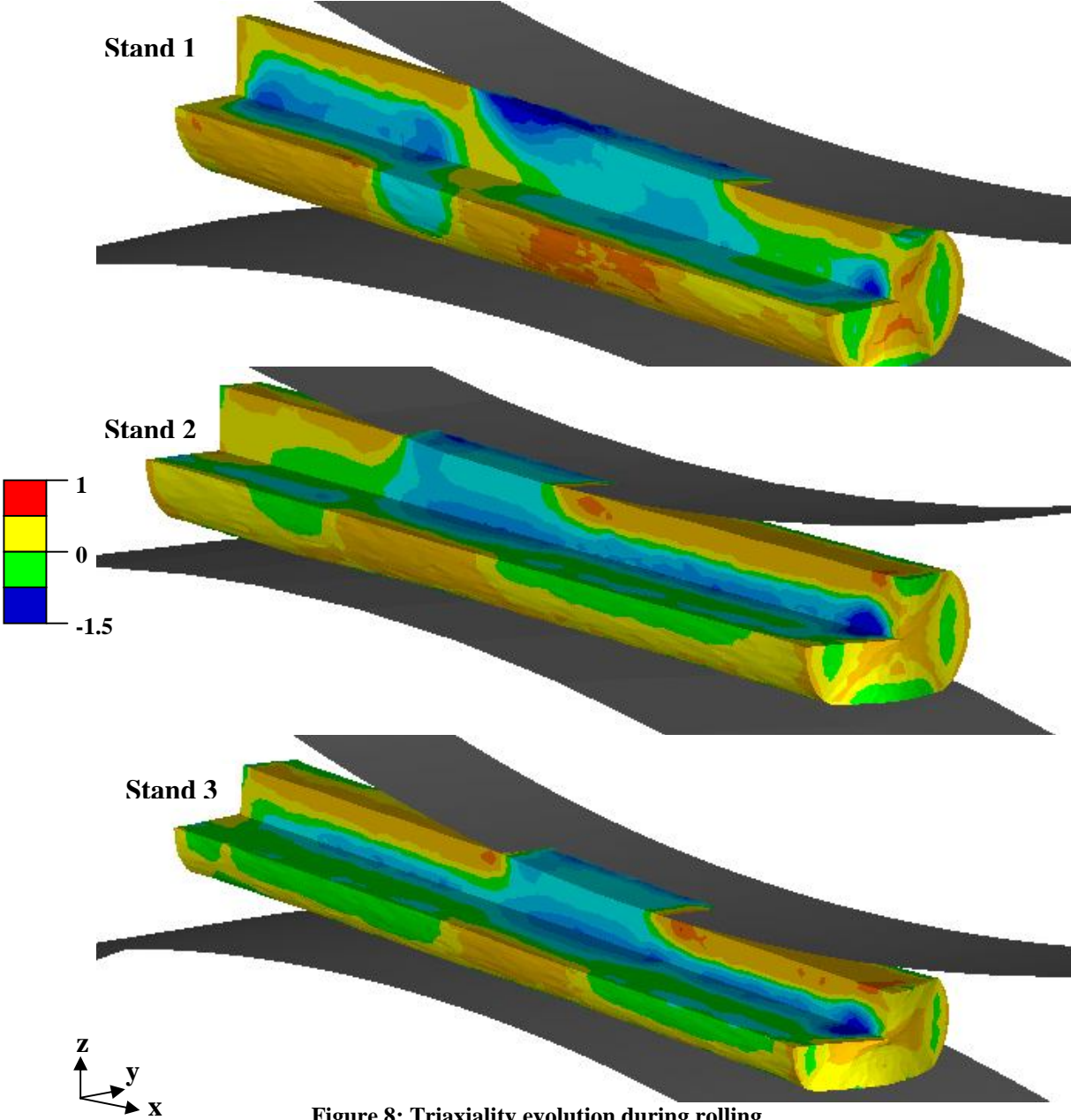


Figure 8: Triaxiality evolution during rolling

I.2.3.2 Damage prediction

A first analysis of damage has been done with the use of a macroscopic non coupled criterion, i.e. Latham and Cockcroft criterion which is written as follows:

$$D_{LC} = \int_0^{\varepsilon_f} \frac{\max(\sigma_I, 0)}{\sigma_{eq}} d\varepsilon_p = V_D \quad (I.3)$$

with  $V_D$  material characteristic constant and  $\sigma_{eq}$  the equivalent stress.

These criteria determine a critical value, constant at fracture and supposed independent on strain path. Damage evolution during wire drawing followed by rolling exhibits in the wire core a severe and constant increase at each pass of drawing and at the first rolling stand, as shown in Figure 9, Figure 10 and Figure 11.

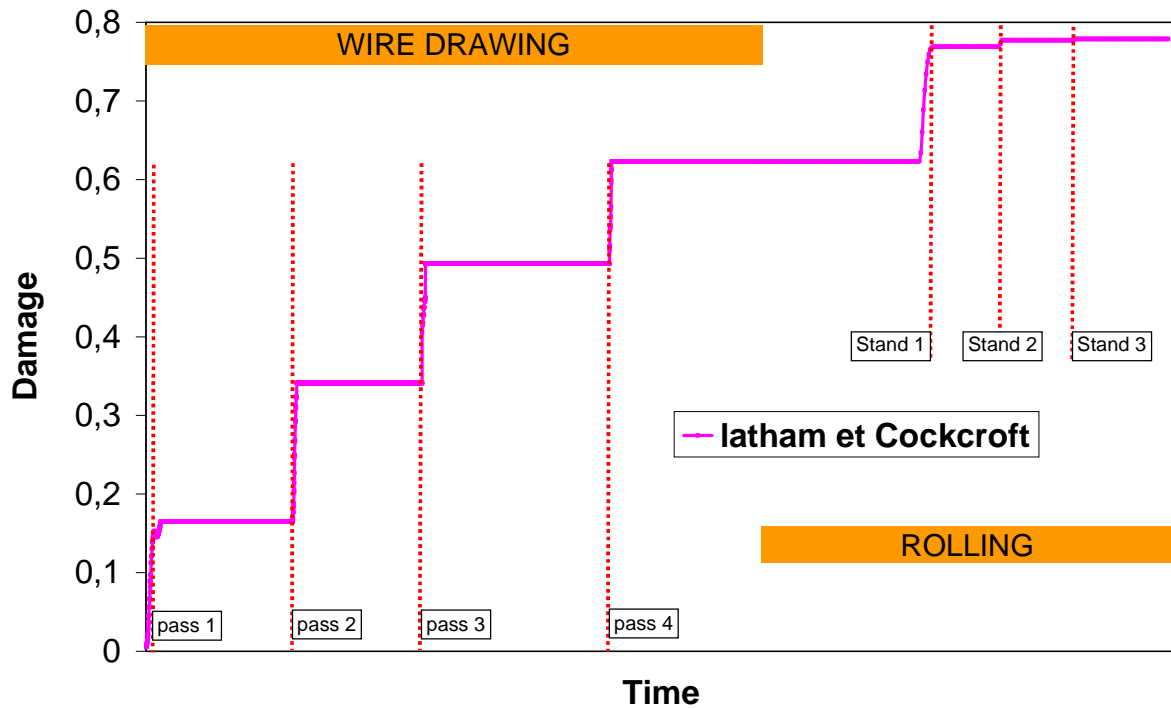


Figure 9: Latham and Cockcroft damage evolution during cold forming processes in the wire core

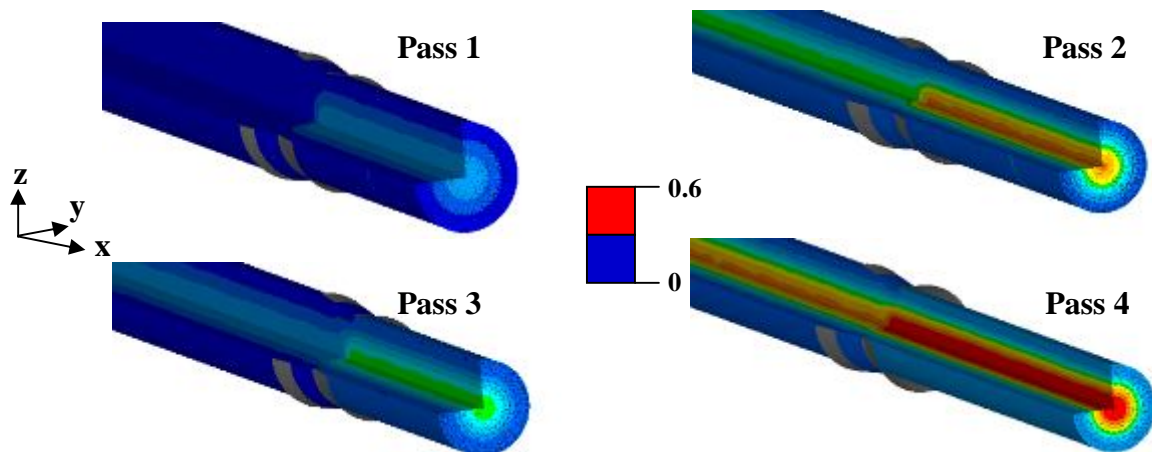


Figure 10: Damage evolution during wire drawing with Latham and Cockcroft's criterion

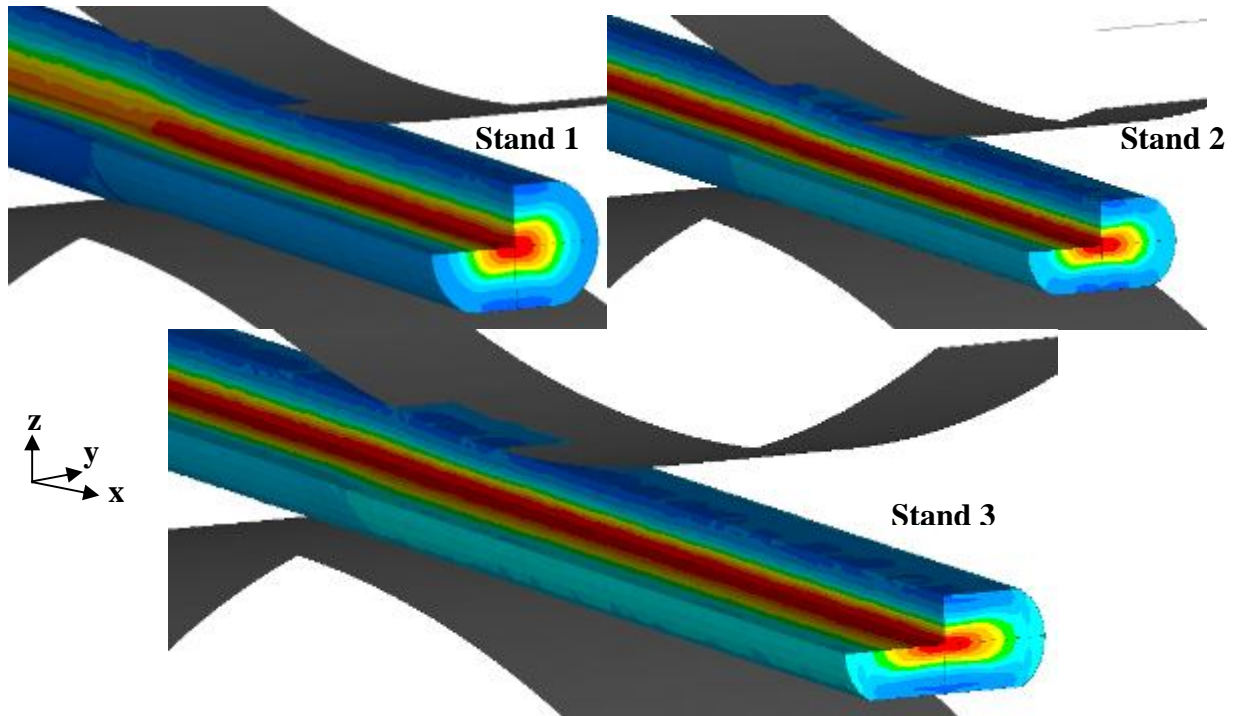


Figure 11: Damage evolution during rolling stand with Latham and Cockcroft's criterion

### I.2.3.3 Final geometry and widening prediction

As mentioned before, a major point to monitor is the output geometry after cold forming processes, as it is a critical aspect of technical specifications. However, when comparing the experimental and computed final cross-sections, a difference appears: the computed section is too narrow by  $\approx 10\%$ , way above the tolerance (Figure 12).

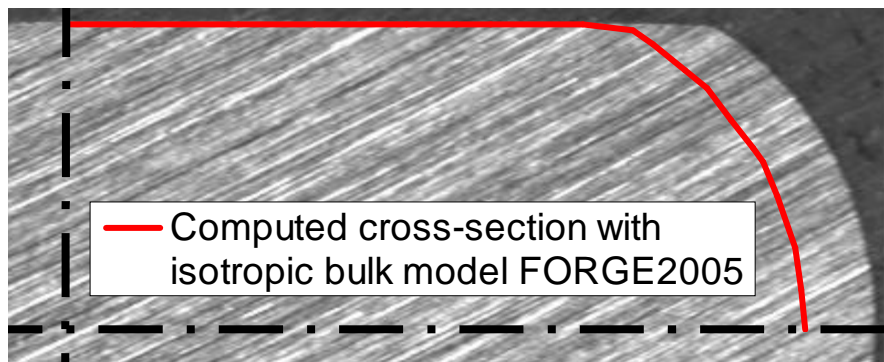


Figure 12: Comparison of experimental and computed (dark red line) output cross-sections

This difference might originate in the anisotropy introduced by the wire drawing process, coming either from a crystallographic or a morphological texture (grain elongation). In the case of high carbon steels, another probable origin of mechanical anisotropy is the progressive orientation of the pearlite colonies along the drawing axis, resulting also in the decrease of

cementite interlamellar spacing (Figure 13, Figure 4 and Figure 14) [8]-[12]. The structure alignment is a major contribution to the development of a strong crystallographic texture [13]-[16]. All this explains the appearance and evolution of a strong anisotropy, as well as changes in the mechanical properties [17], [18]. This mechanical anisotropy may have a non-negligible influence on damage mechanisms as well.

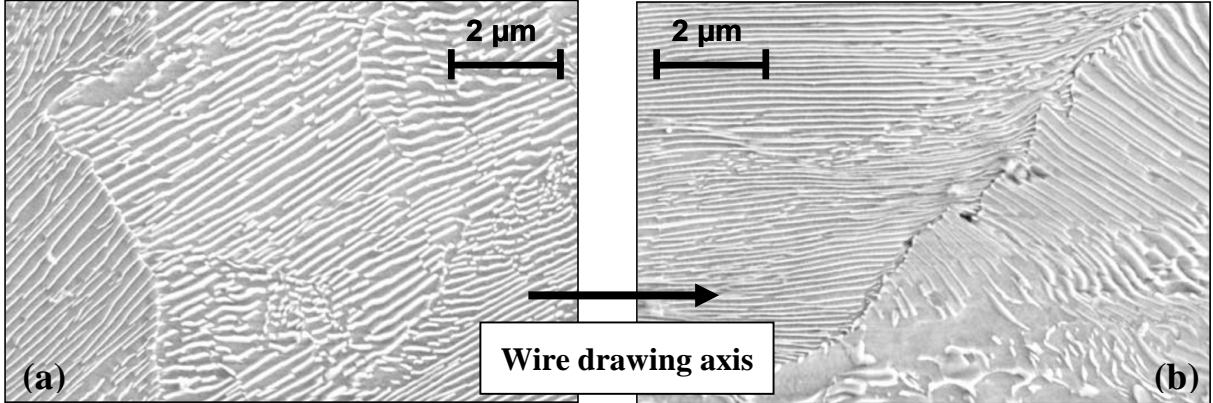


Figure 13: Evolution of the interlamellar spacing (a) before drawing (b) after drawing [3]

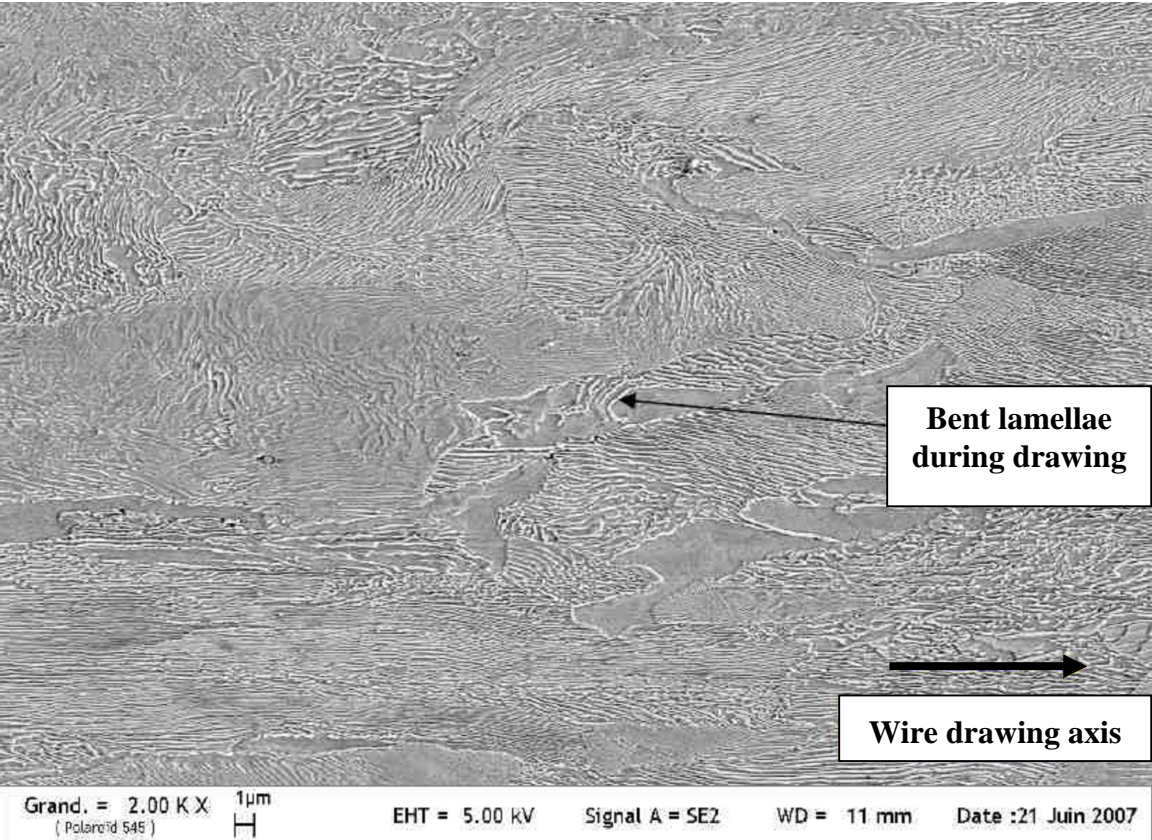


Figure 14: High carbon steel microstructure after drawing [3]

### **I.3 Objectives of the thesis**

This thesis aims at better understanding cold forming processes for high carbon steel in order to propose a semi-automatic multi-criteria process optimization. Before using FEM simulation to optimize both processes, we have to guarantee good control of adequate numerical options and a proper material behaviour (damage and plasticity laws), with geometry (width) and damage as quality criteria.

Mechanical behaviour will be studied thanks to an experimental campaign, as well as friction coefficient between dies and the wire. Then, mechanical analysis will be performed by simulating the two processes, with the material behaviour law previously identified from mechanical tests, in Forge2005®.

Concerning damage mechanisms, the same approach will be used, i.e. a microstructural analysis of damage will be carried out to better understand damage mechanisms; then an adapted damage function will be used in the finite element code to predict damage and fracture risks.

Then the road will be open for the last major issue, semi-automatic process optimization. The objective function will be built on the major requirements for a given product (either final mechanical properties, or geometry, or damage risk, or any multi-objective combination of these). Ideally, optimization parameters may refer to the preform (wire rod diameter), to the drawing process (number of passes, total reduction), and / or to the rolling process (number of passes, reductions, roll shape). But accounting for all requirements and all optimization parameters simultaneously would be far too complex. Part of the work will consist in designing simplified approaches of relevant sub-problems, based on our knowledge of the processes and material evolution.

### **I.4 Organisation of the thesis**

This PhD report is organised as follows.

The following chapter (Chapter II) will introduce a bibliographical review useful to understand the whole of results that I will discuss. High carbon steel microstructure, mechanical behaviour, forming ... will be addressed first. In a second part, a review will be given on anisotropic behaviour laws to guide the reader toward the chosen anisotropic criterion for our process simulation. Anisotropy is a known phenomenon for sheet rolling but very few articles deal with bulk material; this is one of the innovative points of this thesis. Finally, the last section will be dedicated to damage mechanisms and ductile damage models. Both isotropic (to introduce major damage theory) and anisotropic damage models will be discussed. An effort will be made to highlight the complexity of parameters identification and

implementation of each function in order to give some clues as to the relevant damage model adapted to the two cold forming processes.

High carbon steel is used for this study and a complete understanding of its behaviour is required. Hence, experimental measurements will be described in Chapter III, presenting mechanical testing devices for tension, compression, shear and torsion tests. Experimental results will lead to the identification of a numerical behaviour law and to the confirmation of the existence of a strong mechanical anisotropy. Procedure adjustment for numerical parameters identification, i.e. anisotropic coefficients, will also be raised in this part, as well as the identification of damage parameters. Additional tests will be carried out to fit friction parameter.

The first results will concern a complete modelling of wire drawing and rolling processes and will be discussed in Chapter IV. Stress and strain state during cold forming process will be described in depth, insisting on strain heterogeneity. Furthermore, emphasis will be on the width prediction, i.e. comparison between experimental and simulated output cross-sections and thus, to see if the introduction of anisotropic behaviour law in our simulation improve and lead to a correct widening estimation. Finally these numerical results will be complemented with parametric studies on friction, interstand tension and on the influence of transferring or not wire drawing residual stresses from drawing to rolling.

Chapter V will focus on microstructure and damage. In a first step, a detailed experimental study of our two processes will be described. An ultimate wire drawing test procedure (different from the classical wire drawing industrial process) has been run to follow microstructural evolution and explain the appearance of an evolutive anisotropy to extreme limits in deformation. This extreme drawing will lead to the understanding of initiation and propagation damage stages during wire drawing, strongly linked to the anisotropic material flow, thanks to diverse microscopy techniques (optical microscopy [OM], Scanning Electron Microscopy [SEM], Focused Ion Beam / Transmission Electron Microscopy [FIB/TEM]). Then, the microstructural and damage evolution during rolling will be studied. As wire drawing and rolling have different strain paths, due to different process mechanics (wire drawing = axisymmetric section reduction with longitudinal elongation; rolling = vertical compression with transverse and longitudinal elongation), microstructure evolution will be modified as well as damage kinetics. It will be shown that strain heterogeneity during rolling has a deep impact on these two characteristics. A second step will bring new elements for the understanding of damage kinetics by the use of simulation. Virtual spherical markers will be used along forming simulation. Following their morphology as a function of their position in the wire give a very visual understanding of strain components heterogeneity in 3D. Finally,

analysis of a damage criterion will give further insight when comparing experimental and numerical damage maps during the process.

Optimization will be addressed in Chapter VI, starting with a bibliographical review of optimization methods, which are part of a wider optimization strategy. The choice of a MAES strategy (Meta-model Assisted Evolution Strategy) proposed by Emmerich and al. [19], will be justified. Then a second part will be about wire drawing optimization. Objective function, i.e. damage criterion, and optimization parameters will be introduced. A study on a single pass will be presented, focussing on the following points: drawing force as objective function, damage as objective function, influence of reduction and friction, simultaneous minimization of drawing force and damage, study of “skin-pass” (low reduction drawing). Finally, I will go on with the optimization of a four-stepped wire drawing sequence.

Overall results of this work will be summarized in the conclusions and perspectives chapter (Chapter VII), in terms of modelling and anisotropy, microstructure and damage. Directions will be given for further improvements of this study.

## Chapter II Bibliography Review

Steels are widely used in forming. Depending on applications, steels are used in different grades. The higher the carbon content of the steel is, the higher the initial strength is, for a given structure [6]. Thus, low carbon steels are used for staple, paper clip, screw and so on, whereas high carbon steels are used for heavy-duty pieces, e.g. for high strength wire like tire frames. Wires are joined together to make heavy-duty cables.

The carbon content determines the steel microstructure as it is shown in the Fe-Fe<sub>3</sub>C phase diagram (Figure 3); it therefore impacts on mechanical properties. For four decades, microstructure and mechanical properties evolution during forming processes have been investigated by a large scientific community. This has been done e.g. to understand the origin of fracture during wire drawing, which is strongly linked to the microstructure evolution. Then several authors tried to model the microstructure evolution at different scales. The first section presents the assessment of these researches for high carbon steels. Then investigation field is broadened with other lamellar alloys.

The main result of the primary simulation presented in chapter 1 will lead us to study the anisotropic behaviour of our high carbon steel, introduced by the wire drawing process. Plastic anisotropy is defined by different flow properties (tensile yield stress e.g.) in the three spatial directions. This difference in yield stress favours flow in one cross-sectional direction with respect to the other; an experimental manifestation is the ovalization of tensile or compression samples. Thus, anisotropy may be analysed both using stress and strain rate tensors. Since the 50's, many authors have tried to model anisotropy by different ways in order to predict both phenomena simultaneously. But fitting ovalization and yield stress is difficult. This difficulty is usual in sheet forming, where it is very hard to fit the angular dependence of both flow pattern (Lankford coefficient [20]) and yield stress. Thus, paragraph II.2 is devoted to a brief summary of the different kinds of anisotropic laws from the simplest to the more complex representation.

Damage mechanisms on steels have been extensively described and understood since several decades. A lot of criteria and damage laws have been developed in order to make good and accurate prediction of this physical phenomenon. Section II.3 aims at reminding the three steps of ductile damage mechanisms and at making the state of art of damage models.

## II.1 Lamellar microstructure

After the first two processes which are continuous casting and hot rolling followed by some heat treatments, steel is ready to be cold drawn and cold rolled to reach a high strength and a given geometry. To improve ductility and strength in the two cold processes, patenting (austenitization followed by quenching in a lead bath) is performed before cold forming.

### II.1.1 Influence of patenting on microstructure and mechanical properties

Patenting consists in heating the wire in a furnace above the austenitizing temperature (900-1000°C). This high temperature treatment produces uniform austenite of rather large grain size. The subsequent quench of small sections (e.g. wire rods) in molten lead – at a temperature higher than 500°C - gives very fine pearlite, preferably with no separation of primary ferrite [21]. Microstructure after patenting is shown in Figure 15.

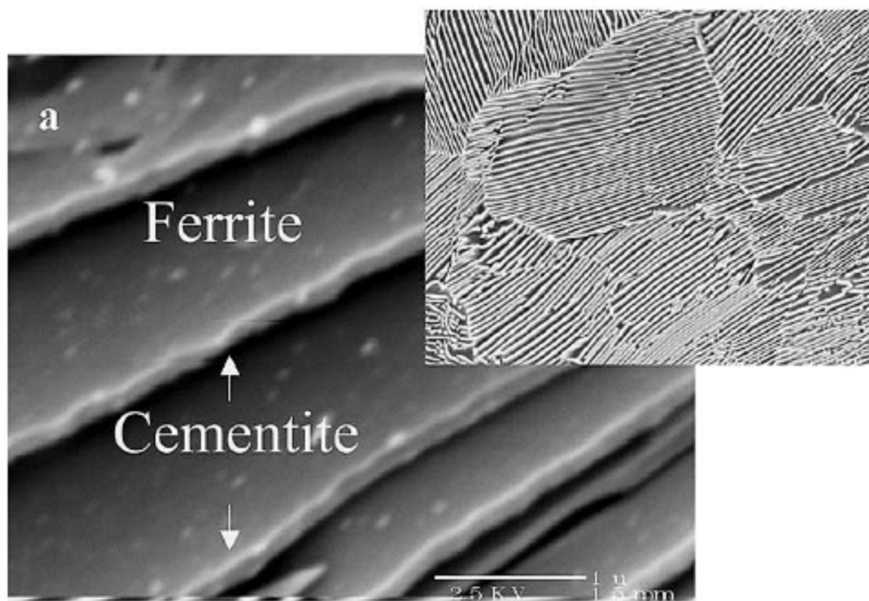


Figure 15: Pearlite in a patented steel wire; an insert shows pearlite colonies [15]

In terms of mechanical properties, patenting leads to an increase of the strength and the ductility as shown in Table 1. (NB: Agt means elongation).

Grade	Step	Rp0,2 (MPa)	Rm (MPa)	Agt%	A %	Z %
C72	Blank	539	978	9.0	14.8	34.8
	patented	722	1146	7.3	12.7	41.3

Table 1: Mechanical properties before and after patenting

Now, this microstructure can undergo different physical phenomena in function of forming processes. We are going to detail these phenomena with the observation scale as classification.

## II.1.2 Micro - Mesoscopic scale

### II.1.2.1 Drawn wire

To study the microstructure evolution and deformation mechanisms, the best example is ultimate drawing (the wire is drawn until mechanical limit is reached) where very high strain is obtained. Steel cord is processed using this technique, and it is very interesting from a scientific point of view.

At a mesoscopic level, it produces changes in pearlite colonies. Both, longitudinal and cross-sections are studied to have a 3D representation of microstructure evolution, which is controlled by different mechanisms in each direction. In a longitudinal view, the effect of drawing on microstructure is a progressive orientation of pearlite colonies by alignment of cementite lamellae (Figure 16) with its main axis approaching the wire axis [11], [12]. A relation can be obtained between drawing strain and the orientation of a colony characterized by an angle  $\alpha$  with regard to the wire axis [15]; its dependence on the initial angle  $\alpha_0$  is illustrated in Figure 17.

Furthermore, wire drawing causes a decrease of interlamellar spacing [8]-[12], [15], [22] as illustrated in Figure 18. Lamellae also become thinner. When the lamellar spacing of pearlite is decreasing, hardening of the drawn pearlitic steels is observed [18] and steel is more ductile. This can be explained by the thin cementite lamellae of fine pearlite being able to undergo substantial deformation by bending [23].

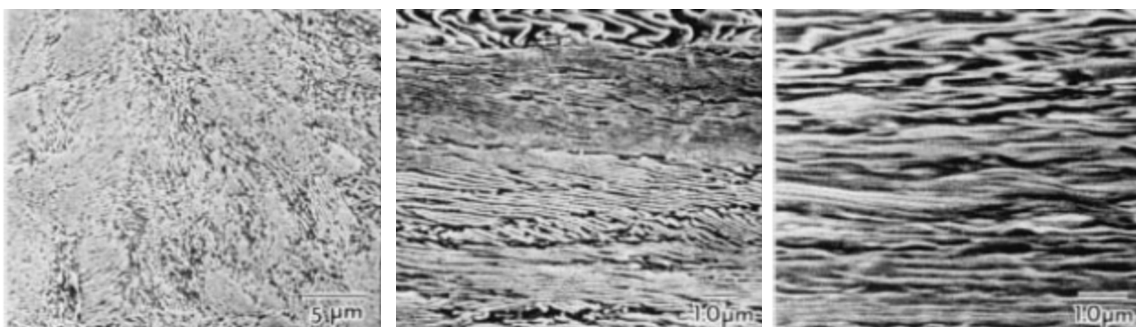


**Figure 16: SEM longitudinal micrographs showing microstructural changes with drawing strain for an eutectoid steel – (a)  $\epsilon = 0$ , (b)  $\epsilon = 0.91$ , (c)  $\epsilon = 2.32$  [11]**

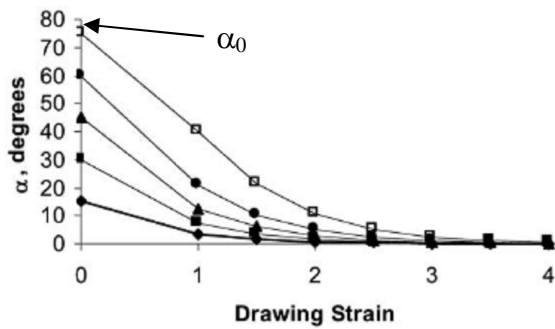


Figure 17: Dependence of  $\alpha$ -angle as a function of drawing strain [15]

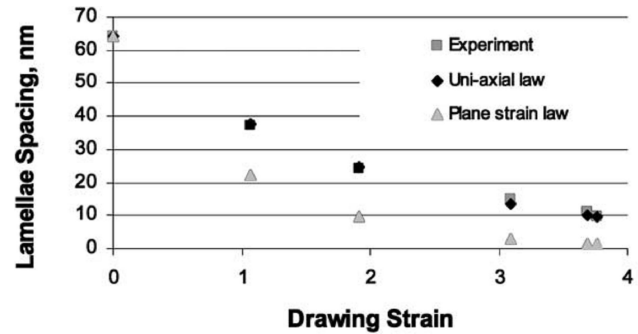


Figure 18: Inter-lamellar spacing as a function of drawing strain [15]

When samples are cut in the transverse direction, micrographs show the familiar swirled microstructure (Figure 19) due to a radial orientation of [001] direction of ferrite [15].

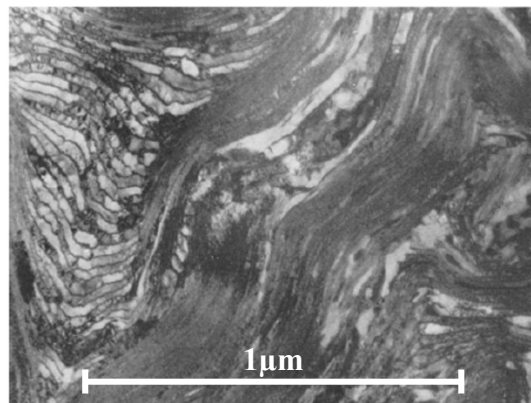


Figure 19: TEM pictures of transverse section of drawn wires of axially oriented pearlite with true strains of 4.2. [9]

In addition to the radial orientation, a crystallographic texture appears in drawn wires [8], [13]-[16]: a [110]-type texture of ferrite. Work performed on large diameter wires [24] indicates that [110] fibre texture results in an alignment of (001) planes, which are cleavage planes in ferrite.

It is clear that damage will be strongly linked to this microstructural evolution. Many data are available on damage of cold drawn steels but most of them concern the macroscopic delamination phenomenon during torsion tests [25], [26] and is not of interest in this study because it happens at higher drawing strain. On the other hand, wire drawing at high strains presents some other interesting damage mechanisms.

M. Yilmaz [27], in a survey of experimental studies on the causes of ductile fracture of high carbon steel wires since 1994, has highlighted a predominant role of non-metallic inclusions also called ceramic inclusions in a broken drawn wire. Because of their strength level, these inclusions are not deformed but broken. Indeed, in an analysis of 121 fractures, 81% are due to the presence of these inclusions (Table 2 and Figure 20). The phenomenon of

reoxidation is the main cause of occurrence of these inclusions: during the continuous casting process, molten steel which was deoxidized beforehand can reoxidize.

Failure reasons	Number of failures	Failure rate (%)	
Failures due to only inclusions	61	50	
Failures that inclusions play roles	98	81	1
Failures due to only friction martensite	9	7	
Failures that friction martensite plays role	19	16	2
Failures due to hardening zones (bainite or tempered martensite)	14	12	3
Failures due to only surface defects	5	4	4
Failures due to foreign bodies during wire drawing	14	7	5
Failures due to foreign bodies during production of wire rod	5	4	6
Total of failures	121	100	

**Table 2: failure reasons during wire drawing [27]**

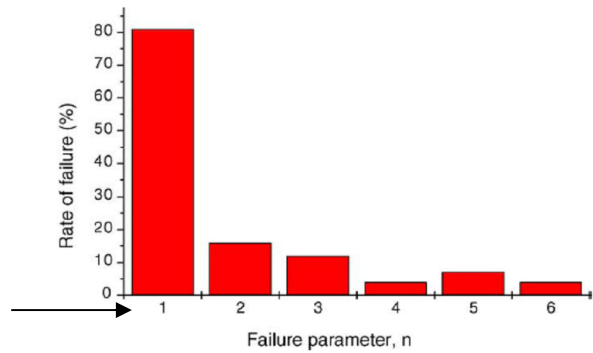


**Figure 20: Failure rate during steel wire production and service [27]**

This observation was also made by S. Tandon et al. [28], who explain that these inclusions locally increase the tensile strength, preventing material flow.

Microscopic observations identified three mechanisms during deformation: slip in ferrite in the plane parallel to the lamella plane, slip in ferrite crossing lamellae, and slip in the interphase at interfaces [9], [18]. At high strain, deformation mechanisms cause the bending and rupture of cementite lamellae. Moreover, plastic strain and dislocation structure development occur in the ferrite interlayer as well as in cementite [9], [18]. In a first step, dislocation mobility favours the diffusion of carbon atoms and in a second step, dislocations are stopped by interstitial carbon atoms and blocked at the interface between ferrite and cementite. Dislocation structure depends on the pearlite fineness [18].

At a very low scale, many authors have shown that successive drawing passes are responsible for cementite decomposition [23], [29], [30], “dissolution of cementite lamellae”, i.e. diffusion of the cementite carbon into ferrite [23], [30], [31], leading to a local increase of carbon content in lamellar ferrite [32]-[36].

### II.1.2.2 Cold rolled sheets

As mentioned in the introduction, only few researchers have worked on flat and sheet cold rolling in terms of microstructure evolution, whereas wire drawing has been studied in depth. However, some interesting results appear in their studies in case of severe cold rolling (up to ~80%).

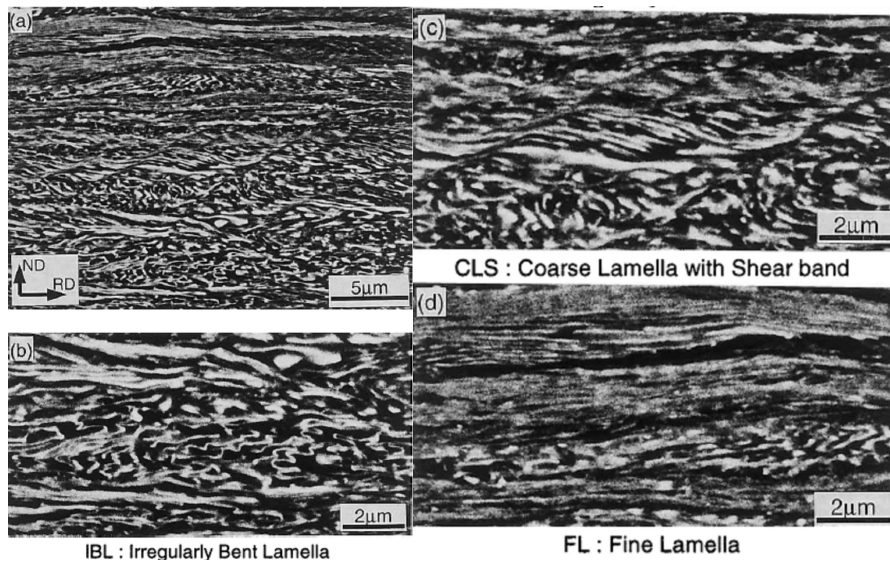


**Figure 21: Typical SEM microstructure of the 0.76C steel transformed at 823 K and cold rolled by 80 %. (a) Low magnification micrograph and the magnified images of (b) IBL, (c) CLS and (d) FL. (ND = Normal direction and RD = Rolling Direction [37])**

Typical SEM pictures of pearlitic steel after severe cold rolling reveal a non-uniform deformed structure [37], [38]. From the micrograph Figure 21a, three kinds of microstructural elements have been identified, they are shown magnified below: bent lamella (IBL, Figure 21b), shear band (CLS, Figure 21c) and fine lamella (FL, Figure 21d). During deformation, the amount of the three types of microstructure evolves differently. As rolling reduction increases:

- FL increases [37], [38].
- IBL decreases [37], [38].
- CLS reaches his highest value at 66.5% and then decreases [38].

Based on the classification of the pearlite structure proposed by Takahashi [39], the two authors [37], [38] agree on the deformation mechanisms leading to the heterogeneous microstructure previously presented:

- IBL is formed by compressing the colony with the lamellar direction nearly perpendicular to the rolling plane.
- CLS is formed when the deformation increases, bent lamella continuously converts into shear bands during cold rolling.
- FL is formed at the beginning of cold rolling in the colony with the lamellar direction nearly parallel to the rolling plane.

## II.1.3 Macroscopic scale

### II.1.3.1 Drawn wire

Tensile solicitation as in cold drawing is used to increase the yield stress by activating a strain hardening mechanism at a macroscopic scale. We have seen in section II.1.2 that tension results in an anisotropic texture and microstructure. Now, mechanical properties are deeply linked to the microstructure evolution as ductility, hardness, stress, strain... Therefore, it results in anisotropic mechanical properties [15], [40].

For instance, ductility increases with the pearlite refinement [18]. In terms of hardness, it increases if: the interlamellar spacing decreases, the dislocation density increases [23] or other alloying elements are used [40], [41]. The yield stress is much higher in case of pearlitic steel with fine-lamellar structure [18] and some authors have shown the dependency of the yield stress on the interlamellar spacing for a number of pearlitic steels containing 0.6–0.8% carbon [23], [42]:

$$\sigma_y = \sigma_{y0} + K_p t_0^{-1/2} \quad (\text{II.1})$$

with  $t_0 = t_{\text{fer}} + t_{\text{cem}}$  ( $t_{\text{fer}}$  is the thickness of the ferrite interlayer and  $t_{\text{cem}}$  the thickness of a cementite lamella). This is similar to Hall and Petch's law, but here the grain size is replaced by the interlamellar spacing as the relevant microstructural dimension.

### II.1.3.2 Cold rolled sheet

In cold rolling, tensile tests enabled the authors to identify a relationship between the true strain and the macroscopic tensile strength for different steels (Figure 22):

- Tensile strength increases with increasing carbon content.
- Tensile strength increases with increasing rolling reduction.

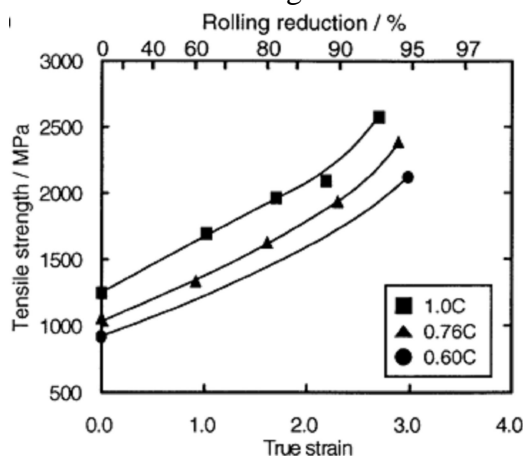


Figure 22: Relationship between true strain in rolling and tensile strength; the 0.6C, 0.76C and 1.0C steels transformed at 823 K and cold rolled [37]

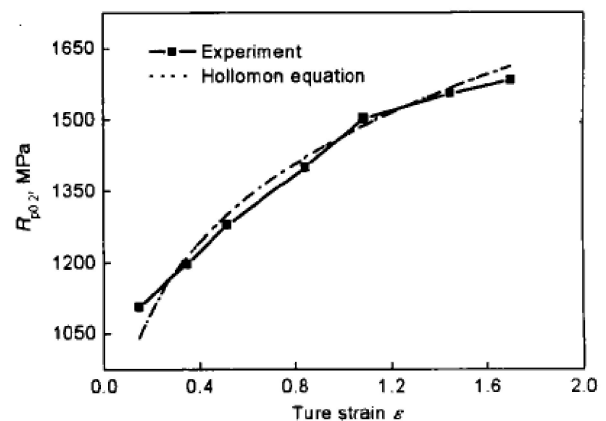


Figure 23: Relationship between yield strength and true strain [38]

As in wire drawing, the interlamellar spacing controls the yield strength of fully pearlitic steels. Two methods can be used to express the yield strength. If the main goal is to precisely evaluate the yield stress, predictive equations can be used together with the interlamellar distance measurement. Several researchers [9], [43]-[45] have used this approach to calculate the yield strength. The measurement of the interlamellar spacing is very difficult and many precautions must be taken, but it gives access to a local measurement of the stress. It is clear that the inhomogeneous microstructure will lead to heterogeneous mechanical properties. On the contrary, if only an estimation of the space-averaged yield strength is needed, a phenomenological, predictive equation using the true strain is sufficient. It is less precise than using the interlamellar distance but gives good macroscopic results as shown in Figure 23 with Hollomon's equation which links the yield stress with the plastic strain.

#### II.1.4 Summary

In this section, we have seen the evolution of lamellar microstructure depending on the solicitation (here, tension as in wire drawing and compression as in rolling), as well as their deformation mechanisms. We have also seen that the microstructural evolution has a deep impact on mechanical properties and damage mechanisms. It appears that flat rolling is less documented in terms of damage evolution and justifies a damage study along cold forming processes for high carbon steel in order to identify a damage law. Moreover, high carbon steels show a strong anisotropy. How could it be taken into account in process simulation? The next section answers that question.

## II.2 Yield functions

In order to represent plastic behaviour of steels, a phenomenological (or macroscopic) elasto-plastic approach is commonly used. It is then typical to employ a yield function (to describe the yield surface), associated to the normality rule and to a hardening law. The yield surface, defined in the stress space, corresponds to the elastic limit and the beginning of the plastic flow and is written in the following way:

$$f = \bar{\sigma}(\sigma) - \sigma_u, \quad f \leq 0 \quad (\text{II.2})$$

In this equation,  $\bar{\sigma}(\sigma)$  is the effective or equivalent stress and  $\sigma_u$  is the material yield stress which represents the plastic threshold stress.

The yield function is a mathematical description of the yield surface shape. The normality rule associated to the yield function expresses relationships between the stress and plastic

strain rate components. The yield function gives the stress at which yielding occurs for a given stress state and its gradient (normality rule) gives the direction of the plastic strain rate:

$$\dot{\varepsilon}^p = \dot{\lambda} \frac{\partial f(\sigma, \varepsilon^p)}{\partial \sigma}, \quad \dot{\lambda} > 0 \quad (\text{II.3})$$

Here,  $\dot{\lambda}$  is the plastic multiplier. This equation is the associated plastic flow law because the yield surface is taken as the dissipative plastic potential  $g$ . When the plastic potential differs from the yield function, equation II.3 is non-associated and becomes:

$$\dot{\varepsilon}^p = \dot{\lambda} \frac{\partial g}{\partial \sigma}, \quad \dot{\lambda} > 0 \quad (\text{II.4})$$

The hardening law expresses the evolution of the yield surface during deformation. It can be isotropic or anisotropic (e.g. kinematic) hardening, representing respectively the yield surface homothetic inflation / translation.

The yield function may be either isotropic (Von Mises, Tresca, Hosford 1) or anisotropic (Hill, Hosford 2, Barlat...); it may be associated or not. In this section II.2, a sample of yield functions is introduced. Isotropic yield functions are presented first, as an introduction to better understand anisotropic criteria. Then, the choice of a criterion for the present work will be discussed.

## II.2.1 Isotropic yield functions

### II.2.1.1 Tresca criterion

The oldest criterion is the criterion of Tresca [55] and is written, in principal axes, by:

$$f = \frac{1}{2} [\text{Max}(\sigma_i - \sigma_j)] - \tau_0 \quad (\text{II.5})$$

It expresses that plastification appears once the highest shear stress, in the Mohr representation, reaches a constant critical value,  $\tau_0$ .

### II.2.1.2 Von Mises criterion

The most used quadratic criterion is Von Mises' [56], written in an orthonormal frame as:

$$f = \frac{1}{2} [(\sigma_{yy} - \sigma_{zz})^2 + (\sigma_{zz} - \sigma_{xx})^2 + (\sigma_{xx} - \sigma_{yy})^2 + 6\sigma_{yz}^2 + 6\sigma_{xz}^2 + 6\sigma_{xy}^2] - \sigma_0^2 \quad (\text{II.6})$$

In principal axes, eq. II.2 becomes:

$$f = \frac{1}{2} [(\sigma_2 - \sigma_3)^2 + (\sigma_3 - \sigma_1)^2 + (\sigma_1 - \sigma_2)^2] - \sigma_0^2 \quad (\text{II.7})$$

The next figure (Figure 24) represents the superposition of the two criteria in generalized plane stresses. This one shows that both criteria coincide under some loadings: intersection

with axes corresponds to simple tension / compression; the first bisector corresponds to equilibrated biaxial tension / compression. However, both criteria disagree in shear loading (second bisector), i.e. the ratio between shear and tensile stress ( $1/2$  vs.  $1/\sqrt{3}$ ). Moreover, this figure shows no Bauschinger effect as Re in tension equal Re in compression. Finally, the isotropy is characterized by the symmetry compared to the bisectors (axis 1 = axis 2).

### II.2.1.3 General quadratic and non-quadratic isotropic criterion

It has been often observed, in experiments or using self-consistent crystal plasticity models, that real criteria lie between the Von Mises and Tresca criteria. Therefore, Hershey has proposed to capture the conclusions of a self-consistent crystal plasticity model by a generalization of both Von Mises and Tresca criteria of the following form [57]:

$$f = \frac{1}{2}(\sigma_2 - \sigma_3)^n + \frac{1}{2}(\sigma_3 - \sigma_1)^n + \frac{1}{2}(\sigma_1 - \sigma_2)^n - \sigma_0^n \quad (\text{II.8})$$

Note that this yield function remains isotropic, since all three directions play the same role (circular permutation of principal stresses). When  $n = 2$  it reduces to the Von Mises criterion. Hosford extended this function to a non-quadratic criterion [58] :

$$f = \left[ \frac{1}{2} \left( |\sigma_2 - \sigma_3|^n + |\sigma_3 - \sigma_1|^n + |\sigma_1 - \sigma_2|^n \right) \right]^{1/n} - \sigma_0 \quad (\text{II.9})$$

He showed that this function is also a good approximation for a full-constraint crystal plasticity model [58], and that the stress exponent is strongly coupled to the polycrystalline structure: the best values for  $n$  are 6 for BCC and 8 for FCC materials [59], as shown in Figure 25.

For a more complete review of isotropic formulations, Yu [60] presents a bibliographical article on strength theories since the beginning.

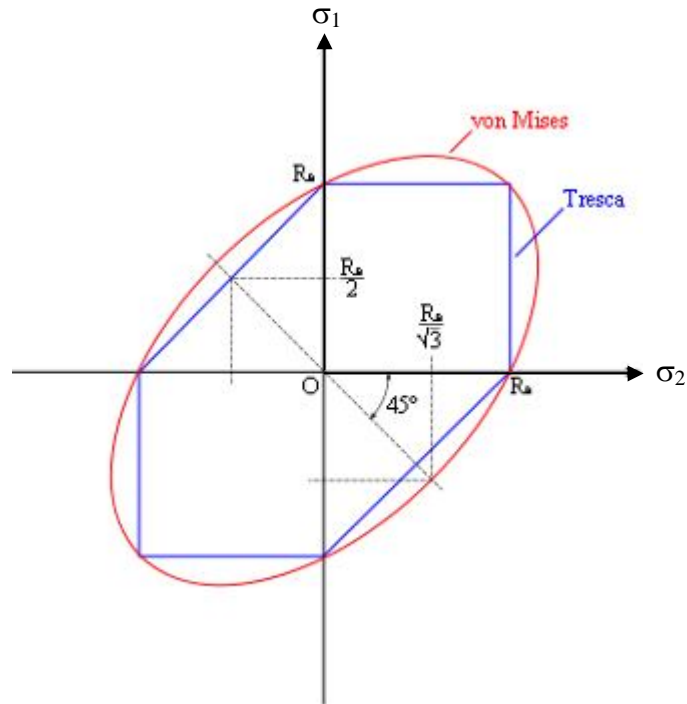


Figure 24 : Comparison between Tresca and Von Mises criteria for generalized plane stresses

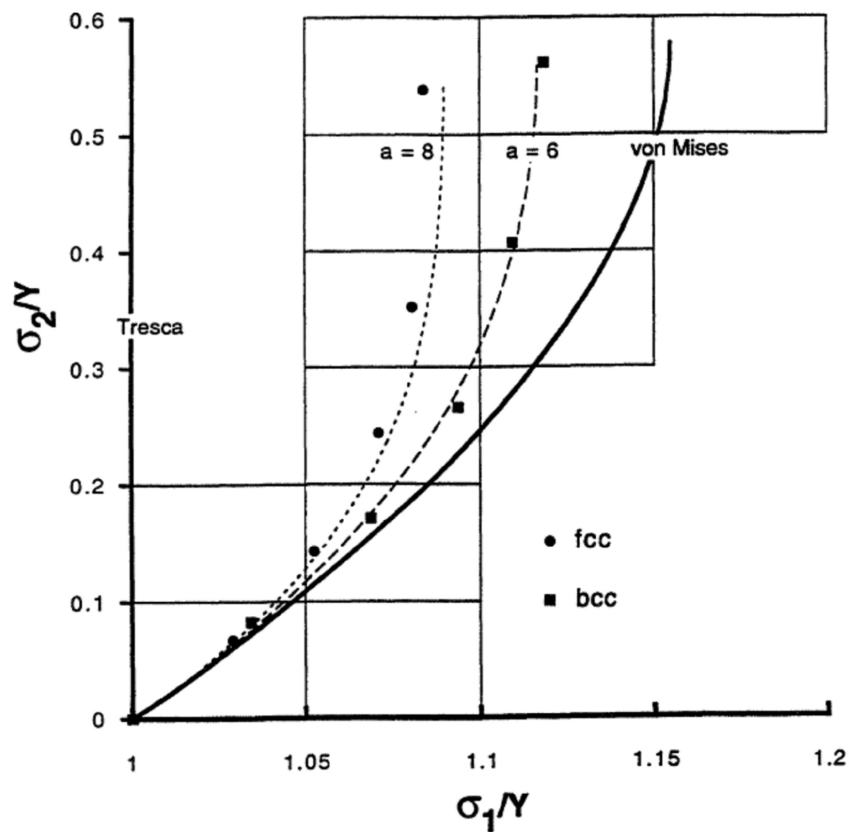


Figure 25 : Representative Section of Isotropic Yield Loci with  $\sigma_3 = 0$ . Tresca and von Mises are compared with calculations based on the  $\{111\}\langle 110 \rangle$  slip for fcc and  $\langle 111 \rangle$ -pencil glide for bcc. Note the  $\sigma_1/Y$  scale is expanded relative to the  $\sigma_2/Y$  scale for ease of comparison. The dash and dotted lines represent eq. 10 with exponents  $a=8$  suggested for fcc and  $a=6$  for bcc ( $a$  corresponds to  $n$  in equation II.8 and II.9 [59])

## II.2.2 Anisotropic yield functions

The previous models are not able to predict correctly, in terms of geometry and plastic properties, the anisotropy introduced by some manufacturing processes such as flat or sheet cold rolling. As a consequence, many authors proposed new or modified criteria.

### II.2.2.1 Hill quadratic criterion

The first yield function accounting for orthogonal anisotropy was introduced by Hill [61] and is based on Von Mises work. To introduce anisotropy, Hill kept the Von Mises quadratic form, but added six coefficients to describe the direction-dependent plastic flow properties:

$$f = \left\{ F(\sigma_{yy} - \sigma_{zz})^2 + G(\sigma_{zz} - \sigma_{xx})^2 + H(\sigma_{xx} - \sigma_{yy})^2 + 2L\sigma_{yz}^2 + 2M\sigma_{xz}^2 + 2N\sigma_{xy}^2 \right\} - 1 \quad (\text{II.10})$$

### II.2.2.2 Hill non quadratic criterion

In 1979, R. Hill generalized his yield criterion under the following form [62]:

$$f = F|\sigma_2 - \sigma_3|^m + G|\sigma_3 - \sigma_1|^m + H|\sigma_1 - \sigma_2|^m + L|2\sigma_1 - \sigma_2 - \sigma_3|^m + M|2\sigma_2 - \sigma_3 - \sigma_1|^m + N|2\sigma_3 - \sigma_1 - \sigma_2|^m - \sigma_0^m \quad (\text{II.11})$$

where  $\sigma_i$  are the principal stresses and  $m$  is the anisotropy exponent. We can say here that after “anisotropizing” Von Mises’ criterion, Hill “anisotropized” Hosford’s criterion (1972).

### II.2.2.3 Hosford non quadratic criterion

In 1979, Hosford [63] generalized his isotropic yield function to take into account normal anisotropy (here for a plane stress situation):

$$f = \left[ \frac{1}{1+R} (|\sigma_1|^n + |\sigma_2|^n) + \frac{R}{1+R} |\sigma_1 + \sigma_2|^n \right]^{1/n} - \sigma_0 \quad (\text{II.12})$$

This criterion is also a generalization of Hill’s quadratic function for plane stress [64].

To summarize and compare the three previous yield criteria we can observe the next figure (Figure 26). We note that the initial shape of the yield surface is quite different and the evolution of the plane stress state is not the same when the  $R$ -coefficient changes.

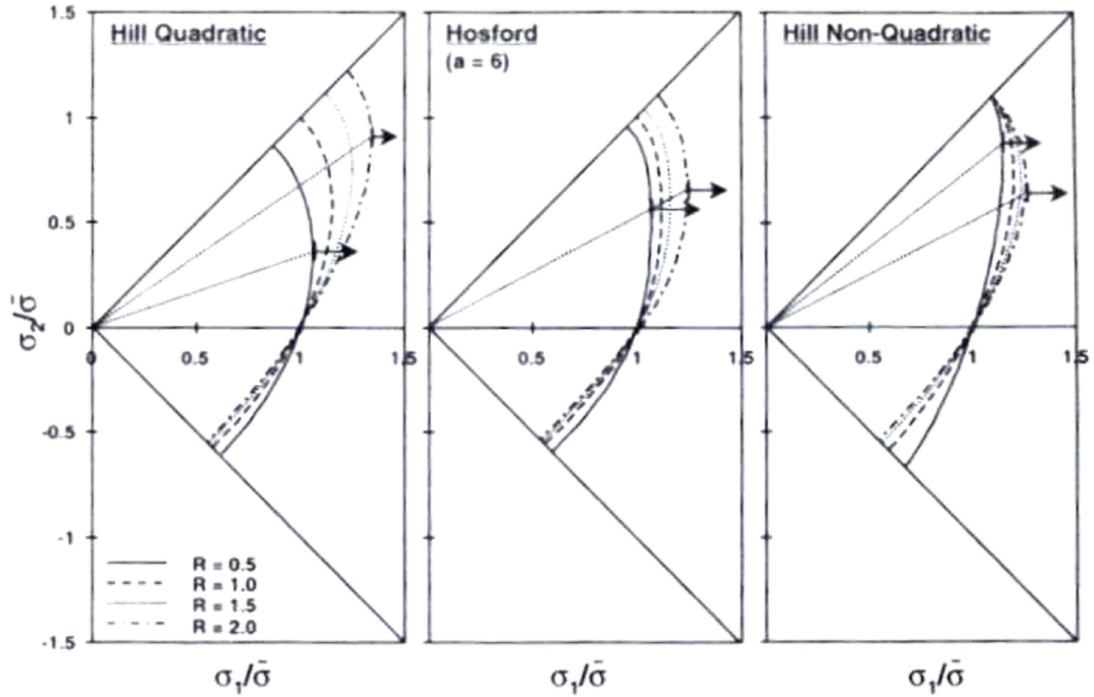


Figure 26: Evolution of the plane stress state with the anisotropic coefficient  $R$ , for three different yield criteria [65]

#### II.2.2.4 Other anisotropic functions

From this date, many yield criteria have been proposed to accurately predict the real process, by refining the yield surface description by taking into account more and more experimental results. Reviews on these improvements can be found in Barlat and al. [65] and in Hu [67].

Many authors must be cited, who tried to give accurate anisotropy predictions: Barlat and Lian [68], Karafillis and Boyce [69], Darrieulat and Montheillet [70], Bron and Besson [71], Banabic et al. [72], Cazacu et al. [73]. In their approaches, anisotropy is introduced by means of a linear stress transformation (anisotropic combinations of the stress components, based on linear transformation, are used in yield function). The main advantages is the easy development of convex formulations which lead to numerical simulations stability, as explained in Barlat et al. [74].

In the Figure 27, some yield criteria shapes are compared to show the range of yield function shapes achievable.

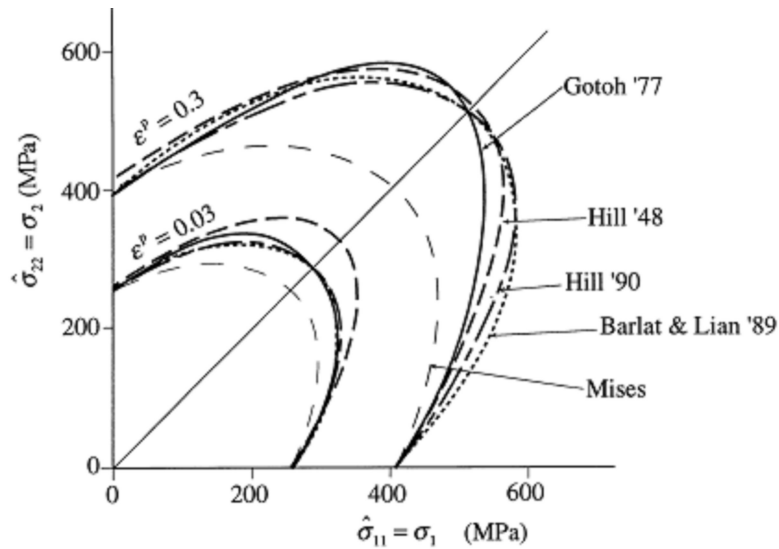


Figure 27 : Comparison of shapes of yield surfaces at small and large strain levels [75]

Other researchers have used a different approach to derive the anisotropic yield function [75][76]-[80]. They used principal stress components and the angle between the first principal axis and the rolling direction to represent every plane stress state. Then, in each stress state, experimental stress points determine the yield locus.

All of these formulations are more and more complicated and some of them cannot even take a completely analytical form. This is why many authors still prefer to use Hill's quadratic criterion rather than developing new theories. In his paper [67], Hu presents a complete list of these authors using models based on Hill's function and explains that if the selected experimental results are obtained under conditions close to those of applications, Hill's criterion can describe the real processes quite well. Moreover if the stress states of applications can be restricted within a specific range, Hill's model can predict the physical process at an acceptably accurate level. However, a problem appears when the real physical problem involves many kinds of stress states and needs a continuous yield model. That is why, Hu [67], proposes a new model that uses multiple yield systems which is able to generate a continuous yield surface in stress space.

### II.2.3 Choice of a yield function

In the following, Hill's quadratic yield function will be used. This simple choice, available in Forge® (and Lam3) has been dictated on the one hand by the strong observed anisotropy, on the other hand by the fact that the multiple complex anisotropic laws developed for sheet forming have been rarely used in bulk forming.

As a consequence, the results will show interesting tendencies, but only semi-quantitative ones.

## II.3 Damage mechanisms and models

### II.3.1 Ductile damage

#### II.3.1.1 Ductile damage characterization

Here, only damage occurring under large plastic strains is of interest. This is called ductile damage, by opposition to brittle damage: it is the most frequently observed mode in metal forming. Damage starts with micro-cavity nucleation due to non-homogeneous stresses and strains field (Figure 28). These voids grow during deformation and coalesce to create local cracks, which then propagate in stable or unstable ways.

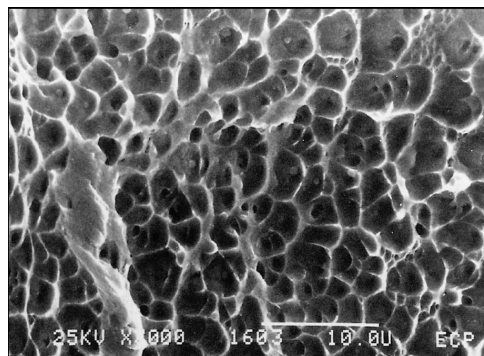


Figure 28 : Stainless austenitic steel fracture surface analysis (fractography) [81]

#### II.3.1.2 Ductile damage mechanisms

Three steps characterize ductile fracture (Figure 29) and are the basis of many damage models: voids nucleation, voids growth and voids coalescence.

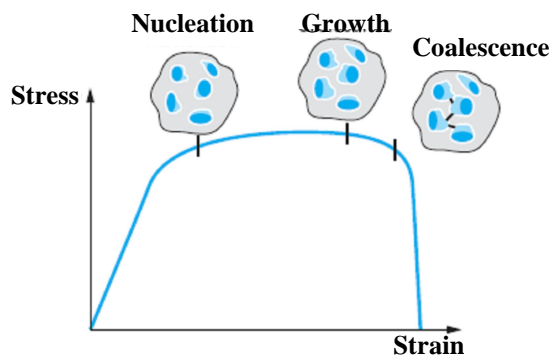


Figure 29 : damage evolution with deformation (from [82])

### II.3.1.2.1 Nucleation

An initially dense alloy, i.e. without cavity, consists of two phases: an elasto-plastic matrix and at least some particles of a second phase (inclusions, precipitates ...), considered as quasi-rigid. It should be noted that metals, even qualified as "high purity", always contain a high density of inclusions.

Example: 99.99% pure Cu containing 100  $\mu\text{g/g}$  of lead in the form of spherical-shaped nodules with a 1  $\mu\text{m}$  radius contains approximately  $2 \times 10^4$  inclusions/ $\text{mm}^3$ , which corresponds to a spacing of about 38  $\mu\text{m}$  between inclusions. [81]

The inclusion / matrix interface is a critical area for nucleation. Indeed, the material flow discontinuity in this area generates stress concentration. The incompatibility of deformation between particles and matrix leads to the formation of a large number of dislocations near the interface. The internal stresses generated are added to those applied by the process and lead to particle fracture (Figure 30 and Figure 32a) or interface decohesion (Figure 31 and Figure 32b) or even matrix cracking in the vicinity of inclusion when the stress exceeds a threshold value.

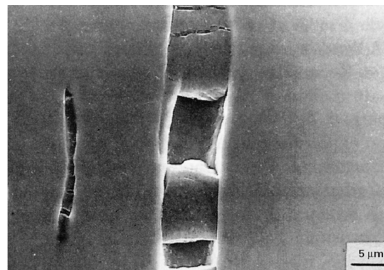


Figure 30: Manganese sulphide inclusion rupture in a stainless austenitic steel 0[81]

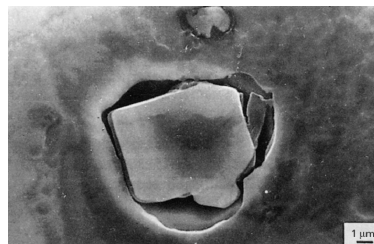


Figure 31: Decohesion between an alumina inclusion and steel matrix 0[81]

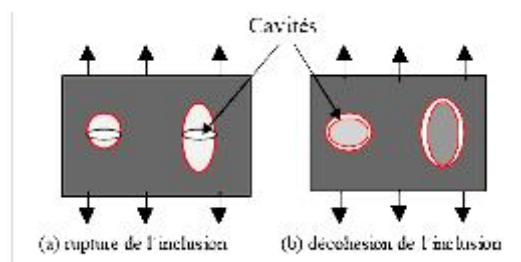
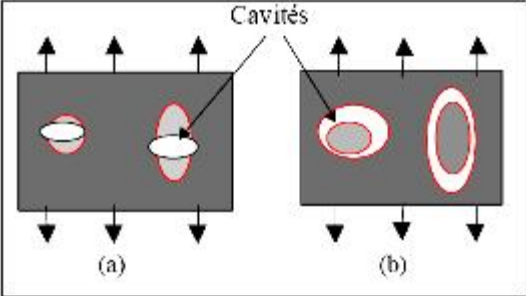


Figure 32: Voids nucleation [83]

At this stage, the cavities created are too small to affect the macroscopic material behaviour. The properties are thus considered unchanged. Nucleation may also be due to grain boundaries considered as heterogeneities that can lead to cavities. Finally one last reason is dislocations pile-up against a barrier that generates a microcavity [84]. The latter two processes mainly explain the occurrence of damage in pure materials, and even pure materials contain a large number of inclusions. So it seems logical to consider these processes as secondary.

**II.3.1.2.2 Growth**

Under the effect of deformation increase, and especially under hydrostatic tension, the size of microcavities increases either into spherical or elliptical or cracks shape. If decohesion is complete between inclusion and the matrix (Figure 33b), the inclusion no longer plays an important role. If this is not the case (Figure 33a), it must be taken into account. During this second stage the material softens.



**Figure 33: Voids growth [83]**

**II.3.1.2.3 Coalescence**

Voids coalescence is the final stage of damage and ductile fracture. Interaction of strain and stress fields around cavities occurs when the distance between them is small; the link is weakened by this interaction and the two cavities join by development of a plastic instability (Figure 34).

The end of the third stage is the beginning of the initiation of macroscopic crack which will lead to the material ruin.

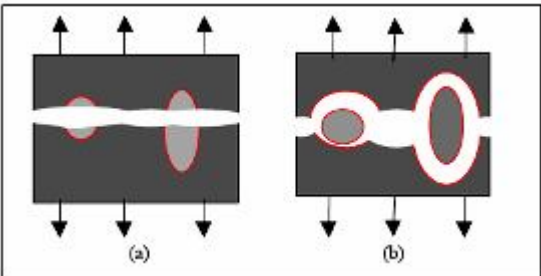


**Figure 34: Voids coalescence [83]**

## II.3.2 Ductile damage models

### II.3.2.1 Introduction

For years, many authors have worked to develop models to predict the kinetics of damage. They started from the following observation: when looking at the force-displacement response of a tensile test on an axisymmetric specimen (Figure 35), they observed a decrease of the force after having reached a maximum. This decrease comes basically from necking, but the shape of the curve is also determined by damage, i.e. nucleation of voids, and researchers tried to find how they can take into account the void nucleation and how they can accurately model the following curve.

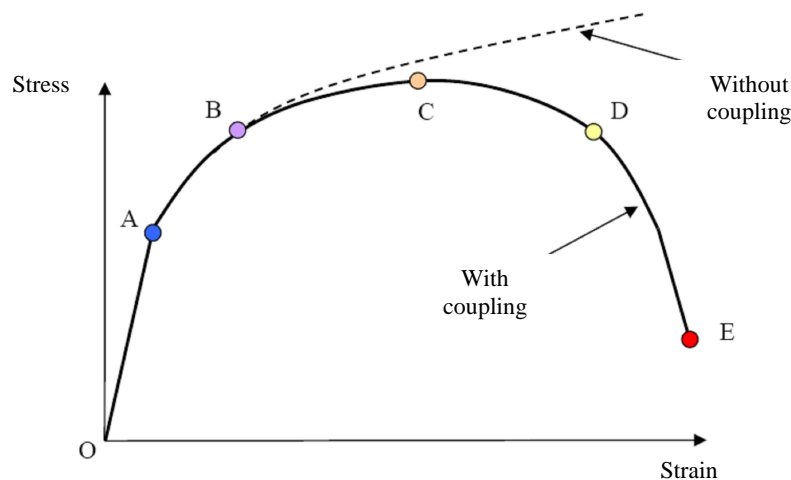


**Figure 35: Tensile curve illustrating coupling between damage and behaviour**

**OA:** Elastic deformation.

**AB:** Cavity nucleation phase – cavities are too small to modify material macroscopic behaviour.

**BC:** Cavity growth – progressive material softening. Tangent modulus is null at point C. Coupling between damage and behaviour cannot be neglected, it becomes predominant.

**CD:** Coalescence phase

**DE:** Macroscopic cracks – they propagate and lead to specimen break (point E).

To answer these questions, two main theories appeared in the sixties. The first one is based on the description of void nucleation and growth (void fraction evolution, density, shape factor and presence of an inclusion in the void), whereas the second one is a more global approach where a group of voids is considered and which looks at the effects on the mechanical properties.

To give a quick review on damage models, we can stay with the previous curve and separate these models in two categories corresponding to the two curves. The first category concerns damage-enhanced constitutive models which seek to represent the curve decrease.

The second one is composed of non-coupled “pure” damage models where authors tried to predict the fracture (dotted line). Indeed, it is conceivable to couple these latter damage functions with the constitutive equations, but it has not been developed.

### II.3.2.2 Non-coupled damage models

#### II.3.2.2.1 *Models based on a microscopic analysis*

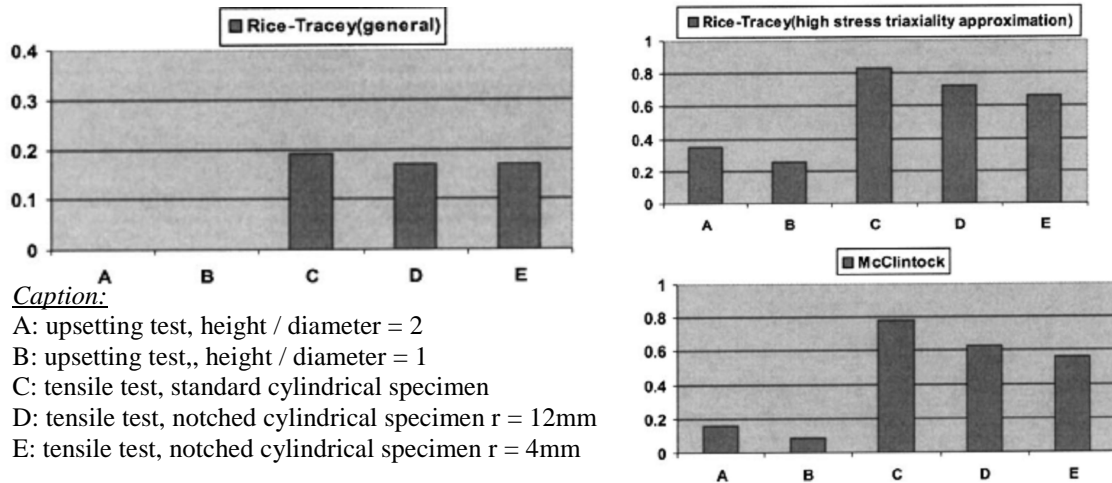
Here, several authors used the micromechanical approaches of cavity growth to create non-coupled damage models (McClintock 1968 [85], Rice & Tracey 1969 [86], Budiansly & al. 1982 [87]). They differ by cavity nature and material behaviour law, but they do not take into account the presence of an inclusion inside. Table 3 gives an overview of the models in terms of mechanical framework and resulting equations.

In a comparative study, Y. Bao and T. Wierzbicki [88] have shown that these models deserve consideration in that they point out important variables, but should be used with care. Indeed, they are valid only for specific load cases. Comparison of  $D$  values at fracture for different mechanical tests (upsetting, tensile tests on traditional cylindrical specimens and cylindrical specimens with different notch radii) highlights a large dispersion (Figure 36), although by nature of the models,  $D$  at fracture should be path-independent.

McClintock’s and Rice and Tracey’s criteria give very different results between an upsetting test and a tensile test. Rice and Tracey’s criterion (assuming high stress triaxiality) gives different results between the three tensile tests. As it is valid only for tensile tests, it gives more homogeneous results.

These authors used SEM fractographies to find the reason of these differences. They highlighted two totally different damage mechanisms for tensile test and upsetting. In the case of the tensile test, the fracture surface is very rough with the presence of dimples and fractured inclusions while for the upsetting test the surface is quite smooth without dimple. A more accurate microscopic analysis enables the authors to conclude on the damage mechanisms of each test. Regarding tensile test, nucleation, growth and coalescence mechanisms of cavities predominate, while for upsetting, it deals with shear fractures (Figure 37 and Figure 38).

To sum up, these models are adapted to a certain damage mode and adjusted to a certain strain path, namely tension (high triaxiality). It is barely applicable to another strain path, and still less to strain path changes. This is the reason why criteria based on void nucleation mechanism (the 3 criteria listed above) provide a fairly good prediction for tensile testing but fail with upsetting test.



*Caption:*

A: upsetting test, height / diameter = 2

B: upsetting test, height / diameter = 1

C: tensile test, standard cylindrical specimen

D: tensile test, notched cylindrical specimen r = 12mm

E: tensile test, notched cylindrical specimen r = 4mm

**Figure 36: Comparison of D fracture values at break for the three void growth models**

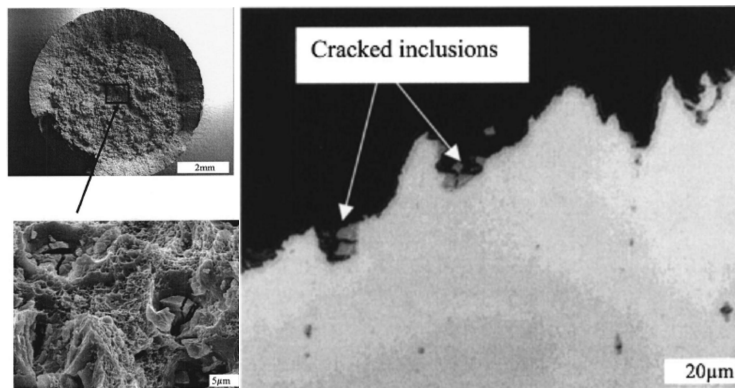


**Figure 37 : Tensile test fractographies highlighting rough surface with dimples [88]**

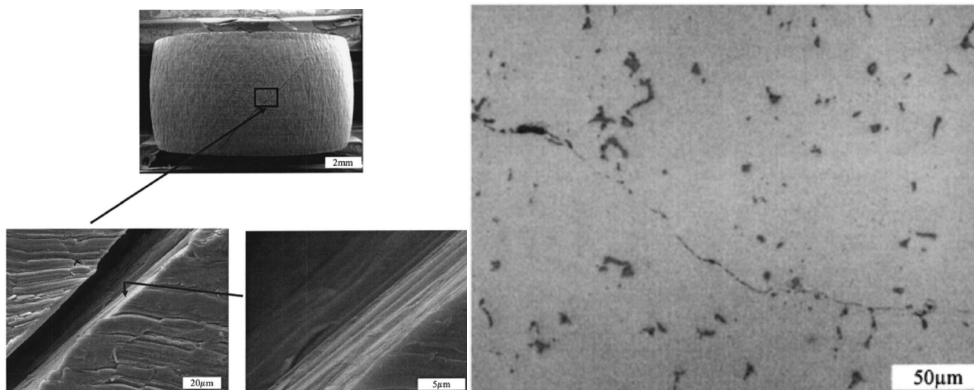


**Figure 38 : Upsetting test fractographies highlighting smooth surface and shear crack propagation through the matrix [88]**

It should be noted that even if some models consider elliptical cavities, none takes damage or material anisotropy into account. In Rice and Tracey's modelling, the inclusion shape change is negligible and therefore simply reflects the change in cavity volume. Furthermore, interaction between cavities (they can be aligned and arranged in series, or cluster) does not exist in the three models previously introduced (see Annex 1 where a different formulation is used and enables to take this interaction into consideration).

Model	Matrix rheology	Void shape	Stress state	Formulation
McClintock (1968) [85]	Plastic hardening	Cylinders with circular or elliptic sections minor axis a and major axis b	Principal axis of stress coincide with inclusion ones	$D = \int_0^{\varepsilon_{eq}^f} \left[ \frac{\sqrt{3}}{2(1-n)} \sinh \left( \frac{\sqrt{3}(1-n)}{2} \frac{\sigma_1 + \sigma_2}{\sigma_{eq}} \right) + \frac{3}{4} \frac{\sigma_1 - \sigma_2}{\sigma_{eq}} \right] d\varepsilon_{eq} \quad (\text{II.13})$
Rice and Tracey (1969) general formulation [86]	Rigid perfectly plastic	Spherical	$\dot{\varepsilon}_{ij}$ , $S_{ij}$ and $\sigma_H$ imposed	$D = \int_0^{\varepsilon_{eq}^f} \left[ 0,558 \sinh \left( \frac{3}{2} \frac{\sigma_H}{\sigma_{eq}} \right) + 0,008 \nu \cosh \left( \frac{3}{2} \frac{\sigma_H}{\sigma_{eq}} \right) \right] d\varepsilon_{eq} \quad (\text{II.14})$
Rice and Tracey (1969)	Rigid perfectly plastic	Spherical	High stress triaxiality hypothesis $\frac{\sigma_H}{\sigma_{eq}} > 1$	$D = \int_0^{\varepsilon_{eq}^f} \left[ 0.283 \exp \left( \frac{3}{2} \frac{\sigma_H}{\sigma_{eq}} \right) \right] d\varepsilon_{eq} \quad (\text{II.15})$
Budiansky, Hutchinson and Slutsky (1982) [87]	Pseudo-plastic Velocity sensitivity (m)	Spherical	Axisymmetric loading, high triaxiality case $\frac{\sigma_H}{\sigma_{eq}} > 1$	$D = \int_0^{\varepsilon_{eq}^f} \left( \frac{\chi}{2} \left[ \frac{3m}{2} \left  \frac{\sigma_H}{\sigma_{eq}} \right  + (1-m)(1+0.418m+0.014\chi m) \right]^{1/m} \right) d\varepsilon_{eq} \quad (\text{II.16})$

Table 3: Void growth model formulation and hypothesis

With :  $\sigma_1$  and  $\sigma_2$  maximum major stresses,  $\sigma_1 > \sigma_2 > \sigma_3$

$$\nu \text{ major strain rate defined as follows: } \nu = -3 \frac{\dot{\varepsilon}_2}{\dot{\varepsilon}_1 - \dot{\varepsilon}_3}, \quad \dot{\varepsilon}_1 > \dot{\varepsilon}_2 > \dot{\varepsilon}_3, \quad \nu = \begin{cases} -1 & \text{in simple compression} \\ 0 & \text{in simpleshear} \\ +1 & \text{in simple traction} \end{cases}$$

n hardening coefficient,

$\varepsilon_{eq}^f$  equivalent strain at fracture,

$\sigma_{eq}$  equivalent stress,

$\varepsilon_{eq}$  equivalent strain,

$\frac{\sigma_H}{\sigma_{eq}}$  triaxiality rate.

$\chi$  sign of  $\frac{\sigma_H}{\sigma_{eq}}$ ,  $\chi = \pm 1$ ,

m material strain rate sensitivity coefficient  $\sigma_{eq} = k \dot{\varepsilon}_{eq}^m$ ,

$\sigma_H$  hydrostatic pressure =  $\frac{1}{3} tr(\sigma)$

### II.3.2.2.2 *Models based on a macroscopic analysis*

These criteria determine a critical value, constant at fracture and supposed independent on strain path. They involve the stress field influence by integrating its evolution along strain path and have the following form [84]:

$$\int_0^{\varepsilon_f} f\left(\frac{\sigma_H}{\sigma_{eq}}\right) d\varepsilon_p = V_D \quad (\text{II.17})$$

with  $V_D$  material characteristic constant.

We can name Latham and Cockcroft, Oyane, Sekiguchi, Norris... who have proposed such criteria. They differ by the choice of the function  $f$ . Indeed, these criteria seem very similar to Rice and Tracey's formulation. From the theoretical models above, the authors know that the triaxiality is a major risk factor and they build a damage function as an increasing function of triaxiality. What distinguishes these macroscopic criteria from Rice and Tracey is the choice of an empirical form of dependence to  $\sigma_H/\sigma_{eq}$ , allowing for different adjustment coefficients supposed to improve the correlation between the results and their experience. Rice and Tracey based their analysis on modelling; criteria such as Oyane's are an empirical generalization.

But in turn, comparisons have proved these criteria valid only in the context in which they were established, i.e. for a given solicitation or a given material. They are just as difficult to transpose to other tests. Moreover, they can represent simple strain paths but are not sufficient to take into account strain paths changes e.g.

We can conclude that these criteria are reliable in predicting fracture only if parameters of function  $f$  are measured by identification tests close to the deformation undergone by the material in the deformation process studied, regardless of damage anisotropy.

### II.3.2.3 Coupled damage models

Among coupled models, two major formulations appear. The first one is based on the continuum thermodynamics with internal variables (like Lemaître's model), and use the concept of damage variable introduced by Kachanov in 1958, whereas the second one relies on the porous media plasticity theory (introduced in II.3.2.3.4.).

For a better understanding of Lemaître's model and its evolution, the concept introduced by Kachanov must be reminded.

### II.3.2.3.1 Damage variable and effective stress concept

Damage mechanics has been developed thanks to Kachanov's work in 1958 [89]. Damage is represented by a damage coefficient  $D$ , which means that the applied force is exerted on an apparent section  $S-S_D$  which does not correspond to the section  $S$  in the flawless material (Figure 39)

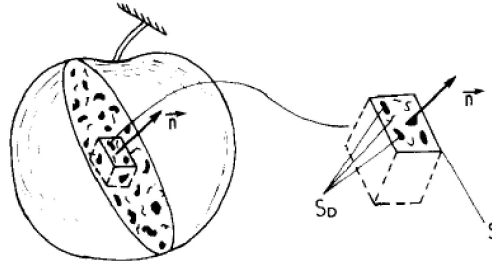


Figure 39: Definition of  $S$  and  $S_D$  [90]

An effective surface is then defined: 
$$\tilde{S} = S - S_D \quad (\text{II.18})$$

Coefficient damage in the  $\vec{n}$  direction is written: 
$$D_n = \frac{S_D}{S} \quad (\text{II.19a})$$

Under the isotropic damage hypothesis, i.e. defects are uniformly distributed in all directions, the equation is then written:

$$D = \frac{S_D}{S} \quad \forall \vec{n}$$

$$D = 0 \text{ for a flawless state,} \quad (\text{II.19b})$$

$D = 1$  for a totally damaged state, fractured material.

Stress applied on a section  $S$  exposed to a perpendicular force  $F$  is written in the following relation:

$$\sigma = \frac{F}{S} \quad (\text{II.20})$$

$D$  enables to couple damage and behaviour through the material effective characteristics, in particular the **effective stress** (in the uniaxial case of isotropic damage, for multiaxial case: use index  $ij$ ):

$$\tilde{\sigma} = \frac{F}{\tilde{S}} = \frac{F}{S - S_D} = \frac{F}{S - S \times D} = \frac{F}{S} \times \frac{1}{1 - D} = \frac{\sigma}{1 - D} \quad (\text{II.21})$$

This ratio tends to infinity at fracture. The damaged material mechanical behaviour is supposed to be the same as the flawless one, if  $\sigma$  is replaced by  $\tilde{\sigma}$ .

For instance, the elastic behaviour in uniaxial tensile test is described by similar equations:

$$\sigma = \tilde{E} \varepsilon_{el} \quad ; \quad \tilde{\sigma} = E \varepsilon_{el} \quad (\text{II.22a, b})$$

with  $\tilde{E}$  the effective young modulus and  $\varepsilon_{el}$  the elastic strain

It follows from the two previous relations that: 
$$\tilde{E} = E(1 - D) \quad (\text{II.23})$$

### II.3.2.3.2 Isotropic Lemaître's model

#### II.3.2.3.2.1 General framework of thermodynamics of damage

In Lemaître's approach [90], [91], the isotropic damage is defined by the damage coefficient introduced in the previous paragraph. Continuum thermodynamics of irreversible processes allows for the modelling of different materials' behaviour. The first thing is to fix the state variables (observable and internal) with its associated variables (Table 4):

Mechanisms	Type	State variables		Associated variables
		Observable	Internal	
Thermoelasticity	Tensor	$\epsilon_{ij}$		$\sigma_{ij}$
Entropy	Scalar	$T$		$s$
Plasticity	Tensor		$\epsilon_{ij}^p$	$-\sigma_{ij}$
Isotropic hardening	Scalar		$r$	$R$
Kinematic hardening	Tensor		$\alpha_{ij}$	$X_{ij}$
Damage	Scalar (isotropic)		$D$	$-Y$
	Tensor (anisotropic)		$D_{ij}$	$-Y_{ij}$

**Table 4: State and associated variables [91]**

The Gibbs specific free enthalpy is taken as the state potential [91] and is expressed as:

$$\psi^* = \psi_e^* + \frac{1}{\rho} \sigma_{ij} \epsilon_{ij}^p - \psi_p - \psi_T \quad (\text{II.24})$$

where:

- $\psi_e^*$  is the elastic contribution affected by damage,
- $\psi_p = \frac{1}{\rho} \left( \int_0^r R dr + \frac{1}{3} C \alpha_{ij} \alpha_{ij} \right)$  is the plastic hardening contribution (when multiplied by  $\rho$ , it is the stored energy  $\omega_s$ ),
- $\psi_T$  is temperature contribution.

The state laws are derived from the state potential and the others derivatives define the associated variables:

$$\begin{aligned} \epsilon_{ij} = \rho \frac{\partial \psi_e^*}{\partial \sigma_{ij}} + \epsilon_{ij}^p \rightarrow \epsilon_{ij}^e = \rho \frac{\partial \psi^*}{\partial \sigma_{ij}} \\ s = \frac{\partial \psi^*}{\partial T} \end{aligned} \quad (\text{II.25a, b})$$

$$\begin{aligned}
R &= -\rho \frac{\partial \psi^*}{\partial r}, \\
X_{ij} &= -\rho \frac{\partial \psi^*}{\partial \alpha_{ij}}, \\
-Y_{ij} &= -\rho \frac{\partial \psi^*}{\partial D_{ij}}
\end{aligned} \tag{II.26a, b, c}$$

The inequality of Clausius-Duhem expressing the second principle of thermodynamics is satisfied when the dissipation rate is positive:

$$\sigma_{ij} \dot{\varepsilon}_{ij} - \dot{\omega}_s + Y_{ij} \dot{D}_{ij} - \frac{q_i T_{,i}}{T} \geq 0 \tag{II.27}$$

Finally, the normality rule of generalized standard materials is introduced. It defines the evolution law of the internal variables which are derived from a dissipation potential ( $F$ ), composed by the plastic criterion function ( $f$ ), the non-linear kinematic hardening term ( $F_X$ ) and the damage potential ( $F_D$ ).  $F$  is written as:

$$F = f + F_D + F_X \tag{II.28}$$

The kinetic laws are written as follows:

$$\begin{aligned}
\dot{\varepsilon}_{ij} &= \dot{\lambda} \frac{\partial F}{\partial \sigma_{ij}}, & \dot{r} &= -\dot{\lambda} \frac{\partial F}{\partial R}, \\
\dot{\alpha}_{ij} &= -\dot{\lambda} \frac{\partial F}{\partial X_{ij}}, & \dot{D}_{ij} &= \dot{\lambda} \frac{\partial F}{\partial Y_{ij}}
\end{aligned} \tag{II.29a, b, c, d}$$

### II.3.2.3.2.2 State potential for isotropic damage

The strain potential for linear isotropic thermo-elasticity and isotropic damage is defined thanks to the principle of strain equivalence: the strain constitutive equations of a damaged material is derived from the same formalism as for a non-damaged material by replacing the stress by the effective stress [91][92]. It is associated to the elastic contribution  $\psi_e^*$  in eq. II.24, written as:

$$\rho \psi_e^* = \frac{1+\nu}{2E} \frac{\sigma_{ij} \sigma_{ij}}{1-D} - \frac{\nu}{2E} \frac{\sigma_{kk}^2}{1-D} + \alpha (T - T_{ref}) \delta_{ij} \tag{II.30}$$

The associated variable  $Y$ , called the energy density release rate, derived from the state potential, can be written as [93]:

$$Y = \rho \frac{\partial \psi^*}{\partial D} = \frac{\tilde{\sigma}_{eq}^2 R_v}{2E} \tag{II.31}$$

with the triaxiality function  $R_v = \frac{2}{3}(1+\nu) + 3(1-2\nu) \left( \frac{\sigma_H}{\sigma_{eq}} \right)^2$  (II.32)

where  $\sigma_{eq} = \sqrt{\frac{3}{2} s_{ij} s_{ij}}$  the Von Mises equivalent stress,

$s_{ij} = \sigma_{ij}^D - \delta_{ij} \sigma_H$  the stress deviator,

$\sigma_H = \sigma_{kk} / 3$ ,

$\left( \frac{\sigma_H}{\sigma_{eq}} \right)$  the stress triaxiality

In the same manner as in plasticity, Lemaître introduced a damage equivalent stress  $\sigma^*$  [94] defined as the uniaxial stress which gives the same amount of elastic strain energy as a multiaxial case and is obtained by equating the uniaxial case with  $R_v = 1$  and the multiaxial case:

$$\sigma^* = \sigma_{eq} \sqrt{R_v} \quad (\text{II.33})$$

and the damage occurrence criterion is:  $\sigma^* = \sigma_D$  (II.34)

### II.3.2.3.2.3 Formulation of the isotropic unified damage law

Experiments of ductile rupture show that damage is not only governed by the associated variable ( $Y$ ), but also by the plastic strain through the plastic multiplier in the normality rule. The accumulated plastic strain rate is defined in accordance with the yield criterion considered and for Von Mises it is:

$$\dot{p} = \left( \frac{2}{3} \dot{\varepsilon}_{ij}^p \dot{\varepsilon}_{ij}^p \right)^{1/2} \quad (\text{II.35})$$

When coupling the normality rule of  $\dot{\varepsilon}_{ij}^p$ <sup>1</sup> with the previous equation and the evolution law for the variable  $r$  (eq. II.29b), it leads to:

$$\dot{p} = \frac{\dot{\lambda}}{1-D} \quad (\text{II.36})$$

Experiments have shown that  $F_D$  must be a non-linear function of  $Y$ . A simple solution is:

$$F_D = \frac{S}{(s+1)(1-D)} \left( \frac{Y}{S} \right)^{s+1} \quad (\text{II.37})$$

Thus:  $\dot{D} = \left( \frac{Y}{S} \right)^s \dot{p}$  (II.38)

with  $s$  and  $S$  material parameters.

---

<sup>1</sup> eq. II.29a in which  $\frac{\partial F}{\partial \sigma_{ij}}$  is reduced to  $\frac{\partial f}{\partial \sigma_{ij}}$  and with the (visco-)plasticity loading function  $f$  determined by the Von Mises criterion

#### II.3.2.3.2.4 Uniaxial behaviour

From the previous state potential, it is possible to define an evolution damage law in which only the strain state appears [95]. In the previous equation,  $Y$  is replaced by its expression in eq. II.31 and for  $\sigma_{eq}$  the Von Mises' plasticity criterion is used (assuming that the material is without threshold  $\frac{\sigma_{eq}}{1-D} = K\varepsilon_{eq}^{1/M}$ ). Then equation II.38 is written as:

$$\dot{D} = p \left[ \frac{K^2}{2ES} \left( \frac{2}{3}(1+\nu) + 3(1-2\nu) \left( \frac{\sigma_H}{\sigma_{eq}} \right)^2 \right) \varepsilon_{eq}^{2/M} \right]^s \quad (\text{II.39})$$

Supposing several hypotheses:

- A radial or proportional loading (principal axes of the stress tensor are constant and the triaxiality is constant) then the evolution law can be integrated with the initial condition:  $\varepsilon_{eq} = \varepsilon_{eq}^D \Rightarrow D = 0$
  - At large deformation,  $M$  is high enough to be considered as infinite
  - Identification of  $s$  shows a value around 1
- $$\left. \begin{array}{l} \bullet \text{ At large deformation, } M \text{ is high enough to be considered as infinite} \\ \bullet \text{ Identification of } s \text{ shows a value around 1} \end{array} \right\} \frac{2s+M}{M} \approx 1$$

$D$  can be expressed in function of  $D_c$ ,  $\varepsilon_{eq}$  and  $\varepsilon_{eq}^R$  (the value of  $\varepsilon_{eq}$  at fracture):

$$D = D_c \left\langle \frac{\varepsilon_{eq}^p - \varepsilon_{eq}^D}{\varepsilon_{eq}^R - \varepsilon_{eq}^D} \right\rangle \quad (\text{II.40})$$

The three parameters defined above may be determined by mechanical testing and inverse analysis. This equation represents the linear ductile plastic damage law in deformation and gives a fairly good account of experimental results [96].

This model takes into account stress triaxiality but includes neither the sign of hydrostatic pressure (i.e. compression damages as much as tension), nor the shear effects. To illustrate these phenomena, Bao and Wierzbicki [97], construct the fracture locus in  $\bar{\varepsilon} - \sigma_H / \bar{\sigma}$  space (Figure 40).

In order to include the observed damage difference between tension ( $\sigma_H > 0$ ) and compression ( $\sigma_H < 0$ ), several authors have extended this model.

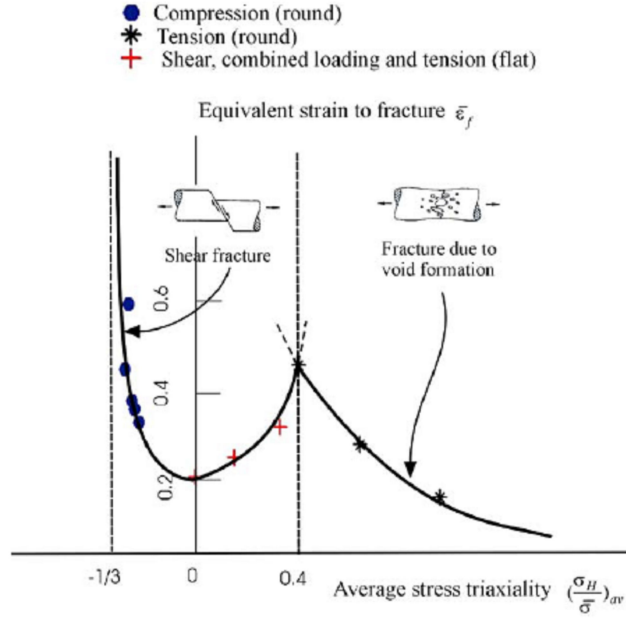


Figure 40: Dependence of the equivalent strain to fracture on the stress triaxiality [97]

### II.3.2.3.3 Tension / compression damage asymmetry, crack closure effects and cut-off value of stress triaxiality

Indeed, during an upsetting test, microcracks and microvoids may partially or totally close leading to a reduction or a stop of damage growth. J.F. Mariage [83] modifies the  $R_v$  relation (equation II.32 in equation II.31) in order to block the damage evolution in compression:

$$R_v = \frac{2}{3}(1 + \nu) + 3(1 - 2\nu) \left( \frac{\langle \sigma_H \rangle}{\sigma_{eq}} \right)^2, \quad (\text{II.41})$$

with  $\langle \sigma_H \rangle = \begin{cases} 0 & \text{if } \sigma_H < 0 \\ \sigma_H & \text{if } \sigma_H > 0 \end{cases}$

With the same purpose, Lemaître and Ladevèze [98] have decomposed the stress tensor in two parts, one for tension and the other one for compression:

$$\langle \sigma \rangle_{ij} = \langle \sigma \rangle_{ij}^+ + \langle \sigma \rangle_{ij}^- \quad \text{avec} \quad \langle \sigma \rangle_{ij}^+ = \sum_{i=1}^3 \langle \sigma_i \rangle e_i \otimes e_i \quad \text{et} \quad \langle \sigma \rangle_{ij}^- = \sum_{i=1}^3 \langle -\sigma_i \rangle e_i \otimes e_i \quad (\text{II.42a, b, c})$$

Equation (II.42a) becomes:

$$Y = \frac{1}{2E(1-D)^2} \left[ (1+\nu) \langle \sigma \rangle_{ij}^+ \langle \sigma \rangle_{ij}^+ - \nu \langle \sigma_{kk} \rangle^2 \right] + \frac{h}{2E(1-hD)^2} \left[ (1+\nu) \langle \sigma \rangle_{ij}^- \langle \sigma \rangle_{ij}^- - \nu \langle -\sigma_{kk} \rangle^2 \right] \quad (\text{II.43})$$

where  $h$  is a microdefects closure parameter that is material-dependent and  $h=0$  for a material which is not damaged in compression.

Some authors propose a different approach to take into account tension / compression damage asymmetry. C. Comi et U. Perego [99], consider two damage coefficients, in order to

decouple tension and compression phenomena by assuming that a non-linear material response is due to different dissipative mechanisms in tension and in compression.

Another tension / compression damage asymmetry is also shown in Figure 40 which highlights a cut-off value of stress triaxiality (-1/3) below which fracture never occurs [99][100].

#### II.3.2.3.4 Framework of porous media plasticity

The method consists in using porous media plasticity to model damaged material [101]. A damaged material is considered as a continuum media with a non-zero strain rate tensor trace. The spherical part of the stress tensor, representing void growth or closure, is therefore included in the flow rule [84]. A Von Mises criterion, defined from the second invariant of the stress deviator is not enough to describe void growth rate. Gurson introduces the first invariant [102]:

$$\psi = \left( \frac{\sigma_{eq}}{\sigma_0} \right)^2 + 2f \cosh\left( \frac{3}{2} \frac{\sigma_H}{\sigma_0} \right) - (1 + f^2) \quad (\text{II.44})$$

with f a damage variable defined as the void volume fraction and  $\sigma_0$  the yield stress ; when f=0, Von Mises criterion is regained.

Then, Gurson's model has been extended by Tvergaard and Needleman [103] to take into account void interaction effect. See Annex 1 for more detail on this framework, which will not be used in the present work.

#### II.3.2.4 Microscopic numerical modelling

An interesting framework concerns the digital representation of physical mechanisms at very local scales and is in progress at CEMEF [104] and in other research laboratories. It consists in a numerical tool enabling a digital modelling of metallic material microstructures with anisotropic mesh and finite elements modelling of polycrystalline microstructures in high strain (Figure 41).

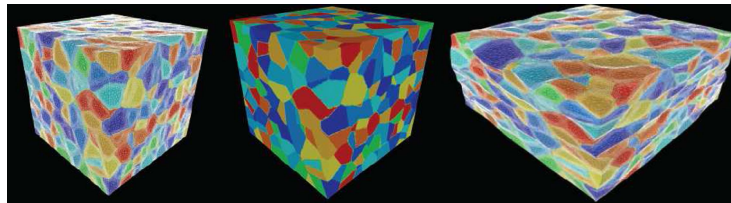


**Figure 41: Initial microstructure with (left) and without mesh (centre) and after 70% deformation (right)**

A recent development is the insertion of inclusions or voids in the representative elementary volume and could be an interesting point of view for future work on ductile damage.

II.3.2.5 Microscopic experimental modelling

A. Gaillac, in his PhD thesis [48], employed void quantitative measurement (quantitative image analysis) coupled to the EBSD (Electron Back-Scattered Diffraction) technique in order to characterize damage of Zr alloys and to study the influence of the microstructural parameters. Thanks to this procedure, he obtained information on the three damage evolution step, i.e. nucleation, growth and coalescence, and established a coalescence and fracture criterion linking the mean distance between voids with the void mean diameter (Figure 42).

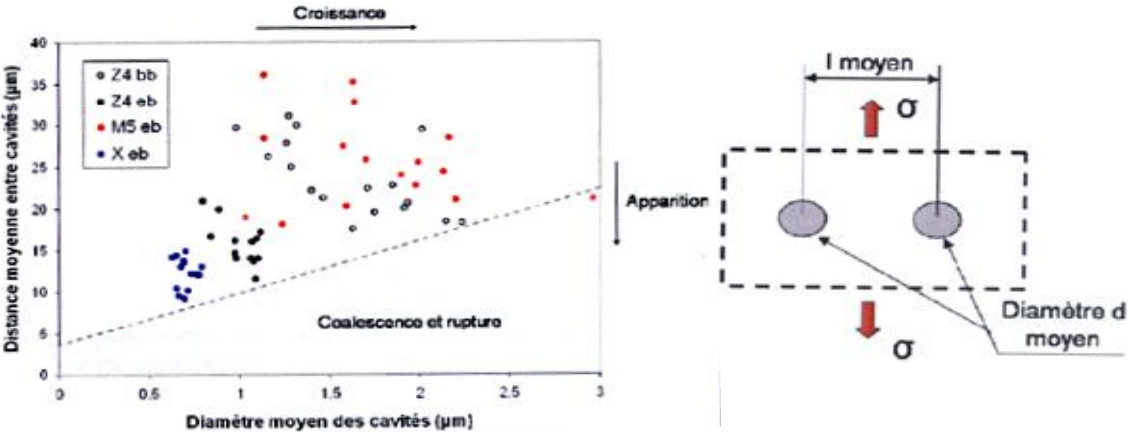


Figure 42: Fracture criterion for a zirconium alloy based on voids measurement [48]

Moreover, he linked microstructure parameters to the ductile damage:

Microstructure		Voids
Inclusions size	→	Nucleation threshold
Crystalline disorientation	→	
Inclusions density	→	density
Texture / stress direction	→	Growth rate
Grain size	→	
Repartition of void nucleation site / stress direction	→	Coalescence threshold and fracture

Table 5: influence of microstructure on ductile damage

### II.3.3 Choice of a relevant damage model

To choose an adequate damage model for our processes, a summary must be done. Moreover, a classification of these models will help us to better understand how they are built and what they seek to represent.

Many studies on microstructural mechanisms leading to the ductile fracture of a material have led to the modelling of the successive steps of ductile damage as presented in the paragraph II.3.1.2. This *physical approach at the microscopic level* seeks to predict the parameters of ductility (defined for the different mechanical tests) by "integration" of the damage along the simple strain path. It is clear indeed that damage and ductile fracture mechanisms are strongly dependent on the strain path and the load imposed, in particular triaxiality. This approach is commonly called **local approach of the rupture**. The fracture is then defined by a critical value of damage that is characteristic of the material and not influenced by the history effects.

Here, a large number of models exist, which mainly refer to cavity growth. This is due to the fact that in the first phase (nucleation), mechanisms are very dependent on the material and therefore there should be a model for each material. Moreover, it is difficult to determine the exact moment of nucleation.

Early models had to restrict to simple cavity shapes and simple strain paths to derive analytical or semi-analytical models of cavity growth [Rice & Tracey, McClintock...]. Models of this kind are adapted to a range of inclusion size, with a certain content, a certain inclusion shape. When comparisons between criteria are made, significant differences appear [84]. More recent investigation tools allow to digitally represent the microstructural features and their properties, so as to predict physical mechanisms at very local scales (porosity nucleation, taking into account the inclusions and the anisotropy of the material). This trend is explored in many physical metallurgy groups, including CEMEF [104].

Regarding the coalescence phase, the study is very complex due to a spatially heterogeneous distribution of cavity size at the end of the growth phase. Most models consider an average volume fraction of identical cavities. Only a few models take into account a more general situation.

The second **approach**, called **global approach** or *mechanical approach of damage at a macroscopic scale*, concerns mechanical parameters leading to fracture such as stress, strain, strain rate, temperature ... These models are based on criteria which take into account an internal variable and predict fracture in terms of a critical value at break. The advantage of this method lies in providing a rigorous formulation to take into account a coupling between damage and material behaviour, whereby damage reduces the resistance to

deformation, and strain increases damage. Conversely, the limitation is that it does not take into account explicitly local physical mechanisms that prove important in the ruin of the material.

From these considerations and in taking into account a few parameters intrinsically linked to my thesis, the choice of Lemaître's damage model has been done. Indeed, the last version of the isotropic Lemaître's model (Lemaître's formulation + crack closing effect in terms of decomposition of the stress tensor + cut-off value of the triaxiality) is already implemented in Forge® and this formulation explicitly dependent of the stress triaxiality may be sufficient to correctly represent the strain path changes between drawing and rolling.

## II.4 Summary

This chapter has been dedicated to the bibliography review in order to present the scientific background of my thesis. Three main parts have been presented.

The first section has dealt with the evolution of lamellar microstructure by explaining the deformation mechanisms during cold forming processes. During cold drawing, three mechanisms have been identified: slip in ferrite in the plane parallel to the lamella plane, slip in ferrite crossing lamellae, and slip in the interphase at interfaces. These mechanisms lead to a longitudinal microstructure with pearlite colonies aligned in the drawing direction and a swirled transverse microstructure. We have also seen that the microstructural evolution has a deep impact on mechanical properties (increase of hardness and yield stress linked to interlamellar distance evolution) and damage mechanisms (governed by the predominant role of non-metallic inclusions). During cold rolling, the microstructure evolution is less documented. However, three deformation mechanisms controlled the evolution during severe cold rolling. At low strain, compression of pearlite colonies nearly parallel to the rolling axis leads to a fine microstructure. When pearlite colonies are perpendicular to the rolling axis, irregularly bent lamellae are formed. Then, when deformation increases, bent lamellae are converted into shear bands. As in wire drawing, mechanical properties deeply depend on microstructural evolution and are also controlled by the interlamellar distance.

In the second part, isotropic and anisotropic yield functions have been introduced in order to be able to model the plastic behaviour of steels in a numerical code. Tresca's and Von Mises' isotropic yield functions have been extended to well correspond to experimental results. However, these functions are not able to correctly predict output geometries and plastic properties in some cases. That is why, anisotropic yield functions have been developed. Here, many modifications from the Von Mises's work and new criteria exist to take into account more and more experimental results. The yield functions are also more and more complicated and many mechanical tests are required to correctly identify parameters. Moreover, models developed for sheet forming are not necessarily relevant in bulk forming. In this context, the simple Hill's quadratic yield functions will be used to describe the anisotropic behaviour of our high carbon steels as it is already implemented in Forge®.

The last section of the bibliography review dealt with ductile damage mechanisms and models. Three steps can be introduced in damage mechanisms: nucleation, growth and coalescence. The major point is that matrix / inclusion interfaces are the critical nucleation sites due to stress concentration in this area. The growth and coalescence of cavities created lead to the formation of microscopic cracks and eventually fracture. Two main theories appear

in the modelling of damage. The first one consists in taking into account voids nucleation and growth. These non-coupled “pure” damage models try to accurately predict the fracture, but only for the solicitation from which it has been developed. It is then hazardous to use it in a different context. The second one tries to represent the decrease in the stress-strain curve after necking by using a more global approach. These coupled models are based either on continuum thermodynamics or porous media plasticity theory. The continuum thermodynamics use the concept of damage variable. As stress triaxiality is explicitly written in this formulation, it should be sufficient to represent the strain path change between drawing and rolling. Lemaître’s isotropic damage criterion with crack closure effect and cut-off value of stress triaxiality, already implemented in Forge®, will be used in this thesis.

## II.5 Résumé français

Ce chapitre a été consacré à un état de l'art de la bibliographie nécessaire à une bonne compréhension de ce manuscrit de thèse. Trois grandes parties ont été abordées.

La première partie a traité de l'évolution des microstructures lamellaires en détaillant les mécanismes de déformation qui peuvent intervenir au cours des procédés de mise en forme à froid. Au cours du tréfilage, trois mécanismes sont identifiables : glissement dans la ferrite dans des plans parallèles à ceux des lamelles ; glissement dans la ferrite à travers les lamelles ; glissement dans l'interphase à l'interface ferrite / cémentite. Ces mécanismes entraînent : un alignement des colonies de perlite selon la direction de tréfilage lorsqu'on regarde en vue longitudinale, et une microstructure très perturbée en coupe transverse. Cette évolution microstructurale a évidemment un impact sur les propriétés mécaniques du fil (augmentation de la dureté, de la contrainte d'écoulement liée à la distance interlamellaire) et sur les mécanismes d'endommagement (gouvernés principalement par la présence d'inclusions non-métalliques). Au cours du laminage à froid, peu de bibliographie existe sur l'évolution microstructurale. Cependant, trois mécanismes sont observables lors du laminage sévère (jusqu'à 80% de déformation). Aux faibles déformations, la compression des colonies de perlite, presque parallèles à l'axe de laminage, entraîne un raffinement de la microstructure par la diminution de la distance interlamellaire. Si les colonies perlitiques sont orientées perpendiculairement à la direction de laminage, des lamelles irrégulièrement courbées se forment. Lorsque la déformation croît, les lamelles courbées sont converties en bandes de cisaillement. Comme pour le tréfilage, les propriétés mécaniques sont étroitement liées à l'évolution microstructurale et à la distance interlamellaire. A partir de ces évolutions microstructurales, des modélisations ont été développées à différentes échelles voire en multi-échelles. Différents modèles tentent de représenter les mécanismes de déformation et de prédire les propriétés mécaniques finales.

Dans la deuxième partie du chapitre bibliographique, les critères (fonctions de charge décrivant l'évolution de la surface de charge) isotropes et anisotropes ont été introduits afin de pouvoir représenter le comportement plastique des matériaux dans un code numérique. Les premiers critères apparus sont ceux de Tresca et de Von Mises dans une formulation isotrope, puis ont été étendus afin de mieux correspondre aux résultats expérimentaux. Cependant, dans certains cas, ces fonctions n'étaient pas encore capables de prédire correctement les géométries finales et les caractéristiques mécaniques du matériau. C'est pourquoi les critères anisotropes ont été développés. Parmi ces critères, beaucoup sont issus de la modification du critère de Von Mises et d'autres ont été créés afin de prendre en compte de plus en plus de résultats expérimentaux. En contrepartie ces fonctions et l'identification des paramètres sont

de plus en plus compliquées. Dans ce contexte, il a donc été décidé d'utiliser un des premiers critères anisotropes apparus, le critère de Hill, pour décrire le comportement anisotrope de cet acier haut carbone.

Dans la dernière partie ont été présentés les mécanismes d'endommagement et leurs modèles. Les mécanismes se décomposent en trois étapes : la nucléation, la croissance et la coalescence. Le site critique de nucléation de l'endommagement se situe à l'interface matrice / inclusions à cause de la concentration de contraintes qui s'effectue dans cette zone. La croissance et la coalescence des cavités créées entraînent la formation de microfissures qui peuvent amener à la rupture. En ce qui concerne la modélisation de ces mécanismes, deux théories majeures émergent. La première consiste à modéliser la nucléation et la croissance de vides. En particulier, ces modèles d'endommagement non couplés tentent de prédire la rupture par la détermination d'une valeur critique constante à rupture qui tient compte du champ de contraintes. Ces modèles ne sont valables que le cadre où ils ont été développés, c'est-à-dire pour une sollicitation donnée, et sont de ce fait difficilement transposables à une autre sollicitation mécanique. La seconde théorie consiste à représenter la décroissance de la courbe contrainte - déformation qui apparaît à la suite de la striction, en utilisant une approche plus globale. Ces modèles couplés sont soit basés sur la thermodynamique des milieux continus (approche de type Lemaître) soit sur la plasticité des milieux poreux (approche de type Gurson). Dans cette thèse, la thermodynamique des milieux continus, qui utilise le concept de variable d'endommagement introduit par Kachanov, sera employée. Puisque la triaxialité des contraintes est explicitement prise en compte dans la formulation de type Lemaître, elle devrait suffire pour représenter et prendre en compte le changement de chemin de déformation entre le tréfilage et le laminage. Le critère d'endommagement isotrope de Lemaître avec l'effet de fermeture des fissures et le seuil de triaxialité de contraintes, déjà implémenté dans le logiciel d'éléments finis Forge®, sera utilisé.

# Chapter III Experimental mechanical characterisation

In order to have an accurate modelling of our processes, i.e. wire drawing and rolling, the mechanical behaviour of our material, valid for large strains has to be identified. For this purpose, some experimental mechanical tests have been achieved all along the cold forming schedule, leading to the identification of a constitutive law. These tests will be presented in the first section of this chapter. Then, in a second part, additional tests will be detailed, confirming the mechanical anisotropy of high carbon steel. Finally, the third section will concern the friction coefficient measurement.

A large part of this work has been done by N. Persem during his master at CEMEF [4] and is presented in [5].

## III.1 Identification of a numerical behaviour law

### III.1.1 Experimental tests

Mechanical tests have been performed at each step of the cold forming processes. Torsion test is the most commonly used in case of large strain. However, solicitations in torsion tests differ from those resulting from the drawing and rolling processes. Therefore an original identification method of the behaviour law was chosen [105] – combining drawing and tensile tests, without torsion. The behaviour law identification consists in plotting the strain – stress curves, obtained from tensile tests after patenting, after each pass of drawing, and two micro-hardness points before and after rolling, as shown in Figure 43. Mechanical tests have been performed at ArcelorMittal Research Centre in Gandrange and a picture of the device is shown in Figure 44. Tensile curves during wire drawing have been shifted along the horizontal axis by a strain value  $d_\epsilon$  corresponding to the wire-drawing strain, using the following approximate relation:

$$d_\epsilon = \ln(R_0 / R)^2 \quad (\text{III.1})$$

with  $R_0$  the initial radius before the 1<sup>st</sup> pass of wire drawing and  $R$  the current radius.

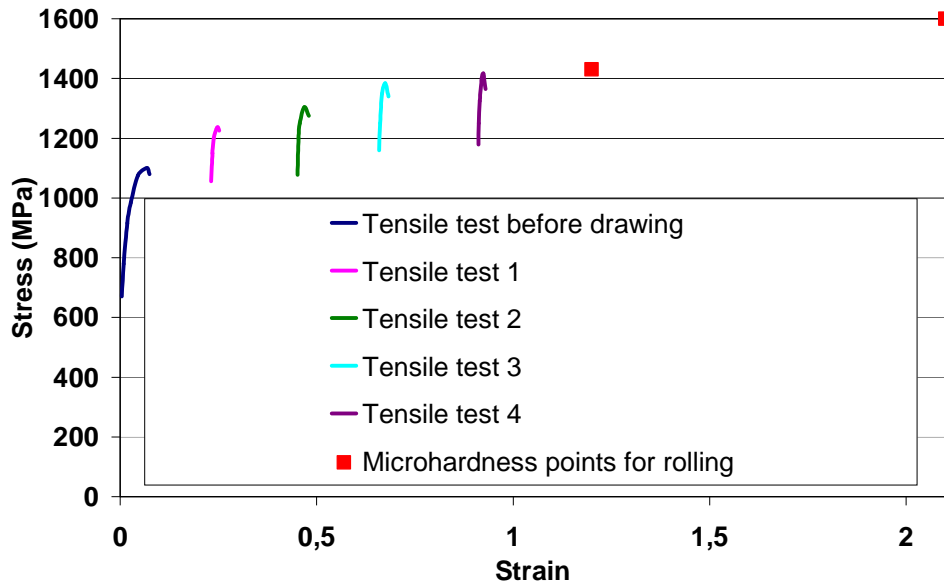


Figure 43: Mechanical tests along cold forming processes

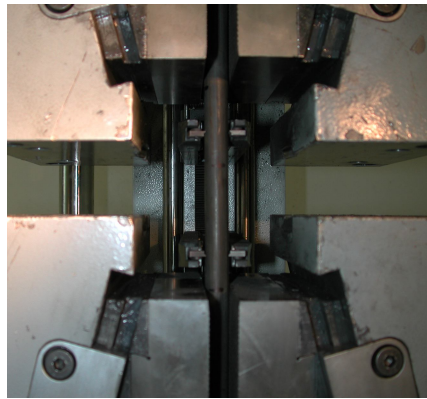


Figure 44: tensile test device

### III.1.2 Identification method

The numerical envelope of the curves for large strains was defined. It takes into account the first part of the tensile test after patenting (until the yield stress), the maximum stress value of all other tensile tests and the two micro-hardness points.

The most appropriate behaviour law available in Forge2005® is the elasto-plastic power law described by:

$$\sigma = \sqrt{3}K(1 + a\varepsilon^n) \quad (\text{III.2})$$

with  $\sigma$  the equivalent stress,  $\varepsilon$  the equivalent strain;  $K$ ,  $a$  and the exponent  $n$  (strain hardening index) are three constant parameters.

An inverse analysis is used to fit the three parameters of the behaviour law ( $K$ ,  $n$  and  $a$ ). Because of its simplicity of implementation and its good results in a small optimization space,

a Newton algorithm is used for this analysis. A more detailed explanation of the inverse analysis can be found in [5].

This method results in the following parameters (Table 6) and in a good correlation between the experimental tests and the numerical law (Figure 45). Moreover, the parameter values have been validated by re-simulating tensile tests with the numerical behaviour law and the comparison is fairly good as shown in Figure 46.

Parameter values	
a	7.32
n	0.13
K (MPa)	100.32

Table 6: Parameter values of the numerical behaviour law

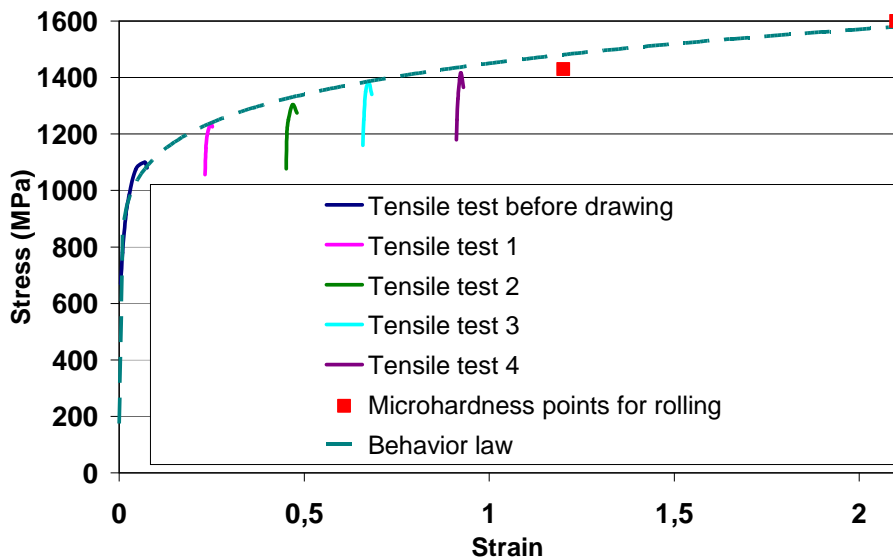
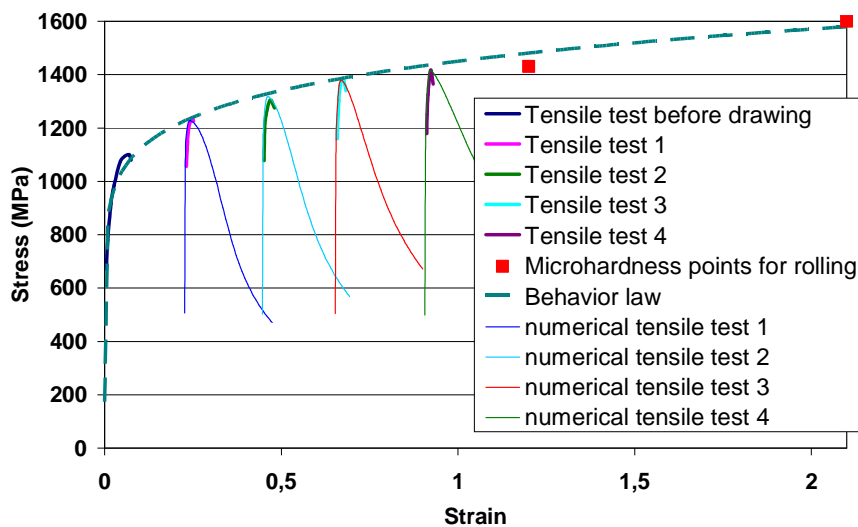


Figure 45: Comparison between the stress-strain curves of the experimental and the numerical characterization



**Figure 46: Re-simulation of the tensile tests for the validation of the behaviour law parameters (all curves are in engineering stress and strain)**

## III.2 Identification of friction parameters

In case of cold forming processes, many parameters have to be fixed. ArcelorMittal has provided us with most of them. The two last parameters are friction during wire drawing and rolling.

### III.2.1 Identification of the friction parameter during wire drawing

Tresca friction law was selected to provide the friction between wire and drawing dies and is written as follows:

$$\tau_c = \bar{m} \frac{\sigma_0}{\sqrt{3}} \quad (\text{III.3})$$

with  $0 < \bar{m} < 1$  the friction parameter,  $\tau_c$  the shear stress and  $\sigma_0$  the tensile stress.

To identify these two parameters, N. Persem in [4] and [5] has measured the experimental drawing force, using a dynamometric axis (Figure 47) situated at the drawing die exit, at the third and fourth drawing pass. The sensor enables us to know the force at the bullwheel axis and since the angle between the drawn wire and the axis is known ( $20^\circ$ ), the drawing force is thus obtained. Then, he adjusted the friction coefficient by comparing the experimental to the numerical drawing force value. With this method, the best friction value  $\bar{m}$  during wire drawing is  $\bar{m} = 0.02$  and gives good results in terms of drawing force, as shown in Figure 48.



**Figure 47: Experimental device for the drawing force measurement [4]**

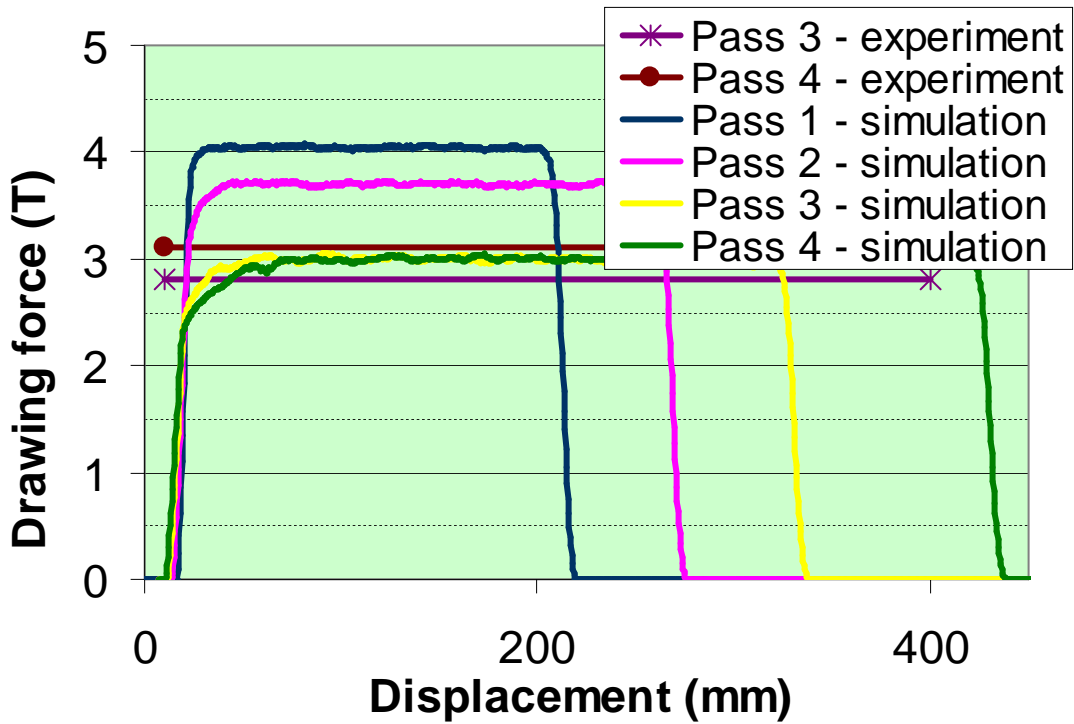


Figure 48: Comparison of the experimental and numerical drawing force [5]

### III.2.2 Identification of the friction parameter during rolling

The friction parameter in rolling was defined thanks to a Plane Strain Compression Test (PSCT, [106] and [107]) performed at CEMEF by P. Montmitonnet. Samples from rolling cylinders were used for the PSCT dies. Two roughness values were also used:  $R_a=2.5\mu\text{m}$  was used to simulate old dies and  $R_a=1\mu\text{m}$  was used to simulate new dies. Results, shown in Figure 49 and Figure 50, give a mean value of the friction parameter during rolling of  $\bar{m} = 0.25$ .

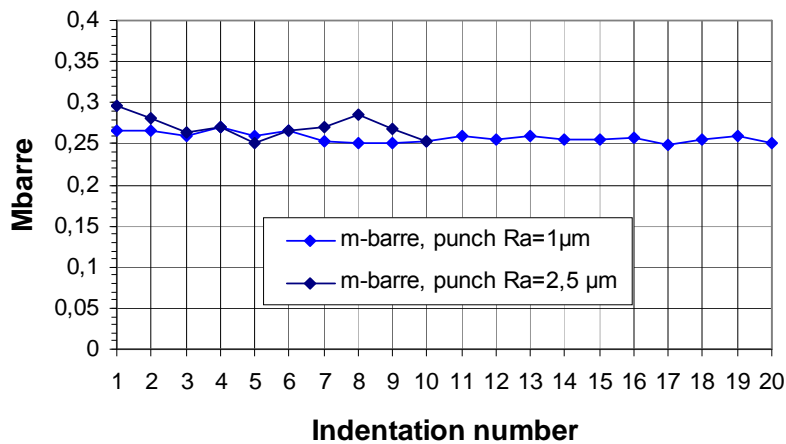


Figure 49:  $\bar{m}$  values during PSCT tests



Figure 50: PSCT samples

### III.3 Highlighting the anisotropy phenomenon

As mentioned in the introduction (section I.2.3), the underestimation of the final widening may come from the anisotropy introduced by wire drawing.

Plastic anisotropy can be easily manifested e.g. by ovalization in tension or compression tests [48] and [61], since the difference in yield stress will favour one cross-sectional direction with respect to the other.

Here, compression tests, in different directions and at different stages of the drawing process, have been chosen to highlight plastic anisotropy.

#### III.3.1 Compression tests during wire drawing

A test campaign has been performed at different stages of wire drawing, using two kinds of samples, the ones oriented in the longitudinal direction, the others in the transverse direction, in order to validate our hypothesis on anisotropy and to identify if there is a preferential direction of anisotropy.

##### III.3.1.1 Longitudinal compression tests

Samples were cut along the wire drawing axis (longitudinal direction), as shown in Figure 51, at three steps: after patenting, during drawing and after drawing (the initial diameters decrease progressively and correspond to the wire diameters).

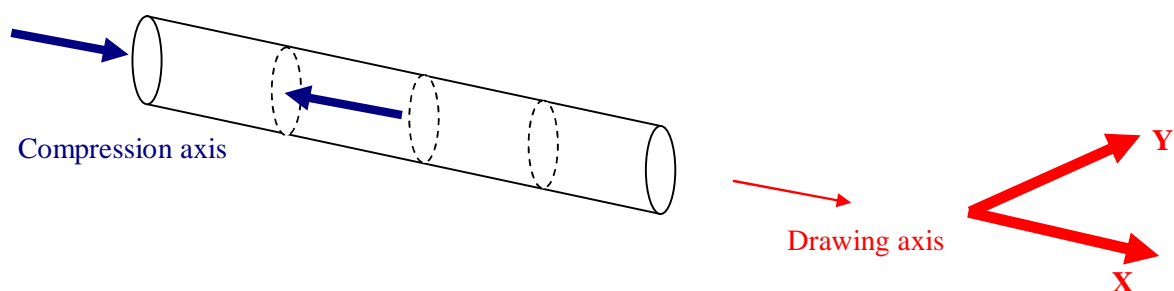
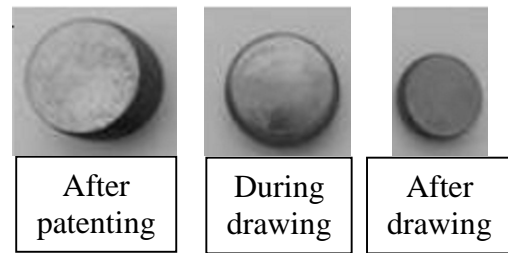


Figure 51: Scheme of longitudinal compression sampling

After compression, samples remain cylindrical (the difference between the small and large diameter of the section, whatever the drawing step, is constant and is about 0.2mm, i.e. 1%), as observed in Figure 52 and in Table 7, and show an isotropic behaviour in the wire section.

Step	N°	Final small diameter	Final large diameter	Height reduction
After drawing	1	12.72	12.84	49.72%
	2	12.7	12.86	49.58%
	3	12.73	12.81	49.44%
	4	12.71	12.8	49.58%
	5	12.71	12.83	49.44%
During drawing	1	16.39	16.54	51.17%
	2	16.13	16.28	50.45%
	3	16.19	16.31	50.06%
	4	16.14	16.26	50.33%
	5	16.17	16.24	49.94%
After patenting	1	17	17.31	30.21%
	2	17.03	17.21	30.12%
	3	17	17.19	30.29%
	4	16.88	17.2	29.85%
	5	17.04	17.28	30.03%

**Table 7: Samples diameters evolution after longitudinal compression**



**Figure 52: Compression tests in longitudinal direction highlight isotropic behaviour in the section (the same scale is used).**

### III.3.1.2 Transverse compression tests

For transverse compression test, samples were cut as explained in Figure 53 at the same stage as for longitudinal compression. All samples have the same dimension: height of 6mm and diameter of 5mm. Figure 54 and Table 8 clearly show a progressive ovalization for transverse samples, which confirms the appearance of anisotropy, more precisely an easier flow in the transverse (radial) as compared to the axial (drawing) direction.

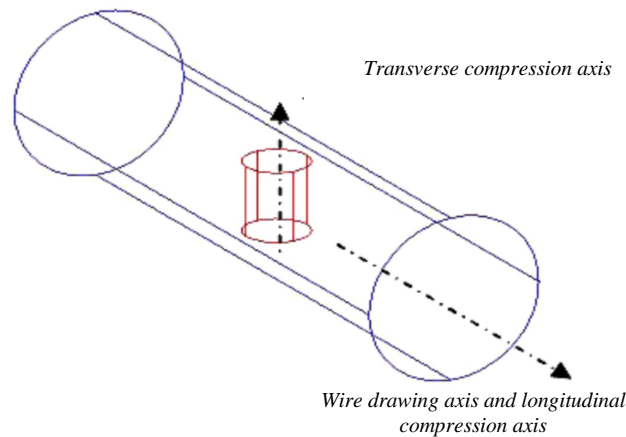


**Figure 53: Scheme of transverse compression sampling**

	Final dimensions (mm)			Ratio	
	Height h	Small axis a	Large axis b	$h_0/h$	b/a
After machining					
After patenting	3.38	6.95	6.96	1.775	1
During drawing	3.39	6.6	7.43	1.77	1.126
After drawing	3.42	6.16	7.69	1.754	1.248

**Table 8: Samples mean diameters evolution after transverse compression**

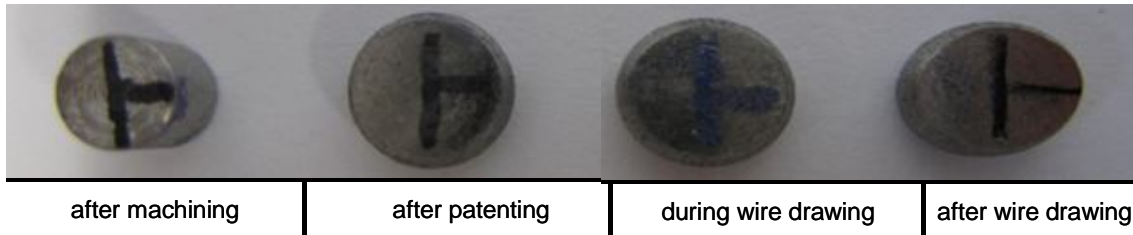


Figure 54: Compression tests in transverse direction highlight evolutive anisotropy. Height reduction is 44%. The horizontal bar of the T is the radial direction; the vertical bar is the drawing direction.

### III.3.2 Comparison of the stress-strain curves

When the mean stress-strain curves of the two compression tests are superposed (Figure 55), it shows a very weak 2% difference of the yield stress between the two directions.

Identifying the true yield stresses, for deformed and hardened material, is a very hard work. Indeed, the heterogeneous residual stresses are added to the microstructural heterogeneity to give a widespread transition between the elastic state and the plastic state<sup>2</sup>: thus a non-linearity of the stress-strain curve appears early. On Figure 55, the plastic threshold could be around 1000 or 1200 MPa considering the beginning of the non-linearity of the curve; however, the stress quickly stabilizes at 1400 MPa in a steady plastic state. That's why, it could be useful to superpose these curves to the numerical behaviour stress-strain curves: the envelope curve, which only takes into account the steady macroscopic plasticity, to define the yield stresses. Figure 56 enables us to fix the transverse yield stress at 1400 MPa and the longitudinal yield stress at 1430 MPa. It can be noted that the difference between the transverse and the longitudinal yield stress is very small (about 2%) compared to the difference between the flow along the two axes (about 20%).

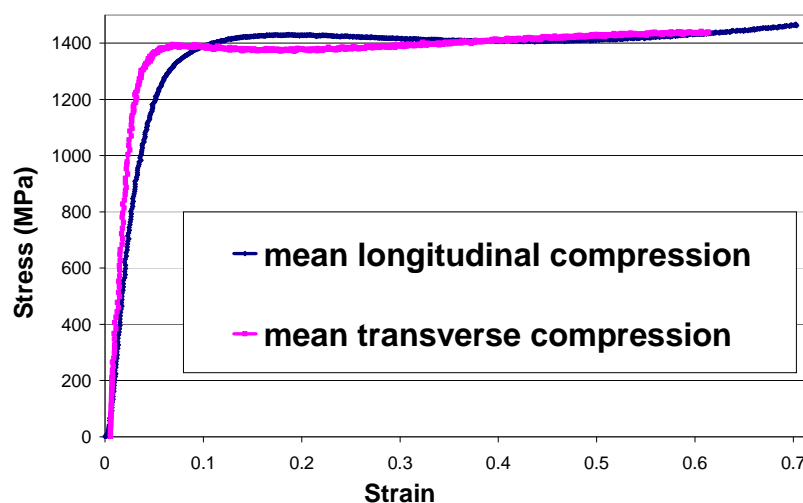


Figure 55: Compression strain-stress curves after drawing

<sup>2</sup> A local plastification first appears in areas with residual tension for tensile tests, or in areas with residual compression for compression tests. Moreover, any microstructural heterogeneity will play the role of a stress localization zone and a local plastification will appear and will progressively expand.

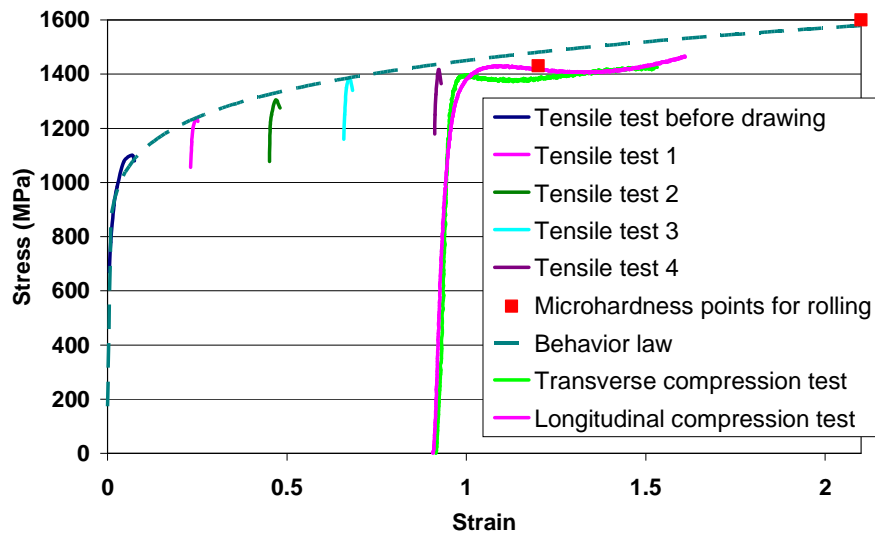


Figure 56: Strain-stress curves at all stages of the cold forming process

### III.4 Further mechanical tests

#### III.4.1 Torsion test

To fully identify the mechanical behaviour at the end of drawing, torsion tests have been carried out directly on the drawn wire, as shown in Figure 57. This test has been done by ArcelorMittal Research Centre.

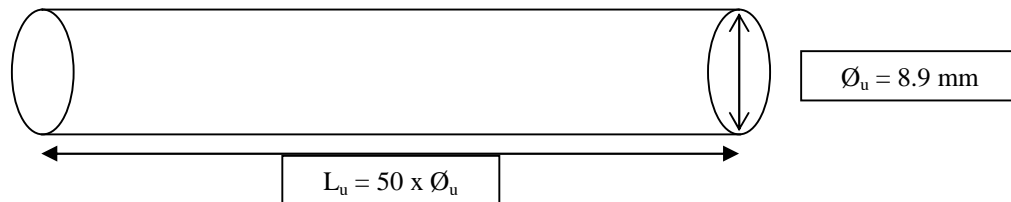


Figure 57: Torsion sample geometry

##### III.4.1.1 Advantages

Three main advantages characterize this test:

- Its wide use because of the very high strain reached
- The geometry remains constant
- There is no mechanical instability

Thus, this mechanical characterization device enables high strains, but strains will be heterogeneous with a linear evolution of  $\bar{\epsilon}(r)$ .

Moreover, strain rate is constant in time as soon as the rotation speed is constant too (by opposition to the tensile or compression tests, where an exponential displacement is required).

However,  $\dot{\varepsilon}(r)$  will be heterogeneous and linear as well. Moderately high strain rates can be reached (1 to 10 s<sup>-1</sup> depending on the machine; this is equivalent to tension or compression). Finally, torsion can be performed in a large temperature range, as compression or tension.

### III.4.1.2 Results

Two torsion tests have been done until break at a constant strain rate (10 rpm). Figure 58 shows the broken wire from different views. The torsion test gives the torque-rotation number curve (Figure 59); the two tests are perfectly superimposed.

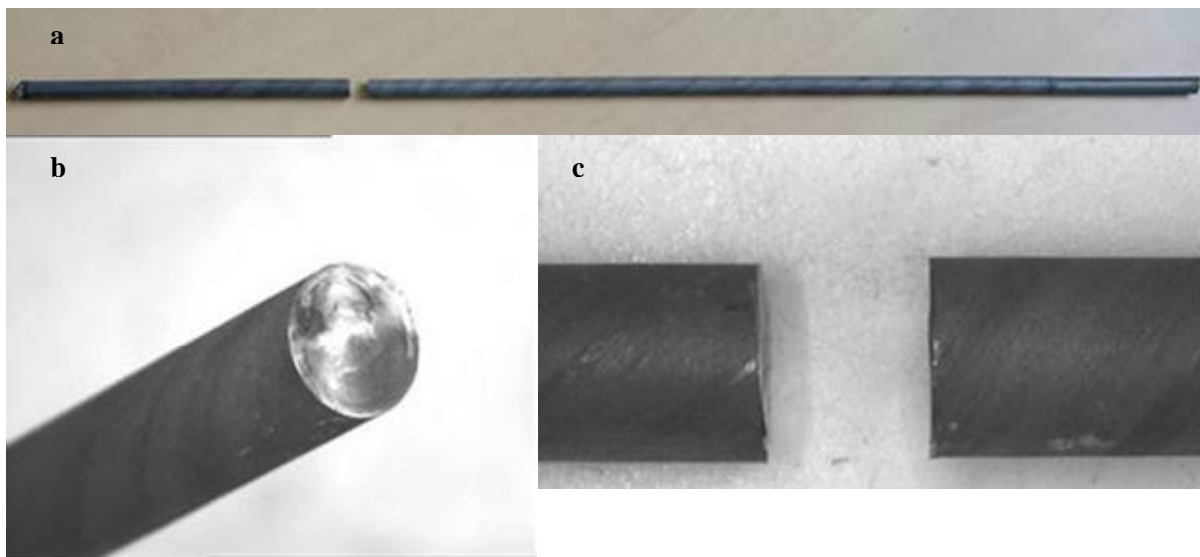


Figure 58: torsion sample pictures after rupture (-a- reconstituted sample -b- fracture surface -c- fibering)

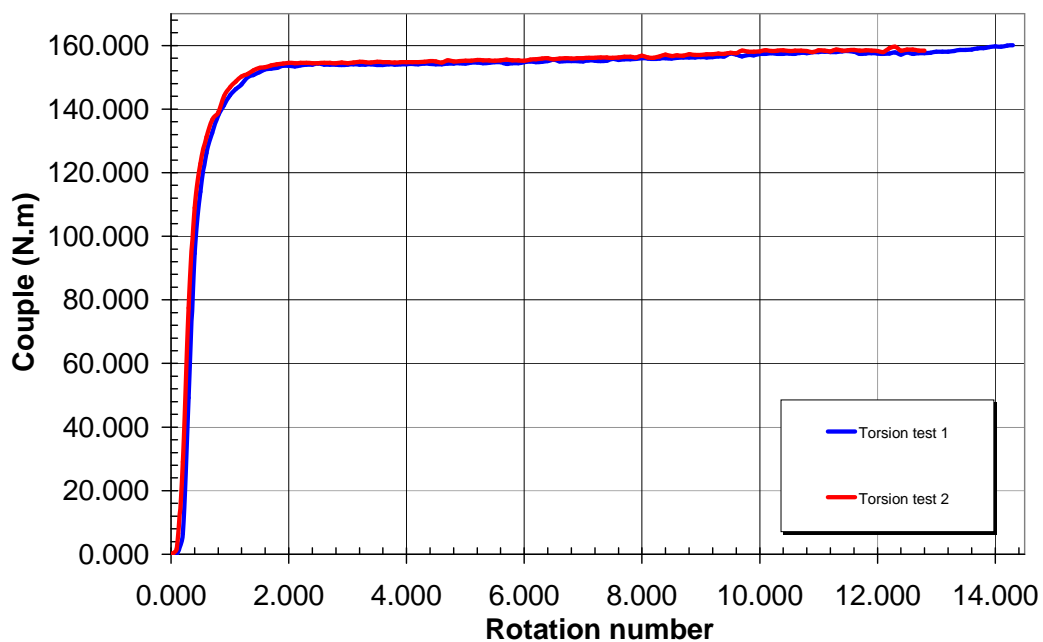


Figure 59: Torque-rotation number curves

### III.4.1.3 Fields and Backofen method for the stress-strain curve

This method is detailed in Annex 3 and enables us to obtain the stress-strain curve, only in the plastic domain, from the torque-rotation number curve.

The stress-strain curves can be plotted in Figure 60 with the two following equations (only valid in the plastic part, i.e. without the hatched part):

$$\begin{cases} \sigma_{\theta z}(R) = \frac{\Gamma(R)}{2\pi R^3} (\tilde{m} + \tilde{n} + 3) \\ \bar{\varepsilon}(R) = \frac{2}{\sqrt{3}} \frac{\pi NR}{l} \end{cases} \quad \text{(III.4a, b)}$$

with :

$$\tilde{m} = 0$$

$$\tilde{n} = 0.0204$$

And from this last graph, the shear stress is  $\sigma_{0XZ} \sim 850$  MPa.

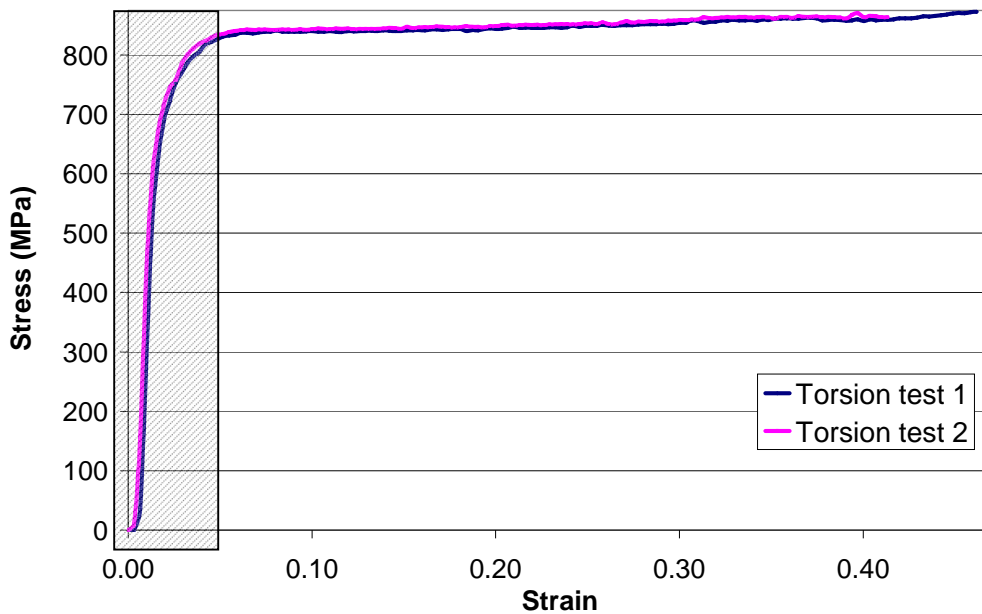


Figure 60: Stress - strain curve for the torsion test

### III.4.2 Ultimate drawing

To confirm the envelope curve identified in section III.1, an “ultimate drawing test” has been done. An ultimate drawing consists in drawing the wire until the material limit. This limit is identified with torsion tests after each pass (to measure the residual ductility) by the fracture of the wire by delamination (Figure 61). The first passes of this ultimate drawing exactly correspond to our process (same initial and final diameters and same reductions). Table 9 and Figure 62 present the results of the ultimate drawing.

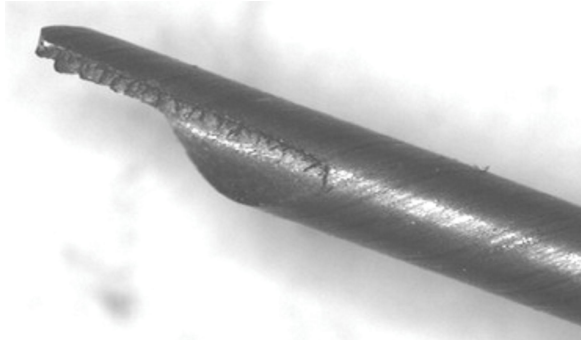


Figure 61: Delamination of a drawn wire after torsion tests

Strain	Stress (Mpa)	Hardening	
		theoretical	cumulated
0.00	1100		
0.25	1285	20.28%	20.28%
0.49	1340	19.72%	36.00%
0.72	1430	18.68%	47.95%
1.00	1476	22.35%	59.59%
1.25	1571	20.01%	67.67%
1.49	1635	19.99%	74.14%
1.73	1744	19.20%	79.10%
1.98	1878	20.40%	83.37%
2.23	1963	19.91%	86.68%
2.47	2141	20.02%	89.34%
2.71	2322	19.12%	91.38%
2.96	2355	20.27%	93.13%

Table 9: Ultimate drawing of the C72

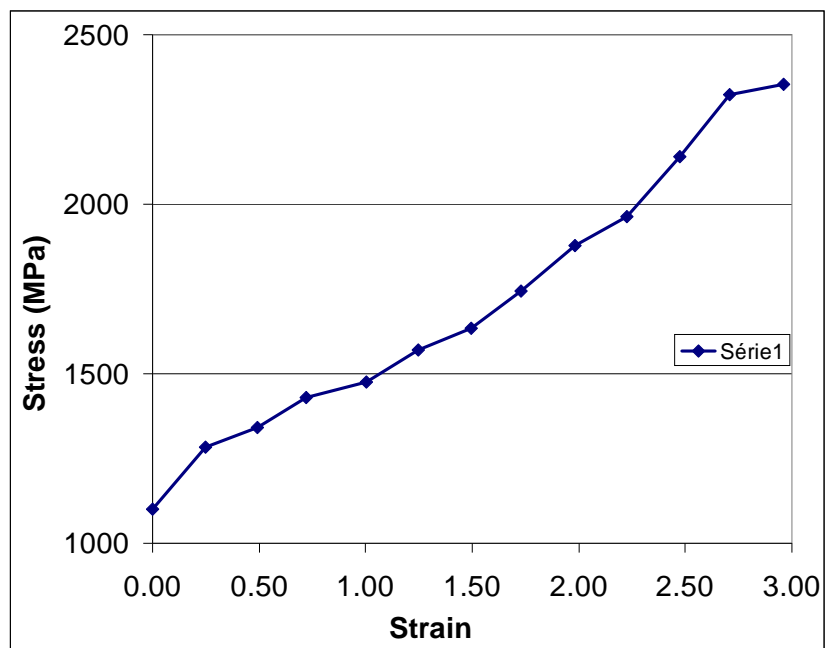


Figure 62: Stress- strain curve of the ultimate drawing

### III.4.3 Complete mechanical behaviour

An interesting comparison consists in superposing this ultimate drawing stress-strain curve to the previously determined stress-strain curve of Figure 45, as well as the torsion curve. This is done in Figure 63.

The relation  $\sigma_0 = \tau \cdot \sqrt{3}$  has been used (as for Von Mises behaviour, despite the anisotropy) to superpose the torsion curve with the other stress-strain curves.

First, a perfect match is observed between torsion (orange curve) and the tension + compression + hardness (envelope, dark green dashed) curve. Secondly, the “ultimate drawing” stress-strain curve (blue dashed line) shows a very good agreement with the other two, up to a strain of 1 which covers the whole industrial drawing process. At larger strain, the two curves diverge, because the microstructures developed during “ultimate drawing” and during wire-drawing + rolling are different: the texture and lamellae orientation is much stronger in ultimate drawing, as will be shown in chapter 5.

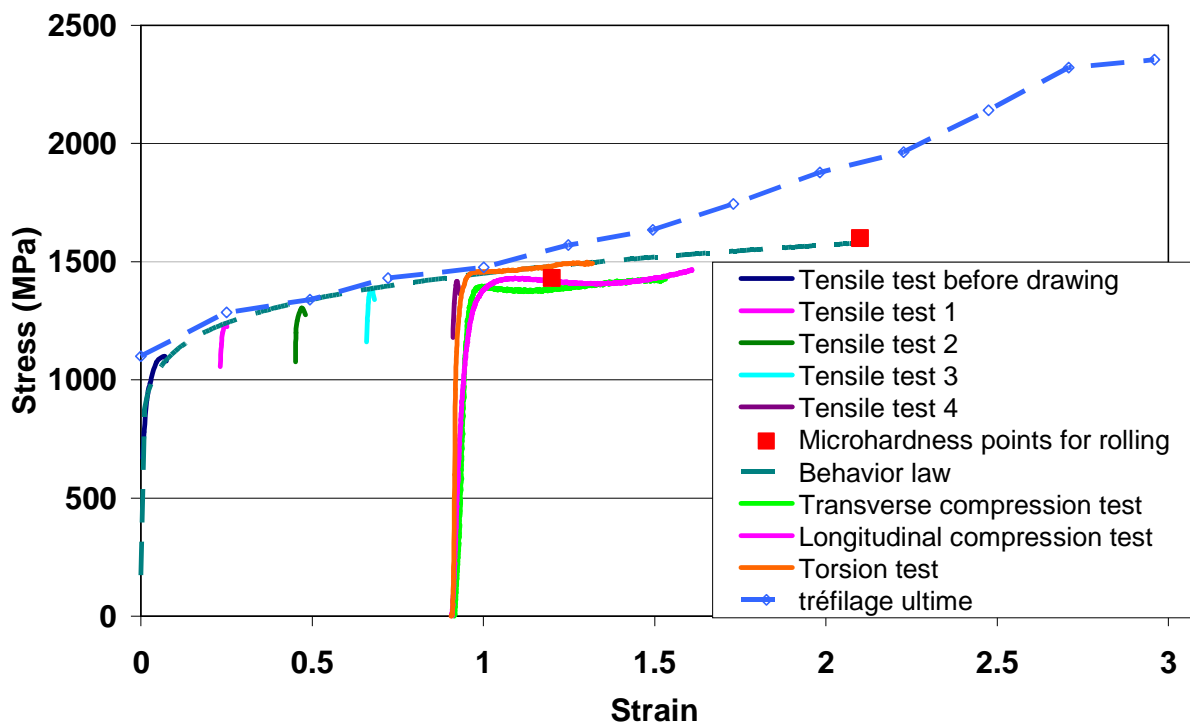


Figure 63: Complete stress-strain curves for C72

## III.5 Identification of Hill's parameters

### III.5.1 Anisotropic constitutive model

As mentioned in the section II.2.3, Hill's yield function is used to define the anisotropic behaviour of our material and is written in equation (II.10). From this relation, the equivalent stress is given as follows:

$$\sigma_{eq}^2 = A \left\{ F(\sigma_{YY} - \sigma_{ZZ})^2 + G(\sigma_{ZZ} - \sigma_{XX})^2 + H(\sigma_{XX} - \sigma_{YY})^2 + 2L\sigma_{YZ}^2 + 2M\sigma_{XZ}^2 + 2N\sigma_{XY}^2 \right\} \quad (\text{III.5})$$

In the anisotropic case, A is taken by convention as [108]

$$A = \frac{1}{2} \sqrt{\frac{3}{\Sigma}}, \text{ avec } \Sigma = FH + FG + GH \quad (\text{III.6})$$

Equation (III.6) is built in order to give a symmetric role to the yield stresses in the anisotropic principle directions X, Y and Z.

From equation III.5, it is easy to recover the isotropic case (Von Mises) with F=G=H 1 and L=M=N=3. Hill's criterion therefore appears as the simplest quadratic generalization of Von Mises criterion.

These parameters have a physical meaning, since they are linked to the axial and shear yield stresses:

$$\begin{aligned} \sigma_{0XX} &= \frac{1}{\sqrt{G+H}}, & \sigma_{0YY} &= \frac{1}{\sqrt{F+H}}, & \sigma_{0ZZ} &= \frac{1}{\sqrt{F+G}}, \\ \sigma_{0XZ} &= \frac{1}{\sqrt{2M}}, & \sigma_{0XY} &= \frac{1}{\sqrt{2N}}, & \sigma_{0YZ} &= \frac{1}{\sqrt{2L}} \end{aligned} \quad (\text{III.7a, b, c, d, e, f})$$

The axis-symmetry of drawing brings further simplification, since all directions in the cross section are equivalent:

$$H = G, N = M, L = 2F + G \quad (\text{III.8a, b, c})$$

Equation III.5 becomes:

$$\sigma_{eq}^2 = A \cdot \left\{ \begin{aligned} &F(\sigma_{YY} - \sigma_{ZZ})^2 \\ &+ G[(\sigma_{ZZ} - \sigma_{XX})^2 + (\sigma_{XX} - \sigma_{YY})^2] \\ &+ 2M\sigma_{XZ}^2 \end{aligned} \right\} \quad (\text{III.9})$$

### III.5.2 Coefficients measurement

#### III.5.2.1 At the end of drawing

Ovalization can be characterized by the shape factor of the section (Figure 64) and related to the anisotropy coefficients, giving a first relation from which F/G can be identified:

$$\frac{b}{a} = \left( \frac{h_0}{h} \right)^{(F-G)/(F+G)} \quad \text{(III.10)}$$

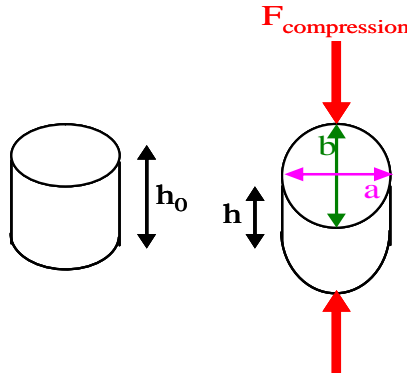


Figure 64: Compression test geometry

Then F (or G) must be extracted from the compression yield stress and M from the torsion yield stress superposed on the complete stress-strain curve (Figure 63). These curves lead to the coefficients reported in Table 10

	Non-drawn	Half-drawn	Fully drawn
<b>F/G</b>	0.995	1.525	2.261
<b>L/M</b>	1	1.07	1.25

Table 10: Reduced parameters of anisotropic Hill criterion ( $\times 10^{-6} \text{ MPa}^{-2}$ ) during wire drawing

These parameters have been validated by re-simulating the compression tests. We first had to identify friction based on barrelling, resulting in a Tresca's friction factor  $\bar{m} = 0.25$ . Then, recomputing compression tests resulted in a good agreement on ovalization as shown in Figure 65 ( $b/a = 1.21$  instead of 1.24 experimentally).

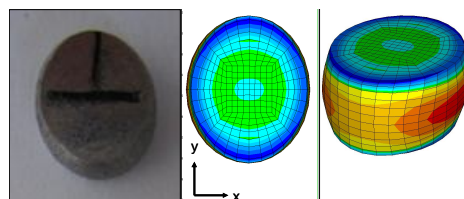


Figure 65: Comparison between experimental and numerical ovalization

But the agreement on the yield stresses is far from satisfactory. In the experiments, the difference between the axial and the radial yield stress is never more than 2% (Figure 55). Fitting ovalization and the radial yield stress as described above leaves us with a ratio  $\sigma_{0XX} / \sigma_{0RR} = 1.3$ . The Figure 66 helps us to understand this phenomenon. In a longitudinal cutting plane XOZ,  $\theta$  is the angle between the wire axis X and any direction in this plane, i.e.  $\theta=0^\circ$  corresponds to the longitudinal compression and  $\theta=90^\circ$  to the transverse compression. In the figure, we have three curves in the vertical axis:

- The measured yield stress (sig0), which is approximately independent of the angle ;
- The yield stress given by Hill’s criterion and fitted with the transverse compression (sig0Hill) ( $\sigma_{0XX}=1796$  MPa in the longitudinal direction,  $\theta=0^\circ$ , and  $\sigma_{0RR}=1400$  MPa in transverse direction,  $\theta=90^\circ$ );
- The ratio small axis / large axis (b/a), describing the flow. It can be compared to the Lankford coefficient in case of sheets (reduction in widening / reduction in thickness in a tensile test). Here, the flow is isotropic in the longitudinal direction X [  $b/a=1$  because  $(G-H) / (G+H) = 0$  ] and anisotropic in transverse direction[  $b/a=1/1.25 = 0.8$  for a 44% compression, because  $(F-G) / (F+G) = 0,393$  ].

It can be noted that the previous identification assures that “b/a Hill” is superposed to “b/a experiment” since we use the experimental values to determine F, G and H.

In Hill’s model, ovalization and stress are dependent on the angle (it can not be deduced that the variation is linear because we only have two points) and their difference  $0^\circ/90^\circ$  are very similar. However, experimentally,  $\sigma_0$  is not dependent of  $\theta$ .

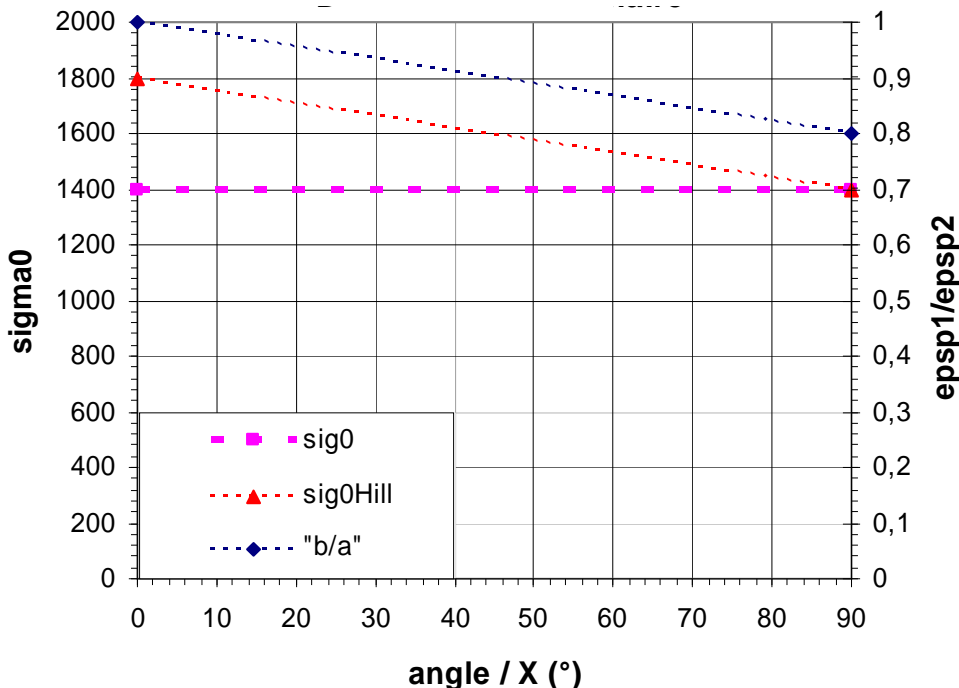


Figure 66: Angular dependence between stress and ovalization

This difficulty is usual in sheet forming, where it is very hard to fit the angular dependence of both flow pattern (Lankford coefficient) and yield stress [65], [109] and [110]. More sophisticated anisotropy models have been developed for this purpose [111], as presented in section II.2.2.4. In the absence of any reliable, widely accepted anisotropy model for bulk material (except maybe polycrystalline models [112] and [113]), and since we are firstly interested in transverse flow, the following study is carried out with the constitutive parameters identified above from the flow pattern in compression.

Remark:

Value of  $G$  (eq. III.7a) could have been obtained from the yield stress of the longitudinal compression and then  $F$  could have been deduced with eq. III.10. This would have increased the stresses by about 25%.

Another solution would have been to use the longitudinal and transverse experimental yield stresses to determine  $F$ ,  $G$  and  $H$ . Thus, we would have found these three parameters approximately equal and we would have deduced that  $b/a \sim 1$  whatever the compression direction: this model would have been quasi isotropic, well describing the stresses but with a very bad description of the flow. But, what is interesting is the widening prediction, which is equivalent in rolling to the  $b/a$  ratio in compression.

That is why we choose the geometric characteristic to measure Hill's coefficients. Even if this criterion is insufficient in terms of stresses, we are going to use it in rolling since we want to see an effect on geometry.

### III.5.2.2 At the end of rolling

Hill's coefficients have been measured at the end of rolling. For this purpose, further mechanical tests have been done because of the three dimensions characteristic of rolling. Compression tests of cubic samples ( $5 \times 5 \times 5 \text{ mm}^3$ ) have been performed along the three axes to identify  $F$ ,  $G$  and  $H$  and compression curves are presented in Figure 67. Moreover shear tests (Figure 68) have been also done in the three shear planes to identify  $L$ ,  $M$  and  $N$ . Shear curves are detailed in Figure 69.

For each direction, four samples have been used and compression tests are reproducible at less than 3%.

Coefficients  $F$ ,  $G$ ,  $H$  have been identified with the same procedure as previously, i.e. with the shape equation (eq. III.10) and with the transverse stress (eq. III.7b). For  $L$ ,  $M$  and  $N$ , the three shear stresses have been used (eq. III.7d, e, f). Identification resulted in the ratios presented in Table 11, which shows that transverse mechanical anisotropy is stopped at the end of rolling. These compression and shear tests have been resimulated for validation and results are shown in Table 12. As for the identification of Hill's coefficients at the end of

drawing, the numerical compression tests agree on geometry but the agreement on stresses is far from satisfactory. Explanations have been already given in the previous section. Numerical shear tests agree with experiments within 5%.

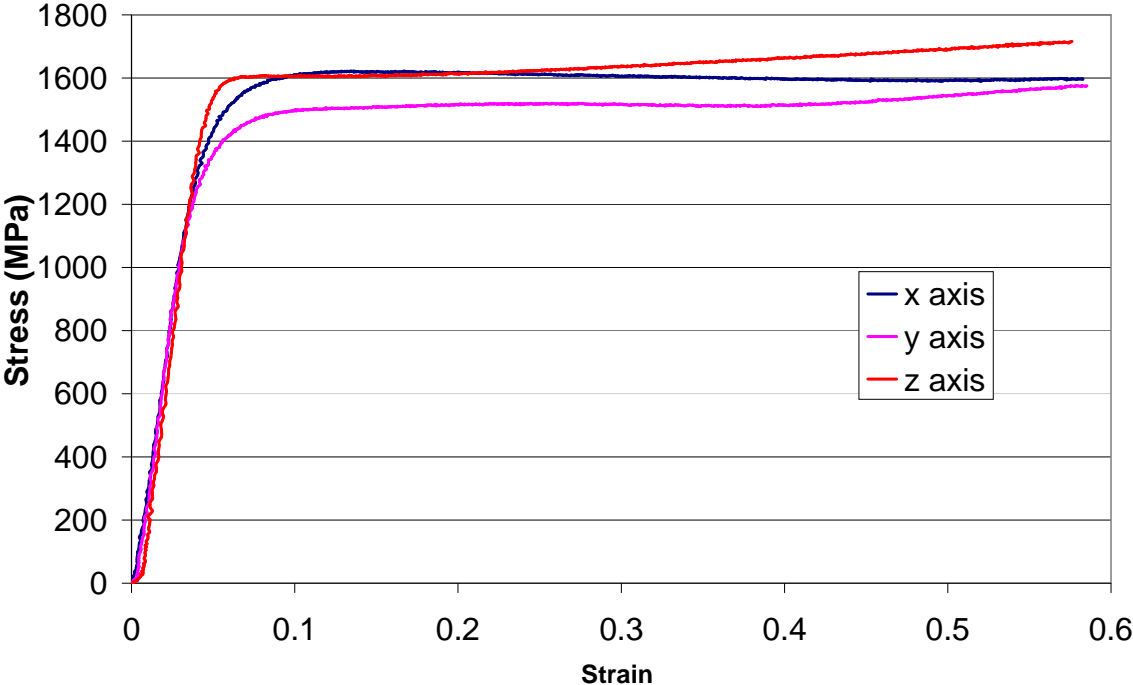


Figure 67: Compression curves after rolling

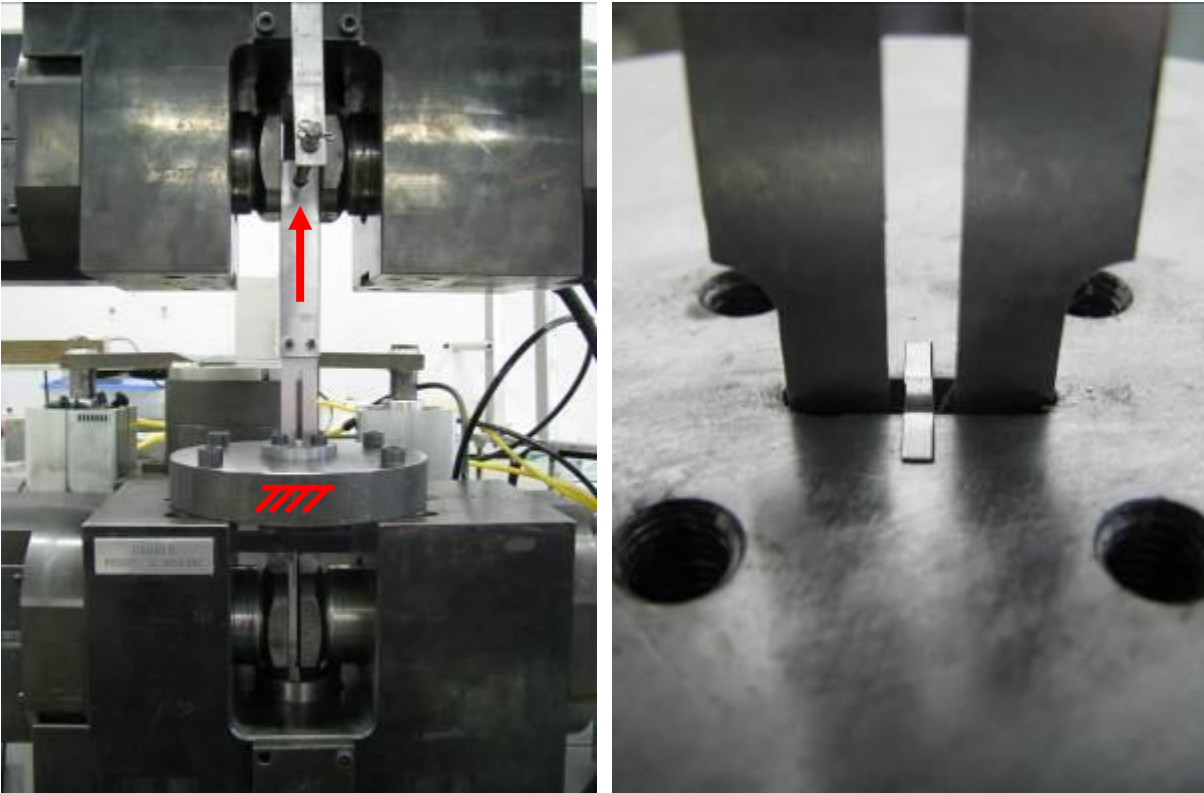


Figure 68: Shear tests: (left) shear assembly – (right) sample after shear

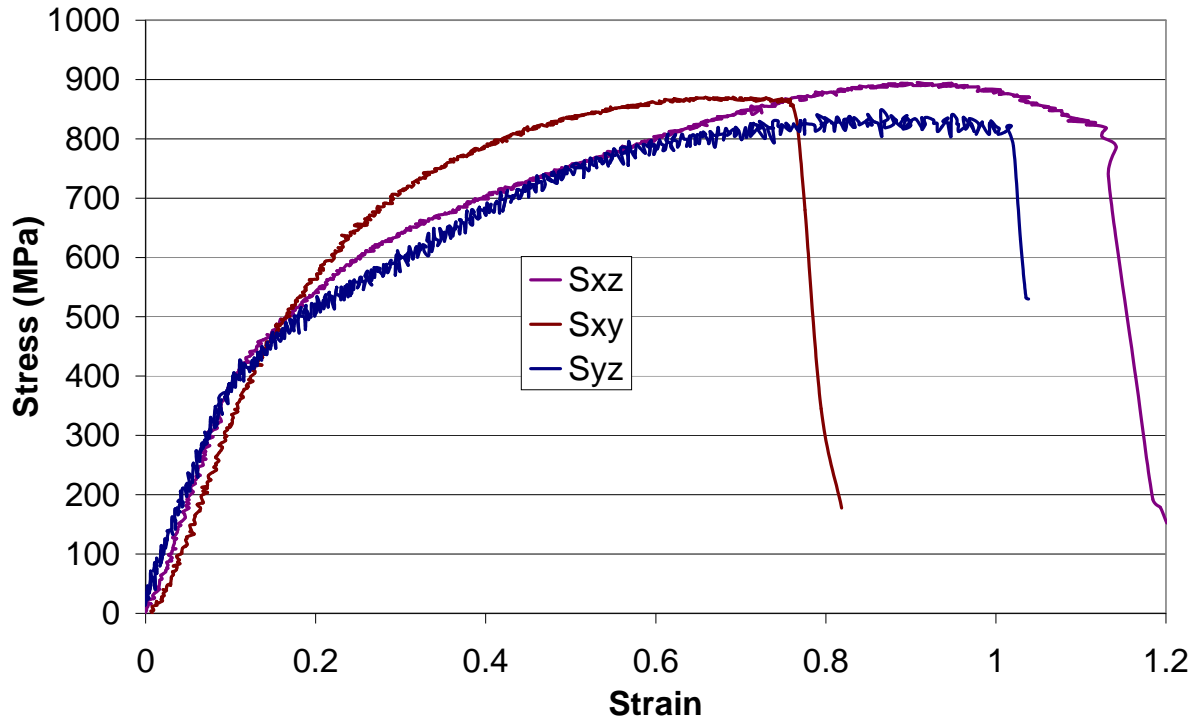


Figure 69: Shear curves after rolling

	Non-drawn	Half-drawn	Fully drawn	Flat-rolled
<b>F/G</b>	0.995	1.525	2.261	2.018
<b>G/H</b>	1	1	1	1.523
<b>L/M</b>	1	1.07	1.25	1.165
$\sigma_{0yy}/\sigma_{0xx}$			0.780	0.814
$\sigma_{0zz}/\sigma_{0xx}$			0.780	0.741
$\tau/\sigma$			0.541	0.545

Table 11: Hill's coefficients evolution during drawing and rolling

	$\sigma_{exp}$ (MPa)	$\sigma_{num}$ (MPa)	<b>X- compression</b>		<b>Y- compression</b>		<b>Z- compression</b>	
			<b><math>d_f</math> exp</b> (mm)	<b><math>d_f</math> num</b> (mm)	<b><math>d_f</math> exp</b> (mm)	<b><math>d_f</math> num</b> (mm)	<b><math>d_f</math> exp</b> (mm)	<b><math>d_f</math> num</b> (mm)
X	1600	2041	2.22	2.20	6.05	5.99	6.42	6.39
Y	1575	1694	6.69	6.55	2.26	2.22	7.49	7.54
Z	1715	1501	7.31	7.38	8.01	8.07	2.2	2.27

Table 12: Experimental and numerical compression tests results

For simplification and from results in Table 11, it is thus correct to keep Hill's coefficients, identified at the end of drawing, constant all along rolling.

### III.6 Identification of Lemaître's parameters

To fully identify Lemaître's parameters, an inverse analysis method is used and coupled to finite element software (Forge2005®). As our study deals with two chained-processes, damage parameters will be identified at the patenting step and will remain constant all along wire drawing and rolling.

The previously identified behaviour law (Table 6 and Figure 45) was fit on the global behaviour (5 tension tests plus 2 hardness values). For the patented state, only the initial part of the curve was taken into account, resulting in a poor description of that part important for damage identification. Thus, as a first step to damage parameters identification, a much precise curve had to be adjusted by inverse analysis, focusing on the tension test on the patented wire. The damage model has been chosen in the previous chapter and is Lemaître's one with some extensions:

$$\dot{D} = \begin{cases} 0 & \text{if } Triax < -1/3 \text{ or if } \bar{\varepsilon}_p \leq \varepsilon_d \\ \left(-\frac{Y}{S_0}\right)^b \dot{\bar{\varepsilon}}_p & \text{if } Triax > -1/3 \text{ and if } \bar{\varepsilon}_p > \varepsilon_d \end{cases} \quad \text{(III.11a, b)}$$

with:

$$Y = \begin{cases} -\frac{\sigma_{eq}^2}{2E(1-D)^2} \left[ \frac{2}{3}(1+\nu) + 3(1-2\nu) \left( \frac{\sigma_H}{\sigma_{eq}} \right)^2 \right] & \text{if } Triax > 0 \\ -\frac{h \sigma_{eq}^2}{2E(1-hD)^2} \left[ \frac{2}{3}(1+\nu) + 3(1-2\nu) \left( \frac{\sigma_H}{\sigma_{eq}} \right)^2 \right] & \text{if } Triax < 0 \end{cases} \quad \text{(III.12a, b)}$$

For steel,  $h = 0.2$  has been proposed [96]. Remember that  $h=0$  means no damage in compression and  $h=1$  assumes the same damage in compression as in tension.

#### III.6.1 Inverse analysis method

The main interest of these methods is to identify parameters which are hard to estimate from experimental observations. In our case, the identification will deal with damage parameters and the observable parameter will be the force – displacement curve. These methods combine experimental and numerical data in order to determine the considered parameters. In a first step, experimental tests are performed and experimental data are collected ( $R_{exp}$ ). These tests are numerically simulated to have numerical data ( $R_{simu}$ ). Correlation between numerical and experimental data is obtained by minimizing an objective function representing the deviation between numerical and experimental values. The best set of parameter is given thanks to a minimization algorithm. A Genetic algorithm is used in the software with 200 iterations and 30 initial parents. The inverse analysis tool is thus used and work as shown in the next sketch (Figure 70).

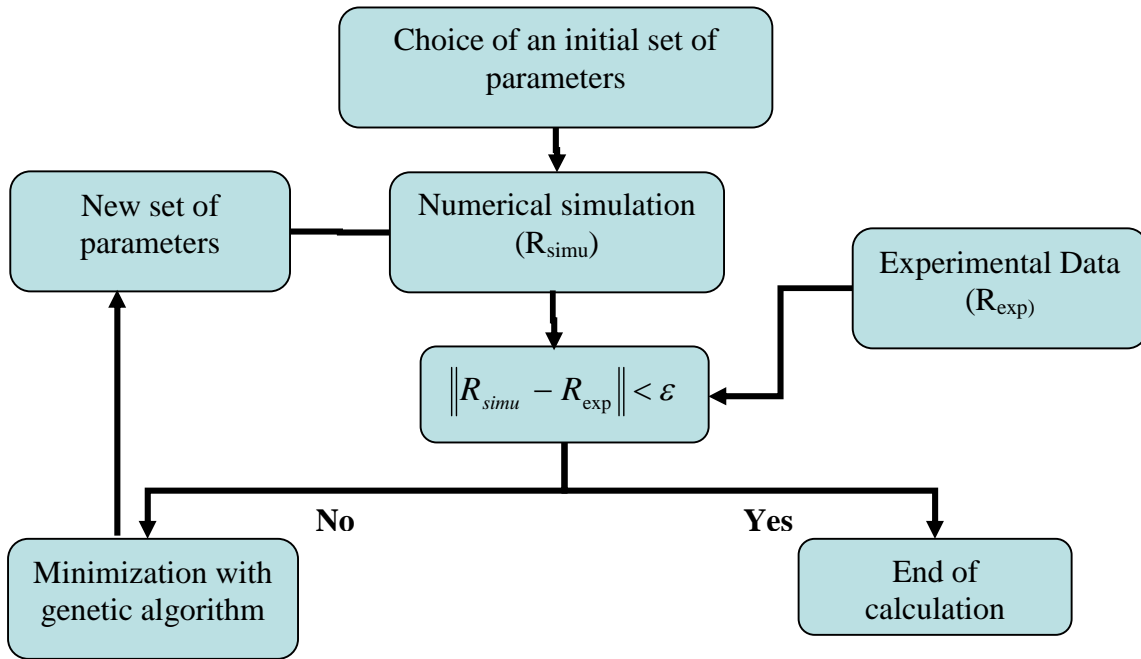


Figure 70: Inverse analysis schematic principle

### III.6.2 Hardening law identification

The following hardening expression is available in the parameter identification software:

$$K(T, \bar{\varepsilon}) = K_0 \left( \varepsilon_0 + \bar{\varepsilon}^{-n} \right) \quad (\text{III.13})$$

This is the same as equation III.2, just written differently.

From eq. III.13, only two parameters have to be identified  $K_0$  and  $n$ , because in our case  $\varepsilon_0 = 0$ , and temperature effects are not investigated. For this purpose, parameters are identified on the first part of the curve, until just after necking, as shown in Figure 71.

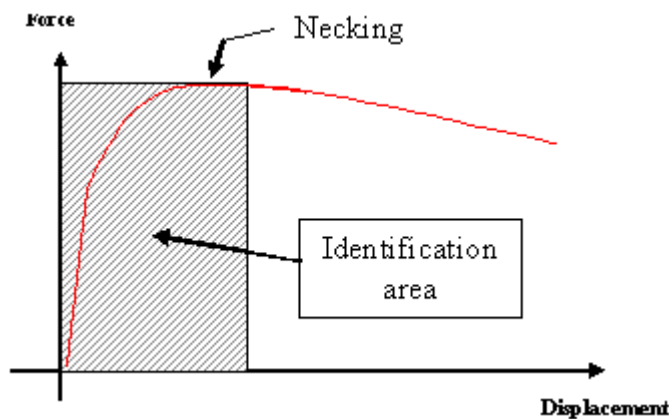


Figure 71: Hardening parameters identification

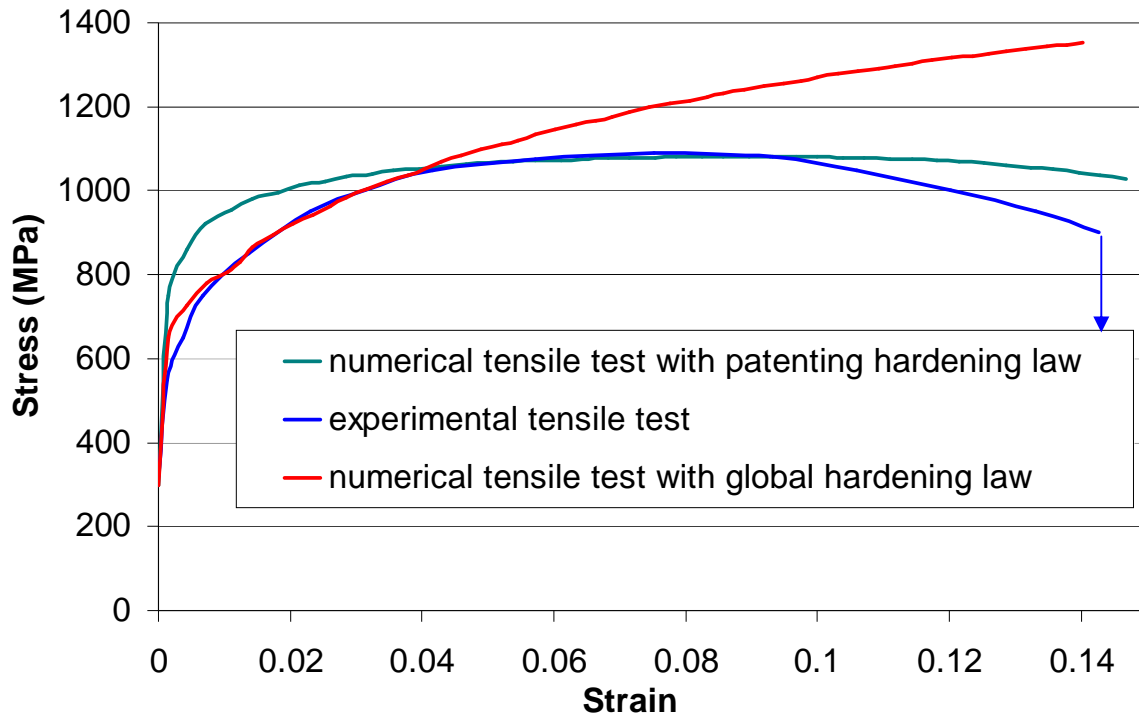


Figure 72: Identification of the mechanical behaviour parameters after patenting (all curves are in engineering stress and strain)

The global hardening law (in Figure 45, Table 6 and equation III.2) is very good on a large strain scale, but fails to represent the individual tension curve on the patented wire. Therefore, using the same form of hardening law, new fits have been performed, focussing on different parts of the engineering stress-strain curve of Figure 72:

- in the first few percent of deformation, the curve in red is for  $K = 320$ ,  $\alpha = 4.89$ ,  $n = 0.49$  ; but it fails to represent the strong curvature of the experimental curve (in blue) around  $\varepsilon = 0.04$ . This could be thought of as the beginning of damage; but such a large damage effect at such low strain, and before necking begins, is hard to believe for a ductile material such as patented high carbon steel. It is more probably a consequence of an inadequate mathematical form (eq. III.13).
- Therefore, we chose to improve the fit around the top of the curve, where necking starts and where damage must become significant. The optimisation then gives (grey curve)  $K_0 = 867.8$  and  $n = 0.0952$ . The description of the beginning of the curve is degraded, but the important part is well described.

We keep this last hardening curve, assuming that the difference with the experimental curve after  $\varepsilon = 0.095$  is due to damage growth. Damage parameters will now be determined to improve the fit in this final, decreasing part of the curve.

### III.6.3 Damage parameters identification

For damage, Lemaitre's model requires four parameters:  $S_0$ ,  $b$ ,  $\varepsilon_D$ . Identification has been done with inverse analysis software using a genetic algorithm as well.

Damage, thanks to its coupling with the elasto-plastic behaviour, has a strong influence on the force – displacement curve. It is characterized by its influence on the decrease of the force-displacement curve after necking. Damage parameters are fully identified on the whole curve as shown by Figure 73.

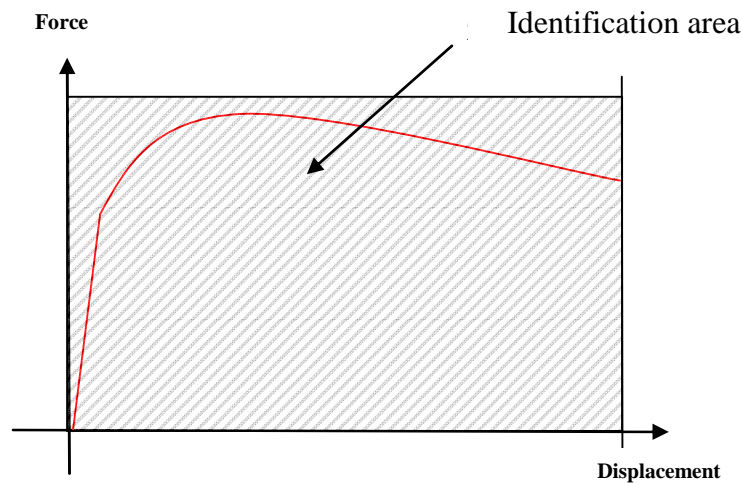


Figure 73: Identification zone of damage parameters

**Remark:**  $\varepsilon_D$  corresponds to the threshold of damage initiation, in terms of equivalent plastic strain. This parameter can be approximately evaluated from simulation of the tensile test until necking displacement. The value of the equivalent plastic strain gives a first approximation of  $\varepsilon_D$ , as illustrated in Figure 74. The identification range of this parameter will be more restricted enabling a faster identification.

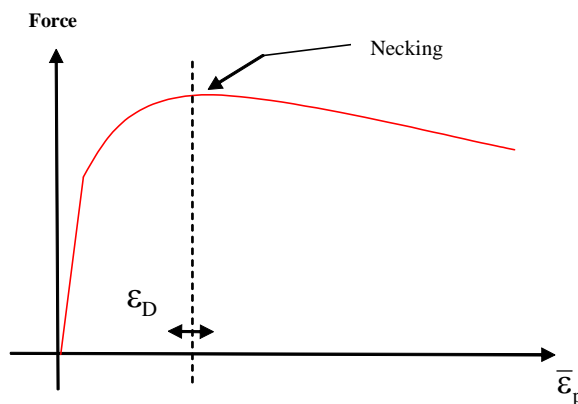


Figure 74: First approximation of  $\varepsilon_D$

**Remark:** the mesh size used in numerical simulation of tensile tests in the identification method has to be the same as those used for metal forming processes simulation. Indeed, as noted in [114], damage is sensitive to the mesh size when it is coupled to the behaviour law. Non-local model enable to avoid this dependence, but these models are not presented here. For more information, see [114].

The inverse analysis gives the following damage parameters:  $S_0 = 5.23$ ,  $b = 3.14$ ,  $\epsilon_D = 0.1$  and the results are presented in Figure 75. The comparison between the three curves (experimental curve, numerical curve with and without damage) enables to observe the influence of damage on the mechanical behaviour and the identification method gives a good correlation between the experiment and the simulation.

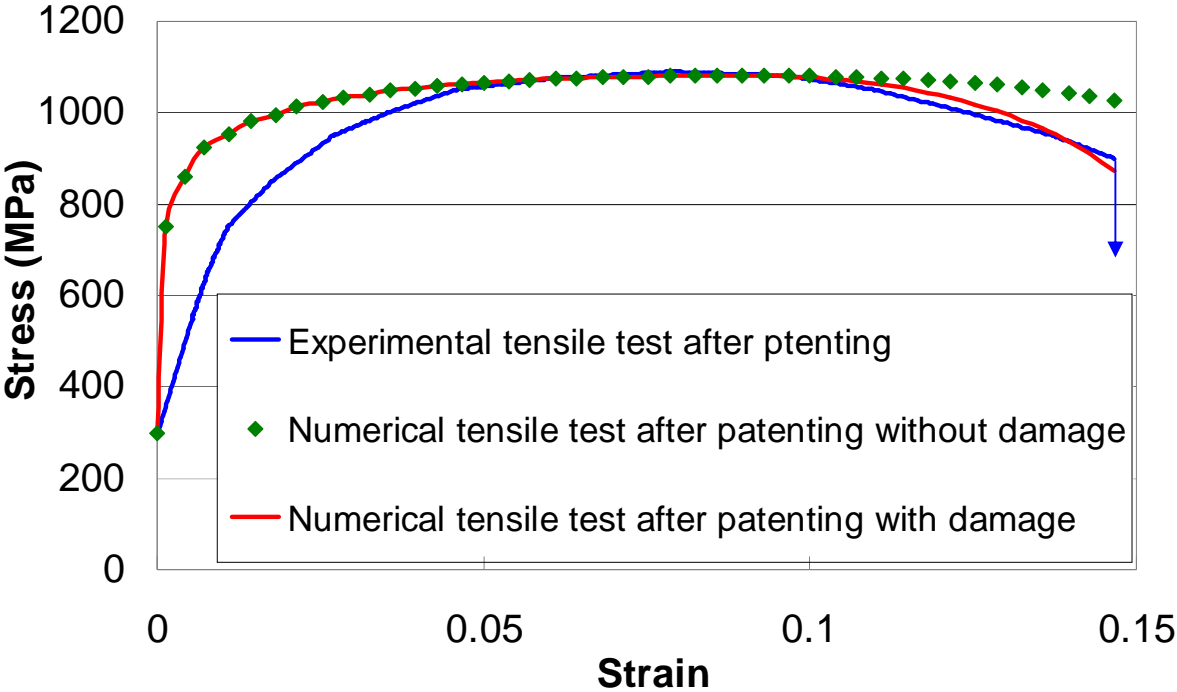


Figure 75: Identification of damage parameters after patenting

### III.7 Summary

In this chapter, all the parameters necessary for the simulation of wire drawing and rolling have been determined from a campaign of mechanical tests (tensile tests, compression tests, torsion tests at each step of wire drawing, ultimate drawing tests and micro-hardness points in rolling).

Firstly, a numerical behaviour law has been identified from tensile tests and micro-hardness points using an original method associated to an inverse analysis. This method enables us to have a strain – stress curve available all along the cold forming schedule. To validate this law, an ultimate drawing has been done and the curve is fitted very well with the envelope curve in the wire drawing strain range. This strain hardening curve will be used in the following chapter through process simulation.

Secondly, friction parameters both in drawing and rolling have been identified from measurements and experimental tests.

Thirdly, the hypothesis of anisotropy, done in introduction, has been verified from compression tests. These tests result in of an ovalization of transverse compression samples exhibiting transverse flow anisotropy. However the yield stress difference between the three directions is small. This phenomenon is well known in sheet forming but can exist in bulk forming as shown with this study.

Then, Hill's coefficients have been identified from the compression tests and torsion tests. These coefficients have been validated by the re-simulation of the compression tests, leading in a good agreement on the ovalization but in a very bad agreement on stresses. For Hill's model, a flow anisotropy (characterized by samples ovalization) induces a strong yield stress anisotropy, which is not the case in reality. However, fitting Hill's coefficient on ovalization should give interesting results on widening prediction. These anisotropic parameters will also be explored in depth in the process modelling of chap. IV. Hill's parameters will be kept constant all along rolling since, in rolling, anisotropy evolution is modified or stopped as shown by mechanical tests at the end of rolling.

Finally, Lemaître's damage parameters have been identified from inverse analysis method, using experimental and numerical tensile test after patenting. Damage parameters will be kept constant during wire drawing and rolling.

### III.8 Résumé français

Ce chapitre a présenté l'ensemble des essais mécaniques nécessaire à la description complète du comportement mécanique du matériau. En outre, ces essais ont permis l'identification de tous les paramètres nécessaires aux simulations de tréfilage et de laminage.

Tout d'abord, une loi de comportement de type élasto-plastique a été établie tout au long de la gamme de mise en forme à partir d'essais de traction et de micro-duretés. Une méthode originale associée à une analyse inverse a été employée. La validation des paramètres s'est faite par la simulation des essais de traction, ainsi qu'un tréfilage ultime.

En ce qui concerne les paramètres des lois de frottement entre outils et fil, ils ont été identifiés pour le tréfilage par la mesure de la force de tréfilage avec un axe dynamométrique capteur) et pour le laminage, par un essai de bipoinçonnement.

Ensuite, l'hypothèse d'un comportement mécanique anisotrope du matériau, annoncée dans l'introduction, a été vérifiée. Pour cela, des essais de compression ont été effectués et il en a résulté une ovalisation des éprouvettes cylindriques, prélevées dans la direction radiale, mettant en évidence une anisotropie d'écoulement transverse. Par contre cette anisotropie n'est pas visible lorsqu'on compare les valeurs des contraintes transverses et longitudinales des essais de compression. Ce phénomène est largement connu dans le cas des tôles mais nous ne connaissons pas d'études en cas de matériau massif.

En outre, les coefficients de la loi de comportement anisotrope de Hill ont été identifiés à partir des essais de compression, ainsi que grâce à des essais de torsion. Ces coefficients ont été validés en resimulant les essais de compression. L'ovalisation expérimentale est alors retrouvée numériquement. Par contre, le critère de Hill n'est pas capable de rendre compte de la faible différence de contraintes entre chaque direction. Néanmoins, il a été décidé de garder ce critère pour la suite des simulations (chapitre IV). L'identification des coefficients, basée sur la mesure de l'ovalisation (caractéristique de l'anisotropie d'écoulement), devrait donner des résultats satisfaisants en termes de prédiction d'élargissement. Les paramètres identifiés en fin de tréfilage seront gardés constants tout au long du laminage.

Finalement, les paramètres de la loi d'endommagement de Lemaître ont été identifiés par analyse inverse, à partir des données expérimentales et des simulations numériques de l'essai de traction après patentage. Ces paramètres seront gardés constants tout au long de la gamme de mise en forme, ce qui suppose simplement que les mécanismes d'endommagement ne changent pas trop.

# Chapter IV Process Modelling

After characterizing the mechanical behaviour of high carbon steel, including identification of friction, Hill and Lemaître's parameters, the next step is to simulate the two cold processes with a finite element software: FORGE2005®. This software has been developed since the 80's at CEMEF [115] and is dedicated to forming processes modelling. Its formulation is based on a lagrangian approach and its principal characteristics are:

- a specific software for axiymmetric and plane strain problems,
- a specific software for 3D problems,
- a velocity-pressure mixed formulation,
- a finite element P1+/P1: linear tetrahedron in 3D and linear triangle in 2D with a bubble term, to enrich velocity discretization compared with pressure discretization,
- management of large deformation,
- automatic 2D and 3D remeshing.

In this chapter, a brief introduction of numerical mechanics will be given. Then, the results of a complete isotropic simulation of the two cold processes will be analysed. Several sensitivity studies will be presented as well. Finally, the results for an anisotropic simulation will be discussed.

## IV.1 The mechanical problem

### IV.1.1 Continuous problem formulation

When forming by plastic deformation is considered, two types of objects are used: non-deformable objects (dies), the deformations are insignificant, and deformable objects (wires, sheets...). Each deformable object is considered as a finite domain  $\Omega$  with its boundary  $\partial\Omega$ . Its behaviour is controlled by fundamental principles of continuum mechanic. A two fields formulation is used which are the speed  $v$  and the pressure  $p$ . Equations are defined at each point of  $\Omega$  in terms of the field  $(v, p)$ .

#### IV.1.1.1 Conservation equations

A first equation is the mass conservation and is written as follows:

$$\frac{\partial \rho}{\partial t} + \text{div}(\rho v) = 0 \quad (\text{IV. 1})$$

with  $\rho$  the volumic mass.

Assuming stationarity, and taking into account that the material is compressible during elastic behaviour, and isotropic, the eq. IV.1 becomes:

$$\operatorname{div} v + \frac{\dot{p}}{\kappa} = 0 \text{ with } \kappa \text{ the elastic incompressibility} \quad (\text{IV. 2})$$

A second equation concerns the fundamental principle of dynamic, also called conservation principle of movement quantity and is written in the following equation:

$$\operatorname{div} \sigma + \rho f = \rho \frac{dv}{dt} \quad (\text{IV. 3})$$

with  $\sigma$  the stress tensor and  $f$  the gravitational volume forces.

In metal forming, two hypotheses are commonly used:

- Gravitational forces are unimportant
- Inertial forces are also neglected

Eq. IV.3 is thus reduced to:

$$\operatorname{div} \sigma = 0 \quad (\text{IV. 4})$$

#### IV.1.1.2 Boundary conditions

Boundary conditions are applied on the domain boundary and govern the equilibrium state of the solid. The boundary  $\partial \Omega$  is decomposed in four parts as described by the Figure 76 and can be written in the following way:

$$\partial \Omega = \partial \Omega_l \cup \partial \Omega_T \cup \partial \Omega_v \cup \partial \Omega_c \quad (\text{IV.5})$$

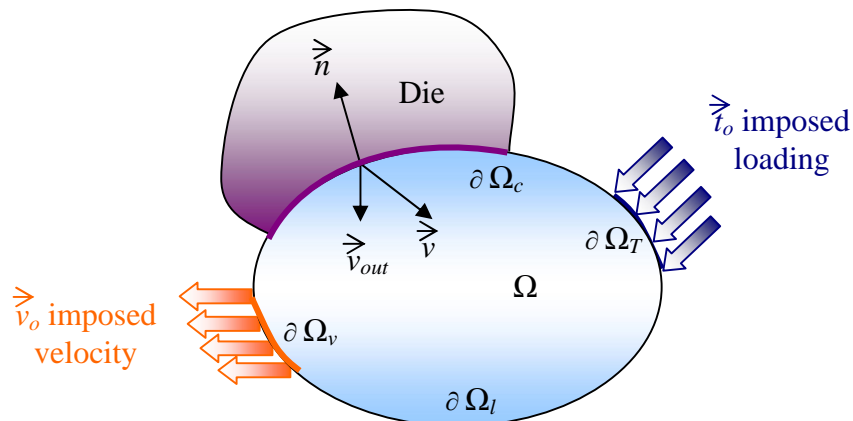


Figure 76: Boundary conditions

With:

- Free boundary condition:

$$\sigma \cdot n = 0 \text{ on } \partial \Omega_l \quad (\text{IV.6})$$

with  $n$  the domain normal.

- Imposed velocity condition:

$$v = v_0 \text{ on } \partial \Omega_v \quad (\text{IV.7})$$

- Imposed stress condition:

$$\sigma.n = t_0 \text{ on } \partial \Omega_T \quad (\text{IV.8})$$

- Boundary contact conditions on  $\partial \Omega_c$ , where two types of conditions can be distinguished:
  - Unilateral contact describing the non-penetration of the material into the dies and is written by Signorini's conditions:

$$\begin{cases} (v - v_{out}).n \leq 0 \\ \sigma_n \leq 0 \\ [(v - v_{out}).n]\sigma_n = 0 \end{cases} \quad (\text{IV.9a,b,c})$$

with  $\sigma_n = (\sigma.n).n$  the contact pressure and  $v_{out}$  the die velocity.

- Friction definition in the tangential direction:

$$\tau = \sigma n - \sigma_n n \quad (\text{IV.10})$$

#### IV.1.1.3 Strong formulation of the continuous problem

The strong formulation is defined by the following system, by decomposing  $\sigma$  in its spherical and deviatoric part:

$$\begin{cases} \text{divs} - \text{grad}p = 0 & \text{sur } \Omega \\ \text{div}v = 0 & \text{sur } \Omega \\ (v - v_{out}).n \leq 0 & \text{sur } \partial \Omega_c \\ \sigma_n \leq 0 & \text{sur } \partial \Omega_c \\ [(v - v_{out}).n]\sigma_n = 0 & \text{sur } \partial \Omega_c \\ \tau - \mu\sigma_n \leq 0 & \text{sur } \partial \Omega_c \\ (\tau - \mu\sigma_n).v_g = 0 & \text{sur } \partial \Omega_c \\ \text{with } v_g = -\lambda\tau \end{cases} \quad (\text{IV.11})$$

#### IV.1.1.4 Weak formulation of the continuous problem

The weak formulation is obtained by multiplying the conservation equations by test functions  $(v^*, p^*)$  and then integrating on the domain. A second step is the use of the divergence theorem. The weak expression of the problem is obtained, consisting of the virtual power principle and of the weak form of the incompressibility equation:

$$\begin{aligned}
& \text{Find } (v, p) \in (V^{CA}, P) \\
& \left\{ \begin{array}{l} \forall v^* \in V_0^{CA} \quad \int_{\Omega} s : \dot{\varepsilon}(v^*) d\omega - \int_{\Omega} p \operatorname{div} v^* d\omega - \int_{\partial\Omega_c} \tau \cdot v^* ds - \int_{\partial\Omega_T \cup \partial\Omega_I} t_0 \cdot v^* ds - \int_{\partial\Omega_v} (\sigma \cdot n) \cdot v_0 ds = 0 \\ \forall p^* \in P \quad \int_{\Omega} p^* \left( \operatorname{div} v + \frac{\dot{p}}{\kappa} \right) d\omega = 0 \end{array} \right. \quad (\text{IV.12})
\end{aligned}$$

with  $V^{CA}$  (cinematically admissible velocity space),  $V_0^{CA}$  (zero cinematically admissible velocity space) and  $P$  defined by:

$$\begin{aligned}
V^{CA} &= \left\{ v \in \left( H^1(\Omega)^3 \mid (v - v_{out}) \cdot n \leq 0 \text{ sur } \partial\Omega_c \right) \right\} \\
V_0^{CA} &= \left\{ v \in \left( H^1(\Omega)^3 \mid v \cdot n \leq 0 \text{ sur } \partial\Omega_c \right) \right\} \\
P &= L^2(\Omega)
\end{aligned} \quad (\text{IV.13})$$

## IV.1.2 Discretized problem formulation

It consists in approximating the admissibility spaces  $V^{CA}$  and  $P$  by spaces of finite dimensions  $V_h^{CA}$  and  $P_h$ , formed by piecewise polynomial functions. The  $\Omega$  domain is thus decomposed in simple elements. The set of these elements form the mesh of  $\Omega$  and defined the discretized domain  $\Omega_h$ :

$$\Omega_h = \bigcup_e \Omega_e, \quad e \in \varepsilon \subset N \quad (\text{IV.14})$$

$\Omega_e$  corresponds to an element of the mesh and  $\varepsilon$  is the interval for the numbering of elements.

The weak formulation in the discretized spaces gives the following system:

$$\begin{aligned}
& \text{Find } (v_h, p_h) \in (V_h, P_h) \text{ such that:} \\
& \left\{ \begin{array}{l} \forall v_h^* \in V_0^{CA} \quad \int_{\Omega} s(v_h) : \dot{\varepsilon}(v_h^*) d\omega_h - \int_{\Omega} p_h \operatorname{div} v_h^* d\omega_h - \int_{\partial\Omega} (\sigma \cdot n) \cdot v_h^* ds_h = 0 \\ \forall p_h^* \in P_h \quad \int_{\Omega} p_h^* \left( \operatorname{div} v_h + \frac{\dot{p}}{\kappa} \right) d\omega_h = 0 \end{array} \right. \quad (\text{IV.15})
\end{aligned}$$

### IV.1.2.1 Time discretization

Forge2005® is based on an updated Lagrangian formulation, updated in time.  $t_0$  and  $t_{fin}$  being the initial and final time of the simulation, the total time is discretized in several time steps, each lasting  $\Delta t$ . The configuration at  $t + \Delta t$  is calculated from the configuration at previous instant  $t$ . By an explicit Euler time integration scheme:

$$X^{t+\Delta t} = X^t + \Delta t V^t \quad (\text{IV.16})$$

#### IV.1.2.2 Spatial discretization

As the mesh is Lagrangian, mesh nodes are moving along with the material, which gives very accurate results in terms of geometry. On the contrary, the element quality decreases progressively. This degeneration is avoided thanks to an automatic remeshing tool. Details on the remeshing method can be found in [114] and [116]. The tetrahedral element P1+ / P1, shown in Figure 77, so-called “mini-element” is used to discretize the domain, as it enables an easier meshing and remeshing [117]. Velocity is linearly approximated on the tetrahedron and enriched by a linear “bubble” function defined on the four sub-tetrahedra formed by the apices and the centre of gravity of the tetrahedron.

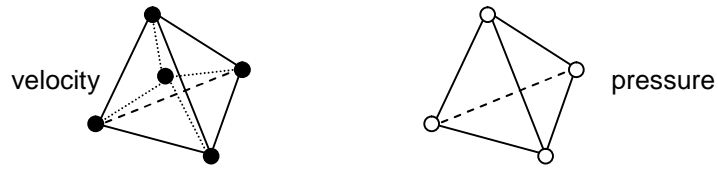


Figure 77: P1+ / P1 element, from [118]

The discretized velocity and pressure fields are expressed as follows:

$$v_h = v_h^l + v_h^b = \sum_{i=1}^{N_n} v_i^l N_i^l + \sum_{j=1}^{N_e} v_j^b N_j^b \quad (\text{IV.17})$$

$$p_h = \sum_{i=1}^{N_n} p_i N_i^l$$

with  $N_n$  and  $N_e$  the nodes and elements number,  $N_i^l$  and  $N_j^b$  the linear basis and bubble function.

The discretized formulation of the problem is thus obtained by replacing in eq. IV.15 the test functions as function of the basis functions.

#### IV.1.2.3 Contact management

In Forge2005®, the contact is managed incrementally thanks to a penalized method. A function  $d(t)$ : it characterizes the distance between the die surface and the node:  $d(t)$  is positive outside the die, equals 0 on its surface and negative inside the die. The non penetration condition is thus:

$$d(t) \leq 0 \quad (\text{IV.18})$$

which can be linearized to the first order [119]. For more details, see [114], [118] and [119]. To take into account the contact condition in the weak formulation, the penalized method is used and the non penetration condition is imposed thanks to a penalization coefficient. Physically, this method consists in applying a repulsive force to the nodes which penetrate into the die, and this force is proportional to the penetration distance. The main advantage is that no additional variable is introduced in the equilibrium problem. The main drawback is that this is not an exact method, which enables a slight penetration of nodes into the dies. Parameters have been chosen that this penetration remains small compared with the characteristic dimensions of our problem and to the tolerances ( $5.10^{-3}$  mm  $<$   $d_{\text{penetration}} <$   $1.5.10^{-2}$  mm).

### IV.1.3 Problem resolution

The equations system can be written in a matrix form as follows:

$$R(v^l, v^b, p) = \begin{pmatrix} R_l(v^l, v^b, p) \\ R_b(v^l, v^b, p) \\ R_p(v^l, v^b, p) \end{pmatrix} = \begin{pmatrix} 0 \\ 0 \\ 0 \end{pmatrix} \quad (\text{IV.19})$$

This system is generally non linear and its resolution is based on a Newton-Raphson algorithm. At each iteration, from an initial triplet  $(v_{ini}^l, v_{ini}^b, p_{ini})$  the algorithm looks for a correction  $(\Delta v^l, \Delta v^b, \Delta p)$  such as:

$$R(v_{ini}^l + \Delta v^l, v_{ini}^b + \Delta v^b, p_{ini} + \Delta p) = 0 \quad (\text{IV.20})$$

The residual R is approximated to the first order via a Taylor expansion and the system becomes:

$$\begin{pmatrix} \frac{\partial R_l}{\partial v^l} & \frac{\partial R_l}{\partial v^b} & \frac{\partial R_l}{\partial p} \\ \frac{\partial R_b}{\partial v^l} & \frac{\partial R_b}{\partial v^b} & \frac{\partial R_b}{\partial p} \\ \frac{\partial R_p}{\partial v^l} & \frac{\partial R_p}{\partial v^b} & \frac{\partial R_p}{\partial p} \end{pmatrix} \begin{pmatrix} \Delta v^l \\ \Delta v^b \\ \Delta p \end{pmatrix} = - \begin{pmatrix} R_l \\ R_b \\ R_p \end{pmatrix} \quad (\text{IV.21})$$

Thanks to orthogonality properties of the bubble function [120], the system can be simplified to:

$$\begin{pmatrix} \frac{\partial R_l}{\partial v^l} & 0 & \frac{\partial R_l}{\partial p} \\ 0 & \frac{\partial R_b}{\partial v^b} & \frac{\partial R_b}{\partial p} \\ \frac{\partial R_p}{\partial v^l} & \frac{\partial R_p}{\partial v^b} & 0 \end{pmatrix} \begin{pmatrix} \Delta v^l \\ \Delta v^b \\ \Delta p \end{pmatrix} = - \begin{pmatrix} R_l \\ R_b \\ R_p \end{pmatrix} \quad (\text{IV.22})$$

By extracting  $\Delta v^b$  from the second equation of the system IV.22 and by re-injecting this expression in the third equation of this system, a new system is obtained that does not include the bubble velocity (the bubble degrees of freedom have been eliminated):

$$\begin{pmatrix} K^{vv} & K^{vp} \\ K^{pv} & -K^{pp} \end{pmatrix} \begin{pmatrix} \Delta v \\ \Delta p \end{pmatrix} = - \begin{pmatrix} R_l \\ R_p \end{pmatrix} \quad (\text{IV.23})$$

with  $\Delta v^l = \Delta v$  and the Hessian matrix and gradients being defined by:

$$\begin{cases} K^{vv} = \frac{\partial R_l}{\partial v^l} \\ K^{vp} = \frac{\partial R_l}{\partial p} \\ K^{pv} = \frac{\partial R_p}{\partial v^l} \\ K^{pp} = \frac{\partial R_p}{\partial v^b} \left( \frac{\partial R_b}{\partial v^b} \right)^{-1} \frac{\partial R_p}{\partial p} \end{cases} \quad \text{and} \quad \begin{cases} R_v = R_l \\ R_p \leftarrow R_p - \frac{\partial R_p}{\partial v^b} \left( \frac{\partial R_b}{\partial v^b} \right)^{-1} R_b \end{cases} \quad (\text{IV.24})$$

This system is currently resolved in Forge2005® by an iterative method: preconditioned conjugate residual [121].

## IV.2 Cold forming processes simulation

In this section, cold forming schedule simulation is detailed for a better understanding of wire drawing and rolling processes. Data input are described both in section I.2.1 and I.2.2 for simulation of both processes. The numerical behaviour law and friction parameters used here are those identified in the previous chapter (see section III.1 and III.2).

First, a complete study with an isotropic behaviour is presented and some sensitivity studies are added. Then, the influence of anisotropy is discussed. The simulation is 2D axisymmetric for wire-drawing, and 3D for rolling, 1/4th of the wire only being modelled thanks to the two symmetry planes.

## IV.2.1 Isotropic behaviour

### IV.2.1.1 Strain rate and strain evolution

The strain rate evolution during drawing is shown in Figure 78. Two shear bands are observed, joining the inlet and outlet points to the core where the strain rate is maximal. The evolution between passes is marginal. The maximum strain rate is of the order of  $100 \text{ s}^{-1}$ , far from the high-strain rate, dynamic range.

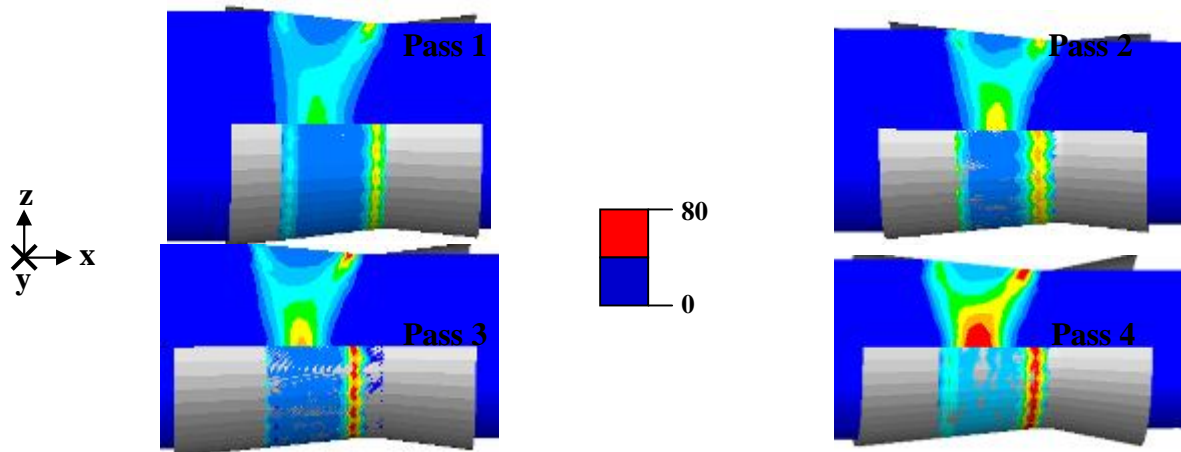


Figure 78: Strain rate state during wire drawing

The strain rate in rolling is displayed in Figure 79. It is maximal on the vertical symmetry plane as compared to the edge, in particular in the first pass (round  $\rightarrow$  flat) because the height reduction shows a pronounced maximum there. As usual, the geometrical singularity of the first contact point presents the highest strain rate. Again, the highest values are between 50 and  $100 \text{ s}^{-1}$ .

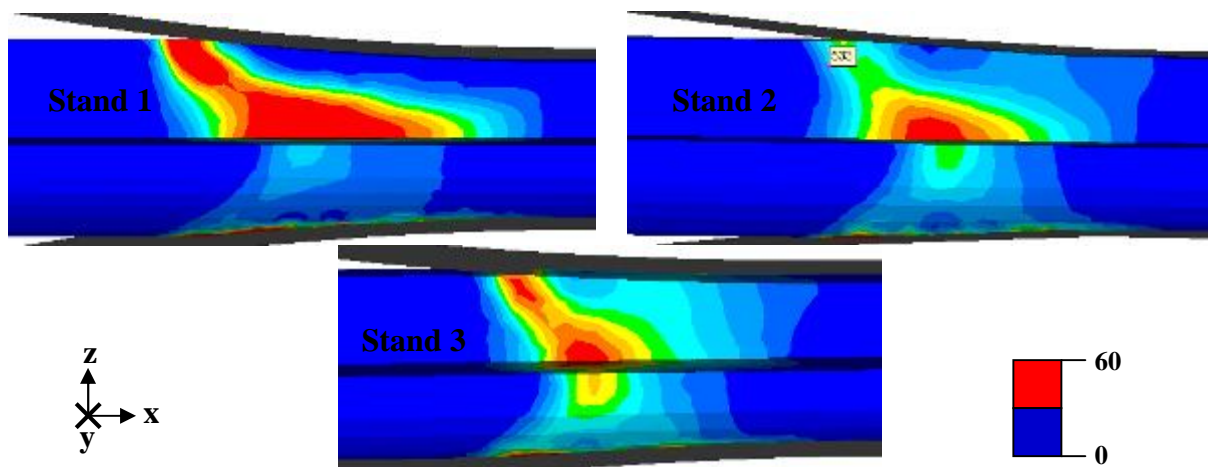


Figure 79: Strain rate state during rolling.  $3/4^{\text{th}}$  of the wire are represented from the side, so that that the upper part displays the vertical plan of symmetry, the lower part the side of the wire.

Figure 80 shows the strain evolution through the four wire drawing passes. It shows that strain is less heterogeneous than strain-rate. Yet the strain is always higher at the surface than in the core (where the strain is necessarily exactly  $2 \cdot \ln(R_0/R)$ ). The radial gradient is due to the shear induced by the curvature of the flow lines. The average strain is roughly 0.25 per pass, corresponding to a surface reduction of 20% approximately. Therefore, the strain after the 4th pass ranges from 0.9 to 1.1.

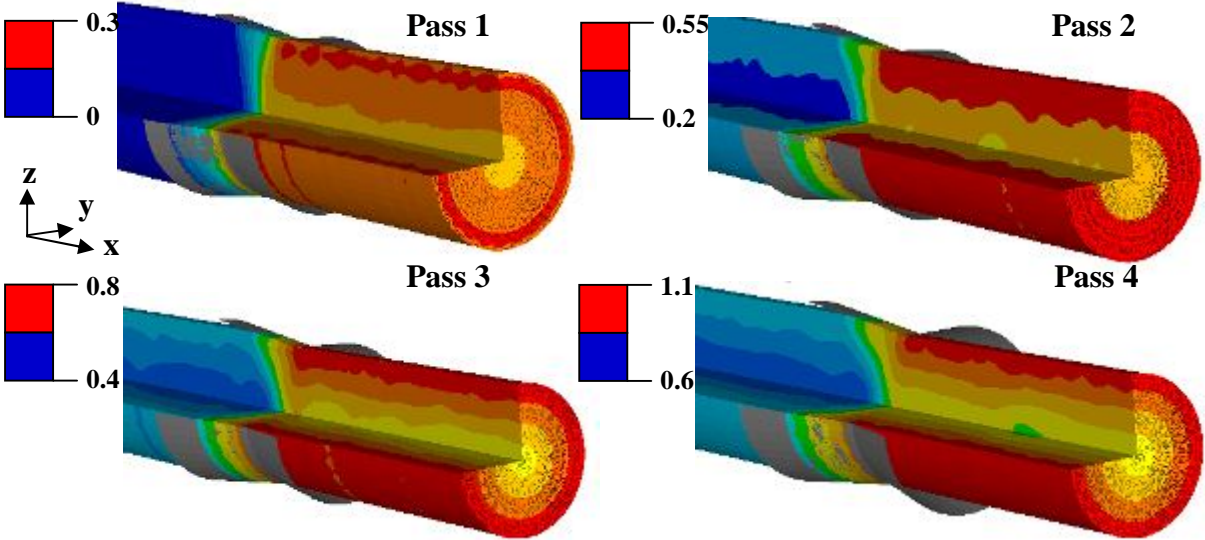


Figure 80: Strain state during wire drawing

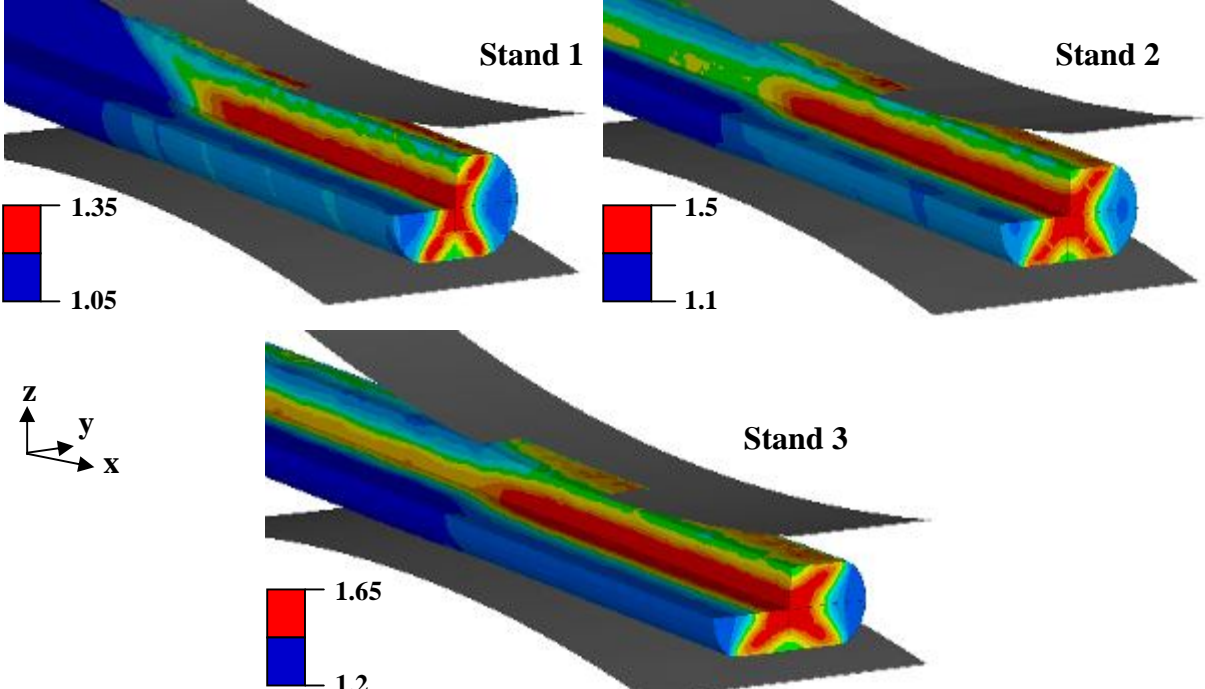


Figure 81: Strain state during rolling. Note the strain at the entry of the first pass, around 1, as a result of the four wire drawing passes.

By comparison, rolling renders strain strongly heterogeneous, as shown by Figure 81. Strains are maximal in a cross-shaped area, centred at the wire core: this zone, commonly called the “blacksmith’s cross”, is well-known in hot bar forging processes, and is characteristic of section rolling. At the end of rolling the maximal strain reaches 1.75 in the wire core.

#### IV.2.1.2 Stress evolution during wire drawing

##### IV.2.1.2.1 *Equivalent stress (according to Von Mises)*

Figure 82 enables to see the progressive hardening, which mainly takes place in the contact zone. We also notice a high skin stress value after wire drawing, which reaches its maximum, 1460MPa, after the last drawing pass. This is a critical value because it is near the elastic limit and, as we will see, comes from a *tensile* longitudinal stress

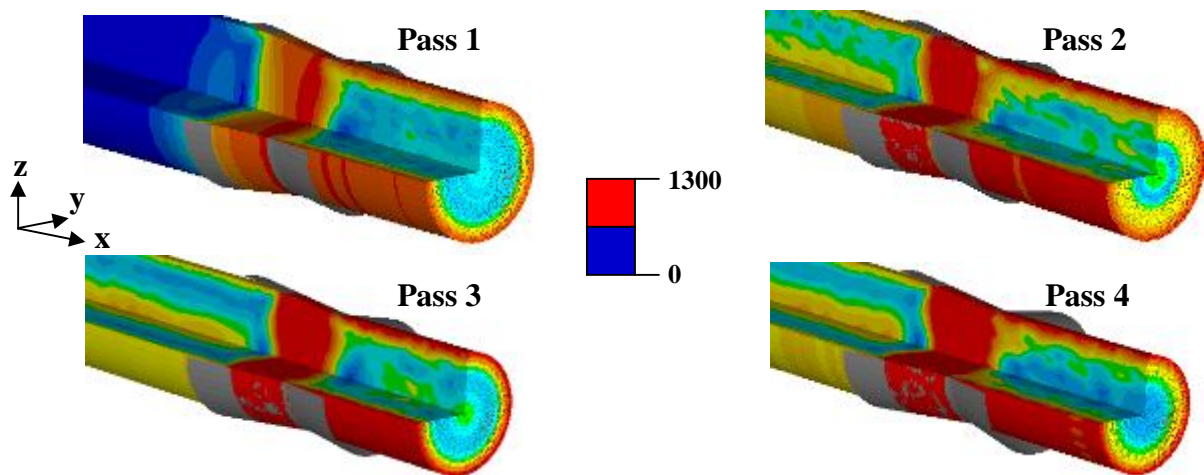


Figure 82: Von Mises stresses state during wire drawing (in MPa)

##### IV.2.1.2.2 $\sigma_{RR}$ radial stress evolution

Figure 83 highlights a strongly negative zone on the contact, with two climaxes at the inlet and the outlet point of the contact zone, whereas in the wire core it exhibits a slight compressive state. It is more visible in Figure 84, where a higher value of the radial stress at the fourth passes can be observed, due to a maximal reduction for this pass (> 22%). The core is slightly compressive only.

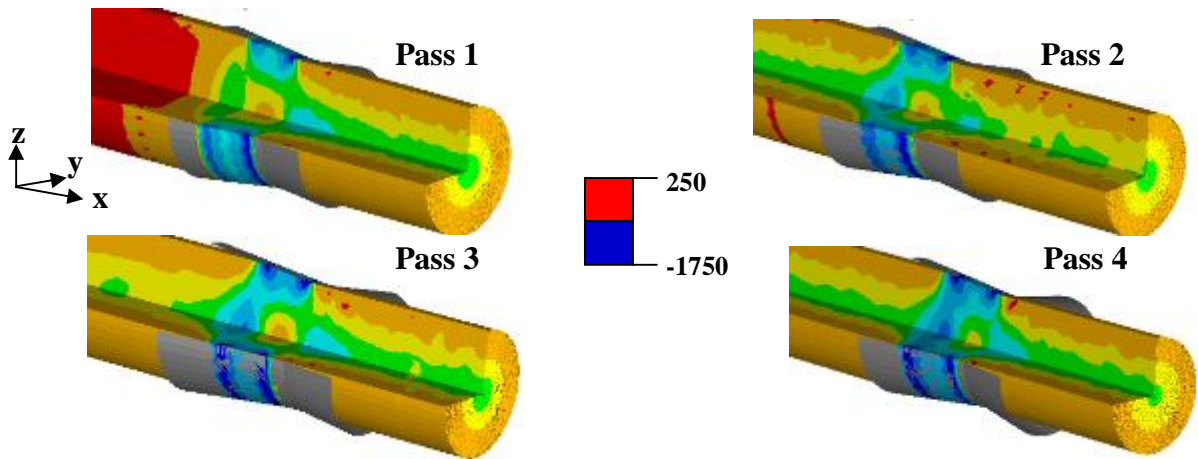


Figure 83: Radial stress state during wire drawing (in MPa)

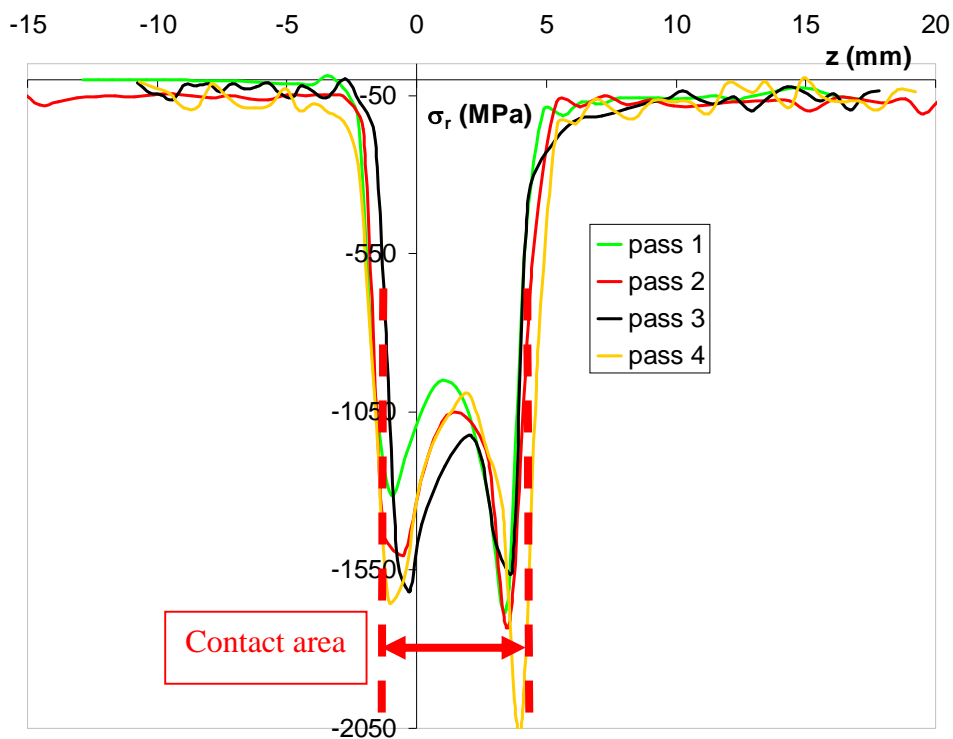


Figure 84: Radial stress evolution along the surface during drawing

#### IV.2.1.2.3 $\sigma_{\theta\theta}$ orthoradial stress evolution

The orthoradial stress mapping, as shown in Figure 85, exhibits a high compression in the work area. Moreover, a tensile stress (700-800 MPa) is observed in the skin after drawing on the skin to satisfy to the stress equilibrium. The Figure 86 focuses on the evolution along the radius. The abscissa zero corresponds to the wire core and the maximal abscissa to the wire skin. It clearly shows a higher compression at the fourth drawing pass in the contact zone.

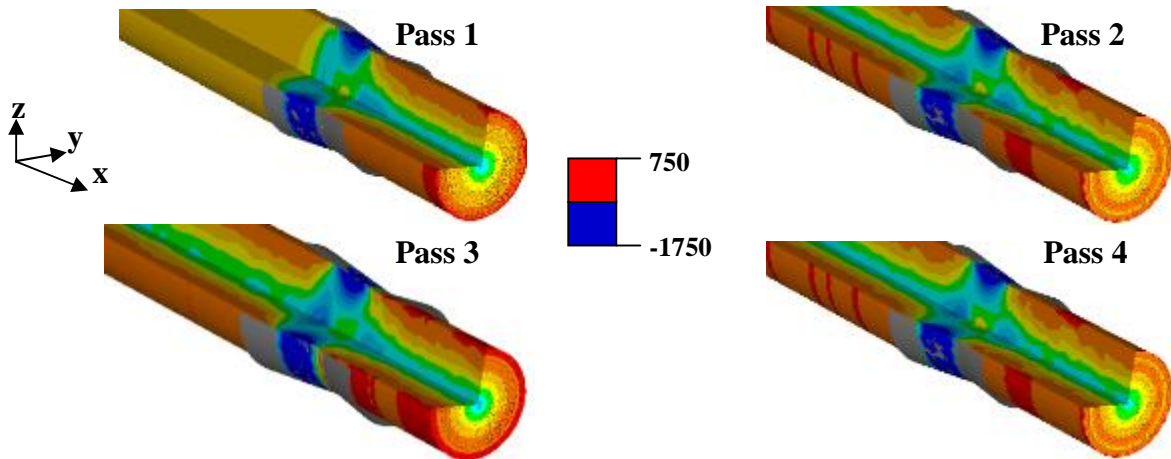


Figure 85: Orthoradial stress state during wire drawing (in MPa)

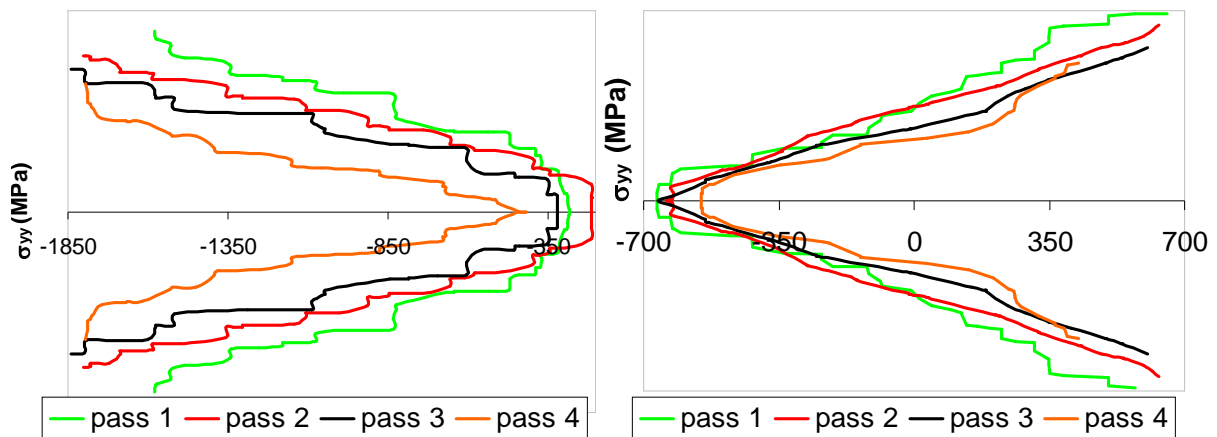


Figure 86: Orthoradial stress evolution along the radius during drawing, in the work area (left) and beyond the work area (right). The stress axis is horizontal, the vertical axis represents the radial coordinate (symmetrized).

#### IV.2.1.2.4 $\sigma_{xx}$ longitudinal stress evolution

This is the most important component, the one that may explain breaks during wire-drawing because it is fundamentally tensile. Moreover, it is strongly heterogeneous in the work area and after, as shown by Figure 87. Indeed, we observe a tensile area in the wire core and a compressive area near the surface. The maximal tensile stress is situated at the joining of the two shear lines. On the contrary after the die, this tendency is reversed, as also observed for the other stress components. The stress profile (Figure 88) quantifies the tensile state in the work area with values between 1000 and 1150 MPa in the wire core and between 1300 and 1500 MPa after drawing on the surface. The same is true for the four passes.

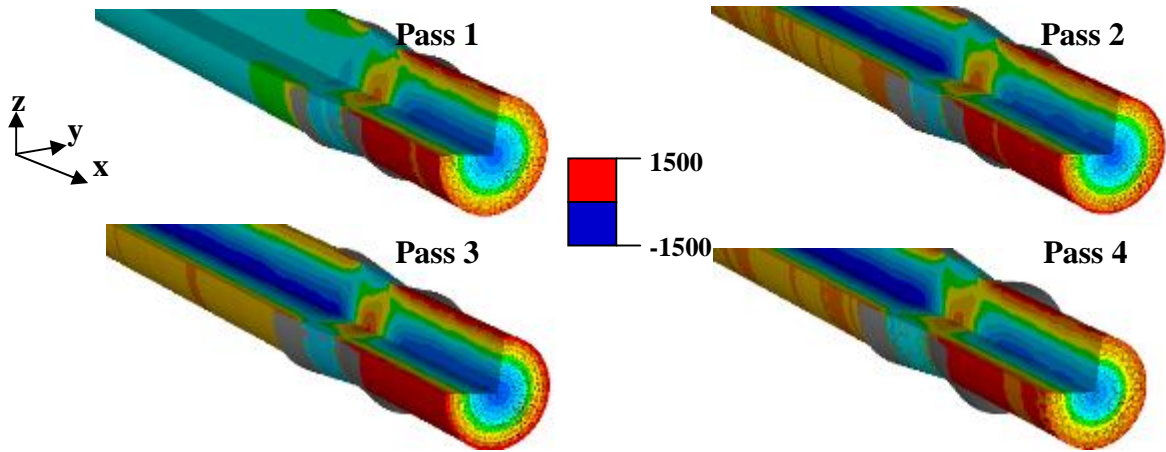


Figure 87: Longitudinal stress state during wire drawing (in MPa)

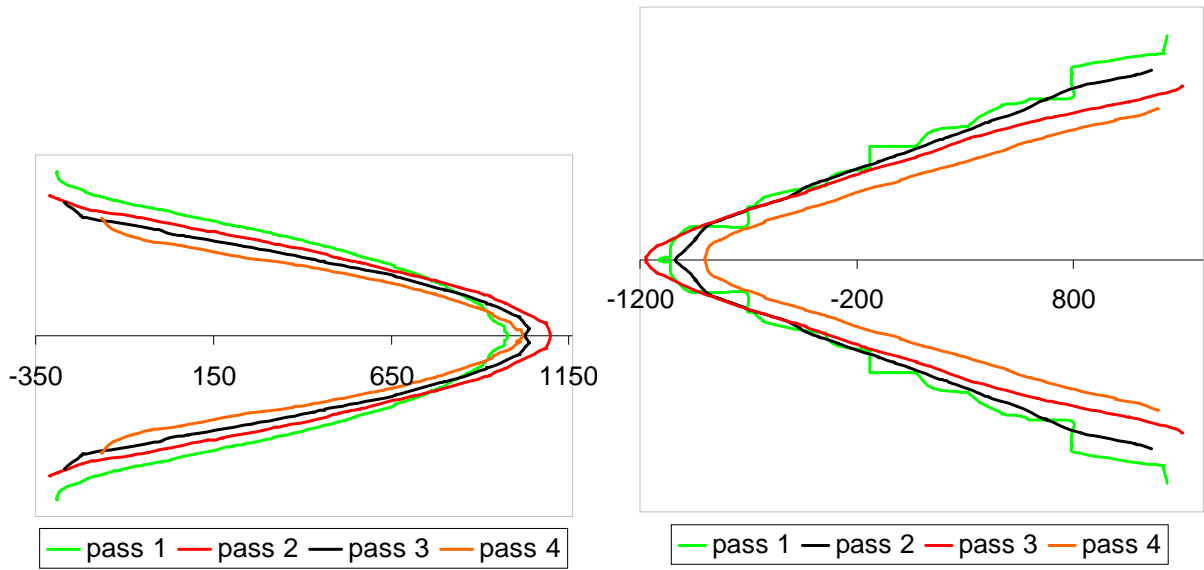


Figure 88: Longitudinal stress (in MPa) evolution along the radius during drawing, in the work area (left) and beyond the work area (right)

#### IV.2.1.2.5 $\sigma_{xx}$ residual longitudinal stress evolution

Residual longitudinal stresses after drawing and load releasing can be deduced approximately from the stress beyond the die during drawing by subtracting the average tension stress. We observe a high compressive state in the wire core, as well as a high tensile state on the surface, which confirms that the surface is a critical area with residual stresses near the yield stress (900 to 1100 MPa in this case, Figure 89).

This stress analysis during drawing enables to conclude on the probable fracture areas. The wire core fracture could initiate in the contact area where the stress state is mainly tensile, whereas at the end of the contact the stress state becomes compressive. This is known as the cup-and-cone fracture, often initiating on hard particles or inclusions. The stress on the

surface, during drawing, may result in surface defects (pores, micro-cracks networks...). The residual stress, combined with in-service stresses, may lead to premature fatigue fracture.

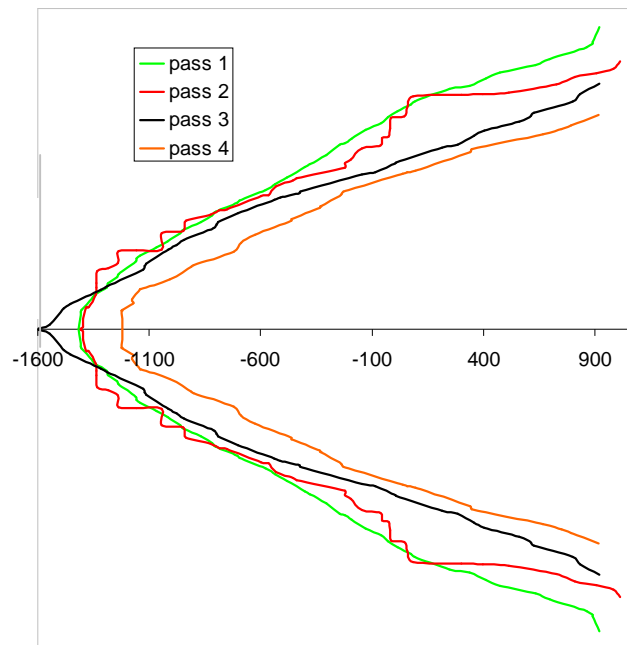


**Figure 89: Residual longitudinal stresses along the radius after each drawing pass**

#### IV.2.1.3 Stress evolution during rolling

##### *IV.2.1.3.1 Equivalent stress (according to Von Mises)*

Figure 90 shows a weakly variable Von Mises stress in the bite during rolling (1400 to 1500 MPa). It is much more homogeneous than at the beginning of wire drawing because at this stage, work-hardening saturates. After the contact, in the elastic state, the vertical gradient strongly increases with a core value around 450 MPa and a surface value around 1250 MPa.

##### *IV.2.1.3.2 Longitudinal stress*

In rolling, the wire is compressed between two rolls, so that intuition suggests a compressive stress. However, the longitudinal stress, shown in Figure 91, exhibits a slight tensile stress in the wire core at the beginning of the contact (about 300 MPa, green), only for the first stand. Stress is tensile on the edges all along the rolling at a very high level of 1600 MPa. This is partly due to the higher tendency to elongation in the centre, so that material in the centre pulls the edge, and partly to spread which further elongates the edges. For the two other stands, the wire stress at the beginning of the contact is slightly compressive. After contact, the top surface turns tensile while the core remains compressive. The four corners are

also under a slight tension. The tensile surface stress decreases from 1300 MPa in the first to 1200 MPa in the third pass.

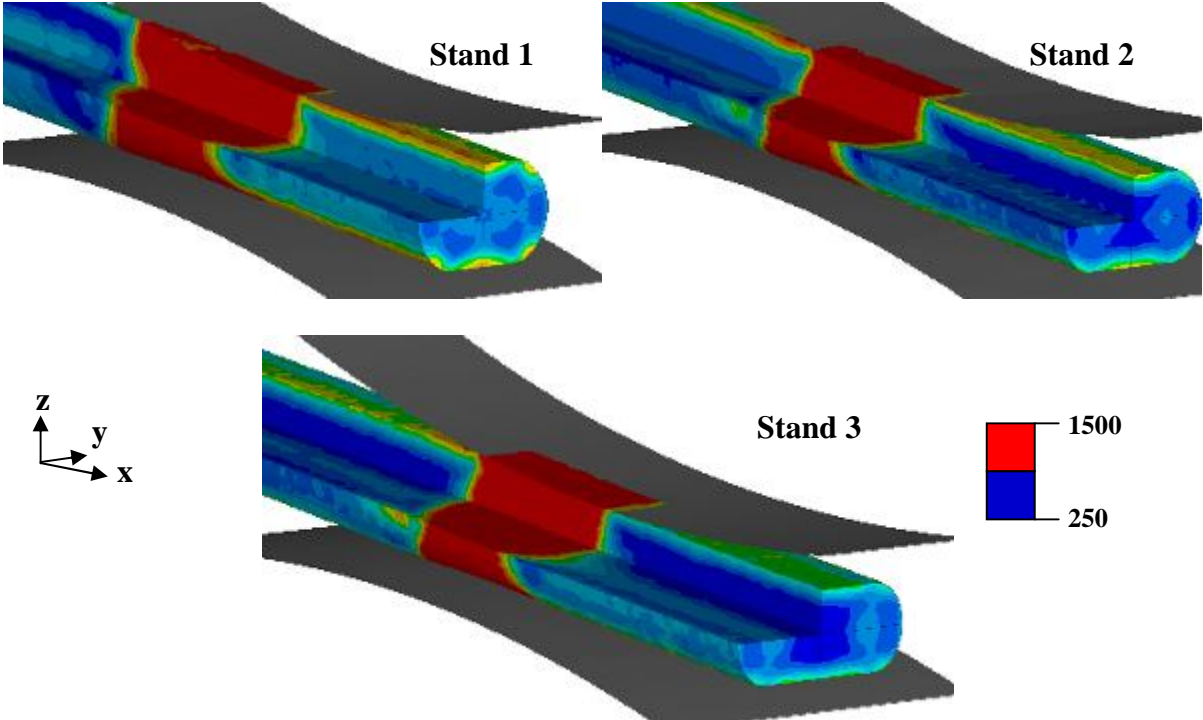


Figure 90: Von Mises stress state during rolling

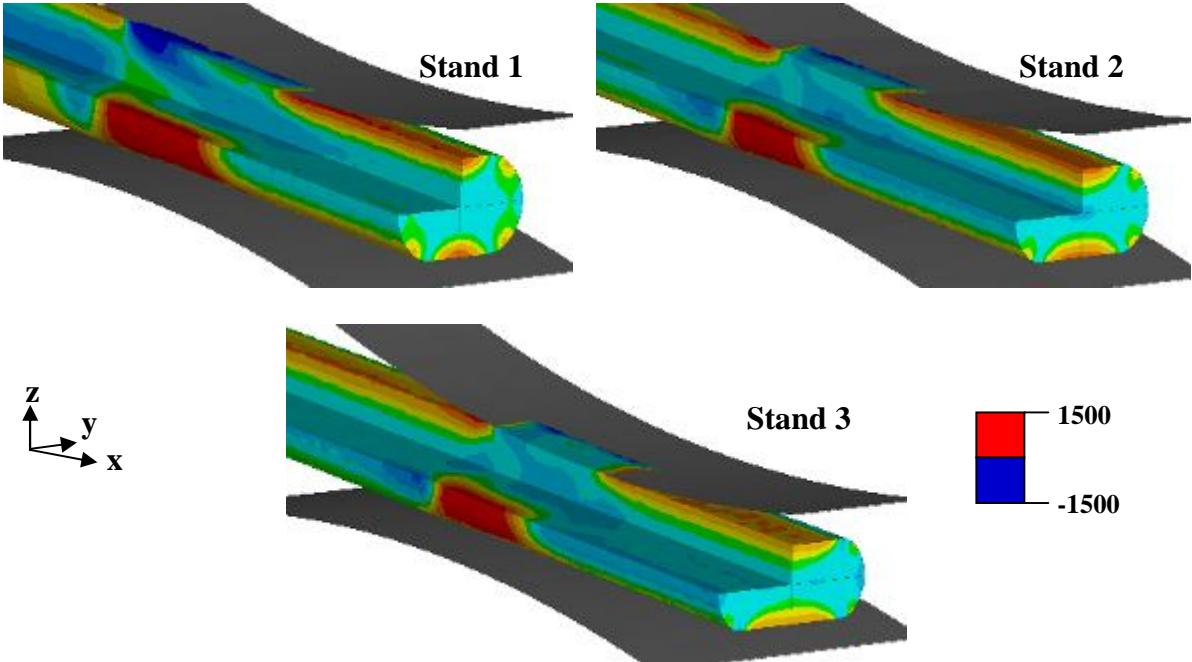


Figure 91: Longitudinal stress state rolling (in MPa)

#### IV.2.1.3.3 *Transverse stress*

The transverse stress presented in Figure 92, shows a high tensile stress at the entrance in the core (about 1200 MPa in the first pass), which decreases farther into the bite. This very high tensile value decreases from pass to pass, to 600 MPa at third pass. Meanwhile, on the surface, a high compressive state is noticeable, with a stress value reaching -1850 MPa. As with the tension, this compressive value strongly decreases farther away in the bite and from pass to pass.

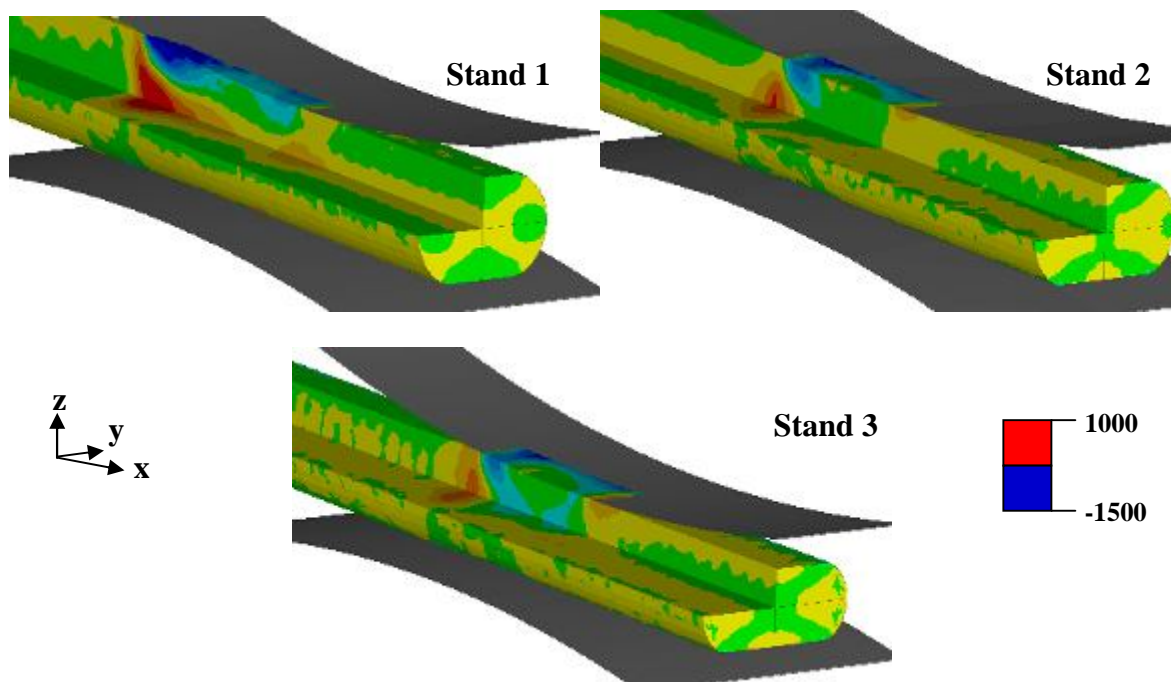


Figure 92: Transverse stress state during rolling (in MPa)

#### IV.2.1.3.4 *Vertical stress*

Finally, in terms of vertical stress state, it is totally compressive under the contact during rolling with a maximal value of -3000 MPa, as shown in Figure 93. We also observed a tensile state on the edges which decreases from 300 MPa in the first rolling stand to 25 MPa at the last stand.

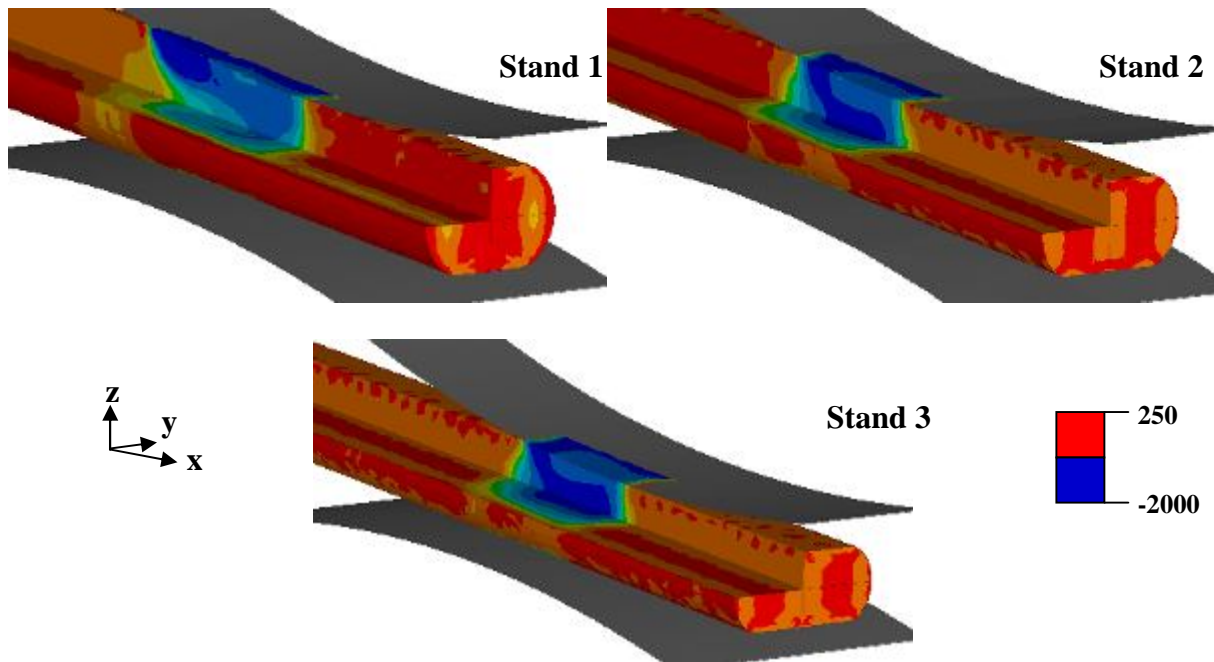


Figure 93: Vertical stress state during rolling (in MPa)

#### IV.2.1.3.5 *Danger zones*

This stress analysis during rolling enables also to locate the probable fracture areas, corresponding to the tensile zone: at the entrance and the exit of the contact where surface crack could initiate; in the wire core where high tensile transverse value are noticeable; on edges where longitudinal stresses are also high.

Experimental and numerical damage analyses will bring further information and is presented in the following chapter.

#### IV.2.1.4 Widening prediction

The last interesting result to compare is the widening at the end of rolling. In the Figure 94, the numerical profile (only one fourth) is superposed to the experimental cross-section after rolling. We notice an underestimation of the widening: the computed section is too narrow by  $\approx 10\%$ , way above the tolerance. This difference might originate in the anisotropy introduced by the wire drawing process. Therefore, the anisotropic behaviour law previously identified is used and results are presented later, in section IV.2.3.2.

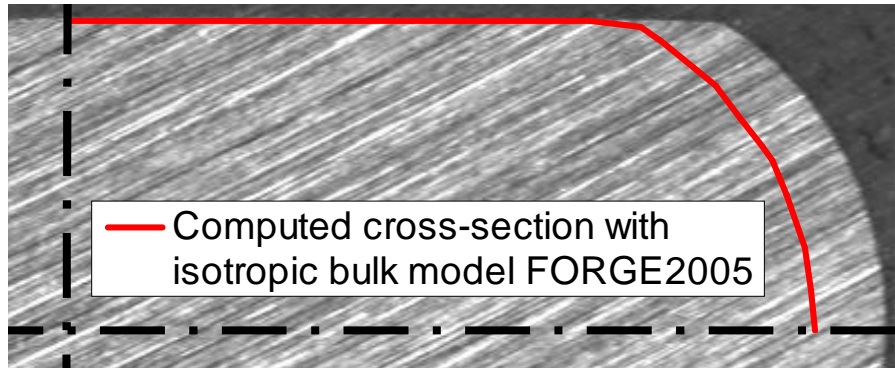


Figure 94: Comparison of the experimental and computed (dark red line) cross sections after rolling

## IV.2.2 Sensitivity studies

To broaden our knowledge on these two processes, some sensitivity studies are added. The first one concerns the influence of the residual stresses transfer from drawing to rolling. The second one is about the influence of the strain map transfer from drawing to rolling.

### IV.2.2.1 Influence of strain map transfer from drawing to rolling

Two simulations have been run, one with complete strain map transfer from drawing to rolling and another one with a constant strain (initialized to the maximal strain value at the end of drawing). Figure 95 shows the comparison of the two previous cases through the first rolling stand. Initialization, with a constant strain before rolling, leads to an underestimation of the global strain level, especially on the contact surface and on the edges. Since the strain is initialized to the maximal strain value at the end of drawing, corresponding to the core value, core strain during rolling are closed in the two calculations.

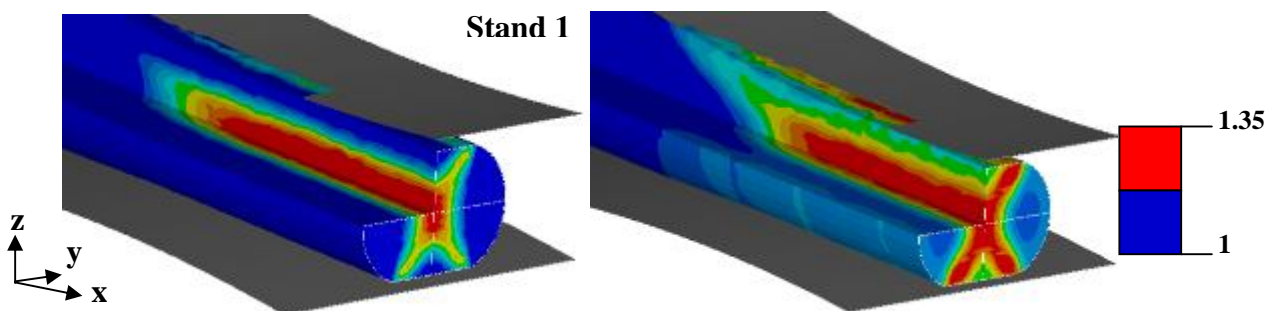


Figure 95: Comparison between two different strain initialization before rolling: constant strain initialization (left) - complete strain transfer (right)

Thus, strain map transfer from drawing to rolling must be taken into account.

#### IV.2.2.2 Influence of residual stresses transfer from drawing to rolling

To study this influence, several curves are presented, which show the evolution of stress components during rolling under two different assumptions: residual drawing stresses are, or are not, transferred as initial stress maps for rolling.

Longitudinal stress in rolling is shown in Figure 96 for the two computation conditions. Comparison of stress evolution is done at three locations: in the wire core, on the contact surface (on the vertical symmetry plane) and on edges (on the horizontal symmetry plane). We notice only a very small difference between simulations with or without wire-drawing residual stresses. The difference is more conspicuous on edges: the x-stress is more compressive in the interstand 1-2 and interstand 2-3 when wire-drawing residual stresses are taken into account. The difference there is approximately 200 MPa.

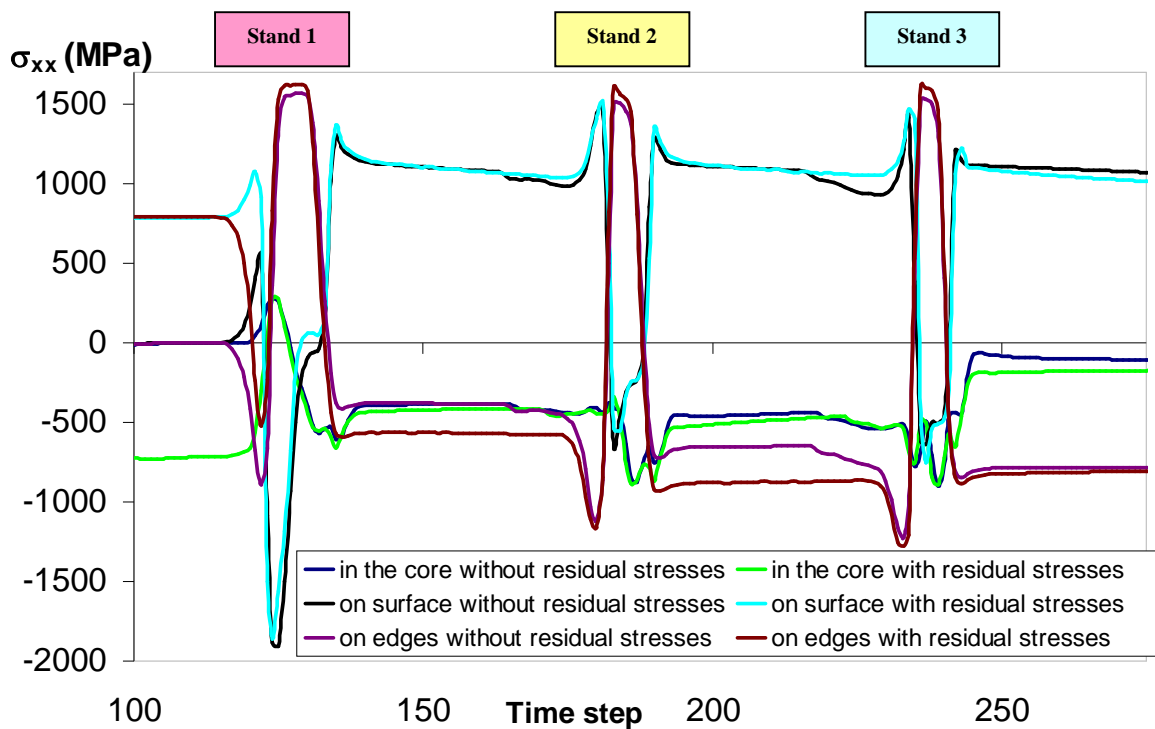


**Figure 96: Comparison of the longitudinal stress evolution during rolling with or without residual stresses transfer**

For transverse stress, the comparison is only made in the core stress and is detailed in Figure 97. Here the main difference concerns the two first stands, where the high tensile stress is decreased by 100 MPa in the absence of residual stresses transfer. As the core tensile value is near the yield stress, the residual stresses transfer cannot be neglected.

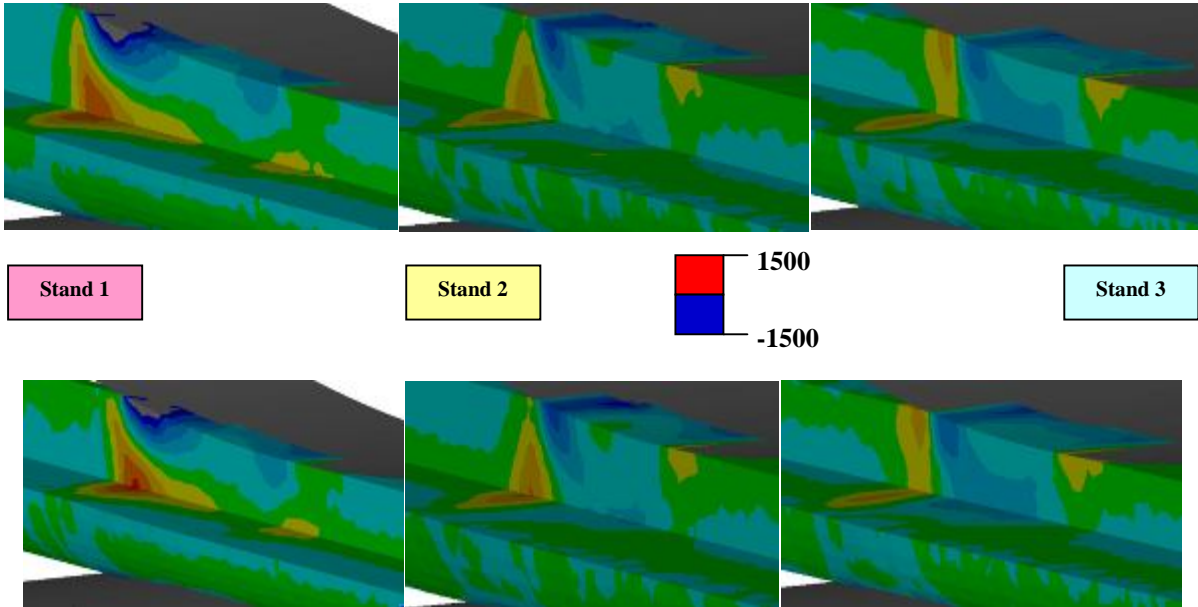


Figure 97: Comparison of the transverse stress evolution in the core during rolling with (down) or without (up) residual stresses transfer

Finally, when stress evolution comparison is made on the vertical stress, presented in Figure 98, the main difference is noticed on edges with a decrease of 150 MPa when residual stresses are not taken into account. The two other curves are globally superposed.

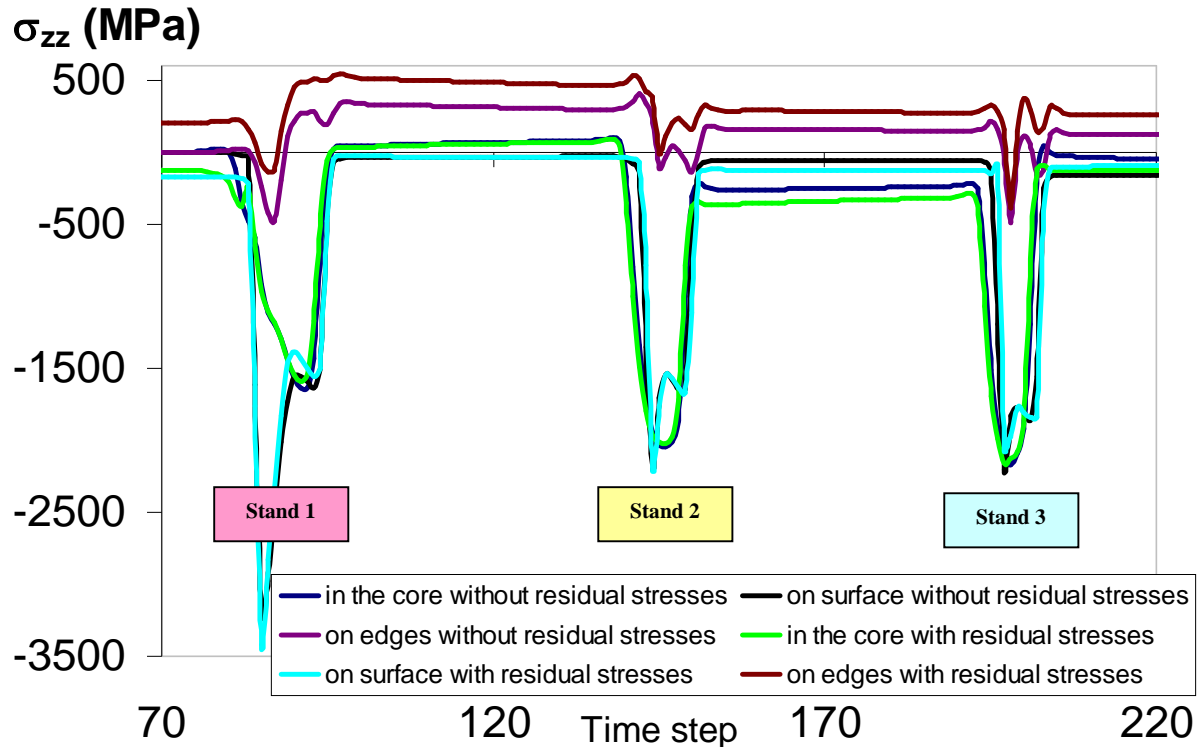


Figure 98: Comparison of the vertical stress evolution during rolling with or without residual stresses transfer

### IV.2.3 Influence of anisotropy

A new complete simulation of rolling has been performed, using an anisotropic behaviour law, Hill's quadratic criterion, identified in chapter III, see III.5. The drawing simulation has not been changed.

#### IV.2.3.1 On strain – stress evolution

Comparison between isotropic and anisotropic simulation are presented below in terms of strain and stress state. Only the first stand is detailed, which is sufficient to highlight the differences.

In terms of strain state (Figure 99), anisotropic behaviour increases global strain and in particular strain value in the wire core is increased of 0.35.

For stress components, anisotropic also increases stresses (Figure 99 and Figure 100). For longitudinal stresses, we observed a more compressive and more tensile state in and after the contact respectively and more tensile state on edges in and after the contact. In the anisotropic case, the transverse stress is increased from 1200 MPa to 1450 MPa. When comparison is made on the vertical stresses, a higher compressive state is noticeable with the anisotropic behaviour under the contact.

This global increase of stress components with anisotropic behaviour has to be handle with care because we have seen in the previous chapter that Hill's criterion is not able to represent the slight stress difference in different directions.

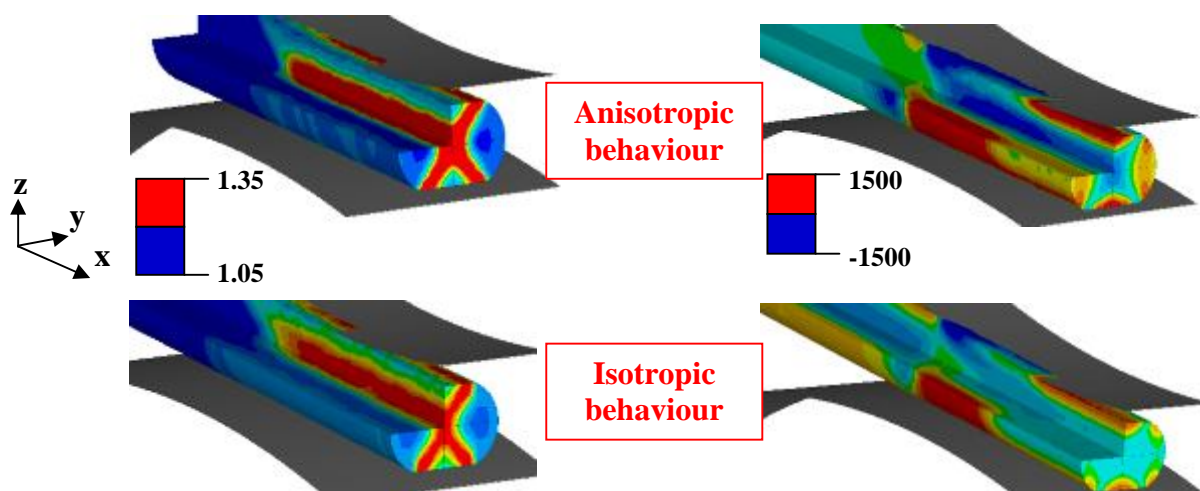


Figure 99: Comparison of strain state (left) and longitudinal stress state (right) for anisotropic (up) and isotropic behaviour (down)

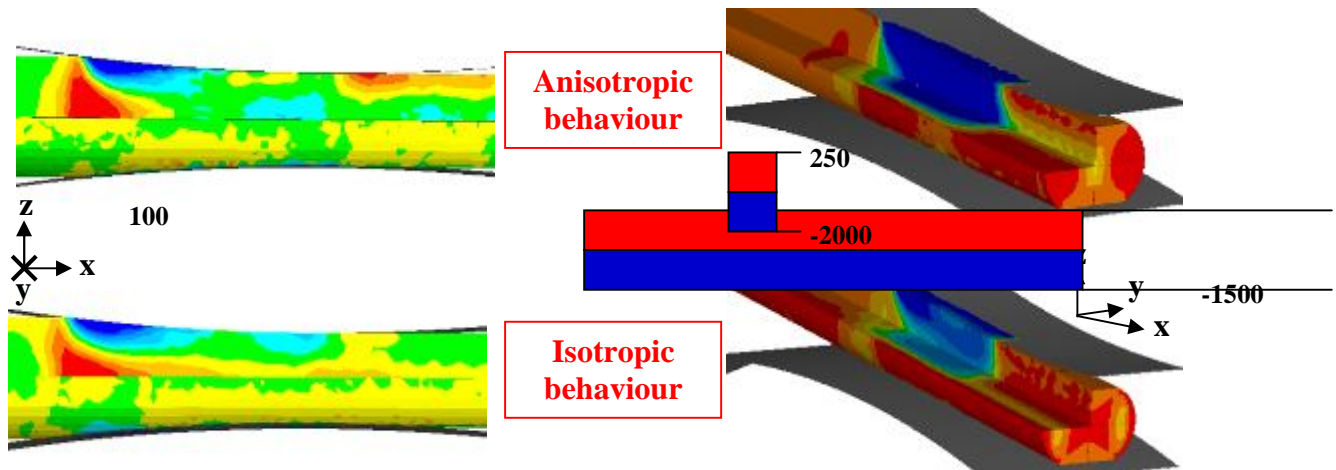


Figure 100: Comparison of transverse stress state (left) and vertical stress state (right) for anisotropic (up) and isotropic behaviour (down)

#### IV.2.3.2 On widening prediction

The use of anisotropic behaviour has been dictated by the underestimation of widening, previously shown in section I.2.3.3 and in section IV.2.1.4. As shown in Figure 101, rolling simulation with the anisotropic law previously established significantly improves the estimation of the final width in terms of widening: yet the underestimation of the experimental width is 5% instead of 10%. As mentioned above, Hill's quadratic criterion is not sufficient to describe our bulk material anisotropy.

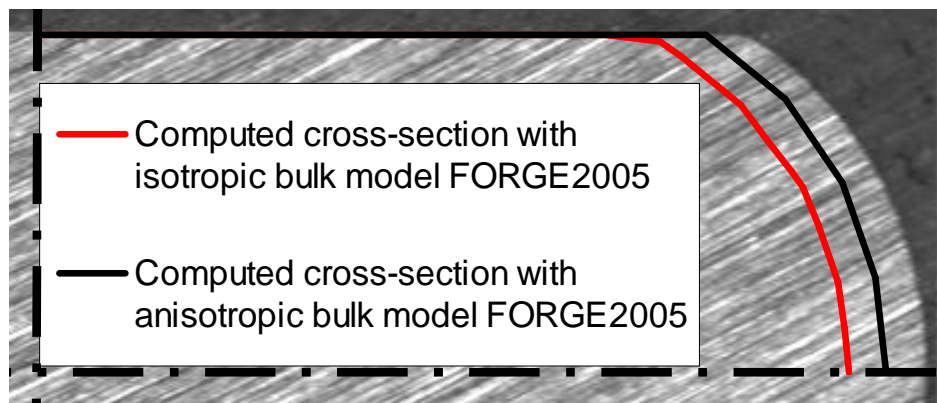


Figure 101: Influence of anisotropy on widening at the end of rolling

#### IV.2.3.2.1 *Sensitivity study on anisotropic coefficients*

This is why this analysis has been complemented with two parametric sensitivity studies. The first one deals with anisotropy factors, namely the radial / axial yield stress ratio and the shear yield stress / mean tensile yield stress ratio (Table 13): width strongly depends on the ratios between F, G and H, while L, M and N affect mainly the side barrelling (Figure 102).

$\frac{\sqrt{2G}}{\sqrt{F+G}} = \frac{\sigma_{0YY}}{\sigma_{0XX}}$	$\frac{\sqrt{F+G} + \sqrt{G+H} + \sqrt{F+H}}{\sqrt{2L} + \sqrt{2M} + \sqrt{2N}} \cong \frac{\tau}{\sigma}$	Widening
1	$1/\sqrt{3} = 0.577$	90%
0.78	0.541	94.5%
0.78	0.427	94.2%
0.78	0.27	95%
0.78	0.171	96.3%
0.53	0.577	98.2%

Table 13: Parameters of anisotropic Hill's criterion

The widening is nearly obtained with  $\sigma_{0YY}/\sigma_{0ZZ} = 0.53$  but this ratio does not correspond to the experimental ovalization.

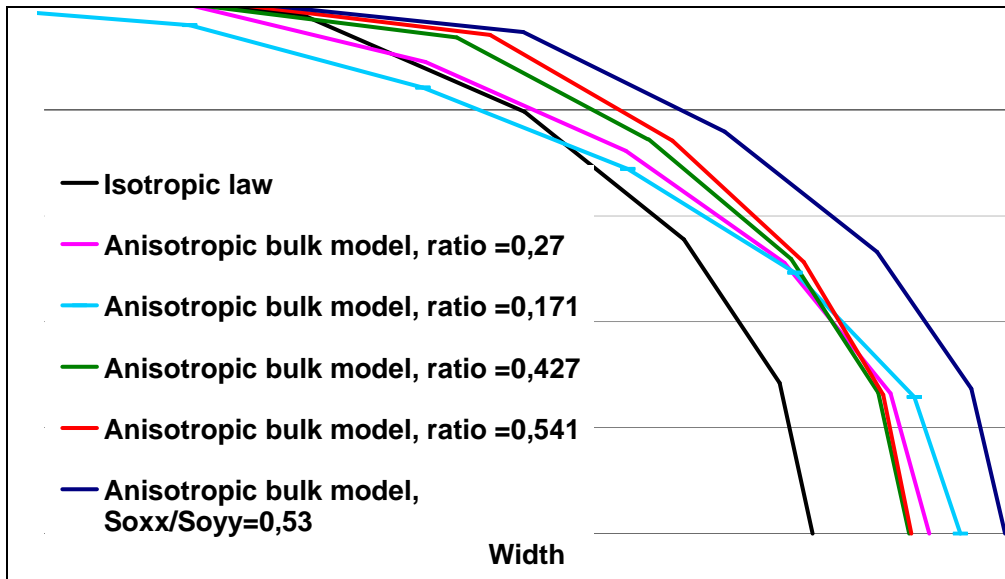


Figure 102: Sensitivity of computed cross-sections to Hill's coefficients

#### IV.2.3.2.2 Sensitivity study on friction

The second study is about friction. In the FEM software, an anisotropic friction law is available. It is based on a velocity-regularized Coulomb model:

$$\tau_{X(respY)} = \text{Min}(\mu_{X(respY)} \cdot \sigma_n, m_{X(respY)} \cdot K \cdot v_g^p) \quad (\text{IV.25})$$

where  $r = \mu_X / \mu_Y$  is the ratio of friction coefficients in the X and Y directions.

$r > 1$  penalizes the flow in the longitudinal direction and therefore enhances transverse flow. Figure 103 shows that the isotropic friction coefficient has no notable impact on widening (default value of friction factor  $m$  is 0,2). Anisotropic friction ( $r=2$ ) expectedly increases

spread, but the width under-estimation decreases only from 5% to 4%: friction does not explain the too small computed widening.

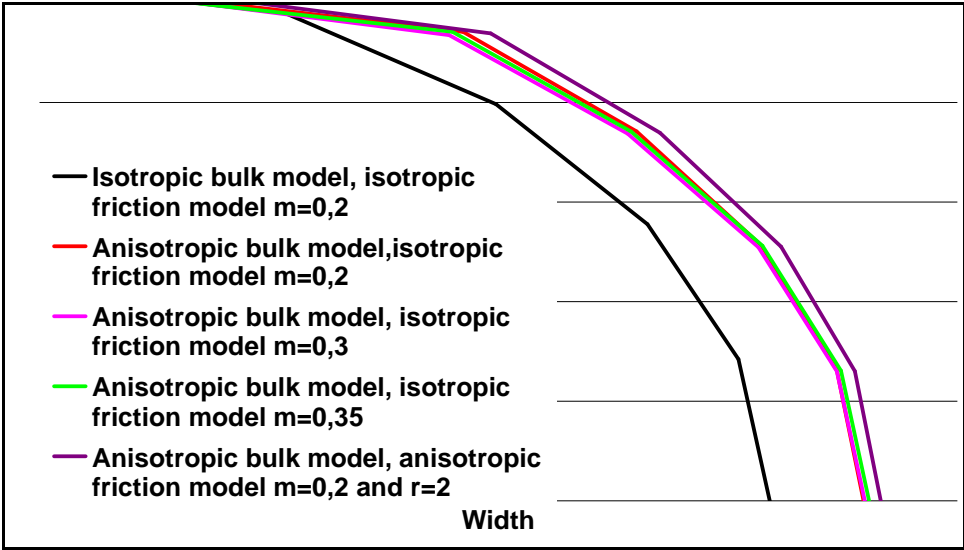


Figure 103: Sensitivity of computed cross-sections to friction parameter

### IV.3 Conclusions

The isotropic modelling enabled to better understand the two cold processes, i.e. wire drawing and rolling, in terms of strain rate, strain and stresses. These analyses highlighted potential danger zones during metal forming. Moreover, the widening prediction is far from satisfactory with an underestimation of 10%. Sensitivity studies have been performed on residual stresses and strain transfer from drawing to rolling. Both have shown that transfer cannot be neglected. Finally, influence of anisotropy has been investigated on stress-strain state and on widening. The main results have exhibited an improvement on the widening prediction with an underestimation of 5%. The remained gap is not explained by Hill's parameters or by friction and shows the inefficiency of Hill's criterion.

## IV.4 Summary

In this chapter, complete modelling of cold forming processes, involve in the production of flat rolled wires, has been analyzed.

In order to better understand numerical results, an introduction to numerical mechanics has been done with presentation of equations of the mechanical problem. Conservation equations and boundary conditions enable to define the system which has to be solved. This system can be expressed in its strong or weak formulation. Then the problem is discretized in time and in space leading to the final system. Finally, the system resolution is briefly detailed.

Then numerical results have been detailed in a second part.

First, complete isotropic simulations of wire drawing and rolling have been presented. The main results have shown that wire drawing is a homogeneous process compared to rolling in terms of strain evolution. Wire drawing exhibits a maximal strain on the surface, whereas rolling is characterized by a maximal strain area called “the blacksmith cross”. In terms of stresses, wire drawing presents a strongly heterogeneous stress map in the drawing die and the stress state is reversed at the exit of the drawing die, whatever the stress component. Rolling also has a heterogeneous repartition of stress components between the core, the flattened surface and the edge. A stress state inversion is also observable after the contact with the rolling stands. This stress analysis during cold forming enables to locate potential initiation fracture areas during drawing and rolling. The numerical widening has been compared to experiment and exhibits an underestimation of 10%. Two additive analyses have been presented, highlighting the importance of transferring the residual stress and strain state from drawing to rolling.

Finally, the anisotropic behaviour, by keeping Hill’s coefficients constant all along rolling, has been analyzed. An anisotropic behaviour law increases strain and stresses during rolling. However for stresses, results have to be handled with care because we have seen previously that identification and validation of Hill’s coefficient is far from satisfactory in terms of stresses. In terms of widening, results have highlighted an improvement of the prediction, but a final underestimation of 5% remains, instead of 10% with an isotropic law. Two sensitivity analyses on Hill’s parameters and on friction do not explain this lack of widening.

## IV.5 Résumé français

Dans ce chapitre, la simulation complète des procédés de mises en forme à froid a été analysée. Afin de pouvoir interpréter et comprendre au mieux les résultats numériques, une introduction à la mécanique numérique a été faite avec la présentation définissant le problème mécanique. Les équations de conservations et les conditions limites ont permis de poser le problème et définir le système à résoudre. Celui-ci peut s'écrire à la fois sous sa forme forte et sous une formulation faible. Le problème est ensuite discrétisé en temps et en espace qui mène au système final à résoudre. Enfin la résolution de ce système est brièvement détaillée.

Dans une deuxième partie, les différents résultats numériques ont été présentés. Tout d'abord, les résultats d'une simulation complète avec une loi de comportement isotrope et avec transfert des contraintes résiduelles et des déformations du tréfilage au laminage ont été détaillés. Les principaux résultats montrent un procédé de tréfilage homogène en terme de déformation comparé au laminage. En effet, en tréfilage, dont la caractéristique principale est d'être un procédé avec une symétrie de révolution, la déformation maximale est située en surface alors qu'en laminage la zone de déformation est localisée dans une croix appelée « la croix de forgeron ». Lorsqu'on analyse les cartographies de contraintes, le tréfilage présente une forte hétérogénéité de répartition dans la filière et on observe une inversion de l'état de contraintes en sortie de filière. Le laminage présente lui aussi une répartition de contraintes hétérogènes entre le cœur, la surface aplatie et les bords libres. L'inversion de l'état de contraintes est également observée en sortie d'emprise. Cette analyse des contraintes au cours des procédés de mises en forme à froid permet de localiser les zones probables d'amorçage de fissures ou du moins d'amorçage d'endommagement. De plus, l'élargissement numérique a été comparé avec l'élargissement expérimental et celui-ci a montré une sous estimation de 10%. Enfin, deux études supplémentaires ont permis de mettre en évidence l'importance du transfert des contraintes résiduelles et de la cartographie complète de déformation du tréfilage au laminage.

Pour finir, l'influence de la prise en compte de l'anisotropie mécanique a été étudiée. Les coefficients du critère de Hill ont été gardés constants tout au long du laminage. Une loi de comportement anisotrope augmente les déformations et les contraintes. En ce qui concerne les contraintes, les résultats sont à manier avec prudence car au chapitre précédent, nous avons montré que la validation des paramètres de Hill n'était du tout satisfaisante en terme de contraintes mais seulement en terme de géométrie. Par contre, en ce qui concerne l'élargissement, le principal résultat est une amélioration dans l'estimation de la largeur finale avec une sous estimation de 5% au lieu de 10%. Deux études de sensibilité, la première sur les paramètres de Hill et la seconde sur le frottement isotrope et anisotrope n'ont pas permis d'expliquer ce manque d'élargissement.

# Chapter V      Microstructure and Damage

The previous chapter has been dedicated to the numerical simulation of the whole cold forming processes, i.e. wire drawing and rolling. One point concerned the prediction of the risk of cracks using the Lemaître's criterion. It showed that the higher damage area corresponded to the wire core. However, the damage mechanisms are not completely understood and it is not yet possible to quantify the risk of cracks and bursts.

The next step is thus to identify the damage mechanisms during cold forming processes. To this end, a fine microscopic metallurgical analysis of damage mechanisms is a crucial point to the development of a numerical model for the quantification of the risk of damage.

First, wire drawing will be studied in terms of microstructure evolution and damage initiation and growth. Rolling, because of a different strain path, will necessarily modify the damage evolution. This is why rolling will be similarly analysed in order to understand the changes in damage evolution.

To reach these goals, several experimental devices have been used, both in CEMEF and ArcelorMittal research centre. The first section of this chapter will present the experimental procedure and devices used for micro and nanoscopic analysis.

## **V.1 Experimental procedure and devices**

### **V.1.1 Experimental devices for micro and nanoscopic analysis**

In order to characterize the microstructure during wire drawing and rolling, optical and microscopic devices have been used: a scanning electron microscopic (SEM Philips XL 30) as well as a transmission electron microscope (TEM) associated with a Focused Ion Beam (FIB) for site-specific TEM sample preparation.

SEM pictures have been done both at CEMEF and ArcelorMittal research centre with both secondary and backscattered electron mode. X-ray diffraction equipment has been also used in order to identify the chemical composition of inclusions. TEM pictures have been taken at CEMEF after sample preparation, by the use of FIB, has been achieved at the CP2M (Centre Pluridisciplinaire de Microscopie électronique et de Microanalyse) at the university of Marseille.

## V.1.2 Experimental procedure of sample preparation

For each pass studied, several samples are prepared in order to have semi-quantitative observations. Samples are both cut from a longitudinal and transverse cutting plane (Figure 104 and Figure 105) in order to have a 3D representation of the microstructure. To correctly interpret SEM - TEM pictures, a clean observation surface has to be obtained. Both procedures for SEM and TEM samples are described below.

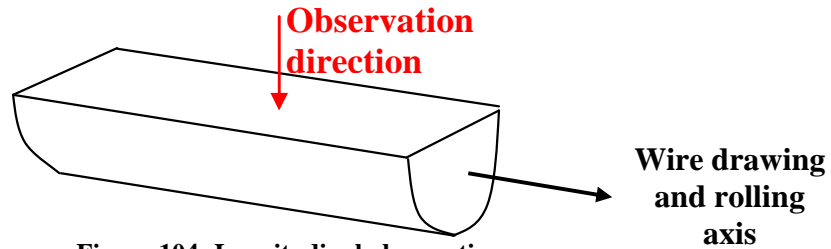


Figure 104: Longitudinal observations

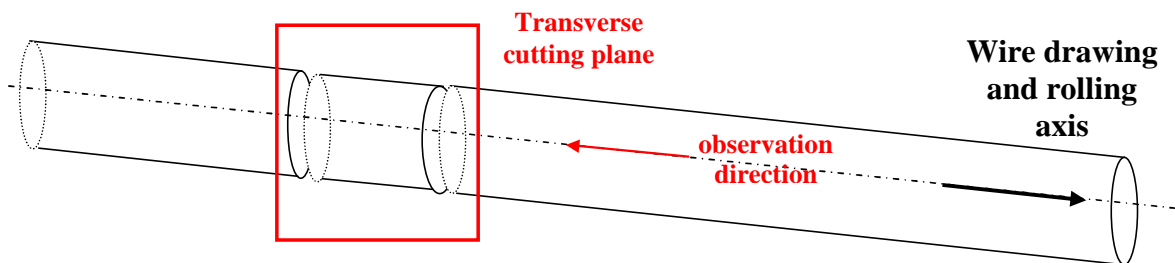


Figure 105: Transverse observations

### V.1.2.1 For SEM pictures

The procedure has been established thanks to the expertise of ArcelorMittal research centre. It consists in four points:

1. Mechanical polishing with grinding papers of decreasing granulometry,
2. Mechanical polishing with diamond-based solution down to  $1\mu$ ,
3. Colloidal silica polishing: it refines the mechanical polishing and does a smooth chemical preliminary etching,
4. Chemical etching with a diluted solution of Nital: 2% or less.

### V.1.2.2 For TEM pictures

As mentioned before, thin layers for TEM observations have been prepared thanks to a FIB. Commercially produced for ten years, principally for semi-conductor industries, a FIB works as a SEM but uses focused gallium ions beam. The ion beam can be used at low intensity for pictures or at high intensity for sputtering or for site-specific cutting. More details about the physical principle can be found in Annex 4. In cutting mode, a software assists the user to make the procedure quasi-automatic. After the deposition of a protection layer on the area of interest, the programme progressively thins the layer as shown in Figure 106. After a last manual thinning, the thin layer is

cut and is retrieved thanks to a glass tip (with a radius of  $1\mu\text{m}$ ) which attracts the thin layer by an electrostatic effect. The maximal observable area is  $6 \times 5 \mu\text{m}^2$ . A complete description of the procedure can be found in Annex 4.

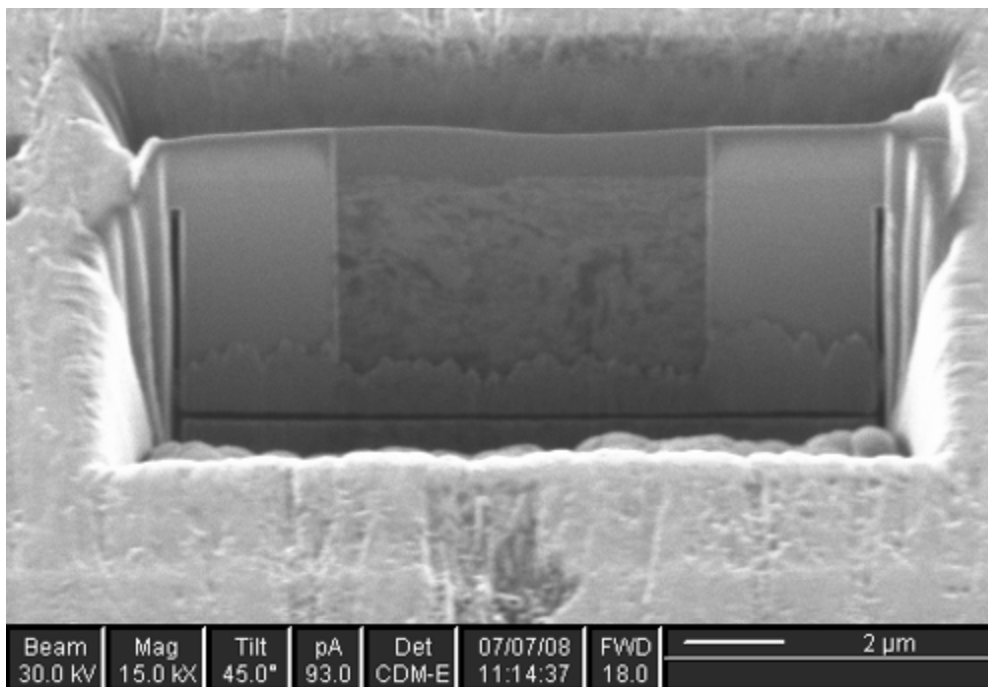


**Figure 106: Thinning procedure with a FIB**

## **V.2 Analysis of the first damage steps during ultimate drawing**

In order to understand the first damage steps, i.e. nucleation and growth, during wire drawing of high carbon steels, an ultimate drawing sequence has been performed. The steel is the same and the first steps of the ultimate drawing correspond exactly to the industrial wire drawing. This type of drawing enables to highlight damage phenomena, which are not easily identified from the industrial wire drawing (too low strain).

### **V.2.1 Ultimate drawing characteristics**

A wire with a diameter of 8 mm is drawn until fracture by delamination (delamination is observed during torsion tests after each ultimate drawing passes). In this case, 16 passes have been done to reach the delamination as shown in Table 14.

Only a few steps were chosen for the microstructural and damage study: before ultimate drawing, after 4 passes (equivalent to the end of drawing in the real process), after 10 passes and at the end of the ultimate drawing. As the previous chapter showed potential damage localization at the core of the wire during drawing, the microscopic observations have been performed there.

N°	Diameter		Hardening		Ln (S <sub>0</sub> /S)
	theoretical	real	theoretical	total	
	8	7.98			
1	7.2	7.2	18.59	18.59	0.21
2	6.6	6.61	15.72	31.39	0.38
3	6	6.05	16.23	42.52	0.55
4	5.45	5.44	19.15	53.53	0.77
5	4.87	4.87	19.86	62.76	0.99
6	4.36	4.36	19.85	70.15	1.2
7	3.9	3.9	19.99	76.12	1.43
8	3.49	3.5	19.46	80.76	1.65
9	3.12	3.11	21.04	84.81	1.88
10	2.79	2.78	20.1	87.86	2.11
11	2.49	2.53	17.18	89.95	2.297
12	2.23	2.23	22.31	92.19	2.55
13	2	2	19.56	93.72	2.768
14	1.79	1.79	19.9	94.97	2.989
15	1.6	1.59	21.1	96.03	3.226
16	1.43	1.45	16.83	96.7	3.411

**Table 14: Ultimate drawing results**

## V.2.2 Microstructural evolution during ultimate drawing: pearlite orientation

### V.2.2.1 Before drawing

The microstructure is pearlitic: ferrite with lamellar cementite. SEM pictures show cementite lamellae in white and ferrite in dark as in shown in Figure 107. The microstructure is homogeneous. Grains are equiaxed, with a random crystallographic texture. The mean interlamellar spacing can be estimated to 175 nm from TEM pictures.

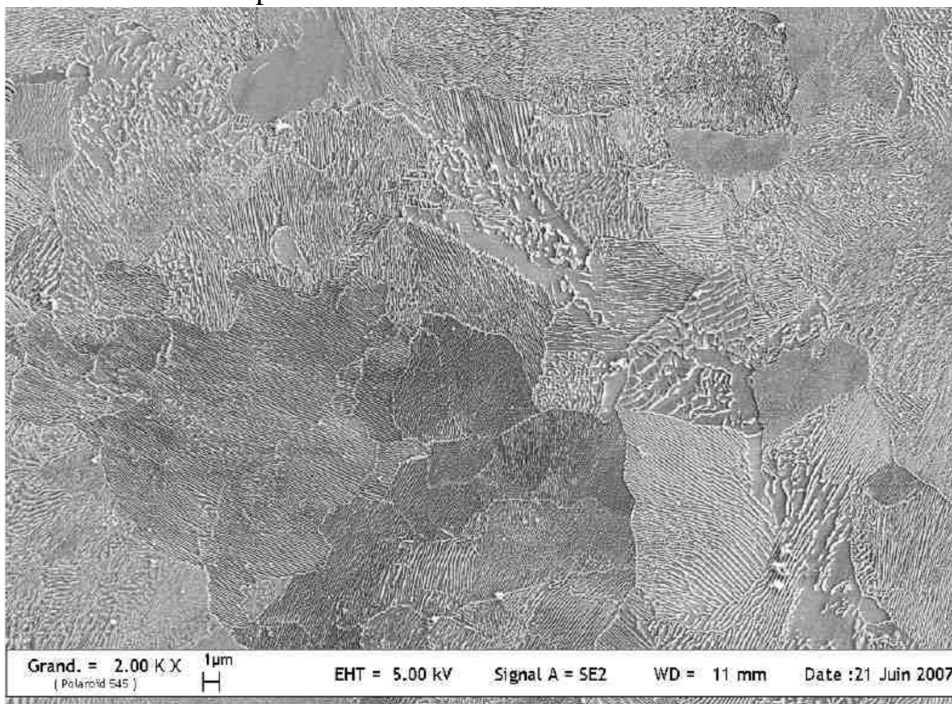


**Figure 107: Initial high carbon steel microstructure (patented wire) [3], SEM**

V.2.2.2 After 4 passes (equivalent to the end of drawing in the real process):  $\epsilon=0.77$

In the longitudinal view, shown in Figure 108, some pearlite colonies are aligned in the drawing direction. Interlamellar distances have strongly decreased compared to those after patenting. Other colonies are still perpendicular to the drawing direction. The interlamellar distance for these colonies is higher than the aligned colonies and first signs of distortion are visible.

Pearlite colonies are randomly oriented in a cross-section as observed in Figure 109. The rough aspect is a consequence of the colloidal silica “polishing”. It introduces a risk of confusion with damage-induced cavities. Therefore, next transverse sample preparations will be done without colloidal silica polishing.

Thin layers observations enable us to follow the evolution of microstructural properties during drawing. Figure 110 shows a pearlitic microstructure with a mean apparent interlamellar distance of 120 nm.

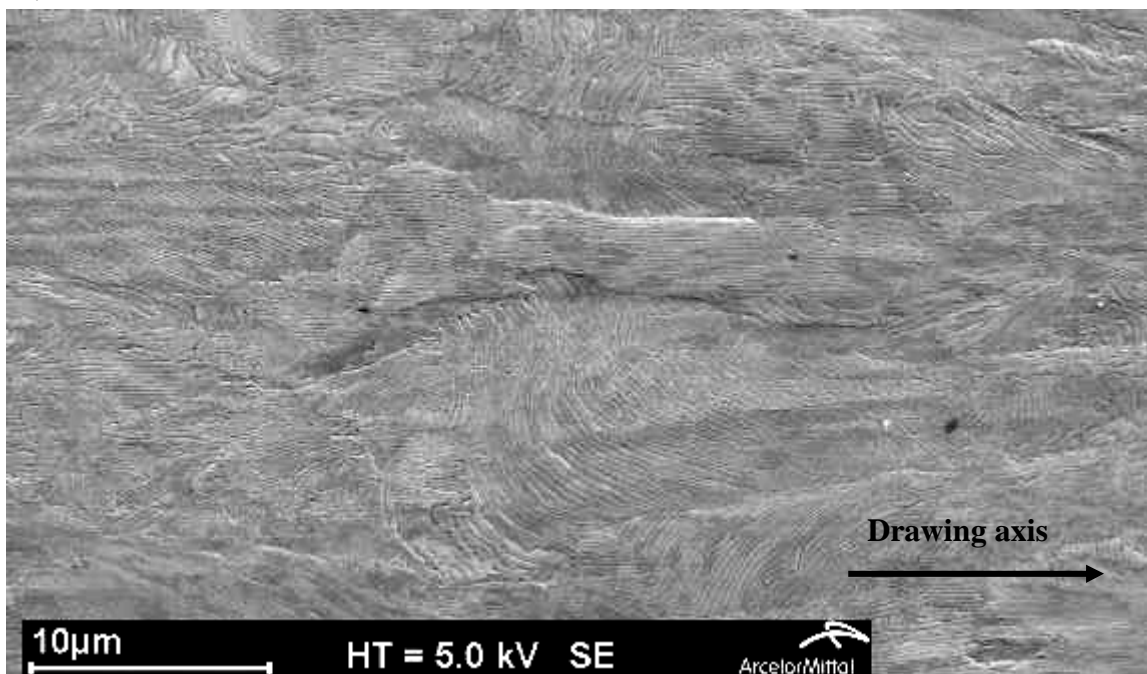


Figure 108: Microstructure at  $\epsilon=0.77$  in a longitudinal view. Pass 4, SEM.

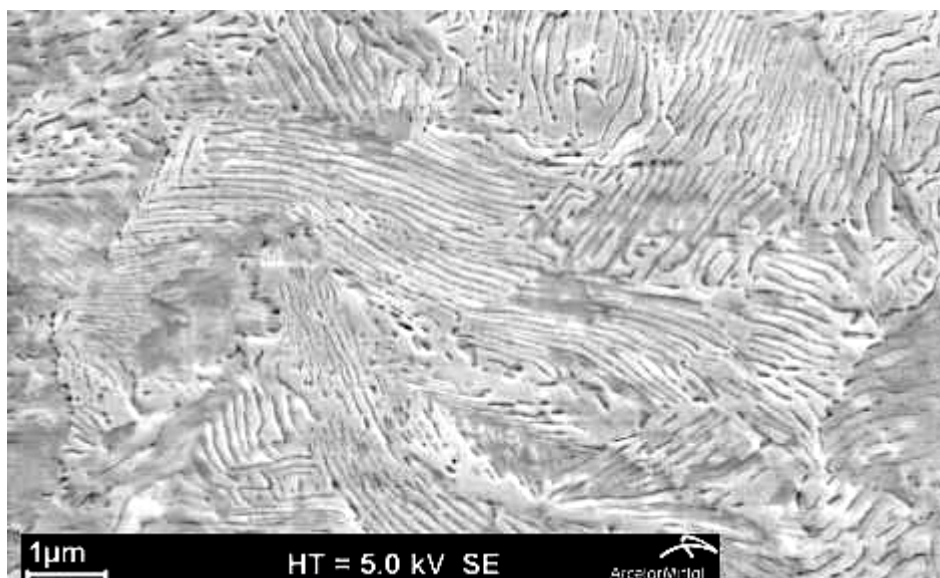


Figure 109: Cross-section microstructure at  $\epsilon=0.77$ . Pass 4, SEM.

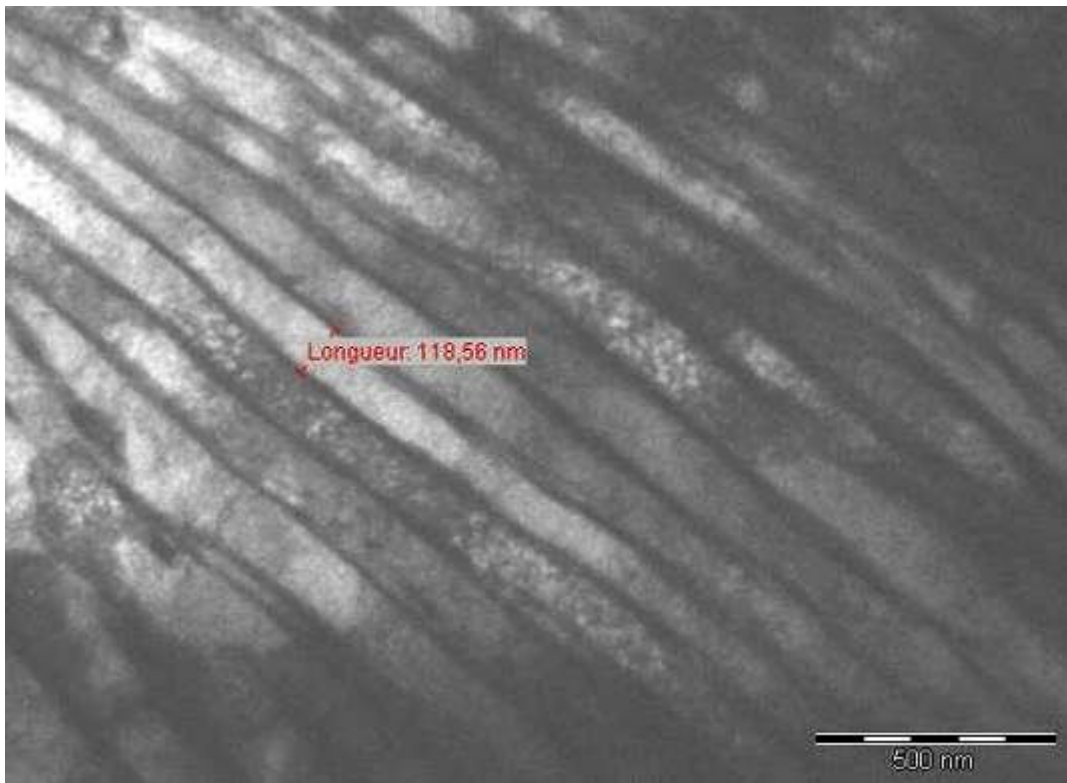


Figure 110: Wire drawing microstructure observed with a TEM at  $\epsilon=0.77$ . Pass 4 on a FIB-cut layer.

#### V.2.2.3 After 10 passes: $\epsilon=2.1$

At  $\epsilon=2.1$ , Figure 111 exhibits a very fibered microstructure. It becomes difficult to distinguish pearlite colonies. Some areas present a distorted microstructure characterized by bent lamellas (Figure 112). The explanation has been already given in the previous paragraph: a non-favourable initial orientation with respect to the drawing axis lead to this kind of microstructure.

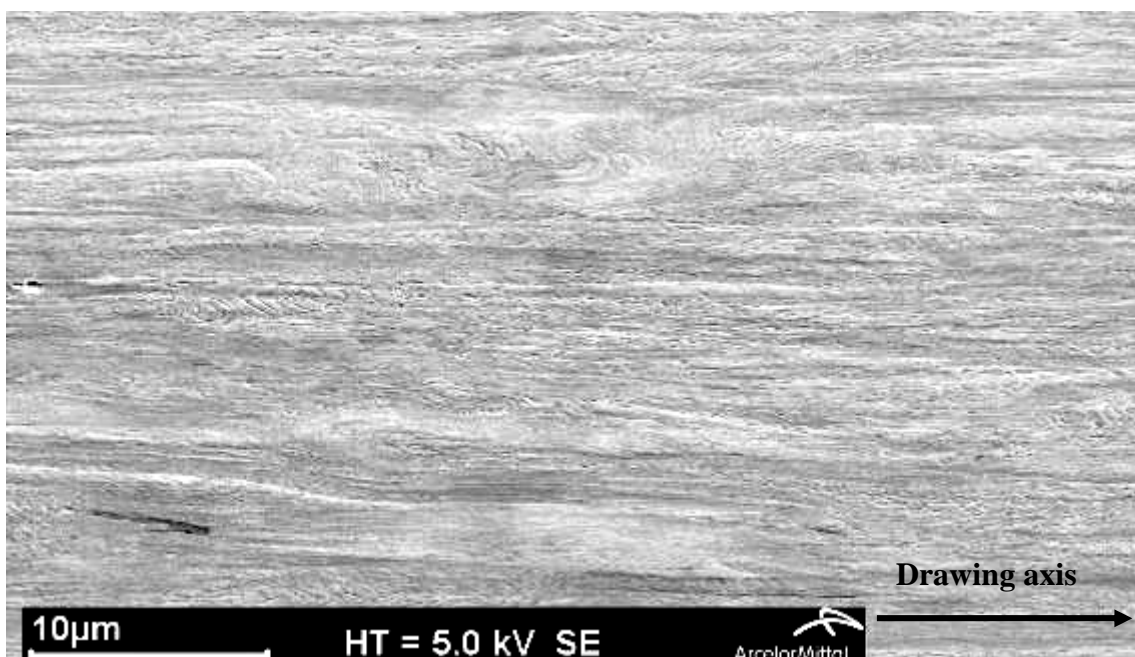


Figure 111: Longitudinal microstructure at  $\epsilon=2.1$ . Pass 10, SEM.

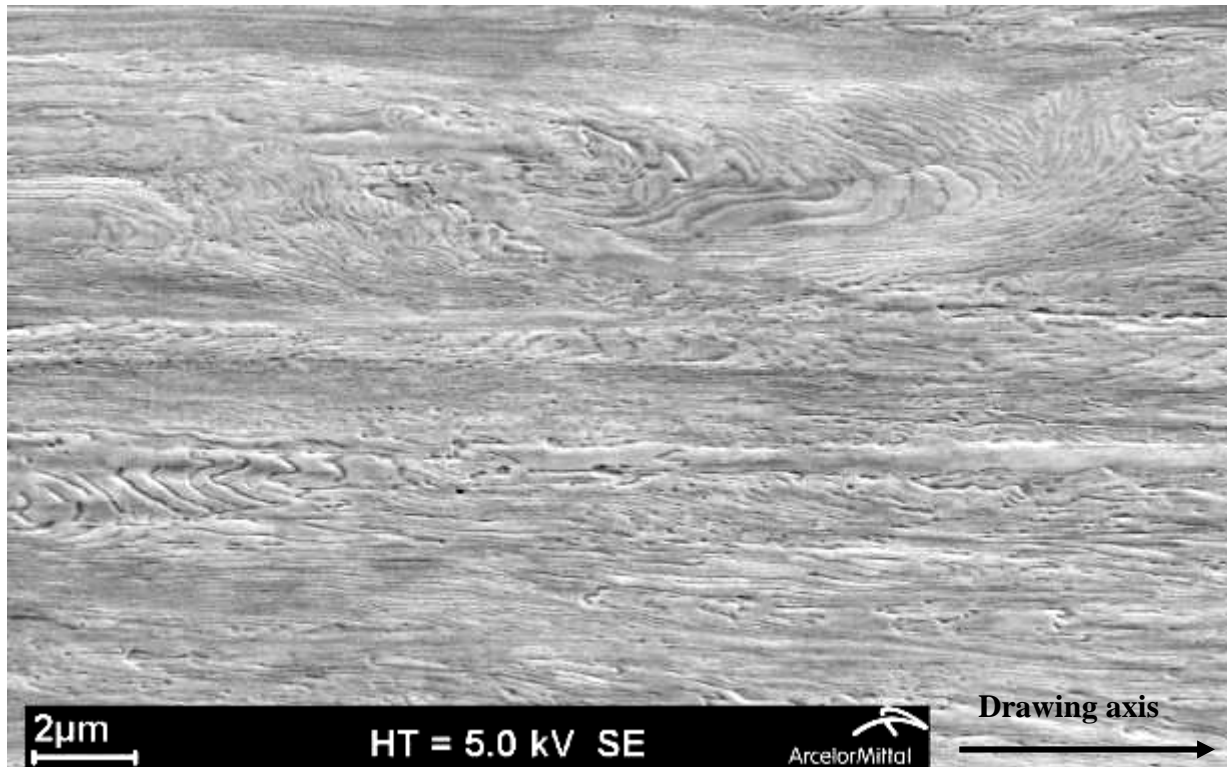


Figure 112: Distorted microstructure at  $\epsilon=2.1$ . Passe 10, SEM.

#### V.2.2.4 After 16 passes: $\epsilon=3.4$

At the end of ultimate drawing, grain boundaries are not easily observable and the interlamellar distance is too small to be measured with a SEM, because of a high level of deformation, as shown in Figure 113. The Figure 114 shows the familiar swirled microstructure already presented in the bibliography review. This figure also shows an important spatial heterogeneity of the apparent interlamellar distance. The origin of this irregularity is the same as for the distorted microstructure presented in the previous paragraph, i.e. if the initial orientation of cementite lamellae is parallel to the drawing axis, then the interlamellar distance will decrease; but for perpendicularly oriented lamellae, this distance will increase and can initiate voids in some cases. From TEM pictures (Figure 115), cementite lamellae are, on the contrary, easily noticeable and the interlamellar distance seems to have decreased to reach a mean apparent spacing of 30 nm. When comparison is made with the Figure 18, the initial interlamellar space is nearly three times higher and this distance is divided by more than fifteen times during a deformation of 3.4, whereas in the article the lamellae spacing decreases from 65 nm to 10 nm. The same comparison can be done on the evolution of the  $\alpha$ -angle presented in Figure 17: all colonies are aligned for a angle equals to zero.

To summarize, during wire drawing, we have seen growing orientation and alignment of the pearlitic colonies along the drawing axis, as well as a decrease of the interlamellar spacing, as it has been shown in the bibliographic review. This orientation is probably one cause of the strong mechanical anisotropy, as well as a strong crystallographic texture highlighted in the bibliographic

chapter. This microstructure evolution is also strongly linked to damage mechanisms and is dealt with in the next part.

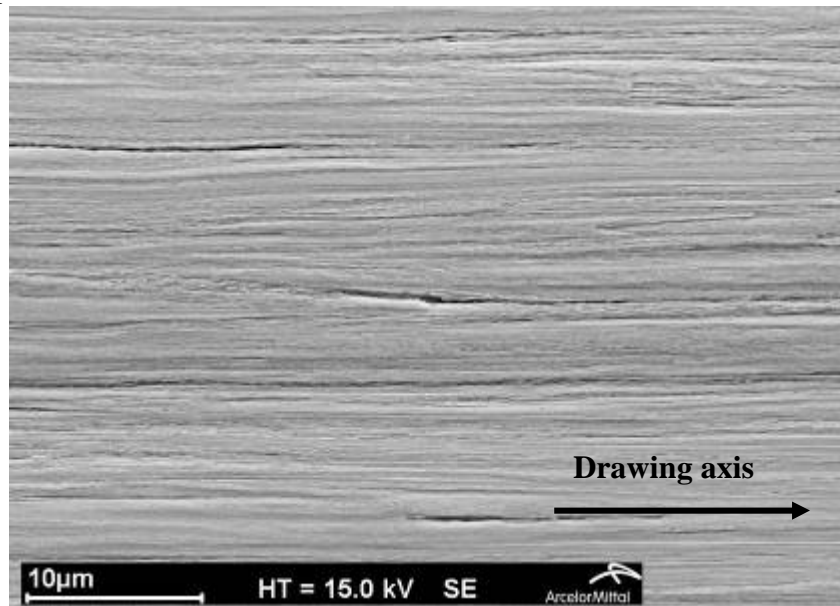


Figure 113: Microstructure at the end of drawing. Pass 16, SEM.

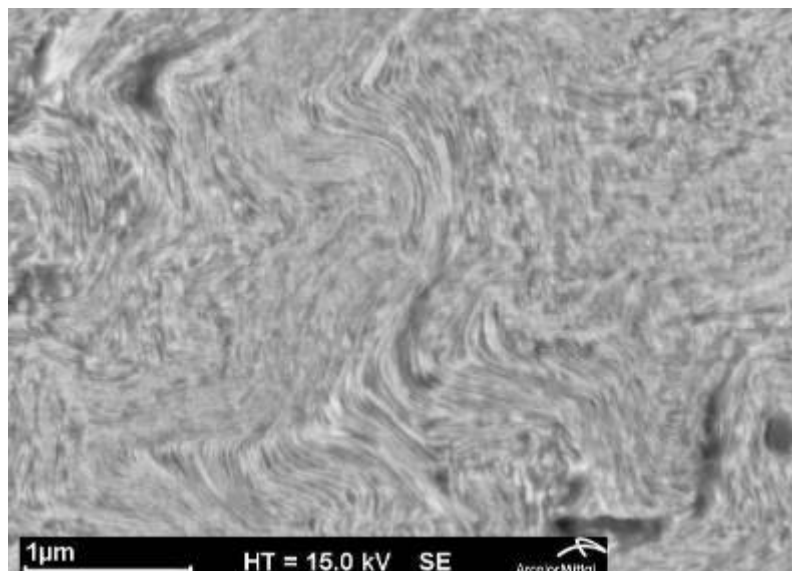


Figure 114: Cross-section microstructure at the end of drawing. Pass 16, SEM.



Figure 115: TEM pictures, in a longitudinal cutting plane at the end of ultimate drawing. Pass 16, FIB cut sample.

### V.2.3 Damage initiation and growth during ultimate drawing

The use of SEM enables us to identify a high number of cavities with inclusions inside. The presence and chemical composition of inclusions have been determined by X-ray spectrometry analysis. In steels, two main categories of inclusions appear which can be distinguished by their resistance to deformation [122]:

- hard inclusions which do not easily deform, called non deformable inclusions,
- soft inclusions which can undergo a certain level of deformation, called deformable inclusions.

Frequently, these two types of inclusions can be found in the same cavity with a deformable inclusions situated on either side of a non deformable inclusion. These inclusions are called complex inclusions.

For confidentiality reasons, the exact chemical composition will not be given in this text. Only the distinction between hard and soft inclusions will be done; it is anyway sufficient to understand each mechanism.

#### V.2.3.1 After 4 passes (equivalent to the end of drawing in the real process): $\epsilon=0.77$

At this deformation level, no crack is identifiable, but damage takes place around and in inclusions. In case of a deformable inclusion (Figure 116), the first damage step corresponds to the elongation and fragmentation of the inclusion in the longitudinal direction. No decohesion takes place with the matrix.

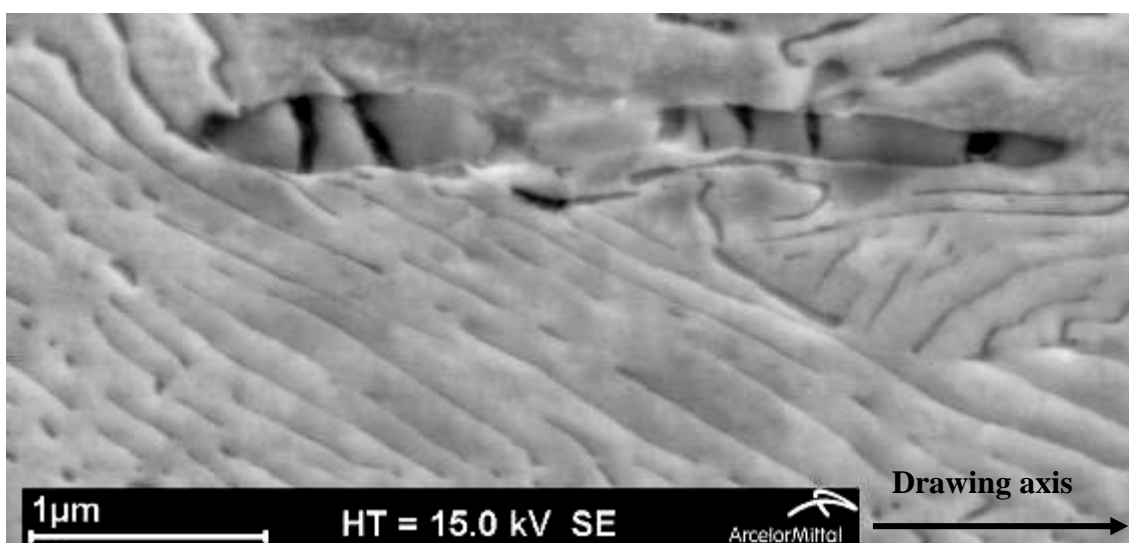


Figure 116: Fragmentation of a deformable inclusion in longitudinal view. Pass 4.

To see any damage initiation around non deformable inclusions, TEM, associated to FIB for the preparation of thin layers, has been used. Figure 117 shows an initiation of damage by decohesion at the inclusion apex with propagation along the ferrite / cementite interface more or less parallel to the drawing axis.

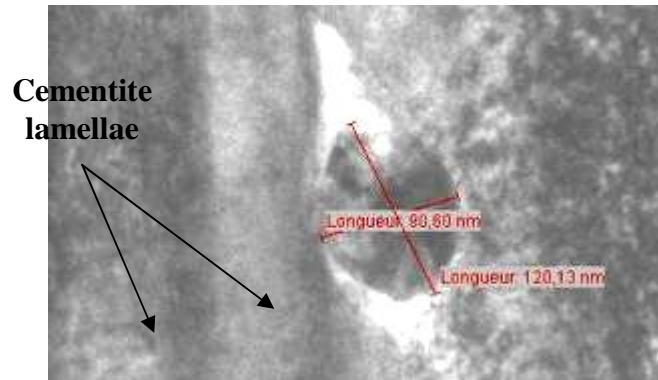


Figure 117: Damage initiation of a non deformable inclusion (TEM pictures). Pass 4

This very local phenomenon has been observed once; interesting anyway but we cannot affirm that it is a major origin of damage.

#### V.2.3.2 After 10 passes: $\epsilon=2.1$

Here, larger non deformable inclusions can be identified. After 10 passes, longitudinal decohesion is much more pronounced as shown by Figure 118.

Observations of deformable inclusions at this deformation step give more information concerning decohesion and fragmentation mechanisms. Figure 119 clearly shows a very elongated and fragmented deformable inclusion with decohesion at the interface with matrix. However, the matrix flow fills up the void created by the elongation and fragmentation damage mechanisms, although no healing phenomenon can take place in cold processes.

Another type of damage has been identified at this step. This one is initiated by microstructure distortion leading to the formation of a transverse cavity as highlighted by Figure 120 (in a longitudinal view). X-ray spectrometry analysis has confirmed that no inclusion is at the origin of this void.

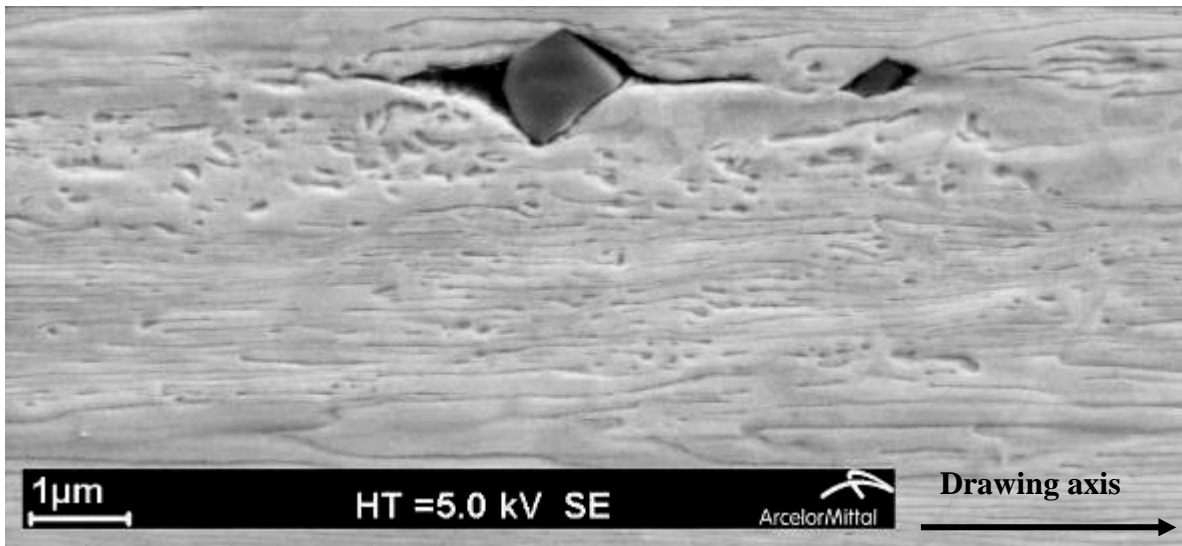


Figure 118: Decohesion of a non deformable inclusion after 10 drawing passes. SEM.

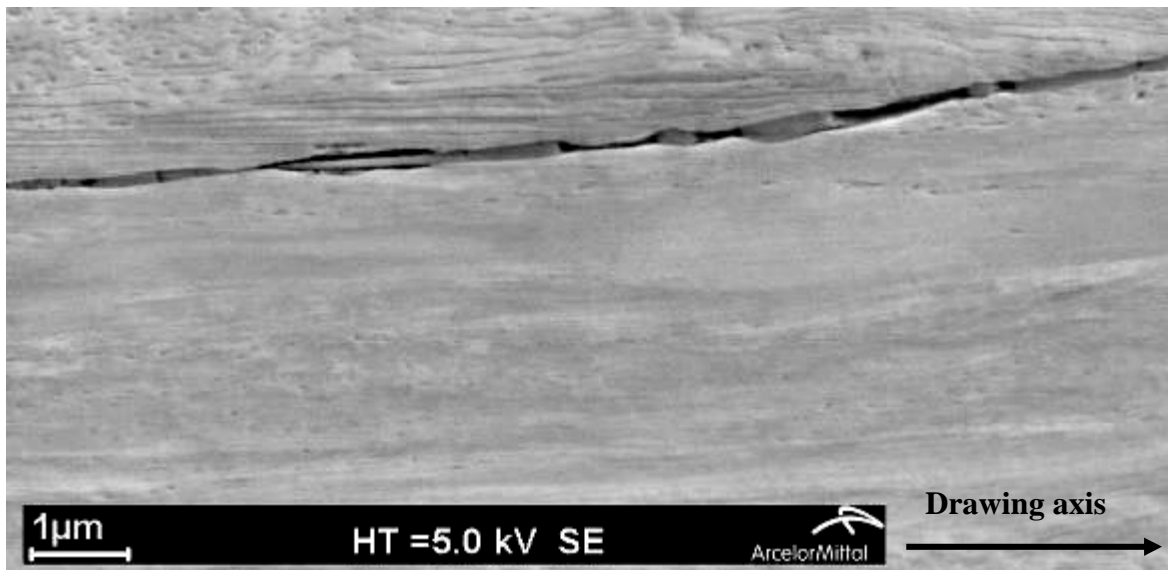


Figure 119: Elongation and fragmentation of a deformable inclusion after 10 drawing passes. SEM.

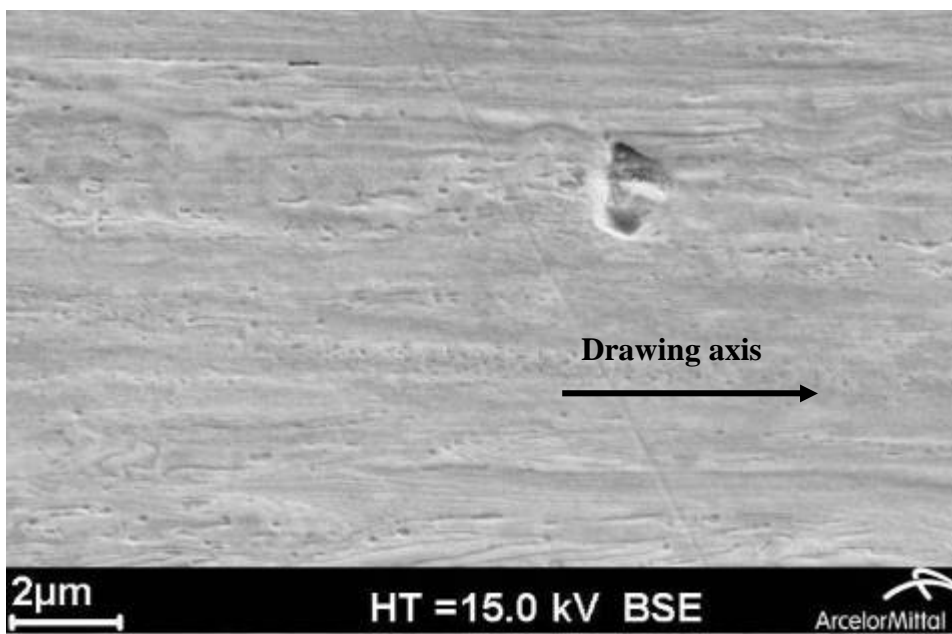
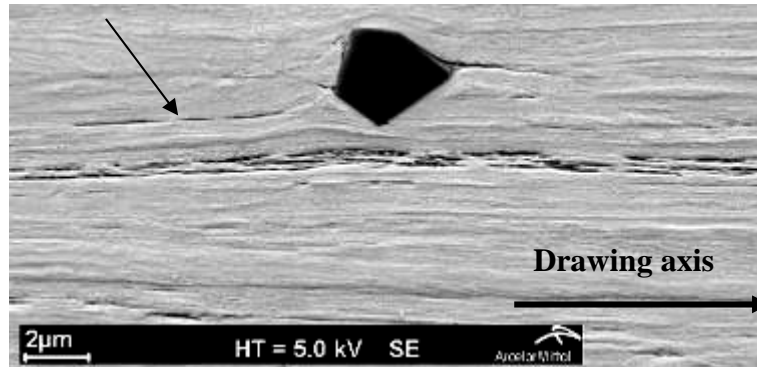


Figure 120: Transverse void in longitudinal view. SEM.

V.2.3.3 After 16 passes:  $\epsilon=3.4$

At the end of ultimate drawing, long decohesions are observable around non deformable inclusions as shown in Figure 121.



**Figure 121: decohesion of a non deformable inclusions at the end of ultimate drawing in longitudinal view. SEM**

Other transverse cavities have been observed at this step and are shown in Figure 122, with a very perturbed microstructure. The broken cementite lamellae are clearly identified in the left figure and confirm that disoriented cementite lamellae, with respect to the wire drawing axis, are the origin of their fracture because they could not undergo high deformation in this direction.

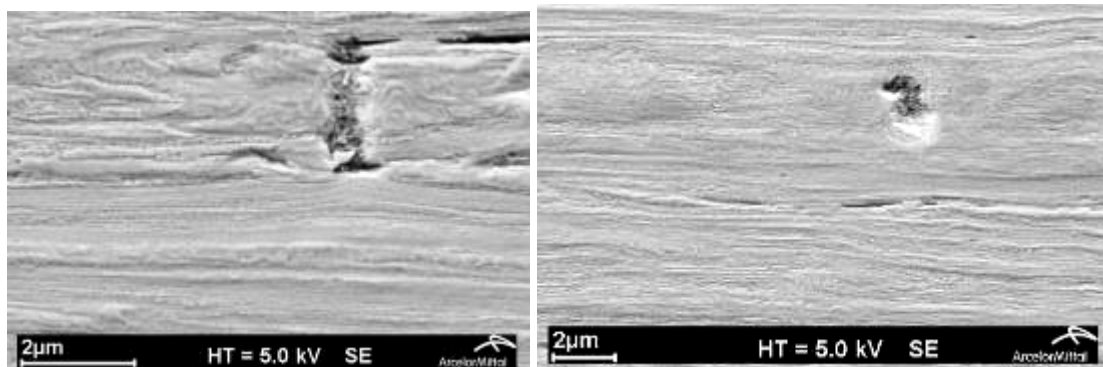


**Figure 122: Two transverse cavities in longitudinal view. Pass 16, SEM.**

To complete the microstructural analysis at this step, TEM pictures have been done on cross-sections. One privileged initiation site was identified. Two voids seem to nucleate at the high disorientation angle pearlitic colonies boundary during their rotation, as shown in Figure 123.

Again, there is no clear evidence that this very local phenomenon contributes significantly to global damage.

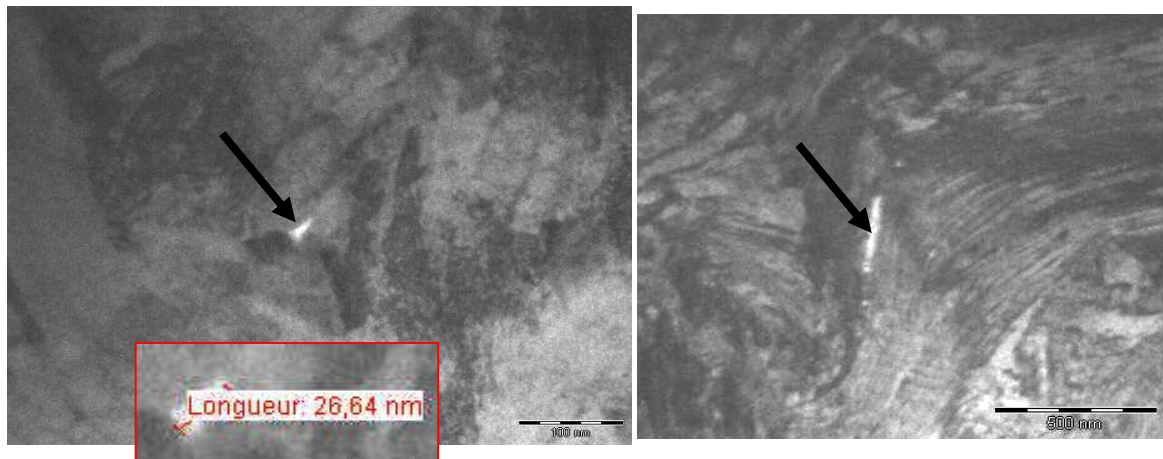


Figure 123: Cavities nucleation at high disorientation angle colonies boundary (TEM pictures). Pass 16.

#### V.2.3.4 Synthesis

Damage study, during ultimate drawing for high carbon pearlitic steels, shows multiple cavities:

- Longitudinal cavities (their orientation has to be linked to the evolutive flow anisotropy introduced by the drawing process). These cavities contain inclusions, or not (they could have been removed by the metallographic preparation). Inclusions can be either deformable or non deformable resulting in different damage mechanisms. TEM pictures enable to validate damage initiation by decohesion at the fourth drawing pass around non deformable inclusions.
- A few transverse cavities, obvious signs of damage linked to microstructure evolution during the drawing process. Indeed, SEM pictures have shown fracture of those lamellae which are initially at a large angle to the drawing axis.
- TEM study enabled to observe cavities situated at multiple colonies boundary as cavities initiation sites.

Figure 124 shows the chronology of damage mechanisms appearance and evolution during ultimate drawing.

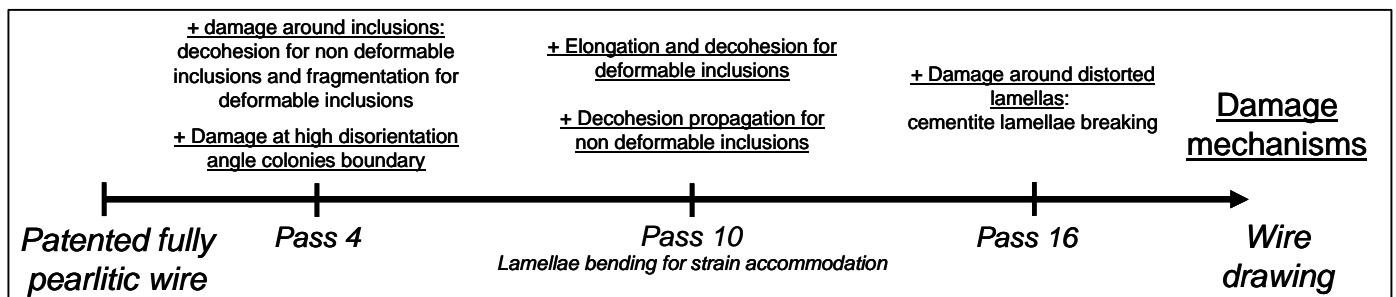


Figure 124: Chronological sketch of damage mechanisms evolution during ultimate drawing of high carbon pearlitic steels

Now, the second step consists in understanding the damage evolution from wire drawing to and during rolling. The strain path change should modify damage evolution induced during wire drawing.

### **V.3 Analysis of damage evolution during wire drawing + rolling**

#### **V.3.1 Process characteristics**

A patented wire with a diameter of 8mm is drawn during four passes, and then it is rolled through three stands and the experimental wire drawing exactly corresponds to the four passes of the ultimate drawing used for the study of the first damage steps. Thus, microstructure and damage state are known at the end of wire drawing and only damage evolution during rolling has to be analyzed. Results of this experimental study could be transposed to the industrial process.

For the experimental observation, specimens have been only sampled at the end of rolling. We will have only the final damage and microstructure state. Transverse and longitudinal cross-sections have been observed to have a three-dimensional representation of the material flow.

#### **V.3.2 Microstructural evolution during rolling**

In a longitudinal view in the core, shown in Figure 125, grains and colonies boundaries are no longer identifiable, due to the high deformation of the blacksmith cross in core, the microstructure is very pertubated. Whereas on edges elongated grains are clearly observable, as shown in Figure 126.

Micrograph in cross-section in the core (Figure 127) exhibits a strongly flattened microstructure due to the vertical compression in the rolling.

Both microstructural observations of longitudinal and transverse cutting plane enable to conclude on the three-dimensional evolution of the microstructure during rolling. The FEM analysis of the strain map during rolling is shown in Figure 128. It exhibits a maximal strain area called the blacksmith cross, red area in Figure 128. This maximal strain area explains the microstructure evolution during rolling. The heterogeneous deformation of rolling leads to a heterogeneous microstructure between the core and the edge. The larger flattening, in the transverse direction, of colonies at the wire core corresponds to maximal area of deformation.

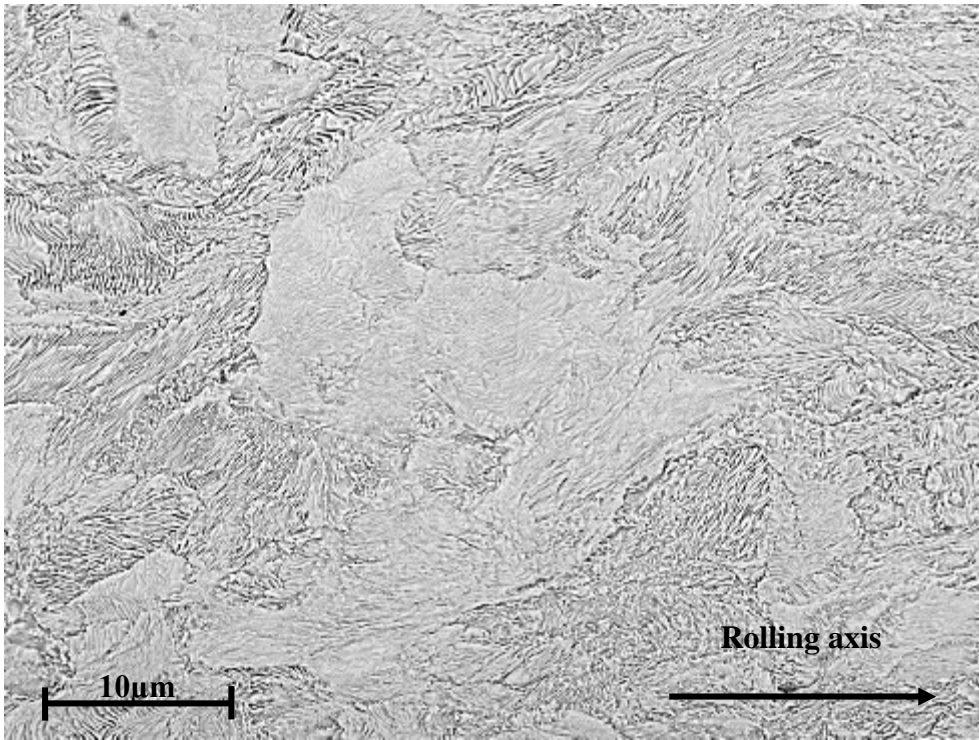


Figure 125: Microstructure after rolling in a longitudinal view in the core. SEM.

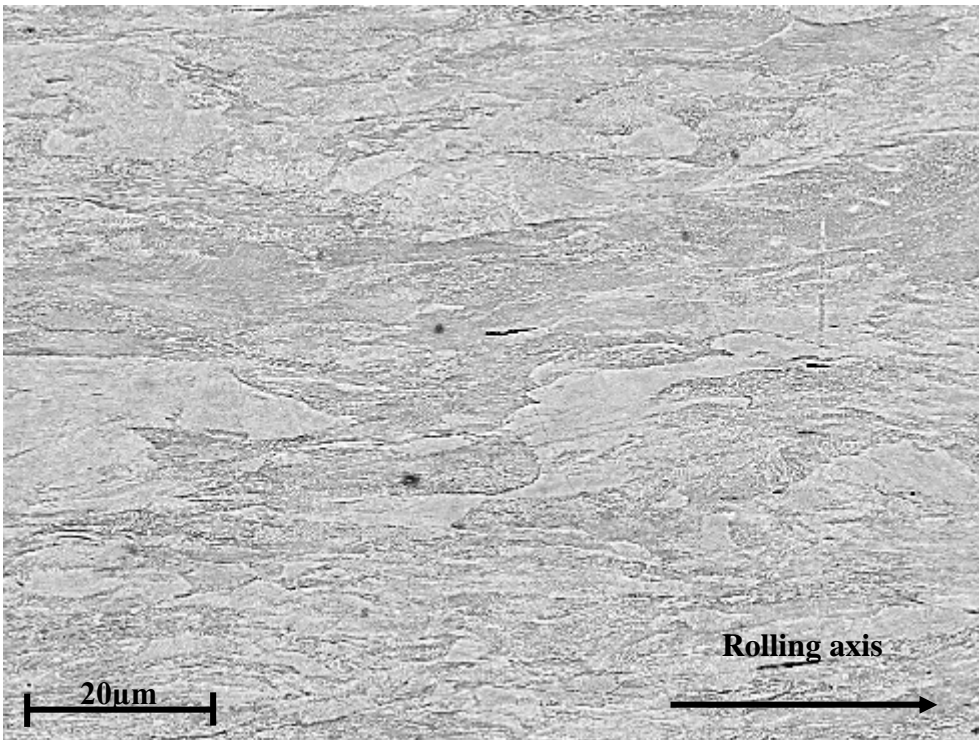


Figure 126: Microstructure after rolling in a longitudinal view and at the edge. SEM.

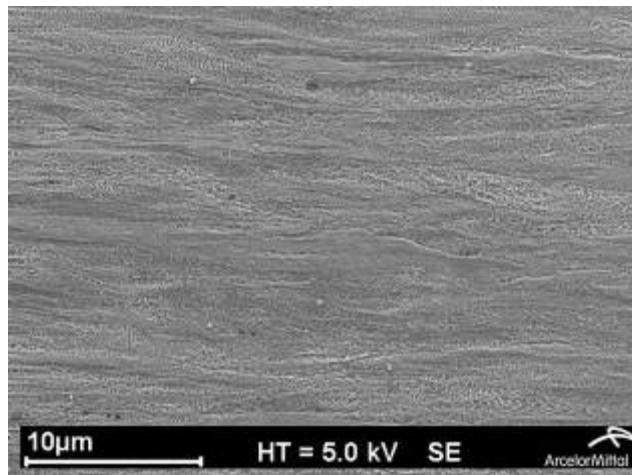


Figure 127: Cross-section microstructure after rolling in the core. SEM.

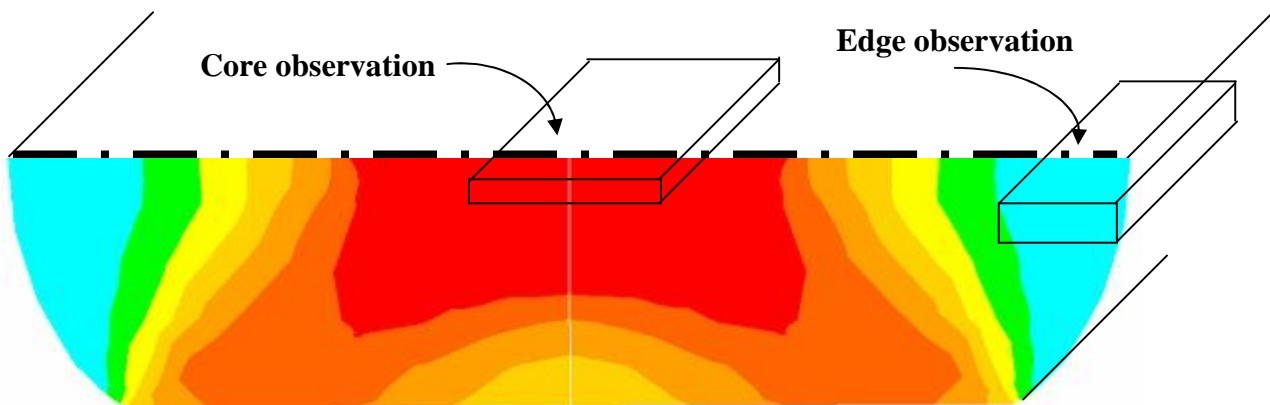


Figure 128: Numerical map of rolling strains; correlation with microstructure evolution (schematic representation of grains)

### V.3.3 Damage evolution during rolling

At the end of wire drawing (fourth pass of the ultimate drawing), damage has been identified at a microscopic scale, characterized by decohesion around non deformable inclusions or fragmentation around deformable inclusions, as well as at a nanoscopic scale with a decohesion initiation at non deformable inclusion apex along the ferrite / cementite interface.

#### V.3.3.1 Transverse cutting plane

The cross-section gives interesting information about longitudinal cavities / inclusions repartition and shape in function of their position in the rolled wire. Figure 129 and Figure 130 clearly show a higher void density, as well as a higher flattening of cavities (black spot of the Figure 129), in the wire core than in the edge. The explanation is the same as in the previous paragraph, i.e. the localization of the deformation in the blacksmith cross. Moreover, inclusions located in the branches of the blacksmith cross seem to have a preferential orientation due to shear stresses in this area, as shown by Figure 131. Further information will be given in paragraph V.4.2.

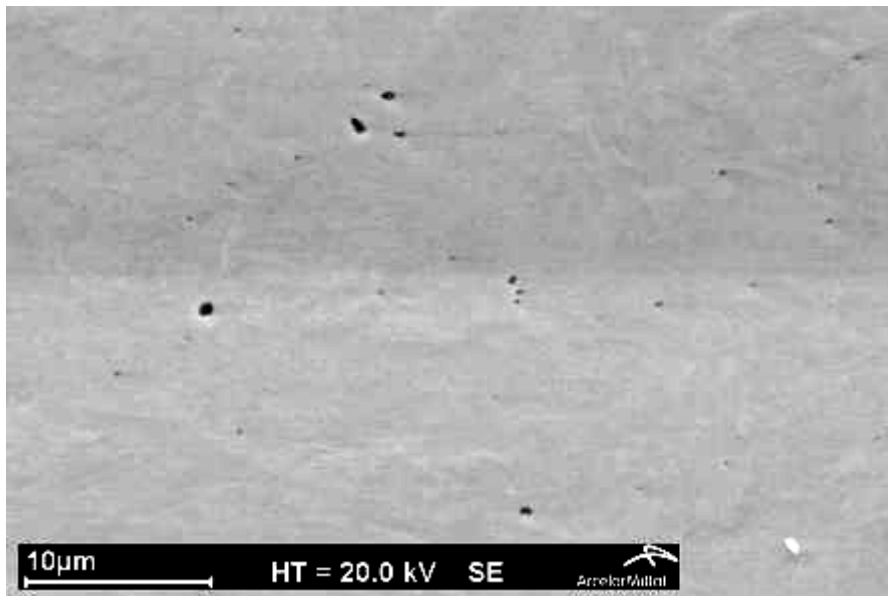


Figure 129: Edge cross-section microstructure after rolling. SEM.

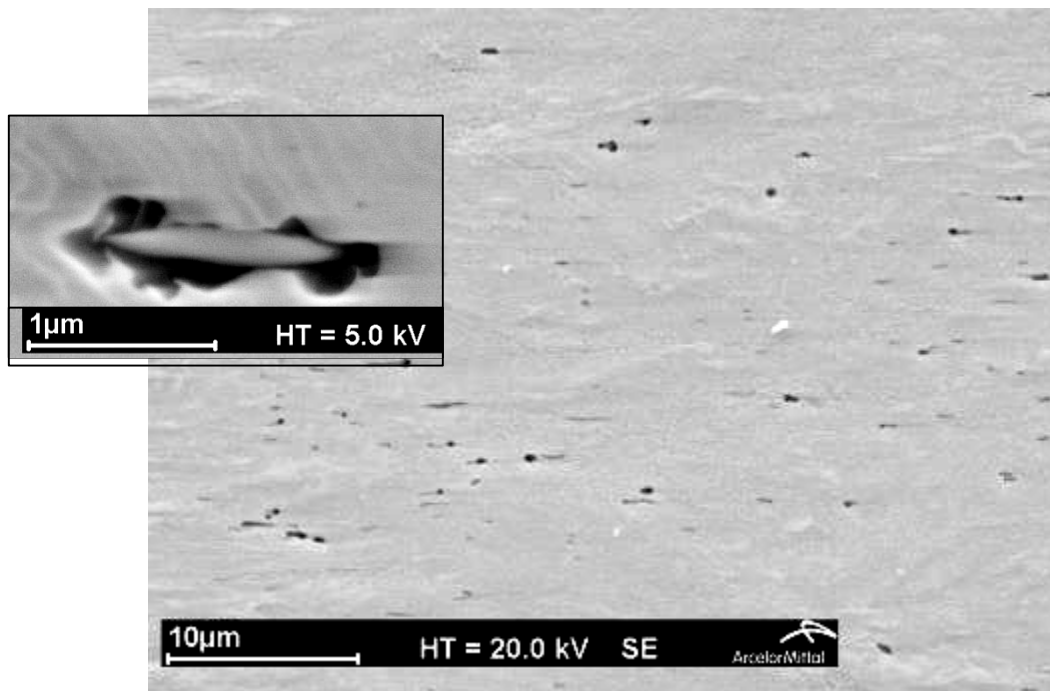


Figure 130: Core microstructure after rolling in cross-section – in the black frame: a zoom on a flattened deformable inclusion at the wire core. SEM.

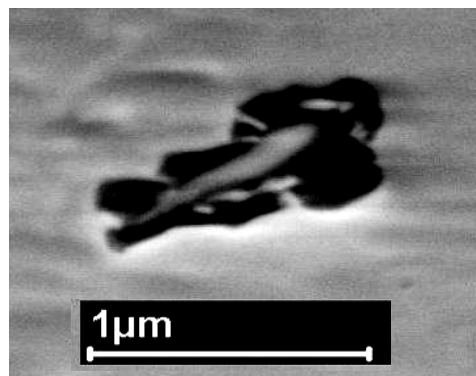


Figure 131: Orientation of a deformable inclusion in the right branch of the blacksmith cross after rolling in a cross-section. SEM.

Observation of non deformable inclusions is similar to those made in ultimate drawing. Indeed, transverse sections figures (Figure 132 and Figure 133) present non deformable inclusions with decohesion at the apex which extends along the longitudinal direction, as shown by micrographs in longitudinal view after ten ultimate drawing passes (Figure 118). But, the strain path change modified the extension modes of decohesions. As wire drawing is characterized by global tension along wire axis, decohesion extension follows the same direction. However, in rolling, since this process is defined by a global vertical compression with a significant transverse flow, the expansion of decohesion follows the transverse direction as observed in the Figure 132 and Figure 133.

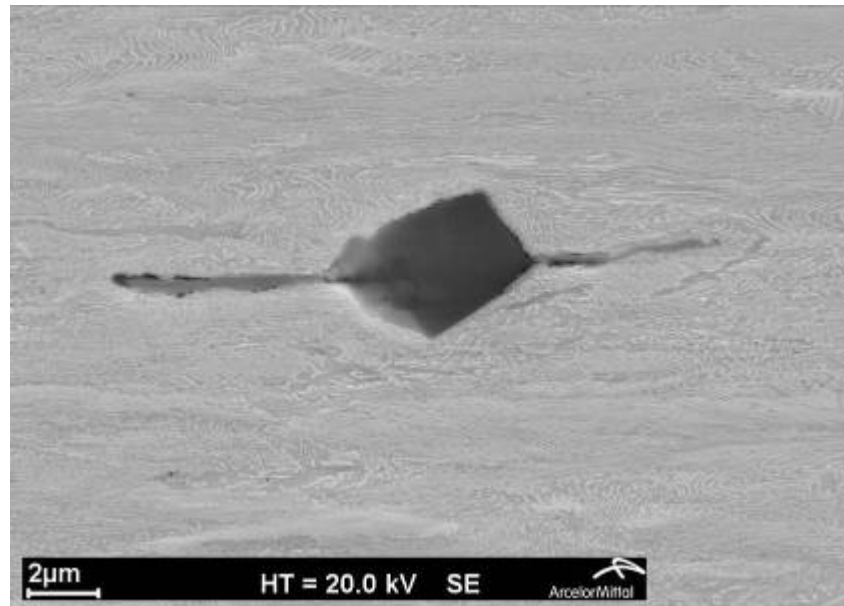


Figure 132: Decohesion and propagation at a complex inclusion apex after rolling in a cross-section. SEM.

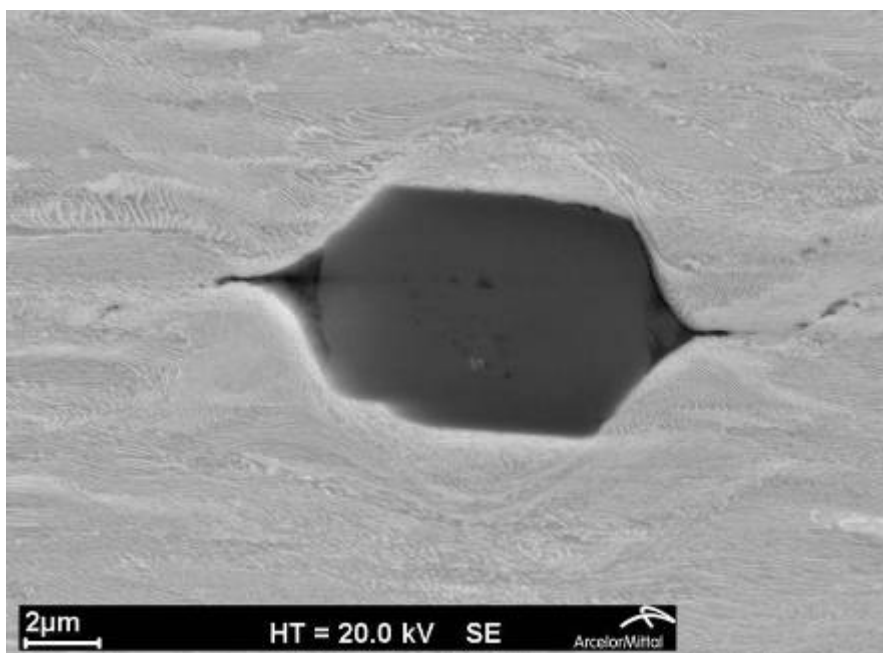


Figure 133: Decohesion and propagation at inclusion apex after rolling in a cross-section. SEM.

### V.3.3.2 Longitudinal cutting plane

In order to understand the three-dimensional evolution of cavities during rolling, it is essential to analyse SEM pictures in longitudinal view.

As for the microstructural study (see V.3.2), evolution of decohesion extension kinetics between the wire edge and the wire core presents a strong heterogeneity. Figure 134 and Figure 135 show the difference between the two locations. As strains are higher in the wire core, decohesions along deformable inclusions are more numerous, longer and more open in the core.

Finally, Figure 136 and Figure 137 confirm alignment of deformable inclusions with their decohesions, along the rolling axis, corresponding either to inclusion alignment or to multiple fragmentation of a single inclusion.

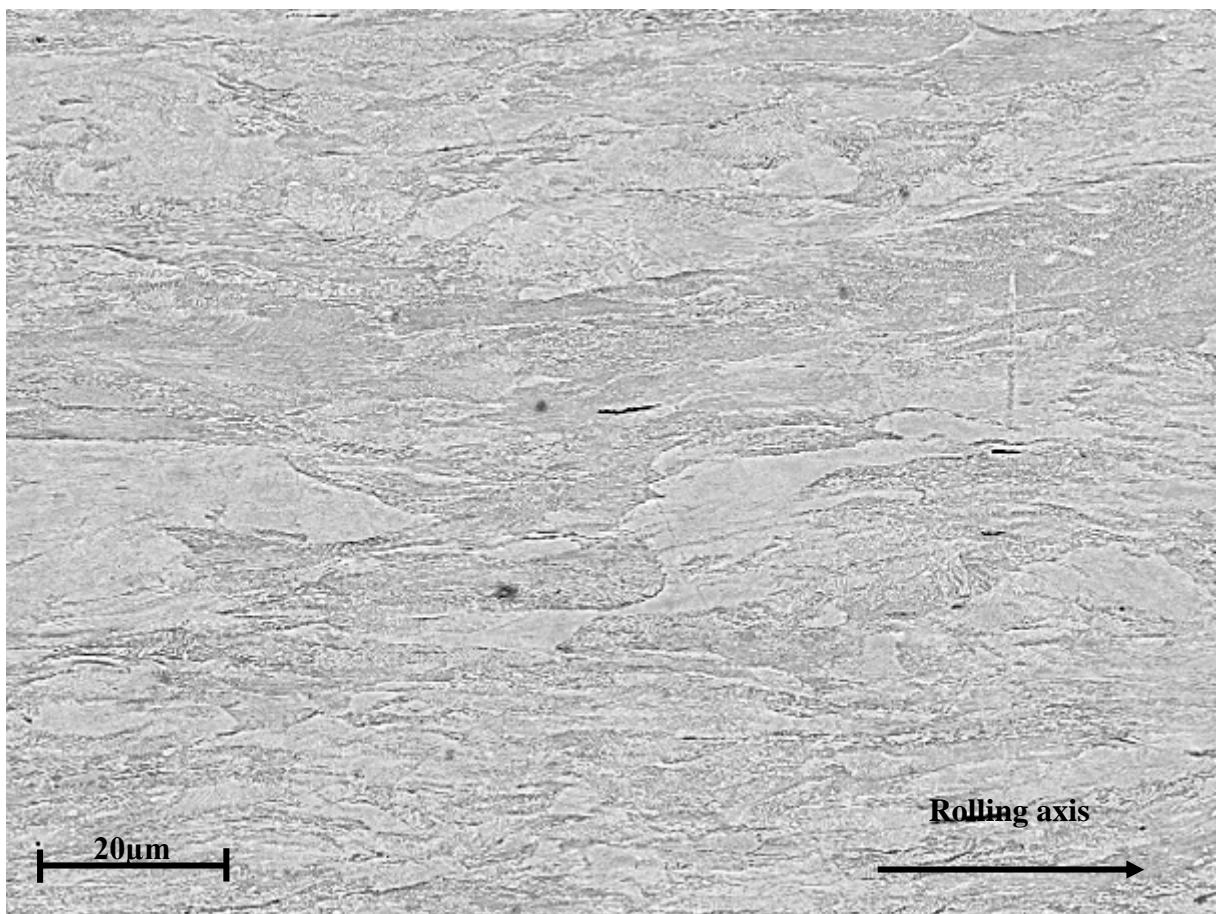


**Figure 134: Fine decohesions and cavities in the wire edge in longitudinal view (x 1k)**

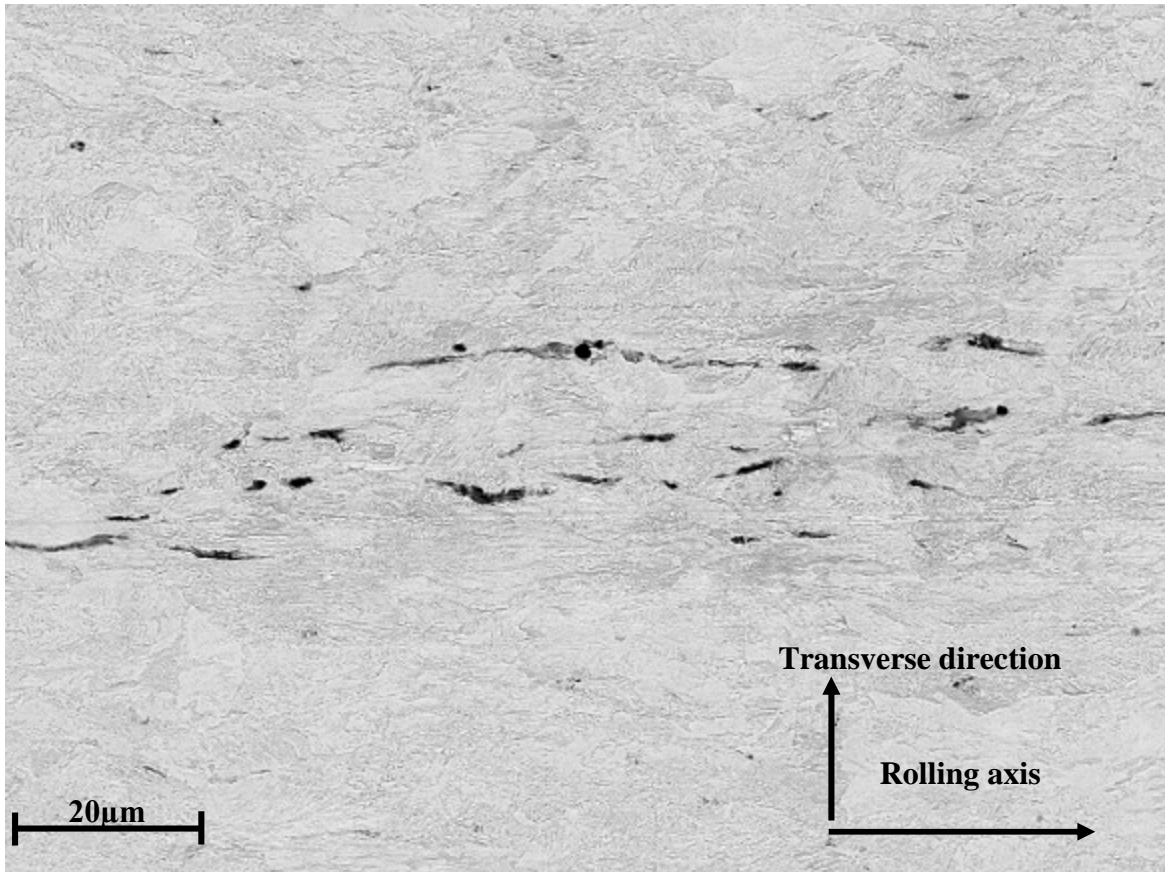


Figure 135: Thick decohesions and cavities in the wire core in longitudinal view. SEM

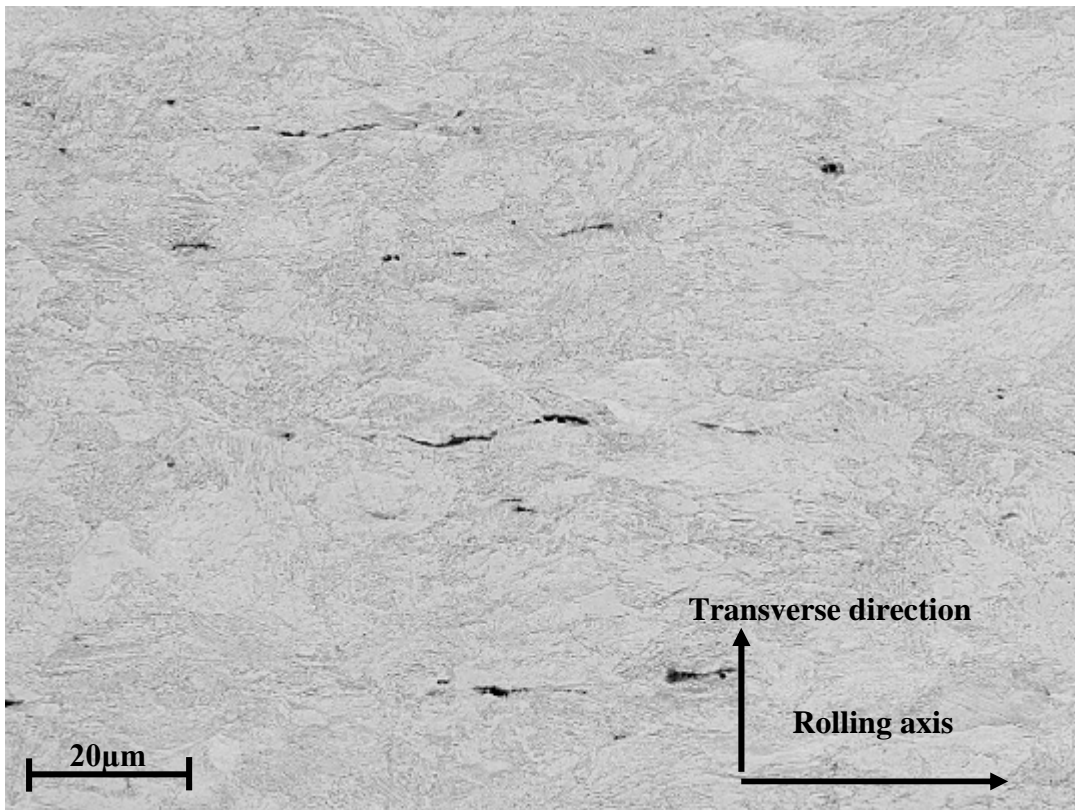


Figure 136: Inclusions and decohesion alignment along the rolling axis in longitudinal view. SEM.

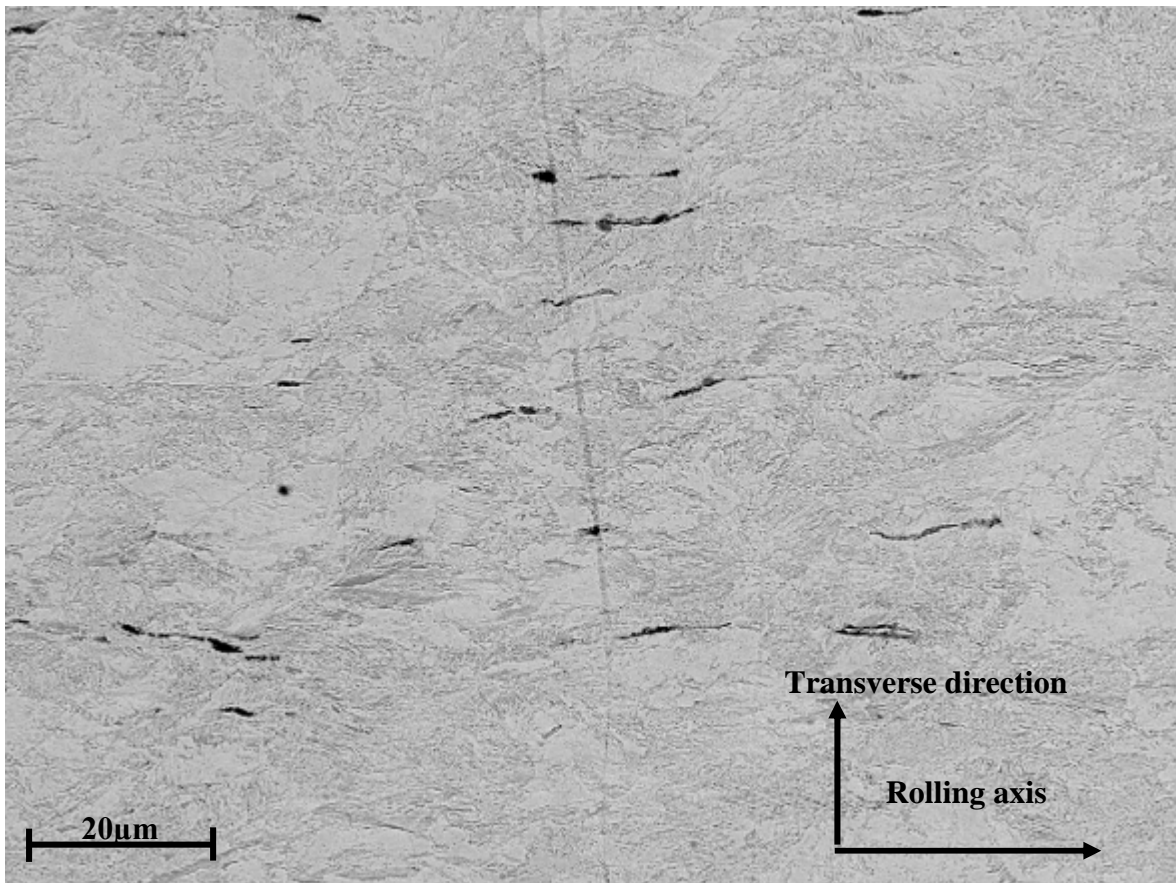


Figure 137: Inclusions and decohesion alignment along the rolling axis in longitudinal view. SEM.

## V.4 Schematic representation of damage at the end of rolling

### V.4.1 From experimental observations

In order to have a three dimensional view and to summarize the damage evolution during rolling, a 3D experimental sketch is presented in Figure 138, superposed on a strain map.

Some particular points need to be precised. Thus, to have more explanations on the experimental damage evolution during cold forming processes and to validate the schematic representation of deformable inclusions geometrical evolution, Forge® has been used to simulate the complete process (wire drawing followed by rolling) using spherical markers and visualize the strain component (and grain shape evolution).

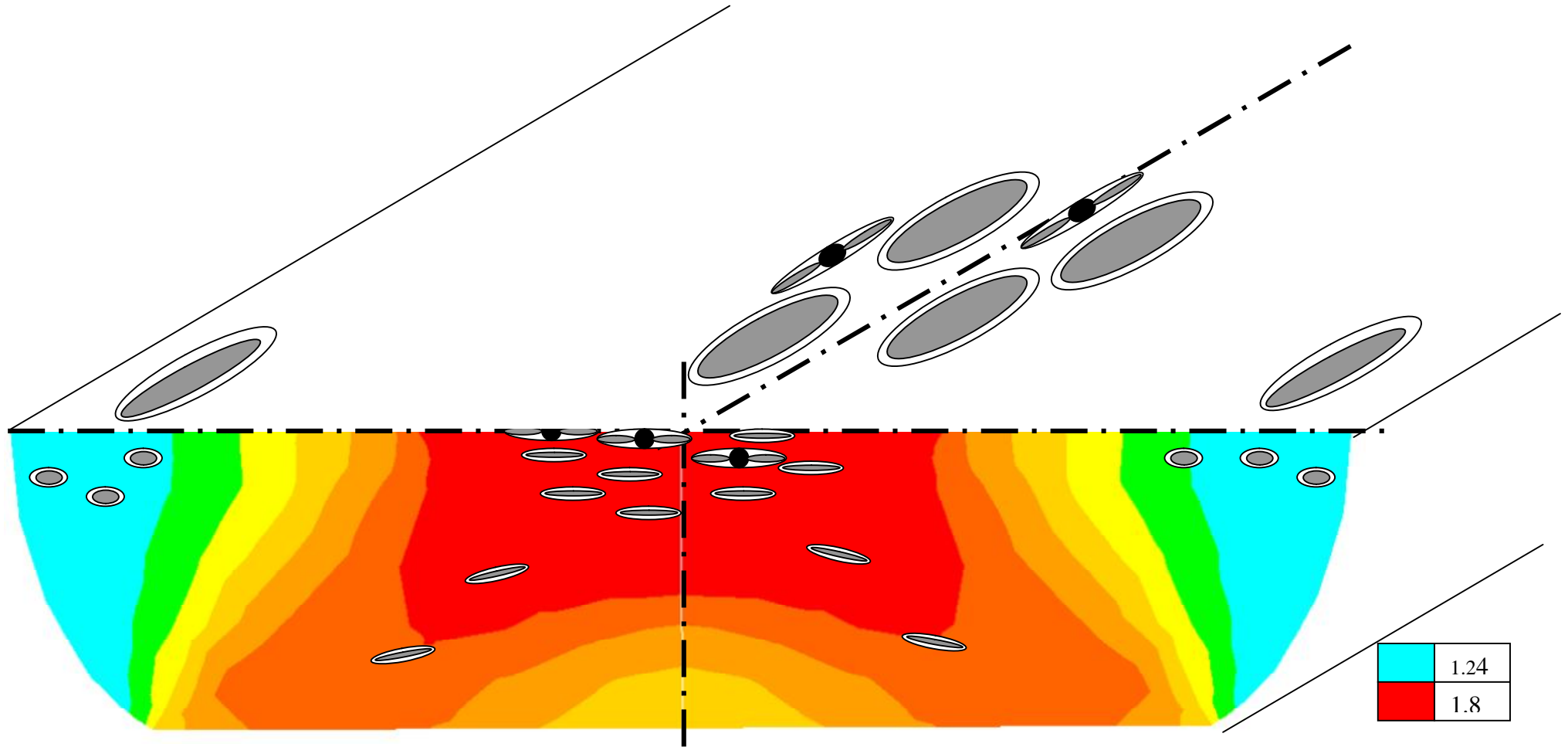


Figure 138 : 3D-sketch of the damage state at the end of rolling

## V.4.2 From process numerical simulation by using spherical markers

Five spherical markers have been placed in the wire as shown in Figure 139. Due to the symmetry of the processes, two symmetry planes are used and only one fourth of the processes is represented. Each marker has a diameter of 0.5mm. Note that these markers are much bigger than deformable inclusions, in order to give an easier visualization. The wire drawing and rolling axis correspond to the X direction. Evolution of spherical markers will be described by the length and the orientation of the a and b vectors, schematically represented in Figure 139.

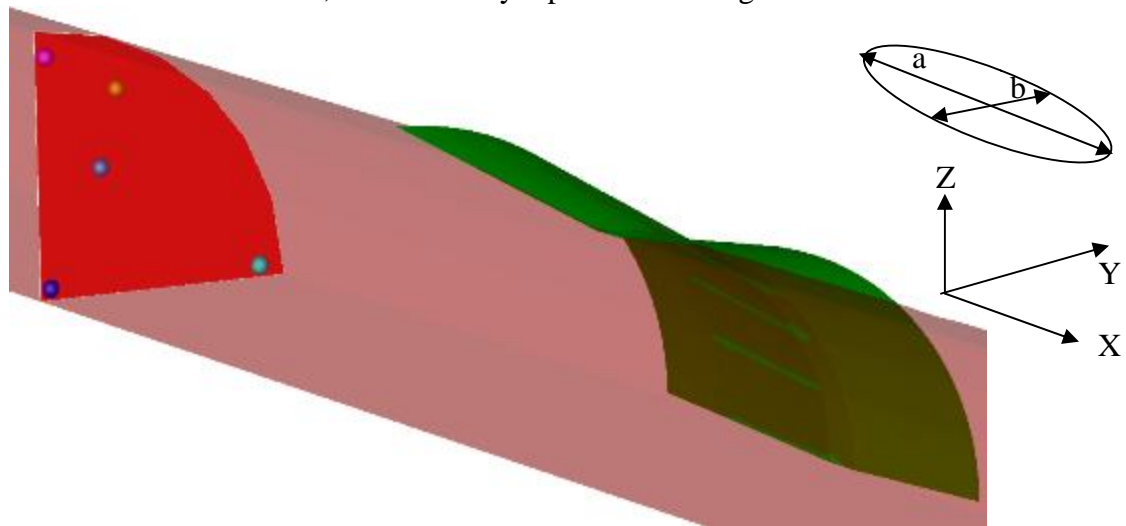


Figure 139: Spherical markers position before wire drawing

After drawing simulation, all the markers have been elongated in the drawing direction, as shown in Figure 140 and Figure 141. The length of the a-axis is 1.25mm and of the b-axis is 0.32mm. This corresponds perfectly to the cumulated reduction in wire drawing.

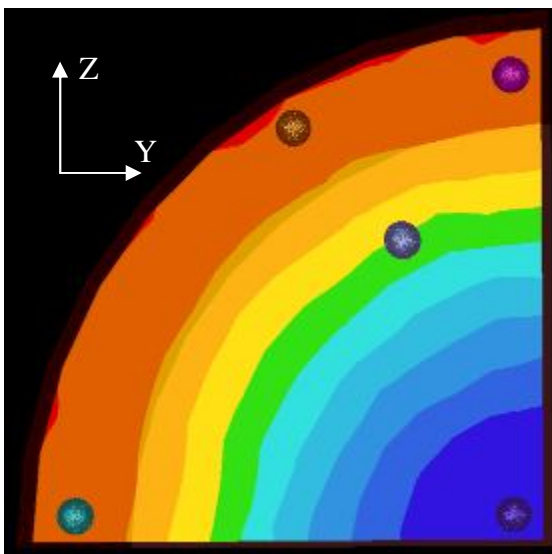


Figure 140: Superposition of the strain map in cross-section with the geometrical evolution of markers after wire drawing. Front view

$$(\bar{\varepsilon}_{\min} = 0.95, \bar{\varepsilon}_{\max} = 1.08)$$

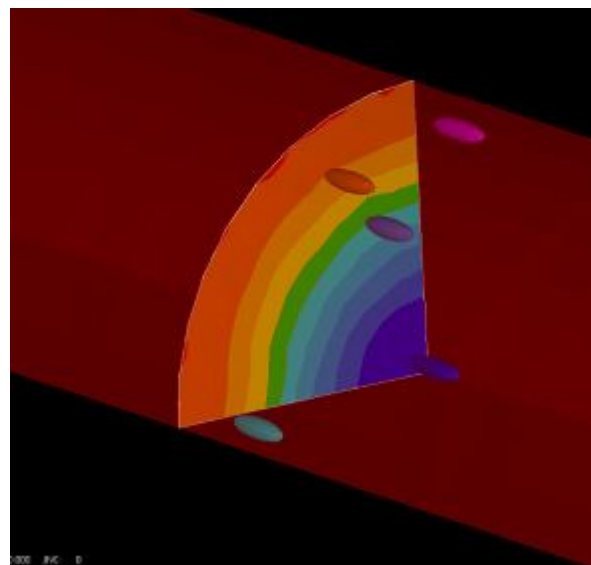


Figure 141: Superposition of the strain map in cross-section with the geometrical evolution of markers after wire drawing. Perspective view

$$(\bar{\varepsilon}_{\min} = 0.95, \bar{\varepsilon}_{\max} = 1.08)$$

Through the first rolling stand, comparison of the geometrical evolution of markers with the strain map in the core and at the edge can be also done. The result is shown in Figure 142 and Figure 143. In the wire core, where the strains are maximal, the marker n°5 is flattened, whereas in low strain area, flattening is less (marker n°1), or null (marker n°3) and only the X-elongation is visible. The X-elongation is the same for all markers and is very small (see below the X-elongation for marker n°4). In the blacksmith cross, b-axis of the markers n°2 and 4 rotates around the X axis. This rotation is explained by the YZ shear stresses shown in Figure 144. For the markers n°4, the geometrical evolution is as follows:

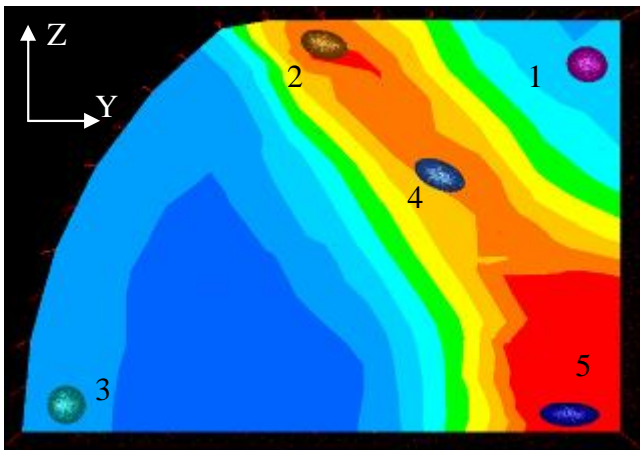
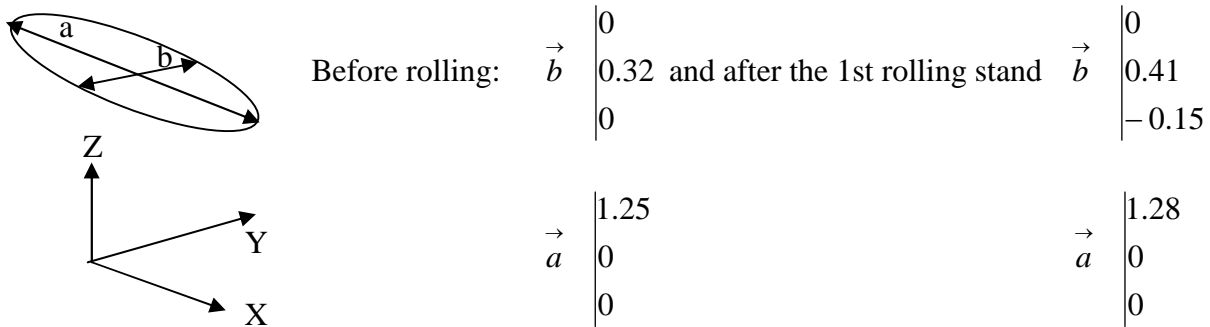


Figure 142: Superposition of the strain map in cross-section with the geometrical evolution of markers after the 1<sup>st</sup> rolling stand. Front view

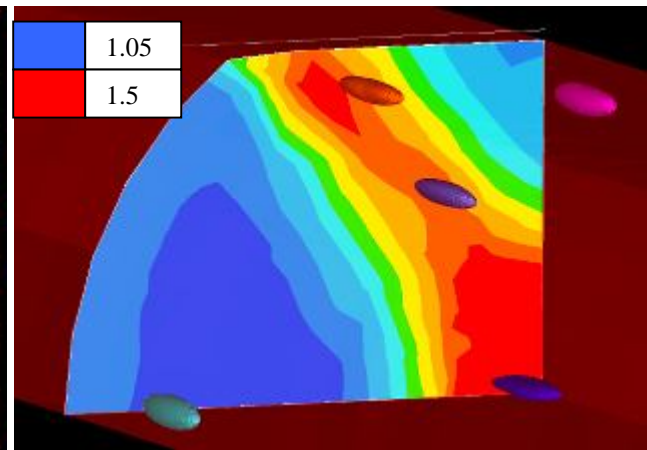


Figure 143: Superposition of the strain map in cross-section with the geometrical evolution of markers after the 1<sup>st</sup> rolling stand. Perspective view

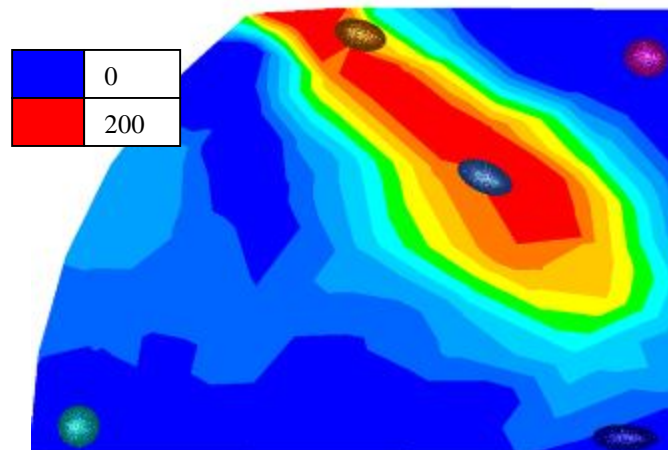
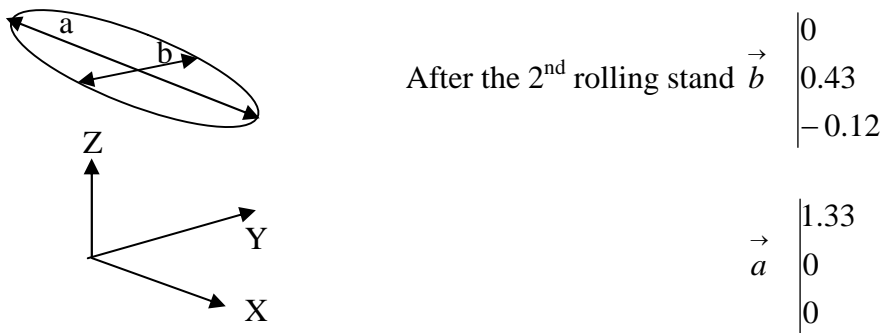


Figure 144: Superposition of the YZ shear stresses map (in MPa) in cross-section with the geometrical evolution of markers after the 1<sup>st</sup> rolling stand. Front view

After the second rolling stand, the X-elongation of all markers goes on as shown in Figure 145 and Figure 146. Markers n°1 and 5 are flattened further. For the marker n°3, only the X-elongation takes place. For the markers in the blacksmith cross, their evolution is detailed below:



The a-axis is elongated along the X-direction but the rotation of the b-axis is anticlockwise. This can be explained by small YZ shear stresses in the second stand as shown in Figure 147.

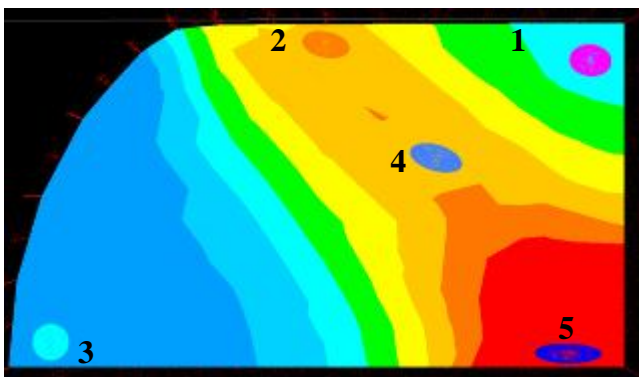


Figure 145: Superposition of the strain map in cross-section with the geometrical evolution of markers after the 2<sup>nd</sup> rolling stand. Front view

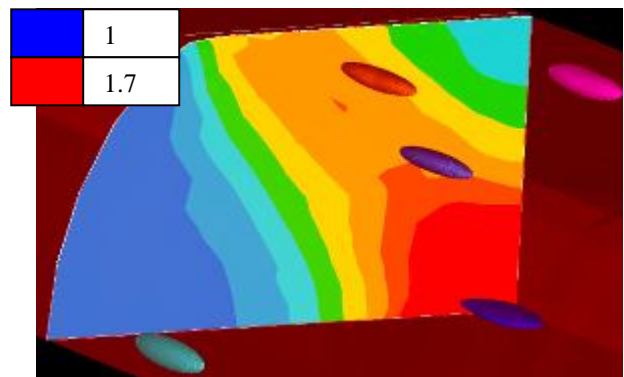


Figure 146: Superposition of the strain map in cross-section with the geometrical evolution of markers after the 2<sup>nd</sup> rolling stand. Perspective view

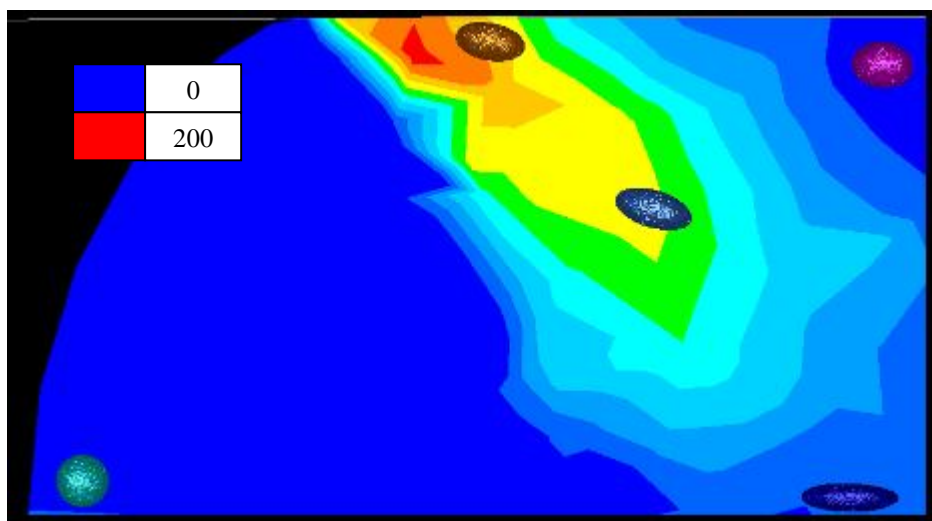
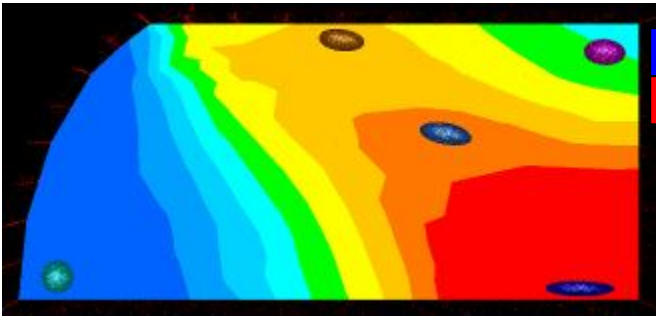
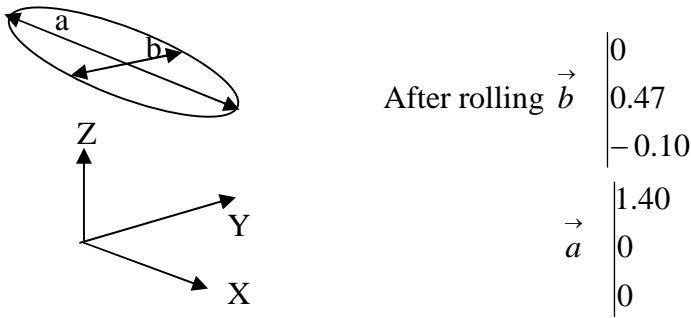
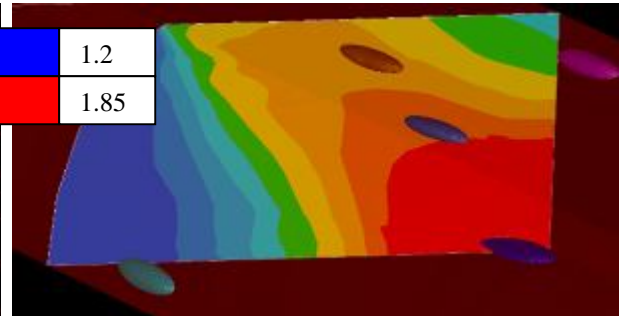


Figure 147: Superposition of the YZ shear stresses map (in MPa) in cross-section with the geometrical evolution of markers after the 2<sup>nd</sup> rolling stand. Front view

At the end of rolling, all tendencies observed in the second stand are confirmed and increased (Figure 148 and Figure 149):



**Figure 148: Superposition of the strain map in cross-section with the geometrical evolution of markers after rolling. Front view**



**Figure 149: Superposition of the strain map in cross-section with the geometrical evolution of markers after rolling. Perspective view**

After rolling, the flattening is as follows:

(Before drawing:  $z = 0.5$  mm and before rolling:  $z = 0.32$  mm):

Marker n°1:  $z = 0.24$  mm

Marker n°2:  $z = 0.2$  mm

Marker n°3:  $z = 0.3$  mm and  $x = 1.40$  for all markers

Marker n°4:  $z = 0.19$  mm

Marker n°5:  $z = 0.14$  mm

### V.4.3 Comparison between the two representations

Now, comparison between the numerical and experimental representation of the geometrical evolution of inclusions after rolling can be done and is shown in Figure 150. The numerical representation validates the different hypotheses linked to the geometrical evolution of deformable inclusions during wire drawing and rolling. It also clearly evidences the rotation of inclusions in the shear band of the blacksmith cross.

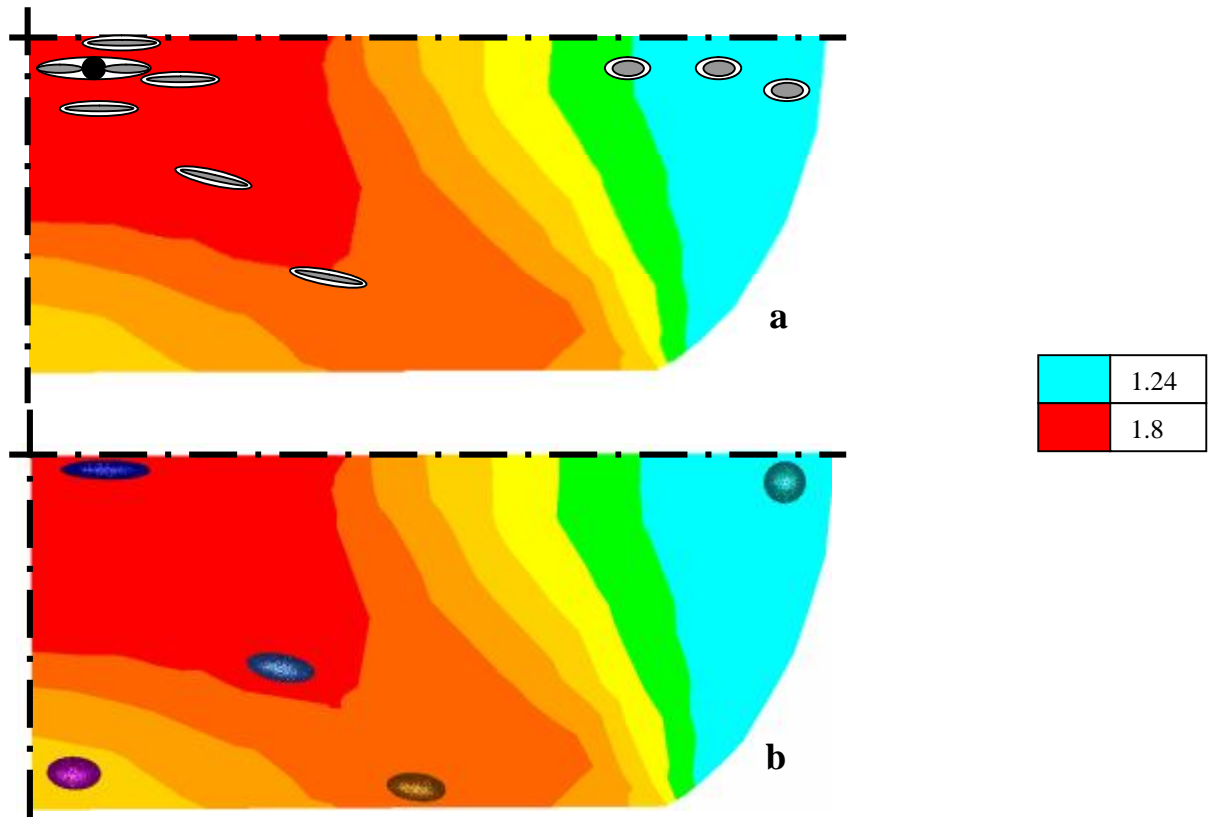


Figure 150: Comparison after rolling between a) the experimental schematic representation of damage and b) the numerical schematic representation of damage with markers, superposed to the strain map

## V.5 Damage prediction with finite element modelling

Forge2005® has been used to predict damage evolution. Lemaître's criterion has been used for this purpose. Its formulation has been described in section II.3.2.3.2 and the available one is used, which takes into account the crack closure effect, the cut-off value of stress triaxiality and the tension / compression damage asymmetry, as presented in section III.6 and mentioned again as follows:

$$\dot{D} = \begin{cases} 0 & \text{if } Triax < -1/3 \text{ or if } \bar{\varepsilon}_p \leq \varepsilon_d \\ \left(-\frac{Y}{S_0}\right)^b \dot{\varepsilon}_p & \text{if } Triax > -1/3 \text{ and if } \bar{\varepsilon}_p > \varepsilon_d \end{cases} \quad (\text{V.1a, b})$$

$$\text{with: } \begin{cases} Y = -\frac{\sigma_{eq}^2}{2E(1-D)^2} \left[ \frac{2}{3}(1+\nu) + 3(1-2\nu) \left( \frac{\sigma_H}{\sigma_{eq}} \right)^2 \right] & \text{if } Triax > 0 \\ Y = -\frac{h \sigma_{eq}^2}{2E(1-hD)^2} \left[ \frac{2}{3}(1+\nu) + 3(1-2\nu) \left( \frac{\sigma_H}{\sigma_{eq}} \right)^2 \right] & \text{if } Triax < 0 \end{cases} \quad (\text{V.2a, b})$$

$h = 0.2$  [96] ( $h=0$  means no damage in compression and  $h=1$  means same damage in compression as in tension),

$$\left. \begin{array}{l} S_0 = 5.23 \\ b = 3.14 \\ \varepsilon_d = 0.1 \end{array} \right\} \text{ These parameters have been identified in section III.6.3.}$$

For wire drawing simulation, a 3D modelling has been performed with previously identified Lemaître's parameters and results are shown in Figure 151. It shows that damage constantly increases during drawing to reach a mean damage value in the wire core of 0.085. By comparison with the triaxiality evolution during drawing (Figure 7 in section I.2.3.2), damage evolution seems consistent. From the fourth pass, damage becomes meaningful on the wire surface (mean damage surface value equal 0.065). Through the 1<sup>st</sup> rolling stand the mean damage value in the wire core is equal to 0.103, as illustrated in Figure 152, whereas the mean damage value on the wire surface is slightly higher and reaches 0.117 but seems again coherent with the triaxiality evolution presented in Figure 8. After the second rolling stand (Figure 153), only damage on the wire surface increases to reach 0.174 and corresponds to the triaxiality evolution depicted in Figure 8. Damage evolution after the last pass of rolling has the same tendencies, i.e. damage increases on the wire surface and reach a mean value of 0.25 but damage value in the wire core stay to 0.11. By comparison with Latham and Cockcroft's criterion (Figure 9, Figure 10 and Figure 11), which only localizes damage in the core, Lemaître's damage function highlights initiation of damage on edges.

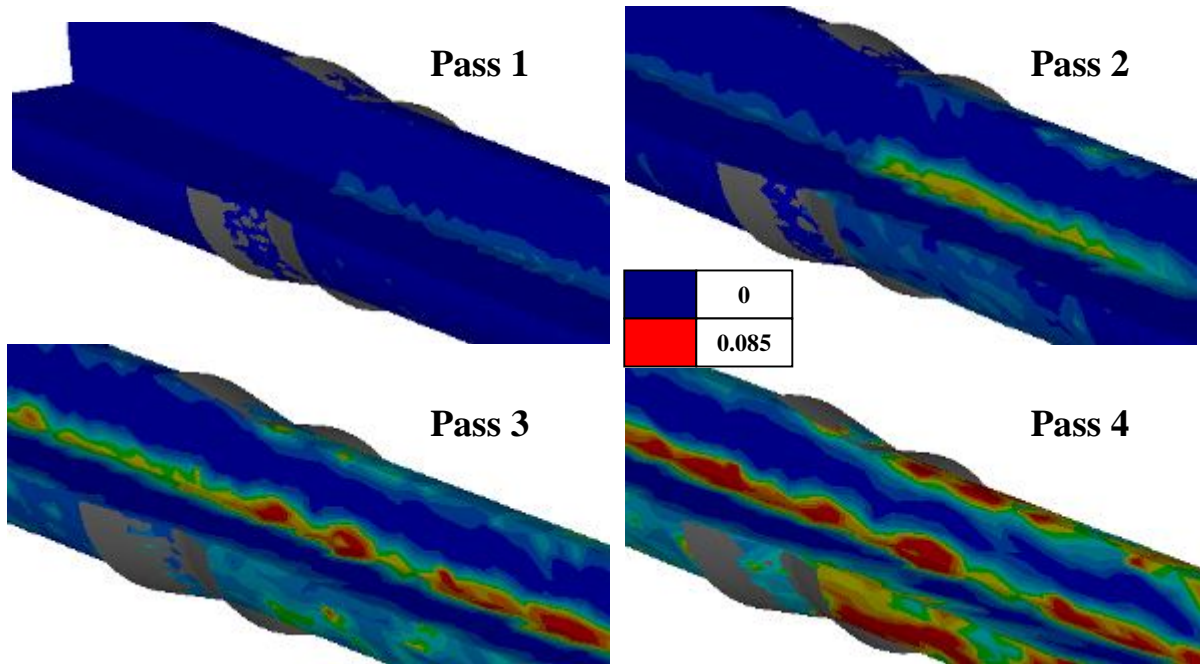


Figure 151: Damage evolution during wire drawing with Lemaître's criterion

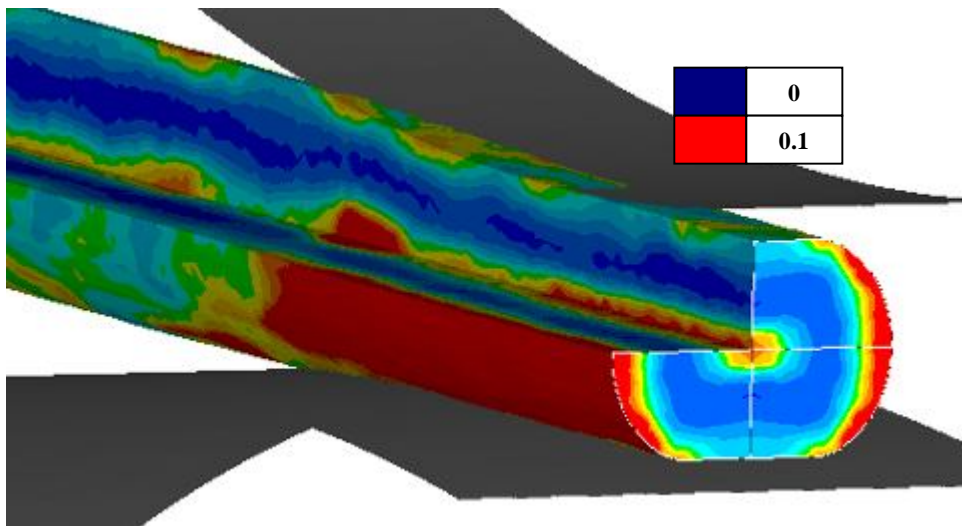


Figure 152: Damage evolution through the 1<sup>st</sup> rolling stand with Lemaître's criterion

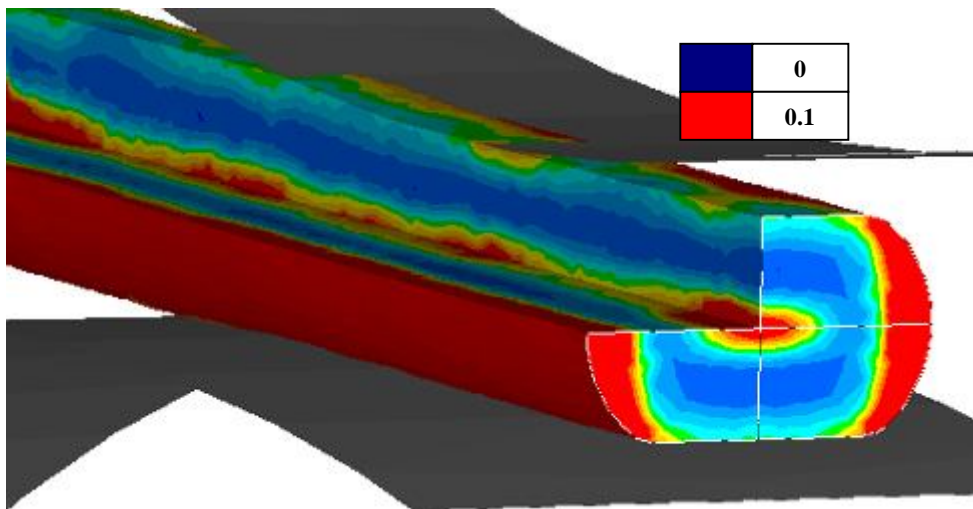


Figure 153: Damage evolution through the 2<sup>nd</sup> rolling stand with Lemaître's criterion

## V.6 Summary

In this chapter V, analysis of high carbon steel microstructure has been achieved. The aim was to:

- Understand the microstructural evolution of pearlitic steels during cold forming processes,
- Observe if this microstructure evolution can explain the mechanical anisotropy,
- Identify the first damage steps during wire drawing,
- Analyse the damage evolution during rolling.

Both scanning electron microscope (SEM) and transmission electron microscope (TEM), associated with a focused ion beam (FIB) for site-specific TEM sample preparation, have provided very interesting results. The use of the FIB was justified by two reasons. Firstly, this method enables to accurately choose the sample location in order to increase the probability of identifying damage site on TEM samples. Secondly, the atomic cutting of the FIB enables to have a pure surface without contamination by chemical reaction or polishing products.

After patenting, the microstructure of the wire is fully pearlitic without any specific orientation of the lamellae. To study the microstructural evolution and damage mechanisms during wire drawing, an experimental “ultimate drawing” has been performed in order to enhance microstructural and damage phenomena, which are hardly identifiable at the end of the real wire drawing process. During the ultimate drawing process, there is a very large elongation of the grains in the drawing direction; at the same time the interlamellar distance decreases dramatically for colonies initially oriented along the drawing axis. Many more pictures would be necessary in order to carry out a statistical evolution of the interlamellar spacing. This microstructural alignment explains the mechanical anisotropy highlighted previously, as well as a crystallographic texture (shown in the bibliography review in the paragraph II.1.2.1).

During rolling, the microstructural anisotropy, caused by the wire drawing, is stopped. This rolling process is not severe enough to fully orient pearlitic colonies since the lamellae orientation remains random. The strain heterogeneity of rolling (blacksmith cross) leads to different microstructures between the edge and the wire core. The length / width ratio changes between the core and the wire edge. The transverse cut presents flattened grains caused by the vertical compression. This flattening is larger in the wire core, where strain is maximal. In a longitudinal cut, the grain elongation in transverse direction is similar at the edge and in the wire core.

In terms of damage, the strong orientation and the cementite lamellae elongation, introduced by drawing, can lead to the occurrence of defects in sensitive areas such as inclusions and grain boundaries. The first signs of damage are observed around inclusions, thanks to TEM pictures, after the 4<sup>th</sup> drawing pass. Damage initiation mechanisms around inclusions are different between non-deformable and deformable inclusions since they have not the same behaviour during deformation. However, the damage propagation step is identical in both cases, some decohesions have been found to propagate along the cementite / matrix interface in the solicitation direction. In addition, a few cavities, due to the breakage of some cementite lamellae, were observed after 10 and 15 drawing passes. These defects are caused by the disorientation of some pearlitic colonies with the drawing direction.

From drawing to rolling, damage propagation kinetic changes because of the strain path modification. A stronger cavities and inclusions density is observed in the wire core and these inclusions flatten in a transverse cut whereas they are not flattened at the wire edge. Decohesion at the matrix / inclusion interface is strongly marked and homogeneous in case of deformable inclusions. These inclusions and their decohesions remain aligned along the rolling axis. For non deformable inclusions, a change in the decohesion propagation direction is observed, with decohesions in transverse direction. We can summarize by saying that decohesions appear in the direction where solicitation is imposed. Indeed, in wire drawing, the main solicitation is a tensile stress and longitudinal decohesion are thus observed. In rolling, a compressive stress is applied, so a transverse tensile effort is applied and transverse decohesion take place. Because of this, lamellae orientation in the vicinity of an inclusion is secondary and do not seem to affect decohesions propagation kinetics. Moreover, no damage due to the rupture of cementite lamellae has been observed. Rolling is not enough severe to lead to these phenomena. Finally, this high carbon steel exhibits a high number of cavities (mainly located in the wire core) aligned, with their inclusions, along rolling axis. Their decohesions have not yet coalesced, but if it happens, this will lead to fracture.

The use of simulation brings further information, in terms of geometric evolution of deformable inclusions and damage prediction. The inclusions rotation during rolling has been explained by the shear stresses. Cold forming processes simulation with damage predicts a increasing of damage in the wire from drawing to the first rolling stand and then stops, whereas damage on the wire surface increase from the end of drawing to the end of rolling and reach a higher value than in the wire core.

It must be emphasized that the states of stress and strain are rather favourable against crack propagation. In wire drawing, an elongated cavity is formed but the only tensile stress and elongation strain are along its length and compression in the direction normal to its axis. So it elongates, but not propagates. Similarly in rolling, these cavities are flattened but the

stress normal to the lips is compressive, whereas tensile stress (transverse eg) is in a direction which may not propagate. This is why a locally high density of microvoids may be found without coalescence and macroscopic crack initiation: these microvoids expand at the same rate as the matrix, they do not propagate strictly speaking (by a stress normal to the lips).

## V.7 Résumé français

Une analyse microstructurale des aciers haut carbone a été réalisée, dont son but était de :

- Comprendre l'évolution microstructurale des aciers perlitiques au cours des procédés de mise en forme à froid,
- Justifier l'anisotropie mécanique par l'évolution microstructurale,
- D'identifier les premières étapes de l'endommagement au cours du tréfilage,
- D'analyser l'évolution des mécanismes d'endommagement au cours du laminage.

Pour atteindre ces objectifs, la microscopie électronique à balayage (MEB) et en transmission (MET), associée à un faisceau d'ions focalisés (FIB) pour la préparation de lames minces, ont été utilisées. Le choix d'un FIB a été dicté par deux raisons. La première est la possibilité de pouvoir choisir le lieu de prélèvement de la lame mince afin d'augmenter les chances d'observer des traces d'endommagement au MET. La seconde raison est l'obtention d'une surface saine de toute contamination, qui pourrait rendre l'interprétation des observations difficile.

Après le patentage, la microstructure est perlitique avec une orientation aléatoire des grains. Afin d'étudier l'évolution microstructurale, ainsi que les mécanismes d'endommagement au cours du tréfilage, un tréfilage ultime a été réalisé afin d'exacerber tous les phénomènes difficilement identifiables en fin de tréfilage industriel. Concernant l'observation de la microstructure, nous avons pu vérifier au cours du procédé de tréfilage une orientation et un allongement des lamelles de cémentite dans le sens du procédé, ainsi qu'une diminution de l'espace inter lamellaire. Cependant nous ne disposons pas, à travers nos observations, d'informations suffisantes pour déterminer quantitativement ces phénomènes. Cette orientation explique en partie l'anisotropie mécanique observée précédemment, ainsi qu'une orientation cristallographique préférentielle seulement comme mis en évidence dans le chapitre bibliographique.

Lors du passage du tréfilage au laminage, l'anisotropie microstructurale (alignement des lamelles de cémentite) causée par le tréfilage, est stoppée. Ce laminage n'est pas assez sévère pour tout orienter puisque l'orientation des lamelles est encore très aléatoire. Par contre le laminage entraîne la rupture d'un grand nombre de lamelles. L'hétérogénéité de déformation du laminage (« croix du forgeron ») engendre une microstructure très différente entre le cœur et le bord du plat avec des ratios longueur sur largeur de grain nettement différents. La coupe transverse présente des grains aplatis par la compression verticale que le laminage impose. Cet écrasement est plus important à cœur, là où les déformations sont les plus fortes. En coupe longitudinale, les grains s'allongent dans la direction transverse de manière similaire que ce soit au cœur ou sur les bords.

En ce qui concerne l'endommagement, la forte orientation, ainsi que l'allongement des colonies perlitiques, introduits par le tréfilage, peut mener à l'apparition de défauts dans des zones préférentielles telles que les joints de grains et de colonies et autour des inclusions. Des premiers signes d'endommagement ont pu être identifiés autour d'inclusions après la 4<sup>ème</sup> passe de tréfilage, grâce à des images MET. Les mécanismes d'amorçage de l'endommagement sont différents en fonction du comportement des inclusions vis-à-vis de la déformation (différence entre des inclusions déformables et non déformables). De plus, quelques cavités, causées par la rupture des lamelles de cémentite, ont été observées après les passes 10 et 16 du tréfilage ultime. Celles-ci sont dues à orientation initiale des colonies perlitiques non favorables vis-à-vis de la direction de tréfilage.

Au laminage, les cinétiques de propagation de l'endommagement sont modifiées à cause du changement de chemin de déformation. Une densité plus forte de cavités et d'inclusions est observée à cœur. Celles-ci s'aplatissent à cœur dans un plan transverse mais restent sphériques sur les bords. Les décohésions à l'interface matrice / inclusion sont très marquées et restent alignées selon l'axe de laminage. Dans le cas d'inclusions non déformables, nous observons un changement dans la direction de propagation des décohésions avec des décohésions en sens transverse. Nous pouvons résumer en disant que les décohésions apparaissent dans le sens où l'effort est imposé. En tréfilage, l'effort est un effort de traction, nous observons donc des décohésions longitudinales. Alors qu'en laminage, le champ de vitesse est majoritairement transverse, ce qui va modifier l'orientation et la forme des décohésions : on parle alors de transport. De ce fait, l'orientation des lamelles au voisinage d'une inclusion est secondaire et ne semble pas affecter les cinétiques de propagation des décohésions. Je n'ai observé aucun cas d'endommagement dû à la rupture de lamelles de cémentite. Le laminage n'est pas assez sévère pour aboutir à ces phénomènes rencontrés à partir de la 10<sup>ème</sup> passe de tréfilage ultime.

L'utilisation de la simulation avec un critère d'endommagement permet d'apporter des informations supplémentaires. La rotation des inclusions déformables au cours du laminage est expliquée par la présence de cisaillement (croix de forgeron) principalement en 1<sup>ère</sup> cage de laminage. Le critère d'endommagement de Lemaître prédit un endommagement à cœur et en surface. L'endommagement à cœur augmente de manière constante au cours du tréfilage jusqu'en 1<sup>ère</sup> cage de laminage puis elle stagne. Alors qu'en surface un endommagement significatif apparaît en fin de tréfilage puis augmente jusqu'à la fin du laminage pour atteindre une valeur plus élevée qu'à cœur.

Pour conclure, il faut noter que l'état de contraintes et de déformation est plutôt favorable contre la propagation de fissures. En tréfilage, une cavité allongée est créée mais la seule

contrainte tensile, ainsi que les déformations se font dans le sens de sa longueur et la compression dans une direction normale à son axe. Donc elle s'allonge mais ne se propage pas. Pareillement, en laminage, ces cavités sont aplaties mais la contrainte normale aux lèvres est compressive, alors la contrainte de traction (contrainte transverse) est dans une direction qui ne doit pas propager. C'est pourquoi, localement, une très forte densité de microcavités peut être trouvée sans coalescence ni formation de macrofissures : ces microcavités s'étendent au même taux que la matrice, elles ne propagent pas (par une contrainte normale aux lèvres).

# Chapter VI Optimization

After having:

- identified the material behaviour,
- simulated its deformation along cold forming processes,
- and studied its microstructure and damage mechanisms evolution during the two processes,

the last major issue concerns process optimization. All the information previously acquired will be used in order to propose improvements in terms of dies geometry.

The present work focuses on better understanding of cold forming processes and damage mechanisms. Thus, in this chapter, a damage criterion will be used as the objective function to optimize the wire drawing process. In order to perform efficient optimizations, a rigorous strategy must be used. Thanks to this methodology, the problem will be correctly defined. Thus the first part of this section concerns a short presentation of this optimization strategy, introducing the different optimization algorithms. Then, the following section explains the choice of the optimization method and how it works. Finally, the last section deals with wire drawing optimization.

## VI.1 Optimization strategy

In his thesis, M. Bonte [123] presents a very interesting methodology to solve optimization problems. He proposes a 3-step method in order to optimize metal forming: modelling, selection and resolution. It can be summarized in the following chart (Figure 154).

### VI.1.1 Modelling

As shown in Figure 154, the first step can be decomposed in four points. This rigorous procedure is aiming at well defining the problem in order to make the resolution easier.

### VI.1.1.1 Choice of the optimization situation / reference configuration

First, the reference situation must be defined, i.e. what is optimization meant for? Three different possibilities appear which depend on the number of optimization parameters, their variation range and the expected accuracy for the desired solution:

- Parts design
- Processes design
- Production

Thus, optimization helps either to create a new product or process, or to improve an existing process. The latter is of interest here, since the manufactured goods are already in production.

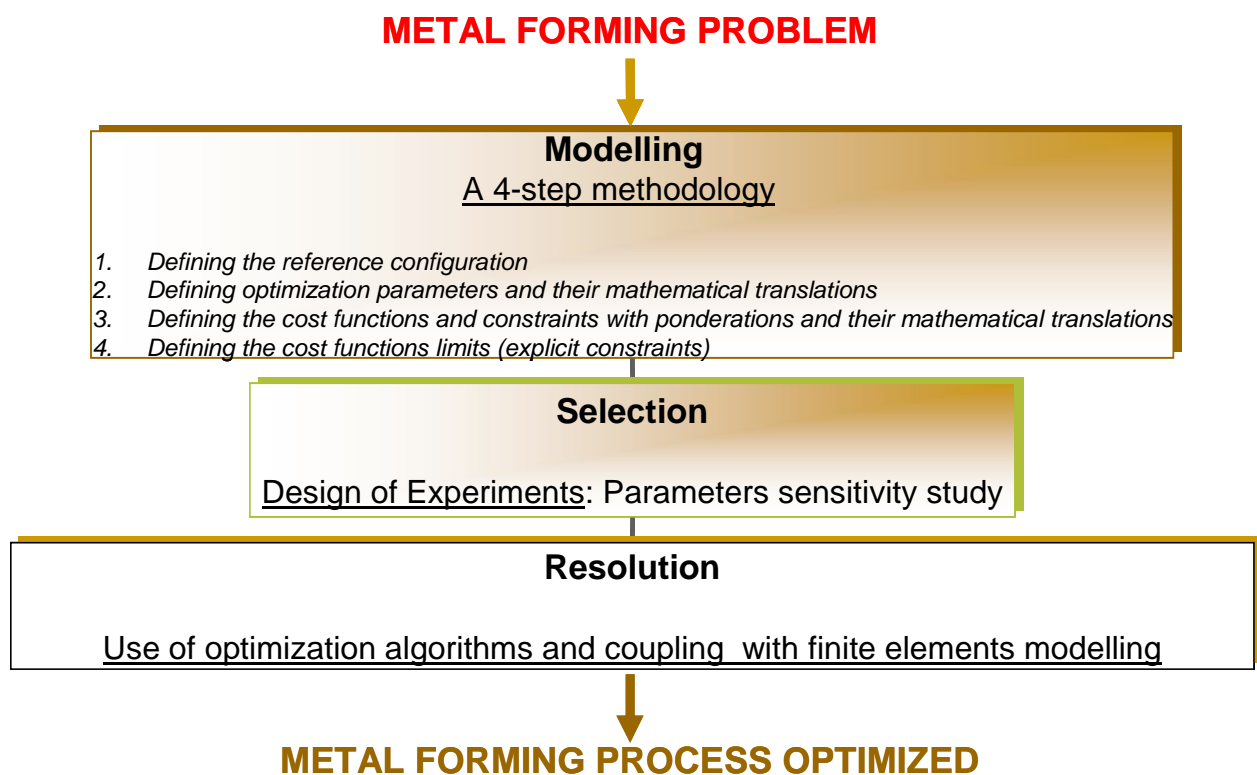


Figure 154: Optimization strategy for metal forming processes (from [123])

### VI.1.1.2 Choice of optimization parameters and their mathematical translations

Many parameters may be optimized: steel grade, entrance or final drawn wire diameter, number of passes during wire drawing and rolling, drawing dies geometry (entrance die semi-angle, land length), roll geometry... Optimizing all parameters would be far too complex. A few essential parameters will be selected, which will be introduced later. The mathematical translation consists in defining the associated variables (design variables) of such parameters, for instance through the parameterization of the tool geometry.

### VI.1.1.3 Choice of objective functions and constraints and their mathematical translations

An optimization problem consists in minimizing a function  $\Phi$  of parameters  $p$ , named *objective function* and is formulated in the following way:

$$\begin{cases} \text{Min } \Phi(p) \\ c_i(p) \leq 0 \quad \forall i = 1, \dots, m_i \\ h_i(p) = 0 \quad \forall i = 1, \dots, m_e \\ p \in \mathfrak{R}^n \end{cases} \quad (\text{VI.1})$$

where  $c_i$  are inequality constraints and  $h_i$  equality constraints.

Generally, the optimization parameters belong to explicitly defined intervals that can also be considered as explicit constraints, see VI.1.1.4. Implicit constraints are associated with objective functions as they are not known in advance but have to be satisfied as well. Differences between explicit and implicit constraints are schematized in Figure 155.

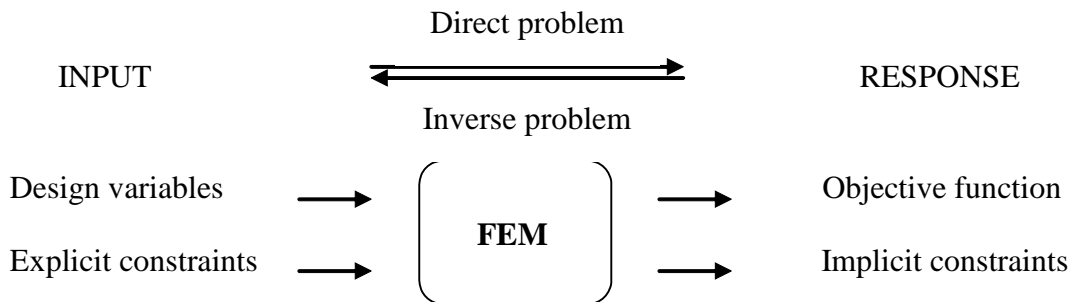


Figure 155: FEM and optimization (from [123] and [124])

In a case of multi-objective optimization, the different objective functions can be combined into a single one by introducing weights in order to give more or less importance to one objective function with respect to the others.

In our industrial case, the considered objective and constraint functions are: geometry, final mechanical properties, dies life time and damage. Each can be defined either as an objective function or as a constraint. For instance, an implicit constraint can be defined as an upper or lower bound of the strength ( $Rm_{\min} < Rm < Rm_{\max}$ ).

The mathematical translation, as in the previous section, consists in giving a mathematical form to objective functions.

### VI.1.1.4 Definition of parameters limits

These limits are also called explicit constraints because they are often linked to the initial form of the product and no numerical simulation is required to determine them. Parameters limits will give the variation range of the process parameters.

### **VI.1.2 Selection**

The second step after modelling concerns the selection, i.e. an effort to reduce the number of objective functions and parameters, and therefore the computational cost, by selecting the most relevant ones. This choice depends on industrial requirements and is based on process knowledge: a given parameter can be very interesting in itself, but have no influence on the minimization of the objective function.

Consequently, this section is based on parameters sensitivity studies. The best-known method to reach this goal is Design of Experiment (DOE). In some cases, DOE will also help the algorithms to find the optimum solution, by speeding up the convergence. Typical DOE plans are factorial designs [124] - [126] and will be explained below.

In complex problems, this step is a major point involving the concept of multi-objectives, as well as multi-parameters.

### **VI.1.3 Resolution**

The last stage of this optimization strategy is obviously the problem resolution by the use of adequate optimization algorithms. Since the 50's, a high number of methods have been developed and improved. In the next section, a chronological review of these methods is made. This overview will guide the reader to the solution chosen for this thesis.

## **VI.2 Optimization methods and their applications to metal forming processes**

Optimization methods can be classified in four main categories:

- Gradient-based algorithms
- Global algorithms
- Approximate algorithms
- Hybrid and combined optimisation algorithms

### **VI.2.1 Gradient-based algorithms**

Gradient-based algorithms belong to the family of deterministic algorithms. The best known are conjugate gradient, SQP, BFGS ... With them there is a direct coupling between the FEM calculation and the optimization algorithm, i.e. each iteration corresponds to one (or several) FEM evaluation(s). In metal forming optimization, these algorithms can be time

consuming because they have a sequential nature that prevents parallel FEM evaluations. The second disadvantage concerns the optimum solution: with these iterative algorithms, there is a risk to be trapped in a local optimum (unless using a more recent algorithms based on the Moving Asymptotes, for instance). The main advantages comprise the fact that they are well-known and widely spread, and their convergence is fast if the relevant derivatives are properly computed, even for a large number of parameters.

Thus, they have often been used in the past in metal forming processes optimisation. Two examples of applications are of interest for this work; they deal with extrusion. Extrusion is a process not so far from wire drawing. Two authors [127]-[128] use this type of algorithm to optimize the die geometry, with extrusion force and die life as objective functions. Another author used the SQP method to optimize the die geometry (semi-die angle and reduction) in multi-step drawing by minimizing the forming energy [129].

Moreover, they are very efficient to find a local optimum within only a few iterations. For a complete presentation of this type of algorithms see [130].

## **VI.2.2 Global algorithms**

The second category of algorithms concerns the evolutionary algorithms, which can be also called global algorithms. They mimic natural selection mechanism from Darwin's evolution theory. Like the biological evolution, these algorithms are based on selection, recombination and mutation to find the optimum. They are called global algorithms because they tend to find a global optimum and they are now widely used in complex metal forming applications (see Table 15) due to their robustness. The main drawback is the high computational cost as they generally need several thousands function evaluations to find a global extremum. Indeed, these algorithms slowly converge because:

1. they have no information about the gradient
2. additional time is spent to be sure not to fall in a local extremum

Evolutionary algorithms appeared in the sixties' and four categories can be distinguished as shown in Figure 156. Evolution strategies (ES) typically consist in three main operators: selection, recombination and mutation. Although they seem similar to Genetic Algorithms (GA), some differences appear. Mutation is the main genetic operator while recombination is not systematically used. In general, ES can more rapidly find a solution, whereas GA would find a more global extremum. However, the requirements of both ES and GA are usually quite high in terms of function evaluations. More information on each category can be found in [131]- [134].

For our applications, several authors used genetic and evolutionary algorithms for hot rolling application [135]-[138]. They used a multi-objective approach to optimize both billet geometry and mechanical properties. A multi-objective approach consists in taking several objective functions into account, and the algorithm looks for the best parameter set that satisfy all the objective functions. Most of the time, the objectives are conflicting, so there exists several optimal parameters that belong to a set, the Pareto's set. This best parameters set can be plotted in the objective functions space, and the corresponding graph is called the Pareto's front [139] and [140], which comes from W. Pareto, an Italian economist and sociologist who is well-known for his observation of 20% of population owning 80% of the wealth. For instance, a typical Pareto's curve is presented in Figure 157, for two objective functions  $f_1$  and  $f_2$ . Each point on the curve corresponds to an optimal parameter set. It is the responsibility of the user to choose one set depending on the importance he wants to give to each objective function. This evolutionary method gives good results but, as mentioned before, a high number of evaluations is required: between 500 and 1000 evaluations in the papers mentioned.

Forming Process	Objective	Design variables
Deep drawing	Maximise distance to FLC	Die geometry
Hydroforming	Maximum expansion	Pressure load path Axial displacement load path
Hydroforming	Minimise inertia variations No necking (thinning) No wrinkling (thickening)	Pressure load path Axial displacement load path
Forging	Minimum folding Minimum energy	Initial geometry
Forging	Maximise forging quality Minimise forming energy Minimise folding potential	Preform geometry
Forging	Minimum energy Minimum shape deviation	Tool geometry

Table 15: Overview on the optimization of metal forming processes using evolutionary algorithms [123]

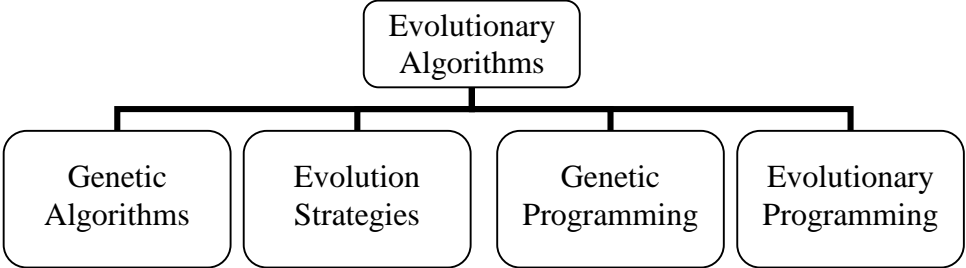


Figure 156: Main categories of evolutionary algorithms [131]

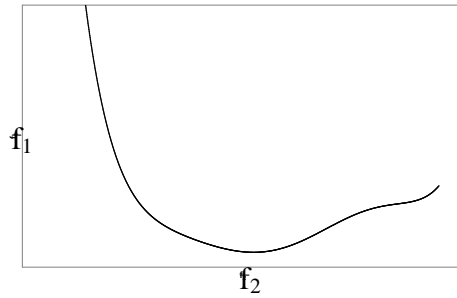


Figure 157: Pareto curve for two objective functions

### VI.2.3 Approximate algorithms

The previous two categories have the calculation time as a major drawback. To overcome this disadvantage, approximate algorithms have been developed. A so-called metamodel is put as a buffer and substituted to the direct coupling between the optimization algorithm and the finite element calculation, as shown in Figure 158.

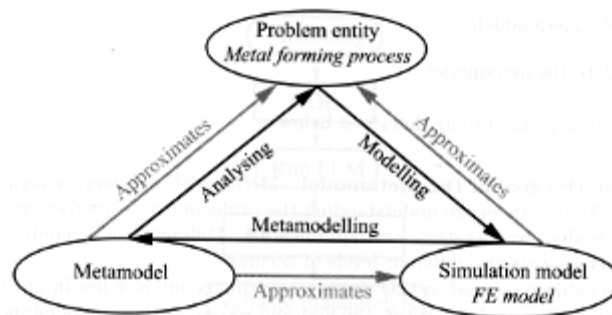


Figure 158 : Metamodelling [141]

The metamodel provides approximations of the objective functions and implicit constraints, which are determined by a few FE simulations, so reducing the number of FEM calculations and allowing for parallel calculations. Then, this typically polynomial approximation can be minimized very quickly. The optimal solution will be an approximation as well. The main disadvantage of this approach comes from the double approximation as shown in Figure 158 and may lead to a significant loss of accuracy. Consequently, the metamodel might not very well represent the problem, unless great care is taken to choose an adequate metamodelling technique. Many such techniques are available in literature. The most well-known two techniques are Response Surface Methodology (RSM) [126][142] and Kriging. The former uses least squares regression techniques to fit a lower order polynomial with “experimental” points (FEM-computed points in our case) (see Figure 159a), and is so able to handle noisy data. The latter is a more flexible regression technique since it is not based on a low order polynomial and exactly fits the “experimental” points, as shown in Figure 159b.

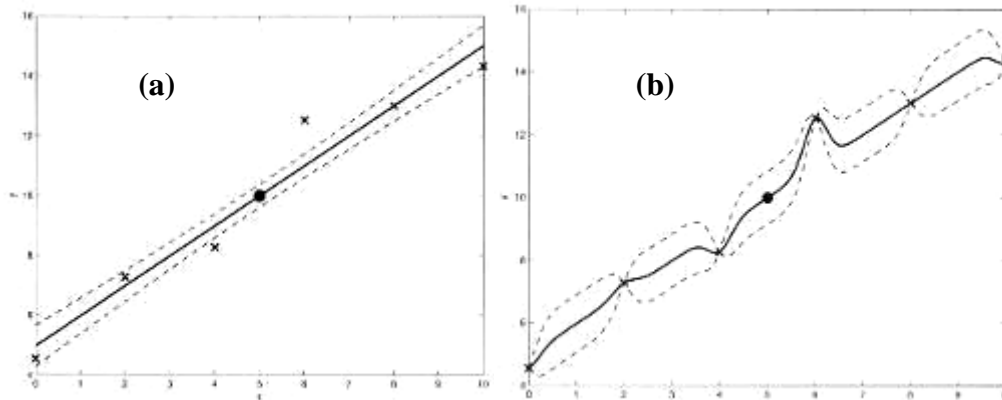


Figure 159 : Comparison between the RSM method (a) and the Kriging metamodel (b) [123]

Other metamodeling techniques can be found for computer simulations, such as Neural Networks (NN), Inductive Learning, Multivariate Adaptive Regression Splines, Radial Basis Functions and Support Vector Regression [123], Moving Least Square or Meshless Finite Difference Method. Table 16 shows a review on such metamodeling techniques and their use in metal forming processes optimization with the associated objective function and design variables. For example, concerning cold forming processes, NN have been applied to solve a curvature problem in cold shape rolling by minimizing the heterogeneity of the strain rate field [143].

Metamodeling technique	Forming Process	Objective	Design variables
RSM	Deep drawing	Minimise external work	Blankholder force
RSM	Deep drawing	Minimise thickness variations Maximise distance to FLC	Blank geometry
RSM	Bending	Minimise springback	Tool geometry
RSM	Deep drawing	Blank holder force	Drawhead geometry
RSM	Deep drawing	Optimum draw-in	Drawhead geometry
RSM	Deep drawing	Blank weight	Blank size and shape
RSM	Deep drawing	Minimise springback	Drawhead geometry
NN	Deep drawing	Minimise springback	Friction parameters
RSM	Deep drawing	Minimise springback	Tool geometry
RSM	Hydroforming	Maximum protrusion height T-shape	Length, thickness, diameter
RSM NN	Hydroforming	Minimise wall thickness variation	Internal pressure Axial displacement
RSM	Flanging	Minimise springback	Sheet geometry Die geometry
Kriging	Forging	Die wear	Billet temperature Die speed
RSM	Forging	Minimise forging energy	Preform geometry Forging load
RSM	Forging	Minimise strain variance	Preform geometry
RSM	Annealing	Constant wall thickness	Annealing temperature Annealing time

Table 16: Overview on the optimization of metal forming processes using approximate algorithms [123]

## VI.2.4 Hybrid algorithms

The three previous groups of algorithms present advantages and disadvantages and the success of a specific algorithm heavily depends on the optimization problem under study [123]. Therefore, several authors had the idea to harmoniously combine two or more methods with the idea of keeping only the advantages of each group.

An important remark concerns the last two categories: approximate and adaptive algorithms. They do not solve a problem by themselves, but they need to be coupled to an iterative or genetic algorithm to find the optimum solution.

A well known hybridization approach is to couple an evolutionary algorithm (EA) with a gradient-based algorithm [144]. The EA makes a global research and when the optimum is localized, the gradient-based algorithm makes a local research to refine the result.

A second hybridization concerns an EA with an approximate algorithm. Here, the approximation approach is used to reduce the computational cost of the EA algorithm [19], [131] and [145]-[149], as it will be more precisely presented in the following section.

## VI.3 Choice of an optimization algorithm

The previous section has reviewed optimization algorithms and their applications to metal forming processes, in particular wire drawing and rolling. They can be decomposed in four main categories, which has its own advantages and disadvantages. In literature, wire drawing and rolling have been mainly optimized by gradient-based and global algorithms. Both present severe drawbacks that limit their use in complex situations. For gradient-based algorithms drawbacks are:

- the possibility of being trapped in a local optimum,
- time-consumption in case of complex processes,
- the requirement of gradient calculations, which is either not accurate enough with a finite difference approach if remeshings take place, or very complex to implement in an analytical way into a FE software,

and for global algorithms the main drawback is time-consumption as well.

By taking into account the fact that:

1. the present optimization problem deals with two different metal forming processes,
2. there already exists robust and efficient algorithms,
3. CEMEF has experience on metamodelling techniques [131], [147]-[150],

the category which presents the most advantages for complex metal forming processes is the hybridization between evolutionary and approximate algorithms. Moreover, this approach

allows for parallel calculations, which is important when a single FEM simulation already requires a large CPU time. This hybridization is known as the MAES algorithm and is introduced in the next section.

### VI.3.1 MAES algorithm

Meta-model Assisted Evolution Strategies (MAES) are presented in detail in [19] and [131]. This algorithm is regarded as quite robust with respect to local extrema. It can be summarized as a hybridization of global algorithms with surrogate models (or metamodels) to solve most of complex optimisation problems.

To reduce the high number of evaluations, Emmerich et al. [19] combine an ES with metamodeling technique. For its flexible use, Kriging has been used as the regression technique to fit the numerical experiments. An overview of MAES is shown in Figure 160. The first step is to randomly choose an initial population of  $N_{in}$  individuals.

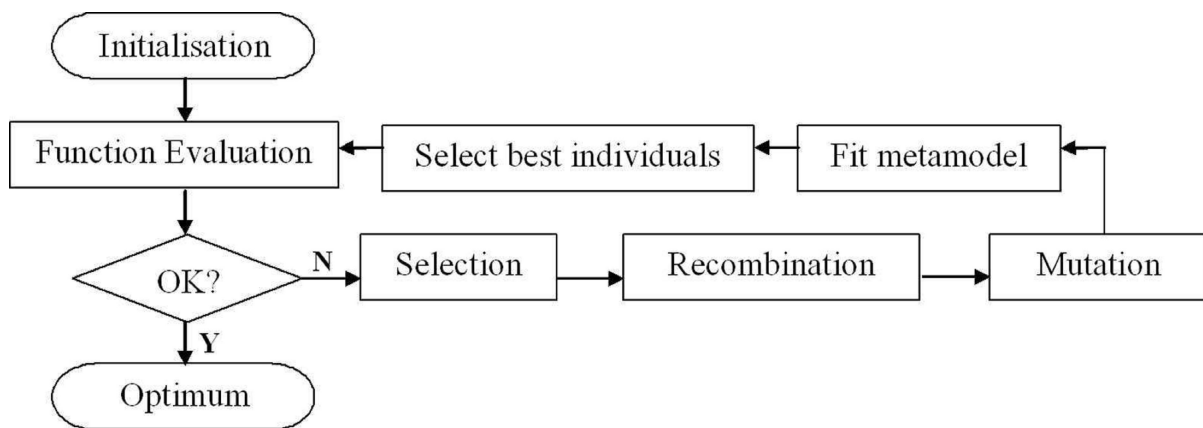


Figure 160: Overview of the MAES from [150]

After running the FEM simulations for the initial population, the  $\lambda$  best individuals are selected, recombined and mutated to generate  $\mu$  children. The results of the previously performed FEM calculations are used to fit a Kriging meta-model, which is used to estimate the objective function values for the  $\mu$  children. It so avoids running all the expensive FEM calculations for the  $\mu$  children. The objective function values  $f$  are not directly approximated by  $\tilde{f}$ , but by  $\tilde{f} - \Delta\tilde{f}$ , where  $\Delta\tilde{f}$  is the Root Mean Square Error of the Kriging approximation.  $\tilde{f} - \Delta\tilde{f}$  is the *merit function*; it represents an estimation of the lowest achievable value of  $f$ . Then, based on these predictions, the 20% best estimated individuals out of the  $\mu$  children are actually evaluated by running the corresponding FEM simulations. Thanks to this approach, the metamodeling technique saves 80% of time-consuming FEM calculations. The Kriging metamodel is then updated, and this procedure is repeated until  $N_{max}$ , the maximum number of FEM simulations, is reached. Past experience [19], in particular for forging optimisation [151], have shown that best efficiency and robustness are

obtained with the following algorithm parameters: the size of the initial population  $N_{in}$  is set to at least two times the number of optimization parameters, the number of parents,  $\lambda$ , is set to two times the number of optimization parameters, while the number of children,  $\mu$ , is set to 4 times  $\lambda$ , and  $N_{max}$ , is set to  $10 \lambda$  (20 times the number of optimization parameters).

### VI.3.2 Parallel calculations

Thanks to this approach, two levels of parallelization can be applied:

1. the parallelization of the finite element software itself, which is here automatically managed by FORGE®,
2. the parallelization of the optimization algorithm.

As the exact number of function evaluations is a priori known for each algorithm iteration, they can easily be carried out in parallel. The combination of these two parallelization strategies allows to significantly reduce the computational time on a simple personal computer with two or four processors or on a cluster of several processors. This way, this hybrid algorithm can optimize rather large and complex metal forming problems.

According to the problem size, each FEM calculation can be run on a certain number of processors,  $p$ . The processors number is determined by evaluating the parallelization performance. The parallel efficiency is expressed as follows:

$$E(p) = \frac{s(p)}{p} \quad \text{and} \quad s(p) = \frac{t(1)}{t(p)} \quad \text{(VI.2a, b)}$$

with  $t(p)$  and  $s(p)$  respectively the calculation time and speed-up for  $p$  processors. With the parallelization approach used, the speed-up increases with  $p$ , while the efficiency decreases from 1, for  $p = 1$ . Above a limit value of  $p$ , which depends on the problem size, for the speed-up stagnates or decreases too. On the other hand, the parallel efficiency resulting from the parallel structure of the ES, by running the  $\lambda$  FEM simulations at the same time on different machines, is always close to 1. Consequently,  $\lambda p$  processors can be used for the parallel calculations, with a very high efficiency.

## VI.4 Wire drawing optimization

### VI.4.1 Use of the optimization strategy (see VI.1)

#### VI.4.1.1 Choice of the optimization case

Here, the reference situation is “production” as the manufactured goods are already produced.

### VI.4.1.2 Choice of optimization parameters and their mathematical translations

As before mentioned, many parameters exist and the choice has been made of the dies geometry. The drawing die geometry can be fully described with three parameters which are introduced in Figure 161: the entrance die semi-angle  $\alpha$ , the land length  $L$  and the reduction through the diameter  $2R$  (the reduction is defined as  $(S_0 - S_f) / S_0$ ) with  $S_0$  the input section and  $S_f$  the output section.

The parameter  $p_{1,i}$  will be the land length; its value will correspond to an isotropic scaling in the X and Z direction with point C as the centre;  $i = 1, \dots, 4$  corresponds to the drawing die number (from 1 to 4).

The parameter  $p_{2,i}$  will be the die semi-angle; its value corresponds to a non-isotropic scaling in the X direction with point C as the centre;  $i = 1, \dots, 4$  corresponds to the drawing die number (from 1 to 4).

The parameter  $p_{3,i}$  will be the reduction; its value corresponds to a translation in the X direction;  $i = 1, \dots, 3$  corresponds to the drawing die number (from 1 to 3, the final wire diameter is fixed).

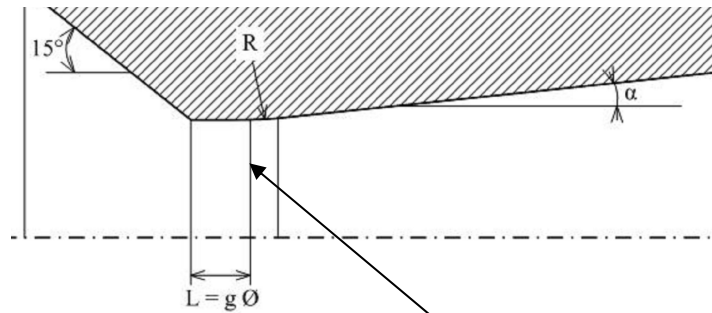


Figure 161: Drawing die geometry and definition of the optimization parameters

### VI.4.1.3 Choice of objective function and its mathematical translation

This step consists in giving a mathematical form of the objective function. Our study aims at improving to the process by minimizing damage. Thus, the Latham and Cockcroft damage criterion is used as our objective function. The Latham & Cockcroft (L&C) damage criterion will be used<sup>3</sup> since we are only interested in minimizing the damage value<sup>4</sup>: it is written:

$$D_{LC} = \int_0^{\varepsilon_f} \frac{\max(\sigma_I, 0)}{\sigma_{eq}} d\varepsilon_p = V_D \quad (\text{VI.3})$$

Alternatively, the force (implicit constraint) will be taken as an objective function. Bi-objective optimization (force and damage) will also be addressed.

<sup>3</sup> In fact, optimization has been performed before the identification of Lemaître's parameters and so, Latham and Cockcroft's criterion has been chosen since it gives good localization of damage.

<sup>4</sup> In the wire drawing optimization, the algorithm minimizes the maximal value of L&C criterion in the wire core.

#### VI.4.1.4 Definition of parameters variation range

The variation range for all parameters is:

- $0.289 \text{ mm} < p_{1,i} < 5.77 \text{ mm}$
- $1.189^\circ < p_{2,i} < 22.54^\circ$
- $2.1\% < p_{3,1} < 29\%$
- $1.25\% < p_{3,2} < 43.75\%$
- $1.4\% < p_{3,3} < 43\%$
- the diameter of the last drawing die is fixed and the reduction is between 3.3% and 29%.

### VI.4.2 **Parameters sensitivity study: optimization of a single drawing pass**

Optimization of the full drawing is too complex as 11 parameters have to be taken into account. Thus, a first study consists in constraining the problem to only one pass with two parameters: the die semi-angle and the land length. The optimization is then running for different reductions and different friction coefficients.

#### VI.4.2.1 Mono-objective optimization

##### *VI.4.2.1.1 Optimization of the drawing force*

Historically, drawing industries used the optimization of the drawing force to design drawing dies. It seems interesting to test the algorithm on the drawing force and to compare the obtained results with this know-how.

Fifty years ago, authors did experimental studies on wire drawing and show the existence of an optimal die semi-angle that is a function of the reduction, as shown in Figure 162. It can be noted that nothing implies that friction is not necessarily constant when the two above parameters change.

These results have been analytically demonstrated, using the analytical method of Avitzur [153]. This method gives a relation between the reduced drawing force, the friction and the die semi-angle: it is written as follows:

$$\frac{\sigma}{\sigma_0} = \left\{ \begin{array}{l} \frac{2}{\sqrt{3}} \left( \frac{\alpha}{\sin^2 \alpha} - \cot g \alpha \right) + \ln \lambda \times \\ \left( \frac{\bar{m}}{\sqrt{3}} \cot g \alpha + \frac{1}{\sin^2 \alpha} - \frac{\cos \alpha}{2\sqrt{3} \sin^2 \alpha} \sqrt{1+11\cos^2 \alpha} + \frac{1}{2\sqrt{3} \sin^2 \alpha \sqrt{11}} \ln \left( \frac{\sqrt{11} + \sqrt{12}}{\sqrt{11} \cos \alpha + \sqrt{1+11\cos^2 \alpha}} \right) \right) \end{array} \right\} \quad \text{(VI.4)}$$

with  $\alpha$  the die semi-angle,  $\lambda = (R_e/R_s)^2$  and  $\bar{m}$  the Tresca friction coefficient.

This equation indeed explains the concept of optimal die semi-angle, as shown in Figure 163 and Figure 164, which plot the reduced drawing force given by equation VI.4 as a function of the die semi-angle for different friction values (at constant reduction) and for different reduction values (at constant friction).

The next two figures (Figure 165 and Figure 166) compare results obtained during MAES and by the Avitzur's method. It can be noted that the concept of optimal die semi-angle is also found with the numerical results and that this value increases with friction and reduction, with both models, as in experiments.

In terms of numerical error, it has been estimated to 1.5 % for the error on the drawing force.

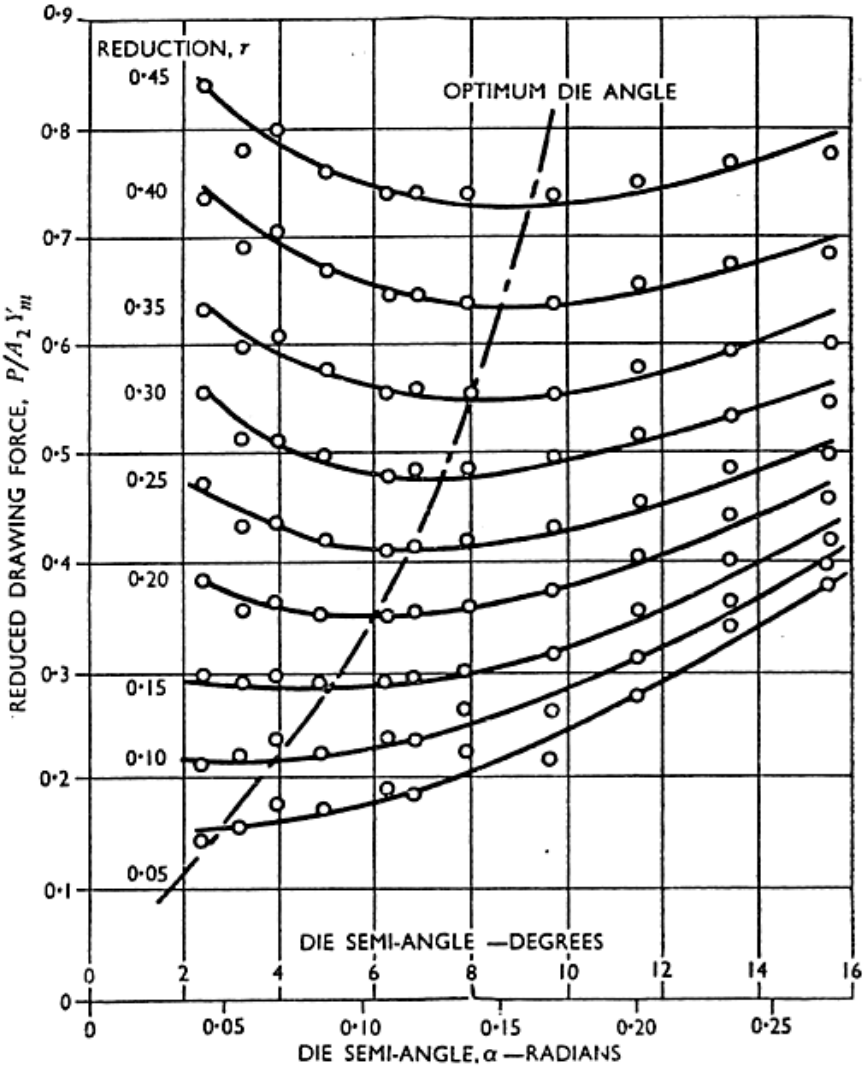


Figure 162: Experimental study on the influence of the reduction and the die semi-angle on the reduced drawing force [152]

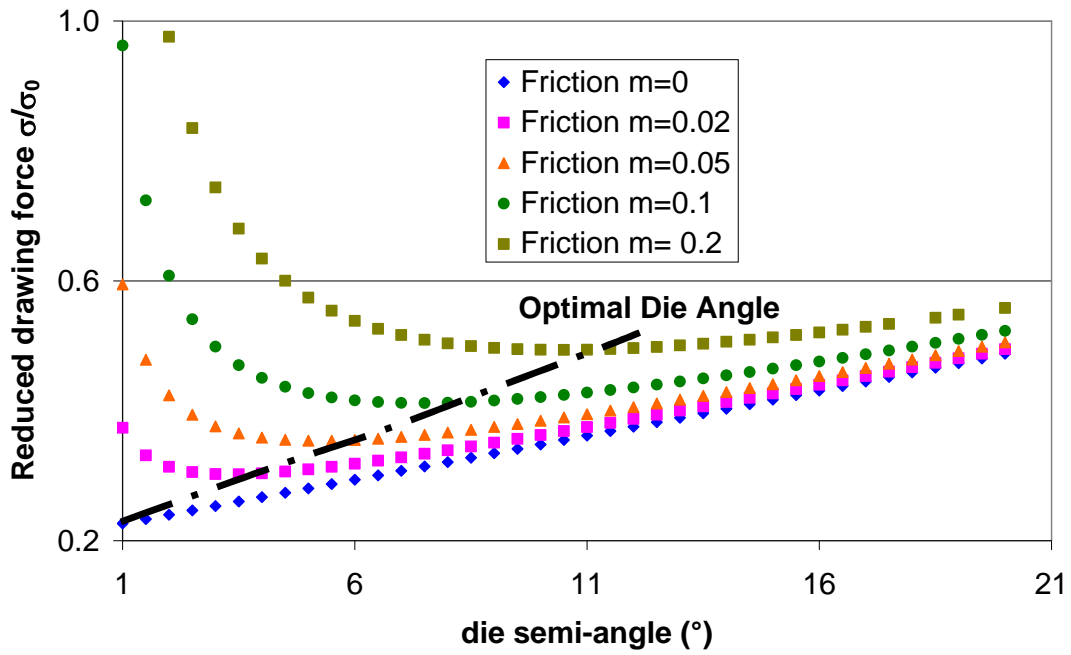


Figure 163: Reduced drawing force in function of the die semi-angle for different friction factors  $\bar{m}$  at constant reduction (20%) with Avitzur's equation

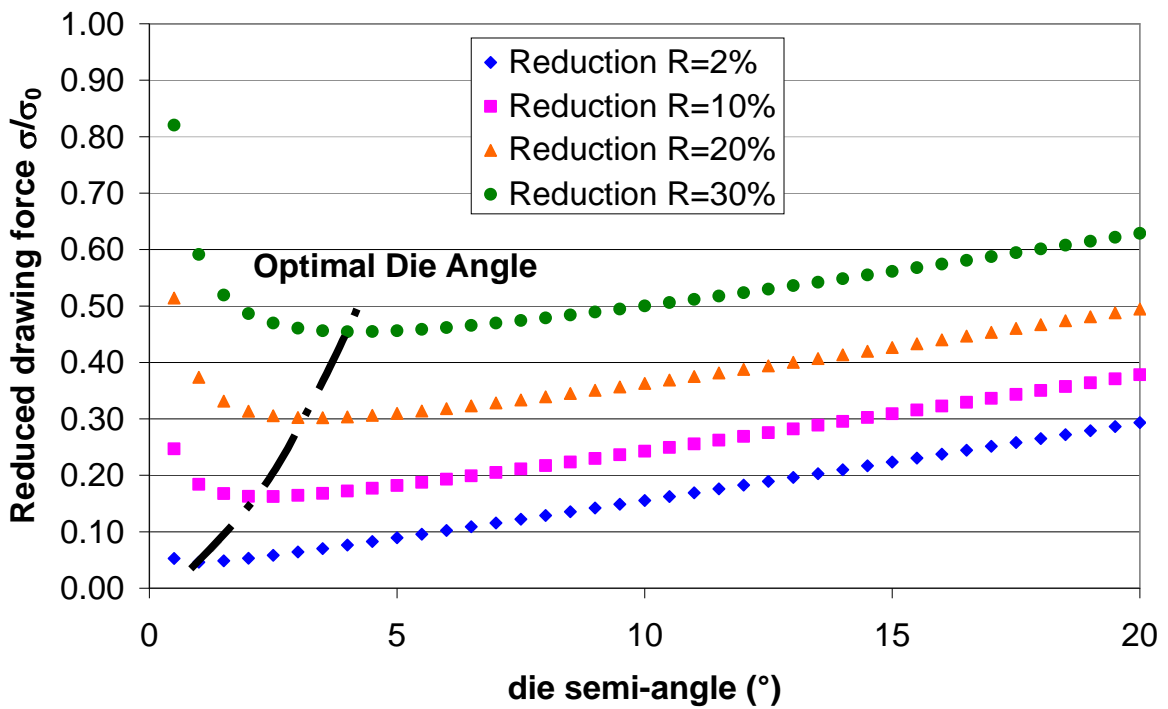


Figure 164: Reduced drawing force in function of the die semi-angle for different reduction at constant friction factor ( $\bar{m}=0.02$ ) with Avitzur's equation

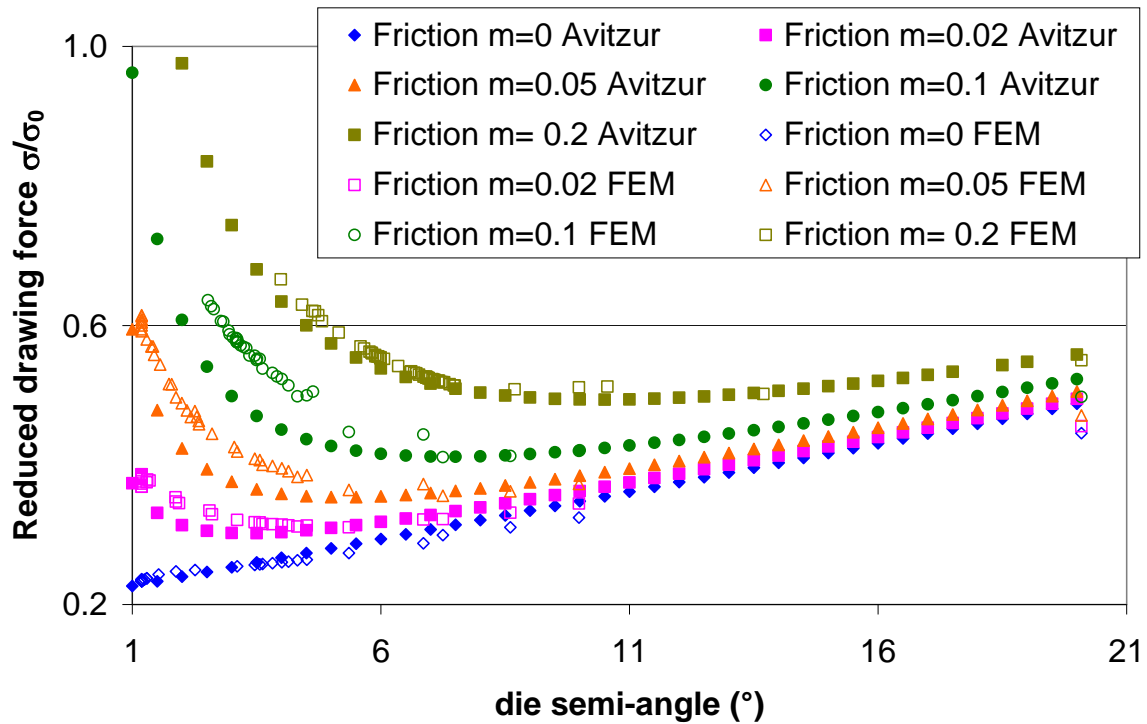


Figure 165: Comparison of the evolution of the reduced drawing force in function of the die semi-angle between the Avitzur's method and the numerical results for different friction factors at constant reduction (20%)

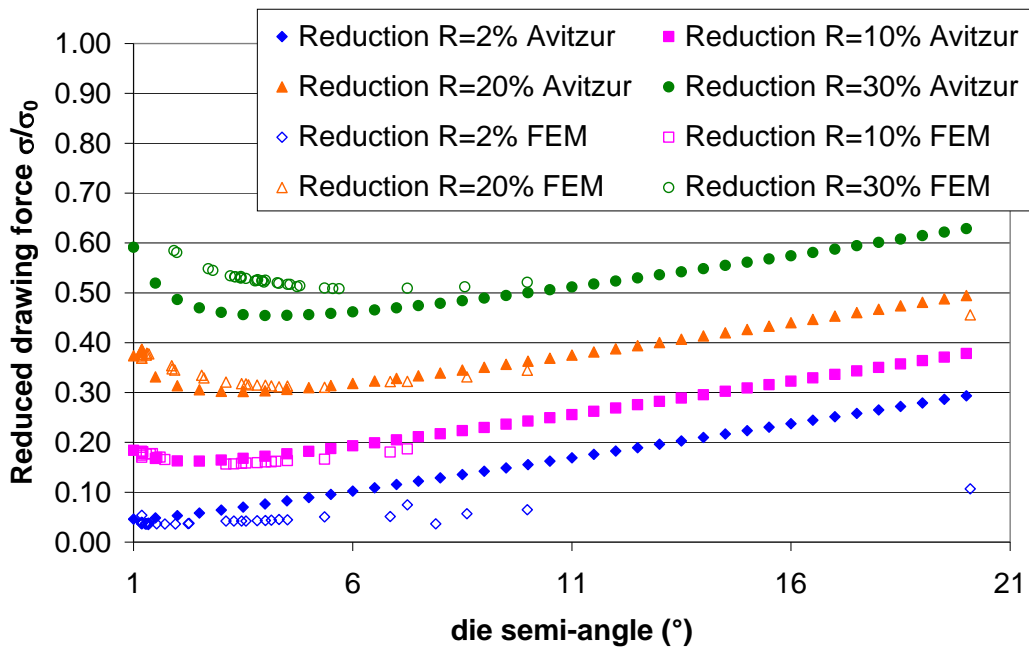


Figure 166: Comparison of the evolution of the reduced drawing force in function of the die semi-angle between the Avitzur's method and the numerical results for different reduction at constant friction factor ( $m=0.02$ )

It is also interesting to look at the influence of the land length on the reduced drawing force. It is done in Figure 167 for different friction factors and in Figure 168 for different reductions. The presented results correspond to different values of the die semi-angle that

have been tested by the optimization algorithm, which explains the scattering of points. It is noticed that the reduced drawing force is increased by an increase of friction and reduction. Moreover, for each friction and reduction value, the minimal drawing force is obtained for several land length values (in the previously defined variation range). It means that the drawing force has a low sensitivity on the land length.

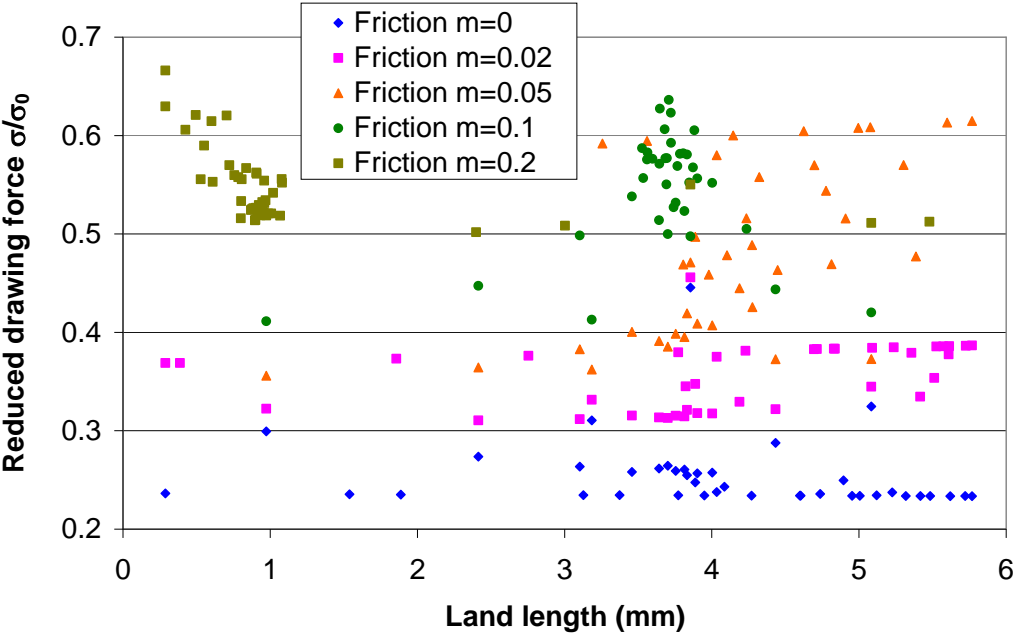


Figure 167: Evolution of the reduced drawing force as a function of the land length for different friction factors at constant reduction (20%)

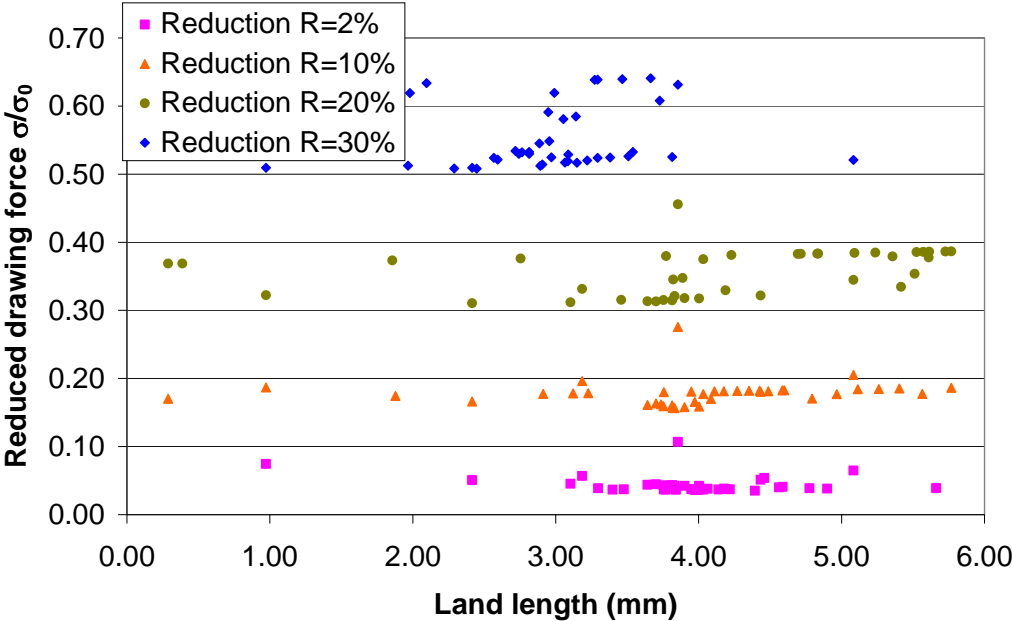


Figure 168: Evolution of the reduced drawing force as a function of the land length for different reduction at constant friction factor ( $\bar{m}=0.02$ )

### VI.4.2.1.2 Optimization of damage

As presented in section VI.4.1.3, the Latham and Cockcroft criterion is used to optimize the drawing die geometry. In this case, the numerical error is about 2.3 % on damage. To validate the choice of the MAES algorithm, it is interesting to evaluate its efficiency at finding the optimum. For this purpose, Figure 169 and Figure 170 present the evolution of the damage along the algorithm iterations, for different friction factors and for different reductions. It can be noted that for most of calculations, the optimum has been found within 20 iterations: this is a very fast convergence of the algorithm, due to a simple case.

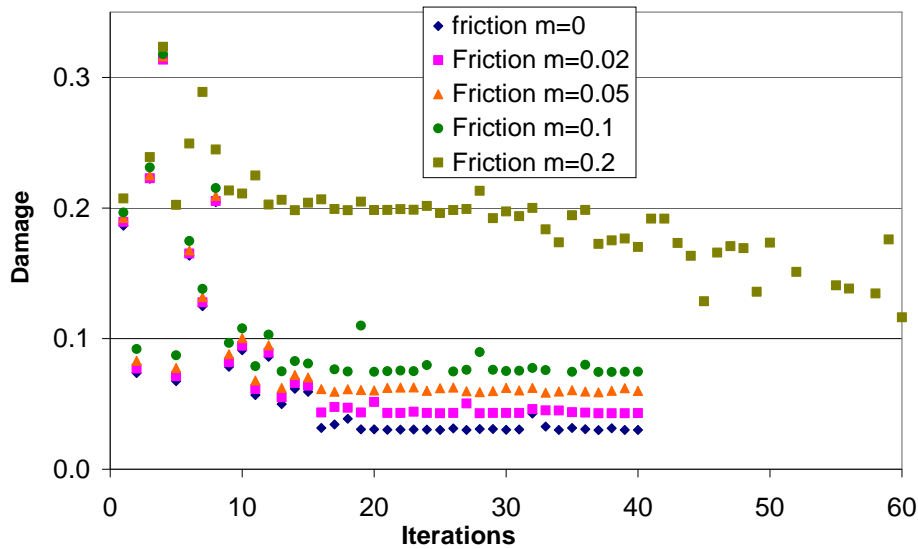


Figure 169: Damage evolution and optimization efficiency for different friction factors at constant reduction (20%)

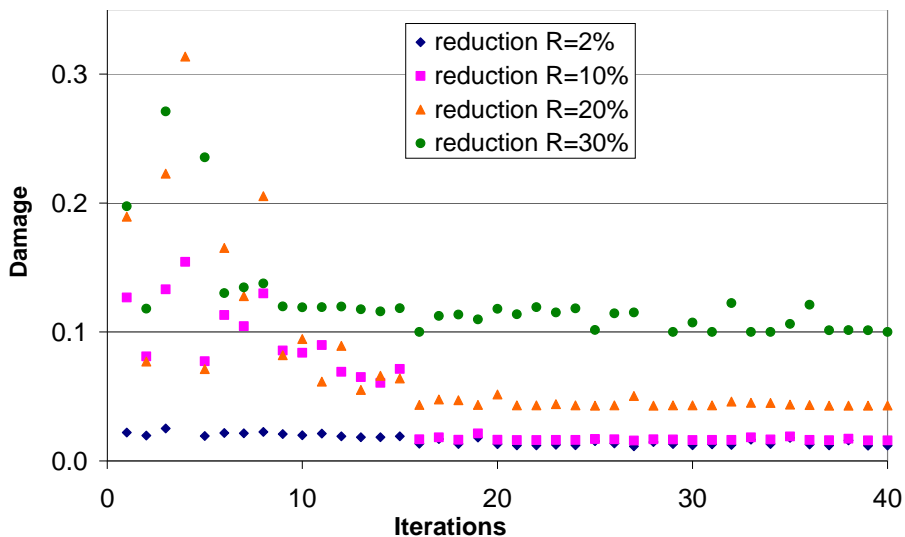


Figure 170: Damage evolution and optimization efficiency for different reductions at constant friction factor ( $m=0.02$ )

The optimal calculated values and their corresponding parameters are presented in Table 17 for different friction factors and in Table 18 for different reductions. Both are compared to the results obtained by minimizing the drawing force. We observe that the minimization of damage gives different optimal parameters and the concept of optimal die angle is very much objectgive-dependent. Generally, damage increases slightly with friction and reduction (and strain for a single pass).

Reduction	Friction factor	L & C	Optimal parameters		$\sigma/\sigma_0$	Optimal parameters		
			Land length (mm)	Die semi-angle (°)		Land length (mm)		Die semi-angle (°)
20%	<b>0</b>	0.030	5.722	1.189	0.234	5.768	0.1	1.189
20%	<b>0,02</b>	0.043	5.768	1.189	0.311	2.414	0.452	5.358
20%	<b>0,05</b>	0.059	4.909	1.189	0.356	0.975	0.613	7.249
20%	<b>0,1</b>	0.074	3.605	2.946	0.411	0.975	0.613	7.249
20%	<b>0,2</b>	0.116	0.288	3.988	0.502	2.400	1.174	13.691

**Table 17: Optimal parameters for a single wire drawing pass optimization, at constant reduction (20%), by minimizing damage (L&C). Comparison with the results of minimization of the reduced drawing force ( $\sigma/\sigma_0$ )**

Reduction	Friction factor	L & C	Optimal parameters		$\sigma/\sigma_0$	Optimal parameters		
			Land length (mm)	Die semi-angle (°)		Land length (mm)		Die semi-angle (°)
2%	<b>0,02</b>	0.011	5.661	1.189	0.035	4.392	0.11	1.308
10%	<b>0,02</b>	0.016	5.768	1.189	0.201	3.833	0.261837	3.110
20%	<b>0,02</b>	0.043	5.768	1.189	0.311	2.414	0.452	5.358
30%	<b>0,02</b>	0.100	3.273	1.189	0.508	2.368	0.474	5.617

**Table 18: Optimal parameters for a single wire drawing pass optimization, at constant friction factor ( $\bar{m}=0.02$ ), by minimizing damage (L&C). Comparison with the results of minimization of the reduced drawing force ( $\sigma/\sigma_0$ )**

When analyzing results for different friction factors (Figure 171 and Figure 172), we observe that for very low friction ( $\bar{m}=0$  or 0.02), the optimal die angle corresponds to the lower bound and that there is no optimal land length. For  $\bar{m}=0.05$ , the optimal angle is slightly above the minimal angle. The influence of the die land is not clear for higher friction (0.1 and 0.2), low angles cannot be tested due to necking, but the tendency would be that the optimal angle is above 3° and long die land becomes dangerous<sup>5</sup>.

<sup>5</sup> For high friction, i.e. 0.1 and 0.2, the optimal die angle is no longer on the lower bound. The reason is that a minimal angle leads to the necking of the wire because of the combination of a high friction factor with a long contact zone.

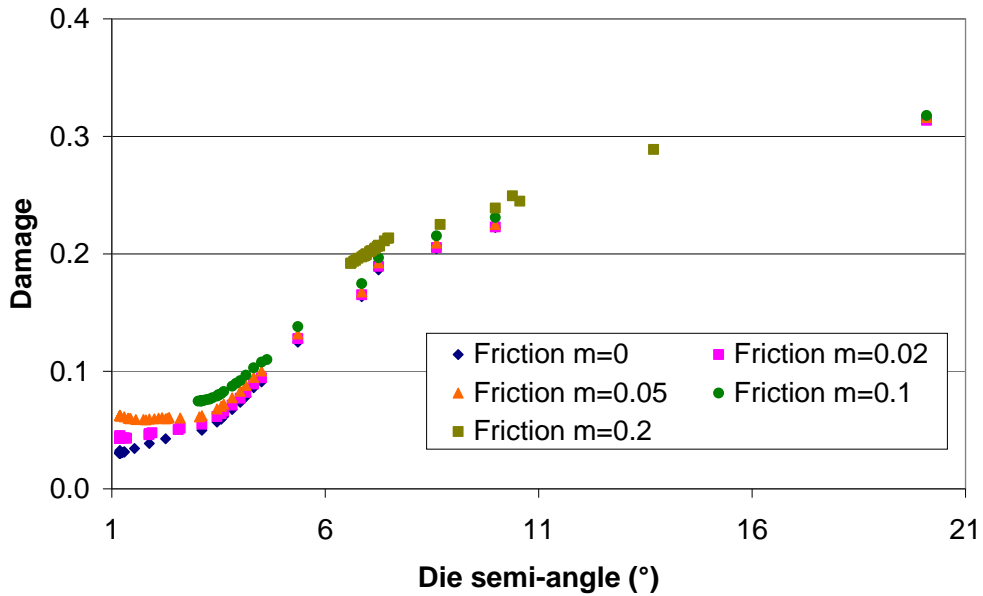


Figure 171: Evolution of damage as a function of the die angle for different friction factors at constant reduction (20%)

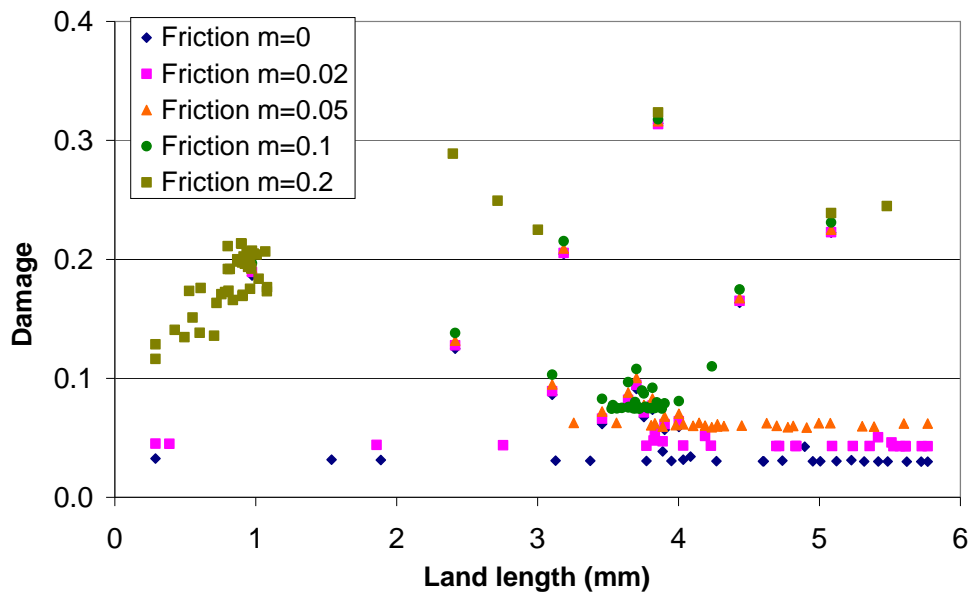


Figure 172: Evolution of damage as a function of the land length for different friction factors at constant reduction (20%)

When analyzing results for different reductions, damage increases with reduction and strain (for a single pass). The optimum die angle is on the lower bound while the optimal land length seems to remain constant. Figure 173 and Figure 174 give more information. The optimal die angle converges to its lower bound while damage seems independent of the optimal land length. All this, is connected with the very low friction selected ( $\bar{m}=0.02$ ), as seen above.

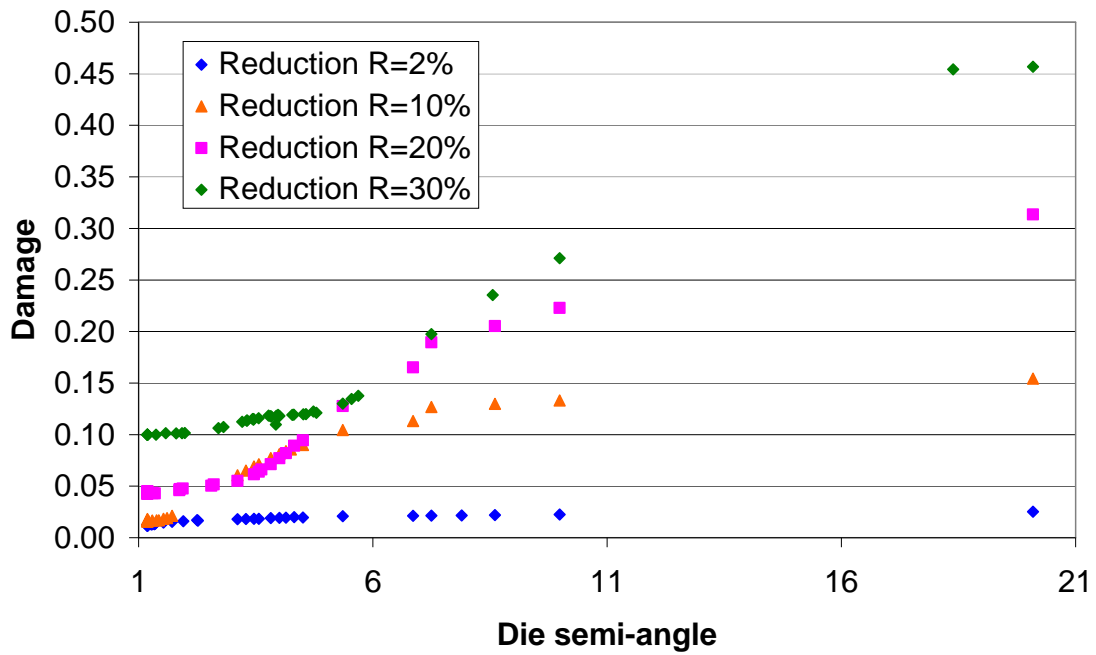


Figure 173: Evolution of damage as a function of the die angle for different reductions at constant friction factor ( $\bar{m}=0.02$ )

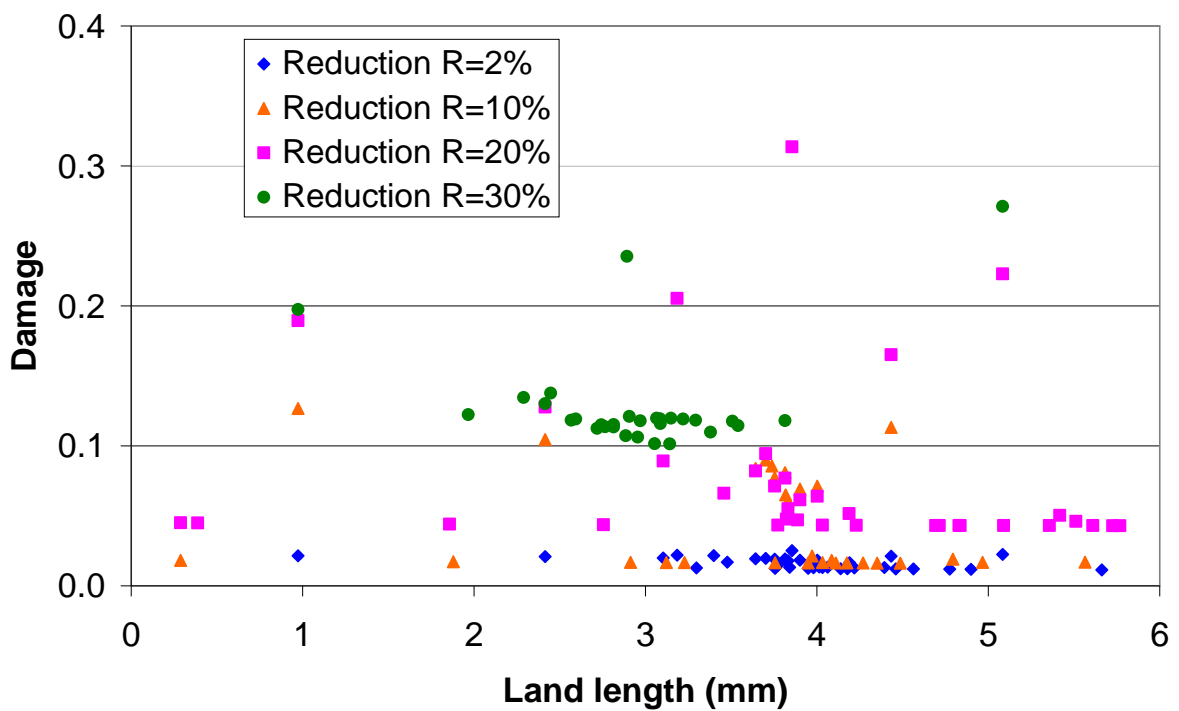


Figure 174: Evolution of damage as a function of the land length for different reductions at constant friction factor ( $\bar{m}=0.02$ )

As the optimal parameters change according to the choice of the objective function, it is now interesting to perform a multi-objective optimization by combining the damage and the drawing force. This can be done in two ways: using a weighted mono-objective

optimization with different weights for damage and drawing force (presented in the next section) or using a multi-objective optimization approach (presented in section VI.4.2.2).

### VI.4.2.1.3 Optimization of damage and force

In this case, the objective function  $\phi$  is written as follows:

$$\phi = \eta\phi_D + (1 - \eta)\phi_F \quad (\text{VI.5})$$

with  $\phi_D$  the damage objective function and  $\phi_F$  the reduced drawing force objective function. Calculations have been performed for a constant reduction (20%) and a fixed friction factor ( $\bar{m} = 0.02$ ): results are reported in Figure 175 for different values of  $\eta$ . It shows that minimizing the drawing force increases damage, and that conversely, minimizing damage increases the drawing force. Consequently, according to the value of  $\eta$ , the weight, different solutions are proposed, which corresponds to different arbitration between the objectives.

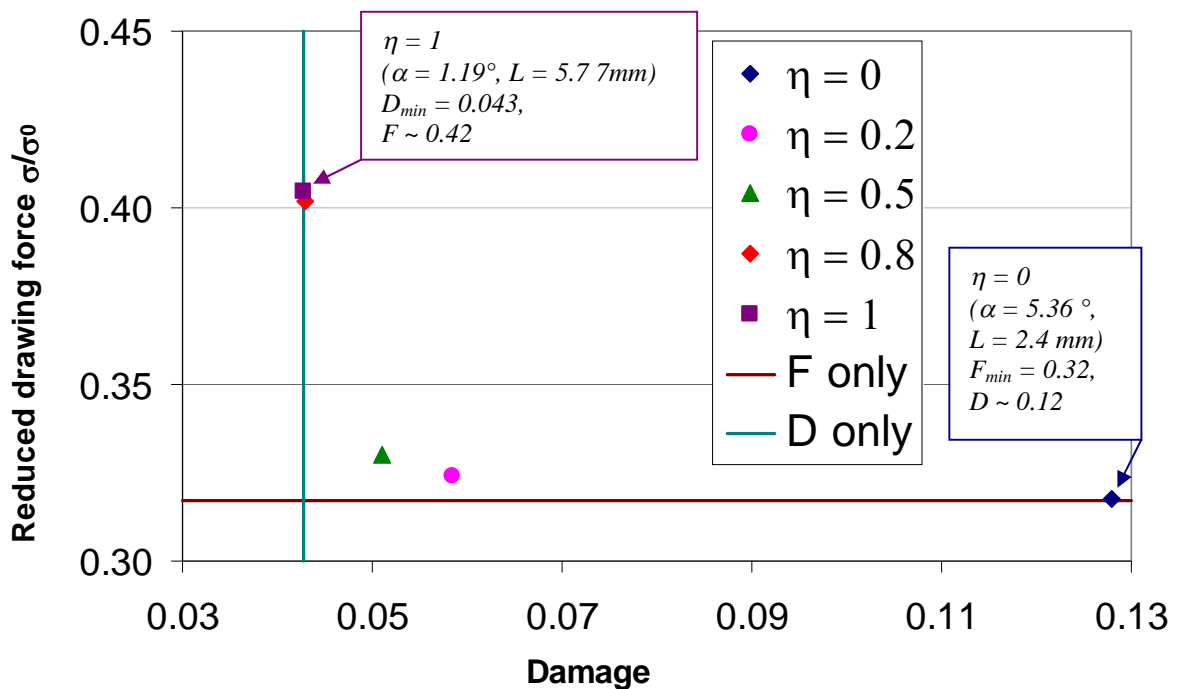


Figure 175: Mono-objective optimization by combining damage and drawing force for constant reduction (20%) and constant friction factor ( $\bar{m} = 0.02$ )

### VI.4.2.2 Multi-objective optimization

A metamodel assisted algorithm, where the exact function is approximated by a surrogate function, is also used in the multi-objective framework [154][156], where there is not a single solution to find but a family of non-dominated solutions that constitute the Pareto front. The utilized metamodel is based on the Meshless Finite Difference Method, and the selected multi-objective algorithm is the Non Sorting Genetic Algorithm, NSGA-II. After initiating the metamodel with a reduced number of individuals, it is continuously updated during the algorithm iterations, by adding new points of the Pareto front, which correspond, as in the single-objective case, to the individuals with the best potential to improve the building of the front. This way, quite accurate Pareto fronts can be obtained by approximately the same number of function evaluations as in the single-objective case.

The multi-objective optimization results are superposed to the mono-objective calculation in Figure 176: they confirms the results previously obtained. This curve provides a better description of the Pareto front: each point corresponds to a set of optimal parameters. The choice of the best compromise between minimizing the drawing force or the damage is left to the user.

The drawing die geometry is historically designed according to the minimization of the drawing force. This curve shows that, by accepting a small increase of the drawing force, there is a possibility to strongly decrease the damage.

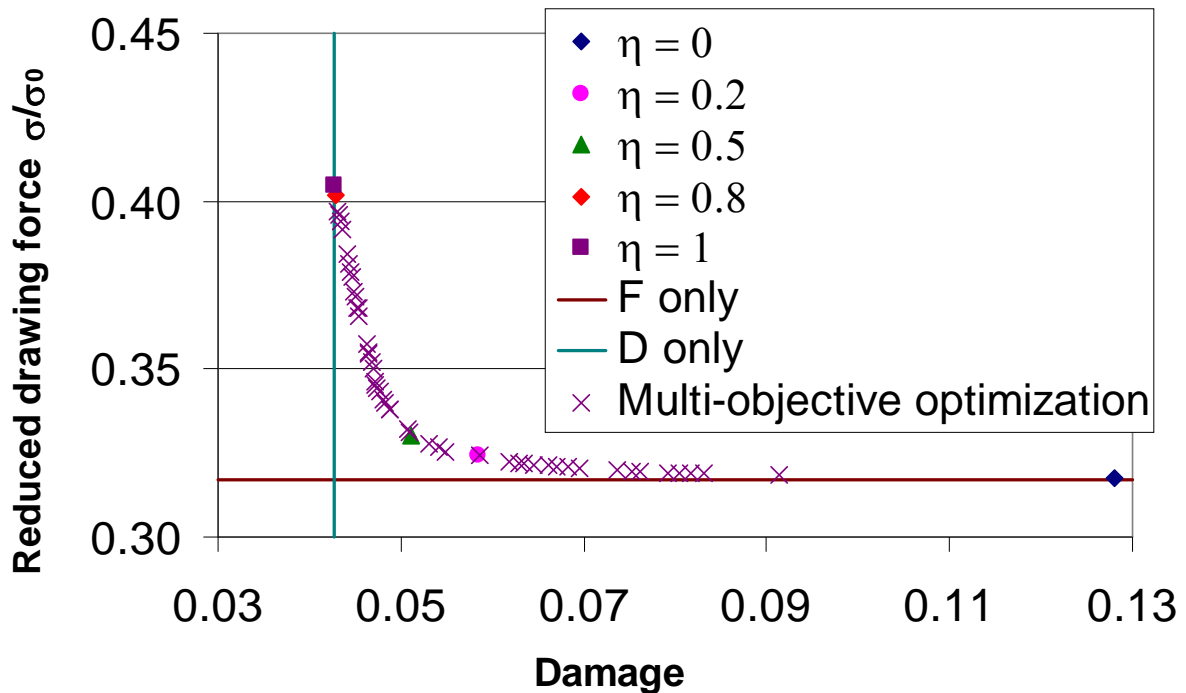


Figure 176: Multi-objective optimization of a single drawing pass for constant reduction (20%) and constant friction factor ( $\bar{m} = 0.02$ )

### VI.4.3 Full wire drawing optimization

The previous section has shown a minor influence of the land length compared to the influence of the drawing die semi-angle. Thus, the former parameter is kept constant in this section. The optimization of the four-stepped wire drawing also concerns damage, while the parameters are the four drawing die semi-angles and the three reductions (initial and final diameters are fixed).

Figure 177 presents the efficiency of the optimization to find the optimum. In this case, with 7 parameters, the MAES optimization needs 60 iterations to find the optimal parameters, which is again quite fast for a problem of this complexity.

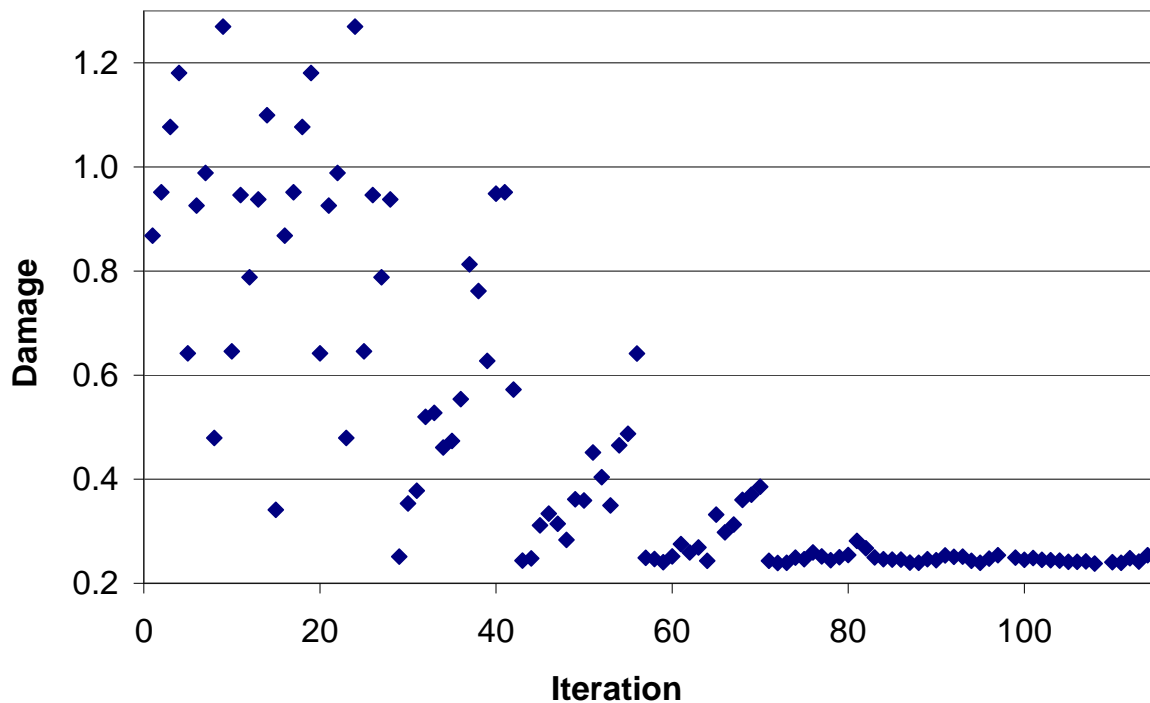


Figure 177: Evolution of damage versus the algorithm iterations in a four-stepped wire drawing problem

Results are presented in Table 19, where optimal parameters are detailed for each drawing die, and Figure 178 and Figure 179 present the evolution of damage as a function of both reduction and die semi-angle for each drawing die. It is observed that the die semi-angle values converge towards their lower bound, i.e.  $1.189^\circ$ , which confirms the results obtained for the optimization of a single pass of wire drawing. Concerning the reductions, the optimization gives four different values with a “bell” evolution. Optimal value of each reduction can be found around values given in the table with  $\pm 1 - 2\%$  as shown in Figure 179. The final damage and minimal value at the end of drawing is 0.24 and nearly 3 times lower than the value calculated with the industrial process, see I.2.3.2.

Drawing die	Friction coefficient	L & C	Optimal parameters	
			Reduction (%)	Die semi-angle (°)
1	0,02	0.240	17.5%	1.189
2	0,02		31.8%	1.189
3	0,02		21.8%	1.189
4	0,02		12.4%	1.189

Table 19: Optimal parameters for a four-stepped wire drawing pass optimization, at constant friction factor ( $\bar{m} = 0.02$ )

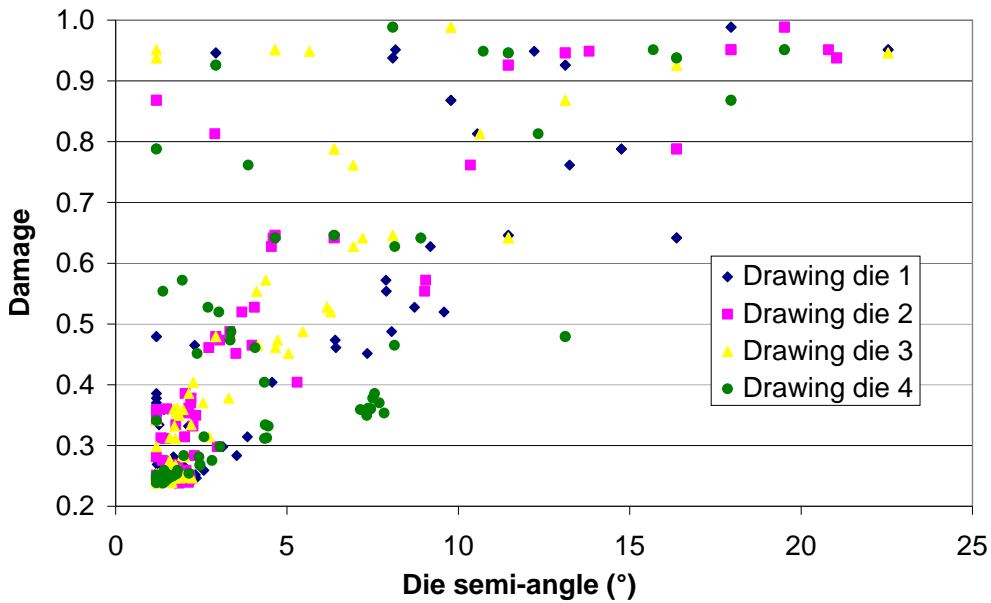


Figure 178: Evolution of damage as a function of the die angle for each drawing die

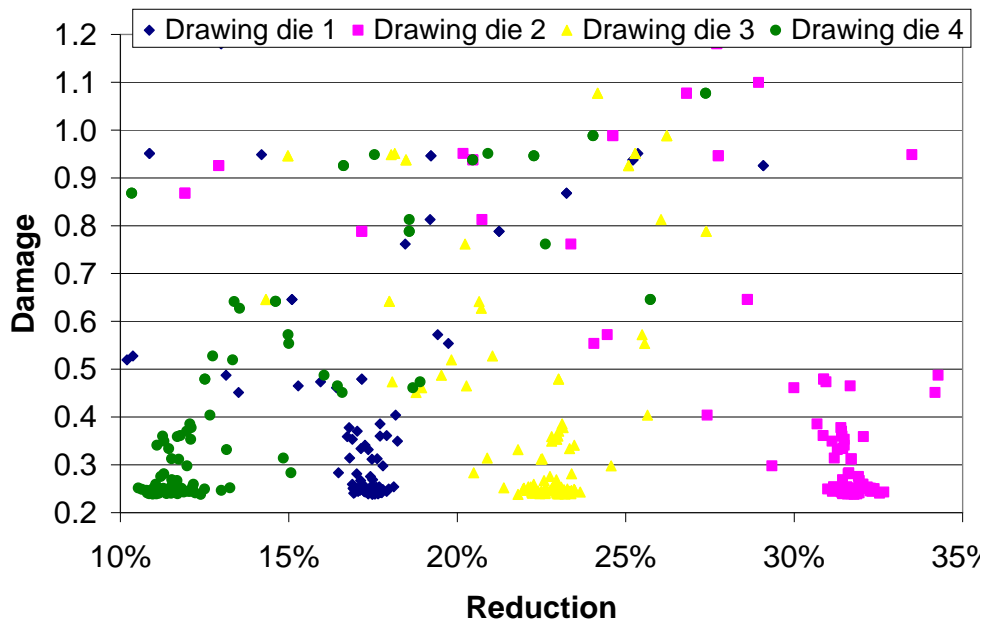


Figure 179: Evolution of damage as a function of the reduction for each drawing die

#### **VI.4.4 Toward more objectives**

Chapter IV has shown, that at the end of drawing the residual longitudinal stresses are quite high (~1000MPa on the wire surface and -1000 MPa in the wire core. With the calculated optimal parameters, with a 12.4%-reduction at the end of drawing, the residual longitudinal stresses are lower than 600 MPa on the wire surface and -500 MPa in the wire core. This wire drawing sequence enables to strongly decrease the residual longitudinal stresses and to homogenize them, as well as decreasing damage (in fact both are linked to the aspect ratio  $L/R$  and friction). Thus it should be interesting to perform a multi-objective optimization with damage, drawing force and residual longitudinal stresses as well to find the best compromise between these three objectives.

Using a very weak last reduction to minimize the residual longitudinal stresses and using a very slightly converging die land has also been proposed for the same purpose. Would the MAES optimization scheme confirm these ideas?

## VI.5 Summary

The first part of this chapter has been devoted to an introduction to the optimization strategy, which can be decomposed into three main stages: modelling, selection and resolution. The modelling highlighted the importance to correctly define the problem, using a four-step methodology, in order to carry out an efficient optimization.

The second section introduced the different resolution methods, i.e. the different classes of optimization algorithms, which guided the reader to the chosen MAES algorithm for the wire drawing optimization.

Finally, this method enabled to resolve and optimize the wire drawing problem. First, a mono-objective optimization of a single pass with two parameters (the die semi-angle and the land length) has been performed for different reductions and different friction coefficients. Damage and drawing force have been used as objective functions. It has been observed that both the reduced drawing force and the damage increase with an increase of the friction value and reduction. Moreover, the land length has a minor influence on both the reduced drawing force and the damage, as compared to the die semi-angle. Then, the optimization provides different sets of optimal parameters depending on the objective function. In the optimization of the non-dimensional drawing force, an optimal die semi-angle is found when friction is non-zero. It increases with the reduction and the friction, as it has been experimentally observed [152]. On the other hand, in the damage optimization, this optimal die angle is no longer observed, and the optimum is found on the lower bound ( $\alpha = 1^\circ$  here), whatever reduction and reasonable friction. At high friction however, the mechanical limit of the wire is reached and the optimal die angle seems to be slightly higher than the lower bound value. Afterwards, the damage and the non-dimensional drawing force have been coupled into a single mono-objective function by using weights, as well as by a bi-objective approach. The Pareto front has been constructed, which gives the optimal curve of this objective function. This curve enables the user to set his priority to damage or to the drawing force. Moreover it shows that damage can be strongly decreased without increasing too much the reduced drawing force. In our opinion, all this clarifies considerably the concept of optimal angle. Moreover, a four passes optimization has been performed. Thanks to the remark above, the die land has been fixed to a constant value for this full wire drawing optimization, leaving only the die semi-angle and the reduction as optimization parameters. Minimizing damage, all the angles have been set to a minimum ( $1^\circ$ ) because of low friction, whereas a bell-shaped curve has been found for reduction. The latter result may correspond to a common industrial practise, at least in the steel-cord drawing industry. To go further, it would be necessary to optimize according to the force as well.

## VI.6 Résumé français

La première partie de ce chapitre a été dédiée à une présentation de la stratégie d'optimisation, qui peut être décomposée en trois grandes parties : modélisation, sélection et résolution. L'étape de modélisation, elle-même décomposée en quatre parties, a montré l'importance de correctement définir le problème afin d'obtenir une optimisation la plus efficace possible.

La seconde partie a consisté en une présentation des différentes classes d'algorithmes d'optimisation, qui nous a guidés vers le choix de la stratégie MAES pour la résolution et l'optimisation du procédé de tréfilage.

Enfin, la dernière partie a été consacrée à l'optimisation du tréfilage. Tout d'abord, une première étape d'optimisation mono objectif à deux paramètres (demi angle d'entrée de filière et longueur de portée) d'une seule passe de tréfilage a été réalisée pour différentes réductions et différents frottement. La force de tréfilage et l'endommagement ont été successivement utilisés comme fonction coût. Les résultats ont montré que l'endommagement et la force de tréfilage augmentent avec le frottement et la réduction. De plus, l'optimisation a mis en évidence une influence secondaire de la longueur de portée par rapport au demi angle d'entrée de filière. Enfin, l'optimisation du tréfilage a montré que le jeu de paramètres optimaux dépend de la fonction coût à minimiser. Dans le cadre de l'optimisation de la force de tréfilage, la notion de demi angle optimal a été mis en évidence, comme l'avait montré des études expérimentales [152]. Cet angle augmente avec l'augmentation du frottement et de la réduction. Alors que dans le cadre de l'optimisation de l'endommagement, cette notion n'est plus du tout retrouvée : l'optimisation fournit une valeur du demi angle qui se cale sur la borne inférieure quels que soient la réduction et le frottement (excepté pour les très forts frottements, où l'utilisation d'un angle minimal entraîne l'apparition d'une striction car les limites mécaniques du fil sont dépassées et de ce fait l'optimisation évite cette borne inférieure). En outre, l'endommagement et la force de tréfilage ont été pondérés dans une seule fonction coût afin d'obtenir les points du front de Pareto. Le front de Pareto donne la courbe d'optimalité entre les deux fonctions coût. Finalement, pour plus de précision, cette courbe a été tracée grâce à une optimisation multi objectif de l'endommagement et de la force de tréfilage. Cette courbe confirme et précise les points obtenus précédemment. Elle permet à l'utilisateur de choisir s'il préfère donner de l'importance à l'endommagement ou à la force de tréfilage. En pratique, elle montre qu'il est possible de diminuer fortement l'endommagement sans trop augmenter la contrainte de tréfilage. De notre point de vue, cela clarifie considérablement le concept d'angle optimal.

De plus, une optimization quatre passes a été réalisée. Grâce à la remarque précédente sur l'influence secondaire de la longueur de portée, celle-ci a été fixés à une valeur constante for cette optimization complète du tréfilage, laissant seulement le demi-angle d'entrée de filière et la réduction comme paramètres d'optimisation. En minimisant l'endommagement, tous les angles sont alors fixés au minimum ( $1^\circ$ ) à cause du faible frottement, alors que une courbe en forme de cloche a été obtenue pour la réduction. Ce dernier résultat correspondrait à une pratique industrielle commune, au moins dans l'industrie du steel-cord. Pour approfondir, il serait également nécessaire d'optimiser selon la force.

## Chapter VII Conclusions and Perspectives

This thesis dealt with the numerical simulation of cold forming processes for high carbon steel. Several goals were initially defined:

- to better understand the material behaviour along the forming schedule,
- to have a more accurate numerical modelling,
- to understand damage mechanisms and to be able to predict damage,
- to optimize processes.

After an introduction of the industrial context and a presentation of both processes, the state of the art has been established on lamellar microstructure, yield criteria and damage mechanisms and models. This bibliography review enabled to choose an anisotropic yield function and a damage law valid for both wire drawing and rolling.

Then, the material behaviour was measured from experiments (tension, compression, torsion, shear tests) throughout this range of steel forming. Using these mechanical tests, a numerical behaviour law has been identified. In addition, compression tests exhibited an ovalization of compression specimens, highlighting a flow anisotropy in transverse direction. Thus a quadratic Hill-type anisotropic law has been chosen to simulate the material behaviour and Hill's parameters have been identified from the above mentioned compression tests at the end of drawing and at the end of rolling. We observed that anisotropy does not evolve too much during rolling. So it has been decided to keep all along rolling Hill's parameters constant, to those identified at the end of drawing. Moreover, friction parameters have been also measured for both drawing and rolling (drawing force measurement and plane strain compression test respectively). Finally, a Lemaître's damage criterion, which explicitly takes into account the change of strain path thanks to the triaxiality, has been identified in order to be able to predict damage evolution during cold forming processes.

In addition, process numerical simulations, with FORGE2005®, have been run. Isotropic modelling has improved our knowledge of the cold forming processes in terms of strain, strain rate, stress, geometry prediction... The main results show that the spread prediction is not accurate -an underestimation of 10% on the total widening. Some sensitivity studies were added to complete this understanding. The first one went through the impact of the transfer of residual stresses from drawing to rolling and highlighted the significant influence of wire drawing residual stresses. The second one discussed the influence of the strain map transfer from drawing to rolling, which can not be neglected either. Then, anisotropic simulations have been performed, with the model identified in the previous chapter. Mechanical

anisotropy has a deep impact on flat rolled wires geometry, bringing the underestimation down to 5%. Friction and Hill's parameters studies did not explain this remaining underestimation.

Besides, a microstructural study coupled with an analysis of damage mechanisms was done on high carbon pearlitic steels during wire drawing and rolling. The mechanical anisotropy comes from the orientation of the pearlitic colonies in the drawing, which itself induces the emergence of a preferential crystallographic texture. This study highlighted the anisotropic nature of damage related to the microstructural evolution. Three damage mechanisms have been identified during drawing: voids formation close to inclusion (initiation and propagation differ from inclusion type) ; voids formation as a consequence of transversal breaking of pearlitic colonies unfavourably oriented with respect to the metal flow; voids nucleation at high disorientation angle colonies boundary. During rolling, anisotropy development is stopped. Rolling process is characterized by strain heterogeneity leading to a different microstructure between the core and the edges of the flat, while wire drawing is a tensile process with homogeneous strain due to revolution symmetry. This heterogeneous deformation affects the evolution of damage including a larger cavities density in the most distorted area. The form factor of the cavities is also linked to this heterogeneity. Decohesion and cavities developed along the axis of the wire during drawing are enlarged in the transverse direction during rolling. Around the inclusions, the expansion kinetic of decohesion is also changed.

The use of simulation enabled to bring further information. The morphological evolution of voids was verified numerically and resulted in a good agreement with the strain field. Moreover, using a damage criterion in our model enabled to locate and predict the risk of damage and fracture of our material.

Finally, optimization calculations have been performed. An evolution strategy assisted by meta-model was adopted. This method has already demonstrated its robustness and efficiency for applications of complex forming processes. It consists in approximating the finite element model in order to estimate the objective function and the results. Only the best probable solutions are actually evaluated by the finite element calculation. Drawing optimization is made on the tools geometry (die semi-angle, land length and reduction) with mono and multi-objective functions: damage and drawing force. Calculations highlighted the insignificant influence of the land length compared to the die semi-angle. Moreover, the concept of optimal die semi-angle has been confirmed when optimization is done on the drawing force. On the other hand, optimization of damage gave totally different optimal parameters: minimizing damage led to a minimal die angle. Finally, this study identified an opportunity to reduce

damage by reducing the die angle without increasing too much the axial stresses and the fracture risk.

On the whole, this work enabled to virtually answer to goals defined in the beginning of the manuscript. However, many improvements can be formulated in order to have more accurate simulations.

First, in terms of rheology, a more complex anisotropic yield criterion must be identified and used in order to improve the widening prediction with numerical calculations. The identification of another anisotropic yield criterion is a hard task which is left for a new thesis. The use of non-associated plasticity seems to be an interesting alternative: Von Mises will be used for stresses and Hill for geometry. Likewise, multi-scale or crystallographic models can be also used.

Secondly, an isotropic damage criterion has been used, but an anisotropic criterion could be more relevant, since microstructural anisotropy has a deep impact on damage mechanisms, as shown by the microstructural analyses in chapter IV. Lemaître proposes an anisotropic version of its criterion but other anisotropic formulations exist, which could be used as well (see Annex 2 for anisotropic damage models).

Thirdly, concerning the microstructural characterization of high carbon steel and damage mechanisms, some improvements can be proposed. The low number of SEM and TEM pictures only enabled to have qualitative information. It could be relevant to deepen this study in order to have quantitative measurements of crystallographic orientations, interlamellar distances, inclusions and cavities densities, mean distances between neighbouring voids...

Finally, optimization calculations have been done only with two cost functions, but many other cost functions can be used as well in order to minimize the strain heterogeneity and stresses or to optimize the drawing die life for instance. Moreover, only drawing optimization has been performed in this study and it is obviously relevant to use the same strategy to optimize rolling. Indeed, experiment carried out during this PhD has proved the potential efficiency of adequate roll optimization.

# ANNEXES

## ANNEX 1: Framework of porous media plasticity

### A.1.1 Gurson's model

Material behaviour is modified by the presence of porosities. A damage variable  $f$  is then introduced, defined as the void volume fraction:

$$f = \frac{V_c}{V_t} = \frac{V_t - V_0}{V_t} = 1 - \frac{\rho}{\rho_0} \quad \text{or} \quad J = \det \bar{F} = \frac{\rho_0}{\rho} = \frac{V_t}{V_0} \Rightarrow f = \frac{J-1}{J} \quad (\text{A1.1a, b, c})$$

The evolution law of  $f$  is obtained thanks to mass conservation:

$$\dot{f} = (1-f) \text{tr} \left( \dot{\varepsilon}_{pl} \right) = \frac{\dot{\rho}}{\rho} = \frac{\dot{J}}{J^2} \quad \text{with equation (1c)} \quad (\text{A1.2})$$

So cavity growth is taken into consideration in volume variation. Damage, via  $f$ , modifies the load surface of the plasticity criterion. A strong coupling will express the loss of capacity of the material to resist load.

A Von Mises criterion, defined from the second invariant of the stress deviator is not enough to describe void growth rate. Based on numerical simulations of the growth of a single cylindrical void in an incompressible plastic matrix, Gurson proposes a formula for a yield criterion including the first stress invariant [102]:

$$\psi = \left( \frac{\sigma_{eq}}{\sigma_0} \right)^2 + 2f \cosh \left( \frac{3}{2} \frac{\sigma_H}{\sigma_0} \right) \quad (\text{A1.3})$$

With:  $\sigma_0$  the yield stress

Remark: when  $f=0$ , Von Mises criterion is regained.

Void interactions are not taken into account in this equation. They may become significant as damage develops. This is why Gurson's model has been extended by Tvergaard and Needleman.

### A.1.2 Void interaction effect

Gurson's model has been extended by Tvergaard and Needleman [103]. They introduce three constitutive parameters  $q_1$ ,  $q_2$  and  $q_3$  and an equivalent porosity:

$$\psi = \left( \frac{\sigma_{eq}}{\sigma_0} \right)^2 + 2q_1 f * \cosh \left( \frac{3q_2}{2} \frac{\sigma_H}{\sigma_0} \right) - (1 + q_3 f^{*2}) \quad (\text{A1.4a})$$

For steels,  $q_1 = 1.5$ ,  $q_2 = 1$  and  $q_3 = (q_1)^2$  (A1.4b, c, d)

$f^*$  is defined in the following way:

$$f^* = \begin{cases} f & \text{si } f < f_c \\ f_c + \frac{f_u^* - f_c}{f_f - f_c} (f - f_c) & \text{si } f > f_c \end{cases} \quad (\text{A1.5})$$

With:  $f_c$  the void volume fraction for the beginning of the coalescence phase,

$f_f$  the initial value of  $f$  at fracture,

$f_u^*$  the ultimate value of  $f^*$  ( $=1/q_1$ ).

$f^*$ , which represents microstructural damage, depicts the rapid material capacity loss to bear stress because of neighbouring void coalescence when  $f$  reaches the  $1/q_1$  limit.

Moreover, they add the possibility of nucleating new cavities, writing

$$\dot{f} = \dot{f}_{nucleation} + \dot{f}_{growth} \quad (\text{A1.6a})$$

With  $\dot{f}_{growth}$  corresponding to the equation (2) and  $\dot{f}_{nucleation}$  is described by a Gaussian curve:

$$\dot{f}_{nucleation} = \frac{f_N}{S_N \sqrt{2\pi}} \exp \left[ -\frac{1}{2} \left( \frac{\varepsilon_{eq}^{pl} - \varepsilon_N}{S_N} \right)^2 \right] \dot{\varepsilon}_{eq}^{pl} \quad (\text{A1.6b})$$

With:  $f_N$  void volume fraction created by nucleation,

$\varepsilon_N$  mean plastic strain at which nucleation is maximal,

$S_N$  standard deviation of the Gauss normal distribution.

Coalescence is taken into account in  $f^*$ .

Shear can be introduced by different ways. A simple one is to add a third component to the equation (A1.6a):

$$\dot{f} = \dot{f}_{nucleation} + \dot{f}_{growth} + \dot{f}_{shear} \quad (\text{A1.7})$$

$\dot{f}_{shear}$  is equivalent to  $\dot{f}_{nucleation}$  by replacing subscript N by SH and  $\dot{\varepsilon}_{eq}^{pl}$  by  $\dot{\varepsilon}_{xy}$ .

## ANNEX 2: Anisotropic damage models

### A.2.1 Continuum thermodynamics: anisotropic Lemaître's model

The damage coefficient, presented in the previous section and defined in an isotropic framework, is a scalar acting identically on all stress tensor components. Anisotropic states need a three-dimensional parameter [91]: a four-order tensor  $\mathbf{D}$ . The state potential, from P. Ladevèze's framework [157], is then written as follows :

$$\rho\psi_e^* = \frac{1+\nu}{2E} H_{ij} \sigma_{jk}^D H_{kl} \sigma_{li}^D + \frac{3(1-2\nu)}{2E} \frac{\sigma_H^2}{1-\eta D_H} + \alpha(T - T_{ref}) \sigma_{kk} \quad (\text{A2.1})$$

where

$$H_{ij} = (\mathbf{1} - \mathbf{D})_{ij}^{-1/2} \quad (\text{A2.2a, b})$$

$$\sigma_{ij}^D = \sigma_{ij} - \sigma_H \delta_{ij}$$

The effective stress tensor is expressed as:

$$\tilde{\sigma}_{ij} = \left( H_{ik} \sigma_{kl}^D H_{lj} \right)^D + \frac{\sigma_H}{1-\eta D_H} \delta_{ij} \quad (\text{A2.3})$$

The law of damage evolution will be a function of the effective elastic strain density, the scalar  $\bar{Y} = \int \tilde{\sigma}_{ij} d\varepsilon_{ij}^e$ , as in the isotropic case. Thus  $\bar{Y}$  is written as:

$$\bar{Y} = \frac{\tilde{\sigma}_{eq}^2 \tilde{R}_v}{2E} \quad (\text{A2.4})$$

with:

$$\tilde{R}_v = \frac{2}{3}(1+\nu) + 3(1-2\nu) \left( \frac{\tilde{\sigma}_H}{\tilde{\sigma}_{eq}} \right)^2 \quad \text{the effective triaxiality function} \quad (\text{A2.5})$$

where

$$\tilde{\sigma}_{eq} = \left( \mathbf{H} \boldsymbol{\sigma}^D \mathbf{H} \right)_{eq} = \left[ \frac{3}{2} \left( \mathbf{H} \boldsymbol{\sigma}^D \mathbf{H} \right)_{ij}^D \left( \mathbf{H} \boldsymbol{\sigma}^D \mathbf{H} \right)_{ij}^D \right]^{1/2} \quad (\text{A2.6a, b})$$

$$\tilde{\sigma}_H = \frac{\sigma_H}{1-\eta D_H}$$

### A.2.2 Framework of media porous plasticity

#### A.2.2.1 Damage-induced anisotropy: GLD model

This model, proposed by Gologanu, Leblond and Devaux (GLD) [157]-[161], considers an incompressible matrix in which microvoids volume, shape and orientation can change for an axisymmetric loading. Three parameters define it (Figure 180, with subscript 1 for the cavity and 2 for the matrix):

Microvoids volume fraction:

$$f = \frac{V_c}{V_t} = \frac{R_{y1} R_{x1}^2}{R_{y2} R_{x2}^2} \quad (\text{A2.7})$$

Microvoids shape factor:

$$S = \ln \left( \frac{R_{y1}}{R_{x1}} \right) \quad (\text{A2.8})$$

Void orientation is given by the vector  $\vec{y}$ .

The plastic potential is then defined as follows:

$$\psi = \frac{C}{\sigma_0} \left\| \sigma' + \eta \sigma_H X \right\|^2 + 2q(g+1)(g+f) \cosh\left(\frac{\kappa \sigma_H}{\sigma_0}\right) - (g+1)^2 - q^2(g+f)^2 = 0 \quad (\text{A2.9a})$$

With:  $\sigma'$  the deviatoric part of the stress tensor,

$$\| \cdot \| \text{ is the Von Mises norm: } \|T\| = \sqrt{\frac{3}{2} T_{ij} T_{ij}}, \quad (\text{A2.9b})$$

$$\sigma_H = \alpha_2(\sigma_{xx} + \sigma_{zz}) + (1 - \alpha_2)\sigma_{yy} \text{ the generalized hydrostatic pressure,} \quad (\text{A2.9c})$$

$$X = \frac{1}{3}(2e_y \otimes e_y - e_x \otimes e_x - e_z \otimes e_z) \quad (\text{A2.9d})$$

where  $(e_x, e_y, e_z)$  is an orthogonal frame with  $e_y$  parallel to the axisymmetric axis of the voids.

Parameters  $C, \eta, g, \kappa$  et  $\alpha_2$  are defined as functions of  $f$  and  $S$  [162], the latter depending on the void type (prolate or oblate, Figure 180 different according to the void type). The parameter  $q$  has been modified to depend on cavity shape (Figure 180)

$$q = 1 + 2(q_1 - 1) \frac{h}{1 + h^2} \text{ with } h = \exp(S) = \frac{R_{y1}}{R_{x1}} \text{ and } q_1 \text{ the Tvergaard parameter (4b) } (\text{A2.10a, b})$$

The evolution law has not changed: 
$$\dot{f} = (1 - f) \text{tr} \left( \dot{\varepsilon}_{pl} \right) \quad (\text{A2.11})$$

The GLD model takes into account damage anisotropy. As for the GTN model, a high number of parameters have to be identified (10 parameters). This can be done or accessible thanks to literature, microscopic analysis and mechanical tests combined to an inverse analysis.

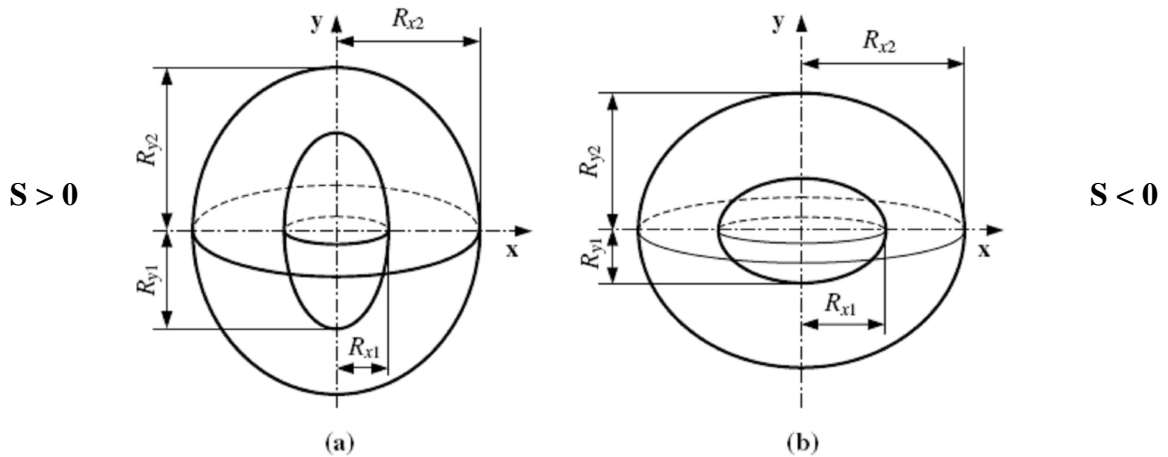


Figure 180 : Geometrical representation of a representative material volume: (a) prolate void shape and (b) oblate void shape [161]

### A.2.2.2 Material anisotropy: Croix's model

P. Croix and al. [163] analyse a case where anisotropy both induced by damage (cavity shape and orientation, treated as in the GLD model), but also by the properties of the matrix. In equation replaced by Hill's type one (1948). In plane stress it gives:

$$\sigma_{eq} = \left[ a^2 \sigma_{11}^2 + \left( b^2 + \frac{H+F}{2} - Hb \right) \sigma_{22}^2 + (2ab - Ha) \sigma_{11} \sigma_{22} + N \sigma_{12}^2 \right]^{1/2} \quad (\text{A2.12a})$$

With:  $a = 1 + \eta(1 - 2\alpha_2)$  and  $b = \eta\alpha_2$  and  $\alpha_2$  defined from eccentricity. (A2.12b, c)  
 Parameters  $a$  and  $b$  represent the part of the anisotropy which is induced by damage.  $f^*$  keeps the same equation as equation A1.5 and the volume fraction evolution is then decomposed in two terms: one corresponding of nucleation and the other one for growth, as for Gurson's model. Nine parameters have to be identified. For instance, the inverse analysis method with an experimental and numerical tensile test on notched specimens, as authors suggest.

### A.2.2.3 Void and inclusion: Siruguet and Leblond's model

An interesting anisotropic model is the one presented by K. Siruguet and J.B. Leblond [164]. Starting from the GLD model, they add the presence of an inclusion inside the void. Whereas void closure is predicted with Gologanu's model in the low triaxiality rate, Siruguet predicts a growth, which has been experimentally observed. This is done by using locking condition at the void boundaries, depending on void shape. (Figure 181):

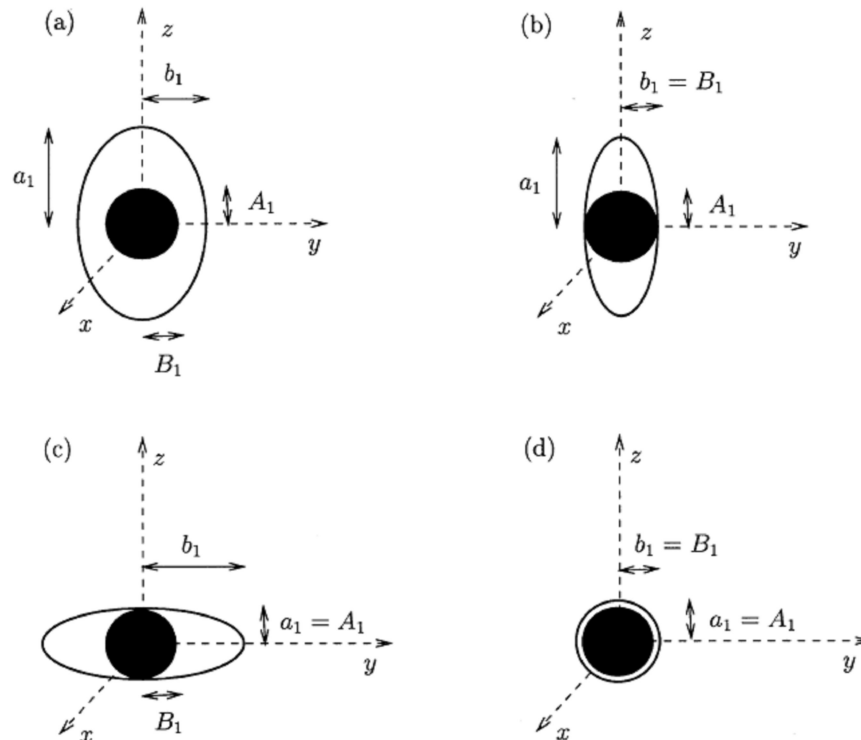


Figure 181 : Locking conditions: (a) no contact (b) radial contact (c) axial contact (d) full contact [164]

The plastic potential law only changes:

$$\psi^I = \frac{C^I}{\sigma_0^2} \left\| \sigma^I + \eta^I \sigma_H^I X^I \right\|^2 + 2q(g+1)(g+f) \cosh\left(\frac{\kappa^I \sigma_H^I}{\sigma_0}\right) - (g+1)^2 - q^2(g+f)^2 = 0 \quad (\mathbf{A2.13})$$

$C^I$ ,  $\eta^I$ ,  $\kappa^I$  and  $\alpha_2^I$  are the new parameters taking into consideration an inclusion depending on locking conditions.

## ANNEX 3: Fields and Backofen method for the stress-strain curves

### A.3.1 Hypotheses

This method is only valid in the plastic domain and there are several hypotheses:

- Isothermal tests,
- Homogeneous and isotropic material (not our case, but corrections can be applied),
- Sample entirely plastified,
- Uniform deformation along the sample, i.e. no flow localization,
- Diameter from a vertical section remains rectilinear,
- Transverse sections remain straight (no displacement along the z-axis) and turn in a rigid body movement at  $\omega$ -speed (deformation obtained by shear of straight sections)

### A.3.2 Strain-rotation number relation

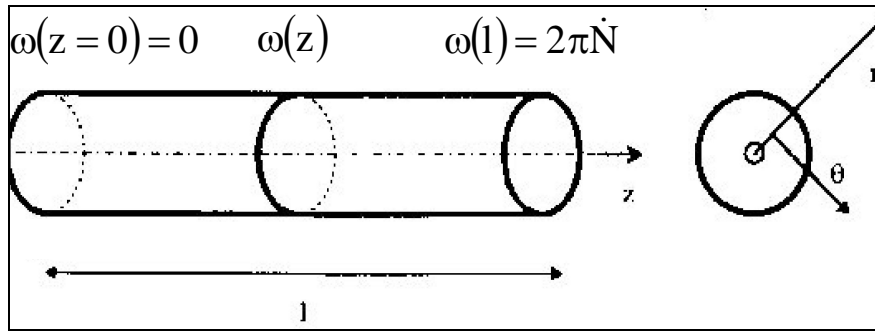


Figure 182: Geometry and notation definition

The analysis concerns a lateral surface at  $r = R$ .

The velocity field in the sample is written as follows:

$$\begin{cases} v_r = 0 \\ v_\theta = \omega(z)R = (2\pi\dot{N})\frac{z}{l}R \\ v_z = 0 \end{cases} \quad (\text{A3.1a, b, c})$$

The strain rate tensor is then written:

$$\underline{\underline{\dot{\varepsilon}}}(R) = \begin{bmatrix} 0 & 0 & 0 \\ 0 & 0 & \frac{\pi\dot{N}R}{l} \\ 0 & \frac{\pi\dot{N}R}{l} & 0 \end{bmatrix} \quad (\text{A3.2})$$

The generalized strain rate, knowing that  $\dot{\varepsilon} = \sqrt{\frac{2}{3}(\underline{\underline{\dot{\varepsilon}}} : \underline{\underline{\dot{\varepsilon}}})}$ , is:

$$\dot{\bar{\varepsilon}}(R) = \sqrt{\frac{2}{3} \times 2 \times \left( \frac{\pi \dot{N} R}{l} \right)^2} = \frac{2}{\sqrt{3}} \frac{\pi \dot{N} R}{l} \quad (\text{A3.3})$$

Finally, thanks to the following relation: 
$$\bar{\varepsilon}(x(x_0, t)) = \int_{t_0}^t \dot{\bar{\varepsilon}}(x(x_0, \tau)) d\tau \quad (\text{A3.4})$$

the equivalent deformation is:

$$\bar{\varepsilon}(R) = \int_0^t \frac{2}{\sqrt{3}} \frac{\pi \dot{N} R}{l} d\tau = \frac{2}{\sqrt{3}} \quad (\text{A3.5})$$

### A.3.3 Stress-torque relation

For this mechanical test, the stress tensor has the following shape:

$$\underline{\underline{\sigma}} = \begin{bmatrix} 0 & 0 & 0 \\ 0 & 0 & \sigma_{\theta_z} \\ 0 & \sigma_{\theta_z} & 0 \end{bmatrix} \quad (\text{A3.6})$$

The measured torque is given by the relation:

$$\Gamma = \int_0^R \int_0^{2\pi} \sigma_{\theta_z} \cdot r \cdot r dr d\theta = \int_0^R \sigma_{\theta_z} \cdot 2\pi \cdot r^2 \cdot dr \quad (\text{A3.7})$$

### A.3.4 Fields and Backofen

The shear yield stress  $\sigma_{\theta_z}(R)$  is only a function of  $\bar{\varepsilon}$  and  $\dot{\bar{\varepsilon}}$ , equivalent to  $N$  and  $\dot{N}$ :

$$\left\{ \begin{array}{l} \sigma_{\theta_z}(R) = \frac{\Gamma(R)}{2\pi R^3} (\tilde{m} + \tilde{n} + 3) \\ \tilde{m} = \left( \frac{\partial \ln \Gamma}{\partial \ln \dot{N}} \right)_N \\ \tilde{n} = \left( \frac{\partial \ln \Gamma}{\partial \ln N} \right)_{\dot{N}} \end{array} \right. \quad (\text{A3.8a, b, c})$$

- $\tilde{m}$  and  $\tilde{n}$  are graphically determined
- They are supposed to be a constant
- They respectively correspond to:
  - The slope of the local tangent to the curve  $\ln(\Gamma) - \ln(\dot{N})$  (at a given rotation number):

$$\tilde{m} = \left( \frac{\partial \ln \Gamma}{\partial \ln \dot{N}} \right)_N \quad (\text{A3.9})$$

In our case, only two torsion tests have been done at one deformation speed. Thus, a simple hypothesis, but possible at room temperature, is  $\tilde{m} = 0$ .

- The slope of the local tangent to the curve  $\ln(\Gamma)-\ln(N)$  for a given rotation

speed:

$$\tilde{n} = \left( \frac{\partial \ln \Gamma}{\partial \ln N} \right)_{\dot{N}} \quad (\text{A3.10})$$

From the Figure 59, it is very simple to obtain the  $\ln(\Gamma)-\ln(N)$ , shown in Figure 183

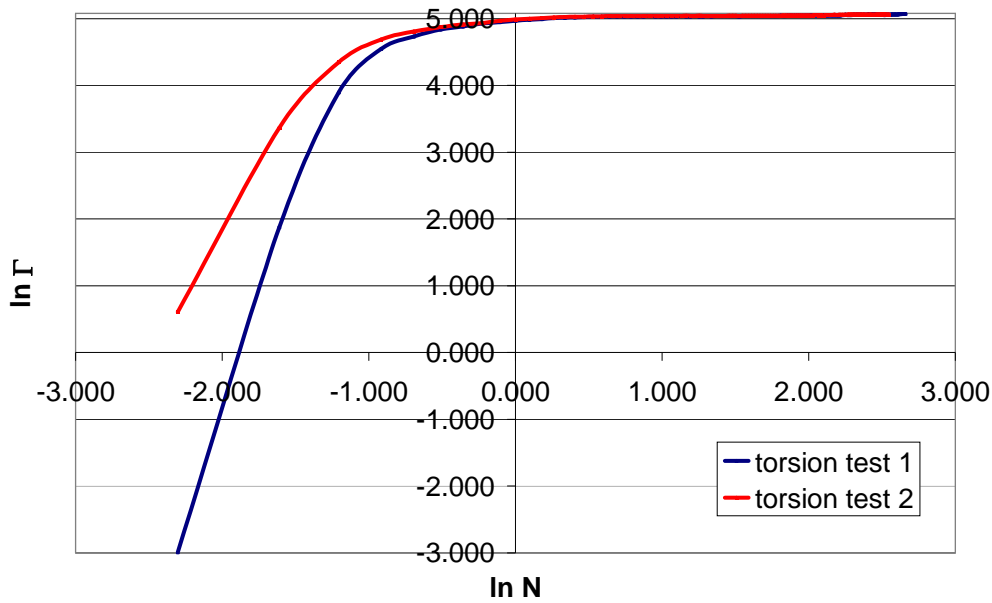


Figure 183:  $\ln(\Gamma)-\ln(N)$  curve

Now, the slopes have to be identified on the linear part of the curve, i.e. from  $\ln N = 0$ . This is done in order to eliminate the elastic part, the elastic-plastic transition, as well as the non-linearity due to clearances and due to the torsion test device behaviour. We are only focused on the established macroscopic plastic part, which is the only part taken into account in the Fields and Backofen analysis.

Figure 184 enables us to identify slopes  $p_1 = 0.0192$  and  $p_2 = 0.0216$ . Thus, the two constants are:

$$\begin{aligned} \tilde{n}_1 &= 0.0192 \\ \tilde{n}_2 &= 0.0216 \end{aligned} \quad (\text{A3.11})$$

And:

$$\begin{cases} \sigma_{\theta_z}(R) = \frac{\Gamma(R)}{2\pi R^3} (\tilde{m} + \tilde{n} + 3) \\ \tilde{m} = 0 \\ \tilde{n}_1 = 0.0192 \\ \tilde{n}_2 = 0.0216 \end{cases} \quad (\text{A3.12a, b, c, d})$$

Finally, the stress-strain curves can be plotted with the two following equations (only valid in the plastic part):

$$\begin{cases} \sigma_{\theta_z}(R) = \frac{\Gamma(R)}{2\pi R^3} (\tilde{m} + \tilde{n} + 3) \\ \bar{\varepsilon}(R) = \frac{2}{\sqrt{3}} \frac{\pi NR}{l} \end{cases} \quad (\text{A3.13a, b})$$

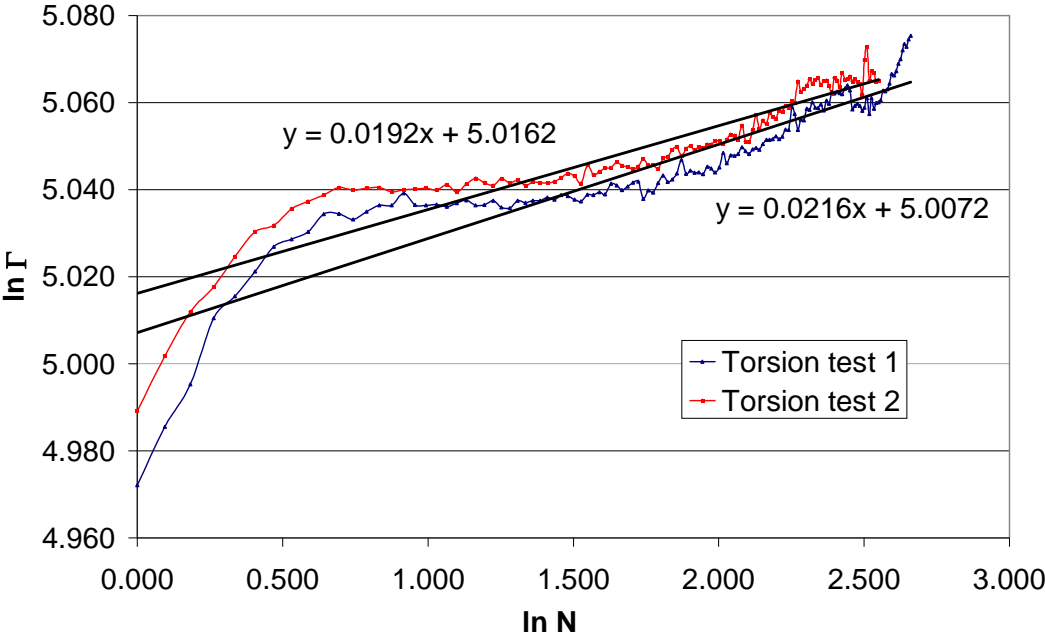


Figure 184: Zoom on the linear part of the Ln(Γ)-Ln(N) curve with the linear tendency curves

## ANNEX 4: Explicative notice of a Focused Ion Beam (FIB)

### A.4.1 Functioning principle of a FIB

Focused ion beam systems have been commercially produced for ten years, principally for semi-conductor industries. It works as a SEM but uses focused gallium ions beam. The ion beam can be used at low intensity for pictures or at high intensity for pulverization or for site-specific cutting.

As shown in Figure 185, the gallium primary ion beam ( $\text{Ga}^+$ ) hits the sample surface and a small quantity of material is atomized, which leaves the surface either as secondary ions ( $i^+$  or  $i^-$ ) or as neutral atoms ( $n^0$ ). The primary beam also produces secondary electrons ( $e^-$ ). As the primary beam scans the sample surface, the ion or secondary electron signal is collected to form a picture.

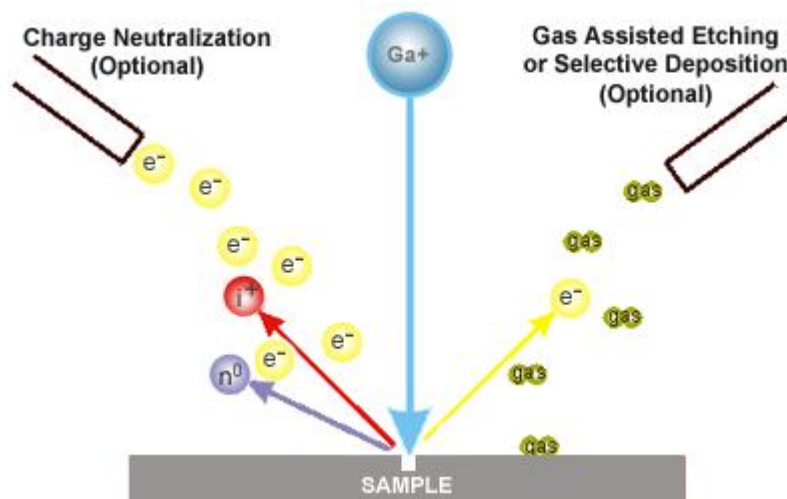


Figure 185: Functioning sketch of a FIB

At low primary beam intensity, a very small amount of material is atomized; modern FIB can reach 5nm of picture resolution. At high primary intensity, a huge volume of material can be taken off, enabling a precise cutting with a scale lower than the micron.

Moreover, an option in the FIB enables the user to locally flood the sample with a gas. This one can interact with the primary beam in order to produce an assisted-gas chemical attack or a selective deposition of an insulated or conductor material.

Up to a recent date, the use of FIB has been done in semi-conductors industries. Applications like defects analysis, circuit modification, and sample preparation for TEM are now usual. Recent developments enable the association between an ion beam and an electron beam. The major advantage is the observation and the acquisition of pictures without degradation of the surface.

#### A.4.2 Site-specific cutting procedure

The site-specific cutting procedure can be decomposed in seven steps:

- a. Obcentricity point definition (rotation point of the sample enable a stable focusing of the concerned area).
- b. Protective layer deposition: a 1 $\mu\text{m}$  platinum protective layer is deposited as shown in Figure 186.

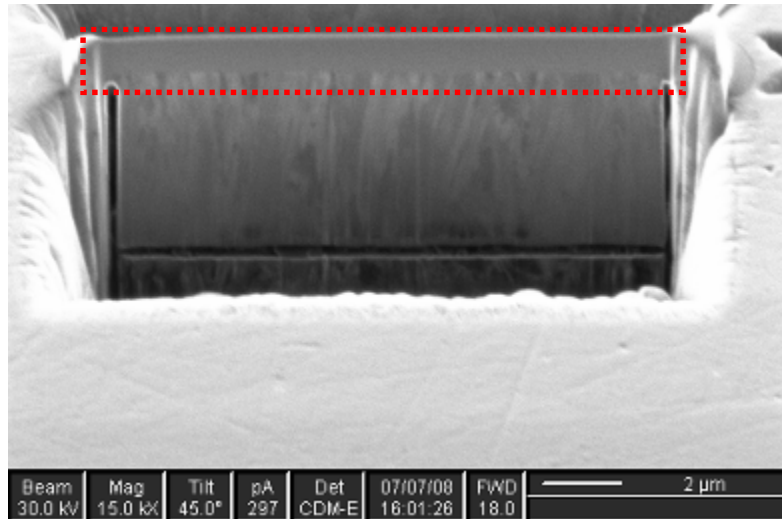


Figure 186: Platinum protective layer deposition

- c. For the automatization of the procedure, two crosses are placed at each side of the zone and are illustrated in Figure 187.

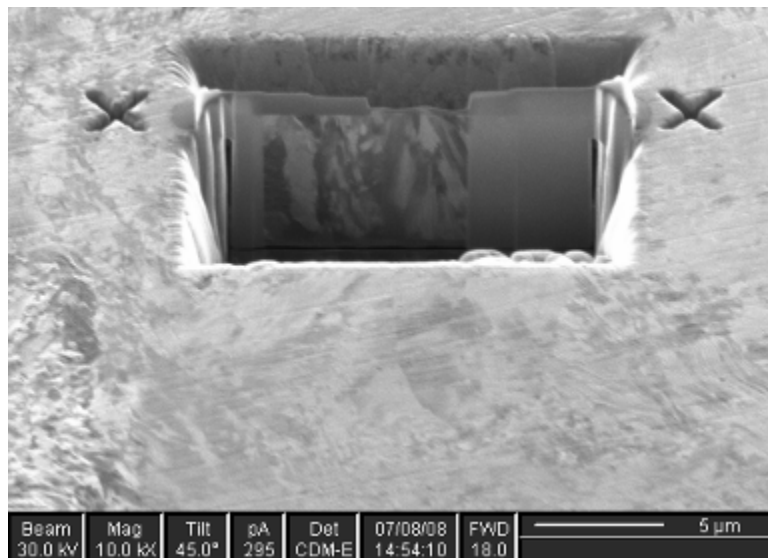
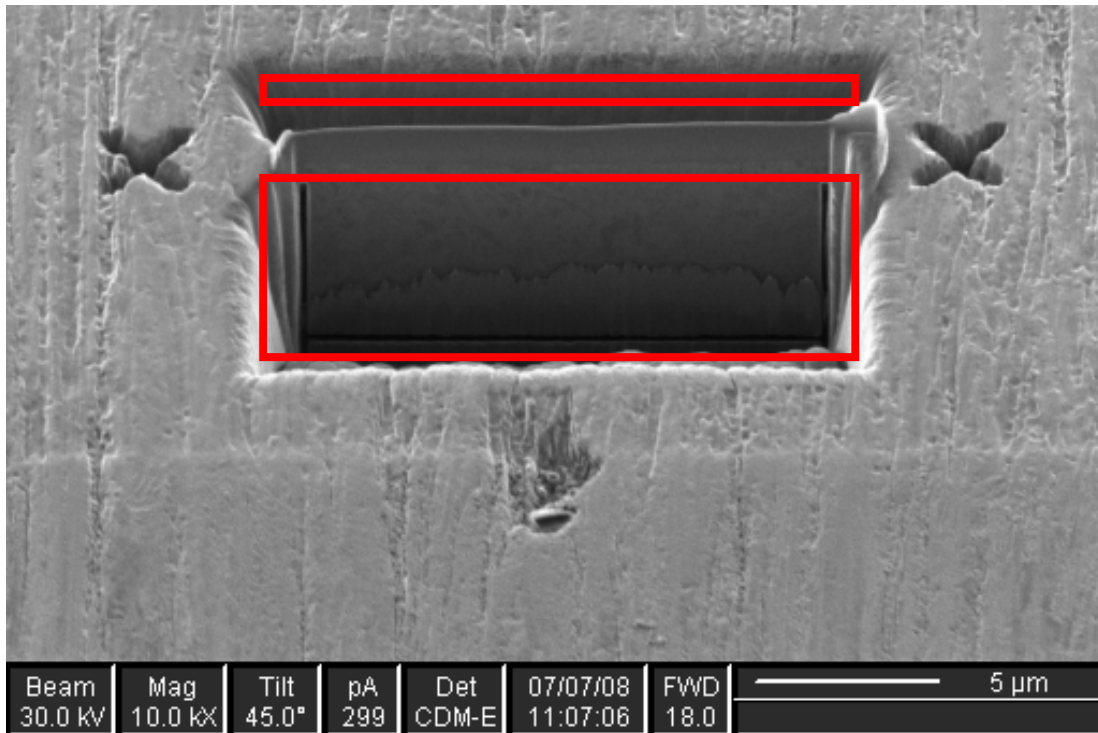


Figure 187: Position of the crosses for the automatic procedure

- d. Use of large beam (high intensity  $\sim 500$  pA) to remove a huge amount of material. Then, 300 pA is used when the layer becomes thin. The Figure 188 shows the eroded zone of both sides of the thin layer (45° view).



**Figure 188: Definition of the work window for the thin layer trimming**

- e. For a deep atomization and a partial cut of the thin layer, the sample is tilted from  $-1^\circ$  to  $+1^\circ$ . This partial cut enables to let go the residual internal stresses. Figure 189 shows the remaining material to maintain the layer.

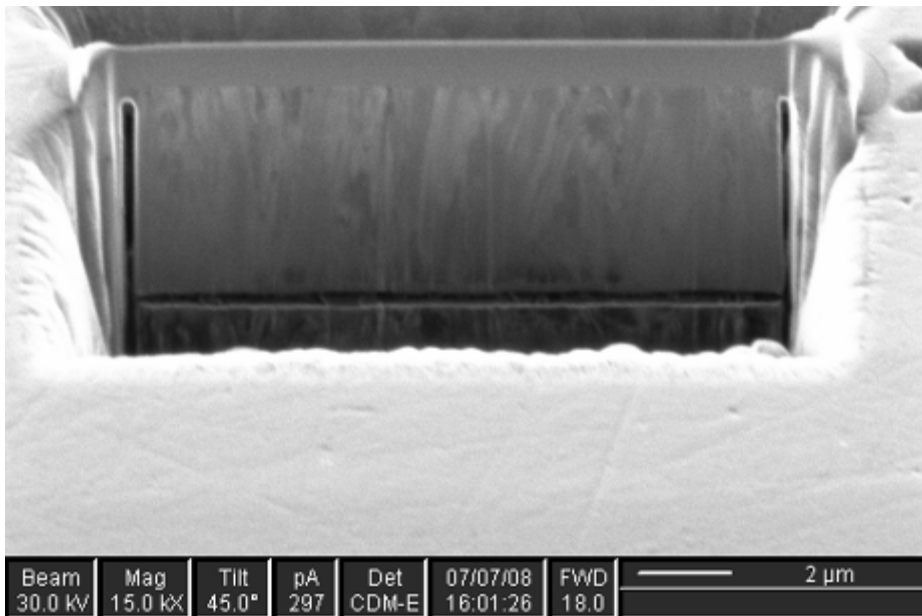


**Figure 189: Sample tilting for a deep thinning and a partial cut**

- f. Manual finishing at 100 pA and 50 pA: The thinning is made at the centre of the layer in order to have a better stability and to prevent the formation of longitudinal waves.

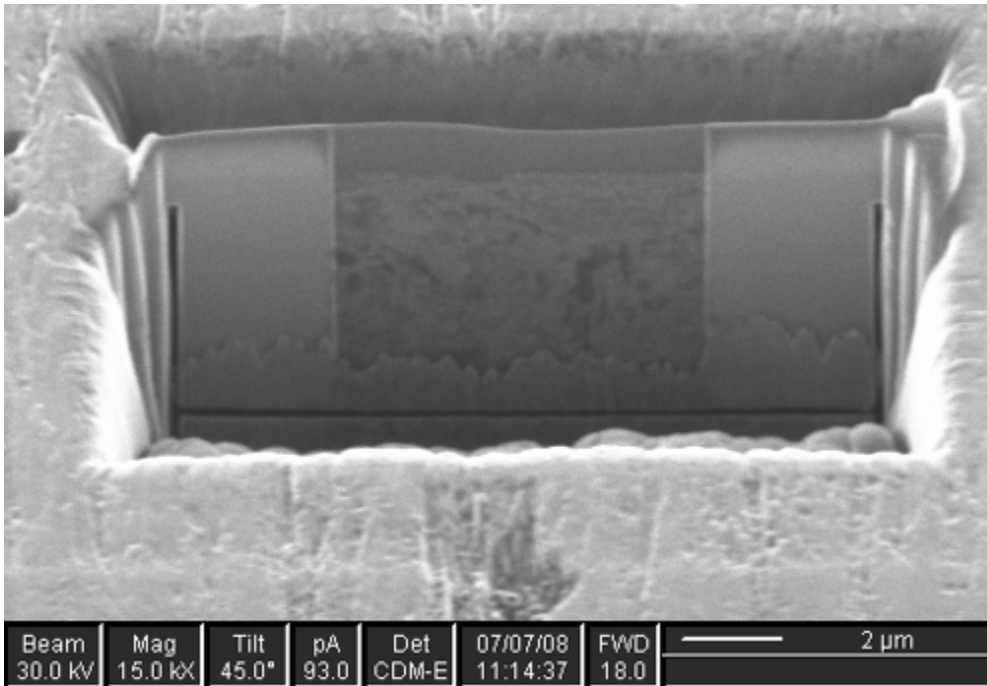


**Figure 190: Manual thinning at the centre of the layer**

- g. Final cut at 300 pA. The two remained strips are cut as shown in Figure 191 and the thin layer falls back (Figure 192).

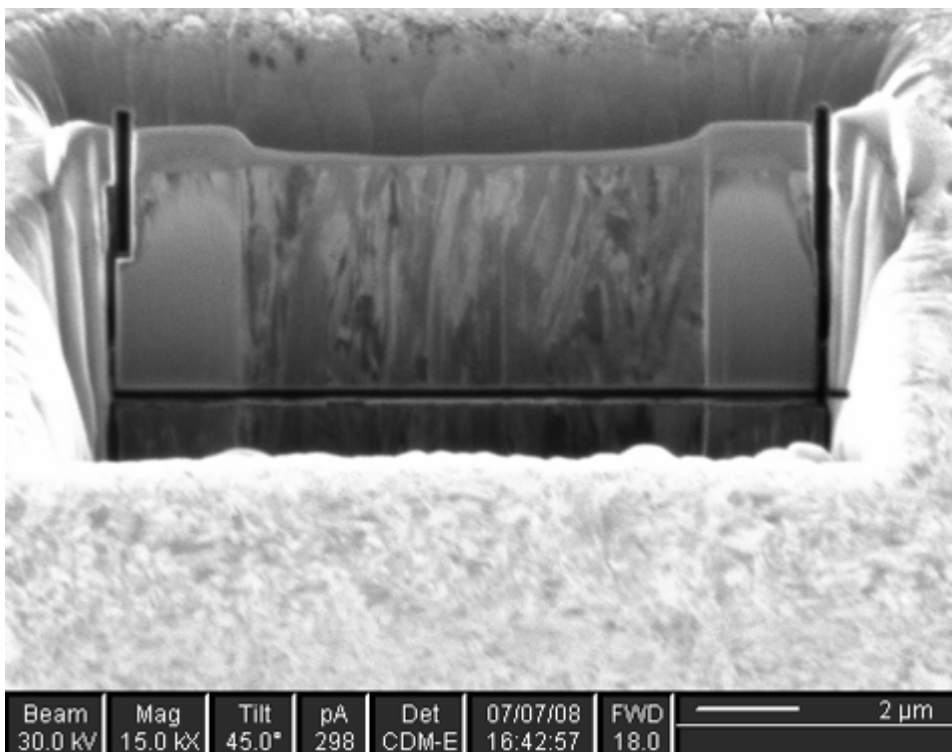


**Figure 191: final cut**

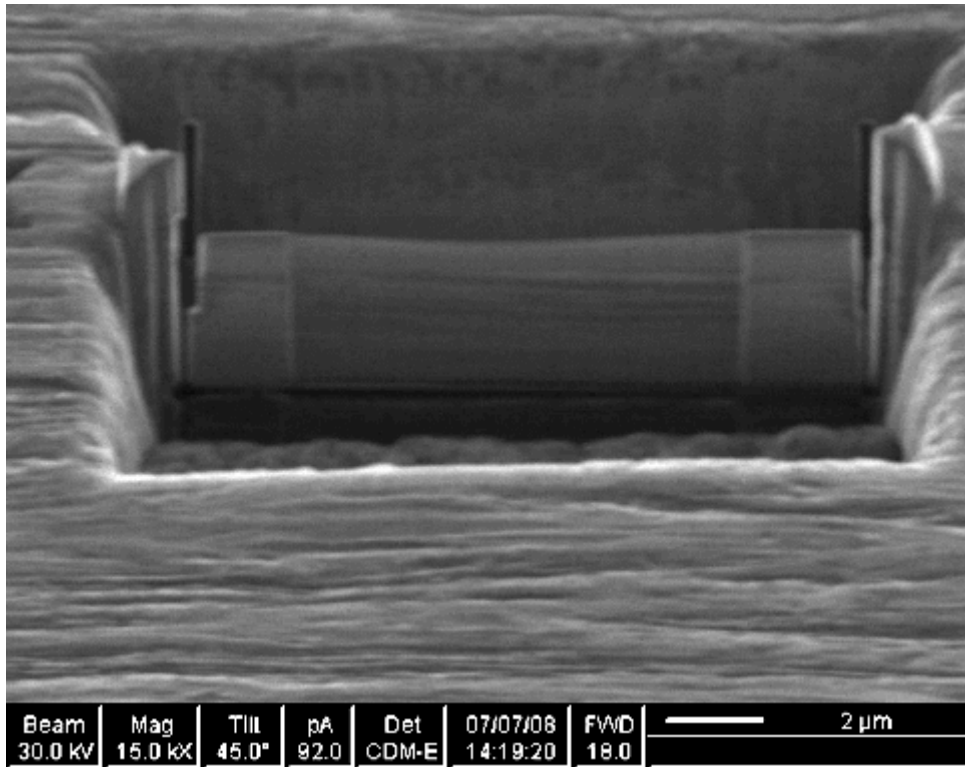


Figure 192: Inclination of the thin layer after successful cut

After removing the samples from the FIB, the cut thin layer is get back thanks to a glass tail with a curvature of  $1\mu\text{m}$  by electrostatism.

# References

- [1] Materials Science and Metallurgy, 4th ed., Pollack, Prentice-Hall, 1988.
- [2] D.S. Zhou and G.J. Shiflet, Ferrite:Cementite crystallography in pearlite, (1992) *Metal. Trans. A*, 23:1259-1269.
- [3] T. Massé and C. Bobadilla, Damage / anisotropy study – Structural Analysis of a high carbon steel wire, (2007) Report R&D ArcelorMittal Gandrange Long Carbon – Bars and Wires, R°155.
- [4] N. Persem, Endommagement et rupture lors du laminage à plat de fils d’acier haut carbone, (2006) Master Report, CEMEF – ENSMP, In French.
- [5] C. Bobadilla, N. Persem and S. Foissey, Modelling of the drawing and rolling of high carbon flat wires, (2007) In AIP Conference, 907:535-540.
- [6] G. Simonnet, Tréfilage de l’acier, (1996) *Techniques de l’Ingénieur, Traité Matériaux Métalliques*, In French, Article M645.
- [7] P. Montmitonnet, Laminage – Objectif et Modélisation, (2002) *Techniques de l’Ingénieur, Traité Matériaux métalliques*, In French, Article M3065.
- [8] J.D. Embury and R.M. Fisher, The structure and properties of drawn pearlite, (1966) *Acta Met.*, 14:147-159.
- [9] G. Langford, Deformation of pearlite, (1977) *Met. Trans.*, 8A:861-875.
- [10] D.A. Porter, K.E. Easterling and G.D.W. Smith, Dynamic studies of the tensile deformation and fracture of pearlite, (1978) *Acta Met.*, 26:1405-1422.
- [11] Wong Jong Nam, Chul Min Bae, Sei J. Oh, and Soon-Ju Kwon, Effect of interlamellar spacing on cementite dissolution during wire drawing of pearlitic steel wires, (2000) *Scripta Mat.*, 42:457–463.
- [12] J. Toribio, B. Gonzalès, J.C. Matos, Fatigue crack propagation in cold drawn steel, (2007) *Mat. Sci. Eng. A* 468-470, 267-272.
- [13] J.J. Heizmann, A. Abdellaoui, B. Bolle, J.B. Pelletier, L. Peeters, Crystallographic texture of pearlitic steel wires, (1997) *Proc. and Appl. of Metal Wires*, 163-173.
- [14] J. Languillaume, G. Kapelski, B. Baudelet, Cementite dissolution in heavily cold drawn pearlitic steel wires, (1997) *Acta Met.*, 45:1201-1212.
- [15] M. Zelin, Microstructure evolution in pearlitic steels during wire drawing, (2002) *Acta Mat.*, 50:4431–4447.

- [16] F. Yang, C. Ma, J.Q. Jiang, H.P. Feng and S.Y. Zhai, Effect of cumulative strain on texture characteristics during wire drawing of eutectoid steels, (2008) *Scripta Mat.* 59:850–853.
- [17] B. Devincere, T. Hoc and L. Kubin, Dislocation mean free path and strain hardening of crystals, (2008) *Science* 320:1745-1748.
- [18] V.I. Izotov, V.A. Pozdnyakov, E.V. Luk'yanenko, O. Yu. Usanova and G.A. Filippov, Influence of the pearlite fineness on the mechanical properties, deformation behavior, and fracture characteristics of carbon steel, (2007) *Phys. Met. Metallogr.*, Vol. 103, 5:519-529.
- [19] M. Emmerich, A. Giotis, M Ozdemir, T. Bäck and K.Giannakoglou, Metamodel-assisted evolution strategies, (2002) In: *Proc. of the Intern. Conf. on Parallel Problem Solving from Nature*.
- [20] W. T. Lankford, S. C. Snyder, J. A. Bausher, New criteria for predicting the press performance of deep drawing sheets, (1950) *Trans. ASM*, 42:1197–1205.
- [21] Heat-treatment of High Carbon Steel Wire – Patenting, article from [www.key-to-Steel.com](http://www.key-to-Steel.com), <http://steel.keytometals.com/Articles/Art52.htm#top>.
- [22] J. Toribio and E. Ovejero, Effect of cumulative cold drawing on the pearlite interlamellar spacing in eutectoid steel, (1998) *Scripta Mat.*, 39:323–328.
- [23] C. Cordier-Robert, B. Forfert, B. Bolle, J-J Fundenberger and A. Tidu, Influence of torsion deformation on microstructure of cold-drawn pearlitic steel wire, (2008) *J. Mater. Sci.* 43:1241-1248.
- [24] K. Shimizu and N. Kawabe, Fracture mechanics aspects of delamination occurrence in high-carbon steel wire. (2001) In: *Proc. of 71st Wire & Cable Technical Symposium*, Guilford, USA: The Wire Assoc Intl, pp35.
- [25] F. Zok and J.D. Embury, On the fracture analysis of delamination fractures in high-strength steels, (1990) *Met. Trans. A*, 21:2565-2575.
- [26] Chul Min Bae, Won Jong Nam, and Chong Soo Lee, Effect of interlamellar spacing on the delamination of pearlitic steel wires, (1996) *Scripta Mat.*, 35:641-646.
- [27] M. Yilmaz, Failures during the production and usage of steel wires, (2005) *J. Mat Proc. Tech.*, 171:232-23.
- [28] S. Tandon, P. Deshmukh, R.S. Mishra, K. Krishnamurthy and R. Tayloe, Fracture criteria prediction in wire drawing using finite element modelling, (2006) *Wire Journal International*, 58-62.

- [29] L. Kubin et al., Modeling dislocation storage rates and mean free paths ..., (2008) *Acta Mat*, doi:10.1016/j.actamat.2008.08.012.
- [30] V.G. Gavriljuk, Decomposition of cementite in pearlitic steel due to plastic deformation (2003) *Mater. Sci. Eng. A* 345(1–2):81-89.
- [31] K. Hono, M. Ohnuma, M. Murayama, Cementite decomposition in heavily drawn pearlite steel wire, (2001) *Scripta Mat.*, 44:977-983.
- [32] F. Danoix, D. Julien, X. Sauvage, J. Copreaux, Direct evidence of cementite dissolution in drawn pearlitic steels observed by tomographic atom probe, (1998) *Mat. Sci. Eng. A* 250:8-13.
- [33] Zhi-qing Lv, Ping Jiang, Zhen-hua Wang, Wen-hui Zhang, Shu-hua Sun, Wan-tang Fu, XRD analyses on dissolution behavior of cementite in eutectoid pearlitic steel during cold rolling, (2008) *Materials Letters*, 62:2825-2827.
- [34] J. Languillaume, G. Kapelski, B. Baudalet, Cementite dissolution in heavily cold drawn pearlitic steel wire, (1997) *Acta Mat.* 45:1201-1212.
- [35] Yu. Ivanisenko, W. Lojkowski, R.Z. Valiev, H.-J. Fecht, The mechanism of formation of nanostructure and dissolution of cementite in pearlitic steel during high pressure torsion, (2003) *Acta Mat.*, 51:5555-5570.
- [36] N. Maruyama, T. Tarui, H. Tashiro, Atom probe study on the ductility of drawn pearlitic steels, (2002) *Scripta Mat.* 46:599-603.
- [37] S. Tagashira, K. Sakai, T. Furuhashi and T. Maki, Deformation Microstructure and Tensile Strength of Cold Rolled Pearlitic Steel Sheets, (2000) *ISIJ International*, Vol. 40, 11:1149–1155.
- [38] X. Zhang, C.X. Wang, X.M. Liu and Q.N Shi, Microstructure evolution and mechanical hardening of hypereutectoid pearlitic steel during cold rolling, (2007) *Acta Met. Sinica*, Vol. 20, 4:287-292.
- [39] T. Takahashi, M. Nagumo and Y. Asano, (1978) *J. Jpn. Inst. Met.*, Vol. 42, 708.
- [40] F. Wetscher, R. Stock and R. Pippan, Changes in the mechanical properties of a pearlitic steel due to large shear deformation, (2007) *Mat. Sci. Eng. A* 445-446, 237-243.
- [41] Hyung Rak Song, Eui Goo Kang, Won Jong Nam, Effect of alloying elements on work hardening behavior in cold drawn hyper-eutectoid steel wires, (2007) *Mat. Sci. Eng. A* 449–451:1147–1150.

- [42] D. Park, E.G. Kang, W.J Nam, The prediction of the occurrence of the delamination in cold drawn hyper-eutectoid steel wires, *J. Mater. Process. Tech.*, 187-188 (2007)178-181.
- [43] J.G. Sevillano, (1979) in: *Proceedings of the 5<sup>th</sup> International Conference on the Strength of Metals and Alloys (ICSMA5)*, eds. P. Haasen, V. Gerold, and G. Kostorz (Pergamon Press, Oxford, UK, pp819.
- [44] J.G. Sevillano, Substructure and strengthening of heavily deformed single and 2-phase metallic materials, (1991) *J. Phys. III France* 1:967.
- [45] O. Bouaziz and C. Le Corre, Flow stress and microstructure modelling of ferrite-pearlite steels during cold rolling, (2003) *Mater. Sci. Forum* 1399:426-432.
- [46] A. Milenin, Z. Muskalski, S. Wiewiórowska, P. Kustra, The Multi-scale FEM simulation of the drawing processes of high carbon steels, (2007) *Journal of Achievements in Materials and Manufacturing Engineering*, Vol. 23, 2:71-74.
- [47] A. Milenin, Z. Muskalski, The FEM simulation of cementite lamellae deformation in pearlitic colony during drawing of high carbon steel, *Numiform '07, Materials Processing and Design: Modeling, Simulation and Applications*.
- [48] A. Gaillac, Endommagement d'alliages de Zirconium, Impact sur la laminabilité, (2007) PhD report, Laboratoire SIMaP, Institut National Polytechnique de Grenoble, In French.
- [49] G. Proust, C.N. Tomé, G.C. Kaschner, Modeling texture, twinning and hardening evolution during deformation of hexagonal materials, (2007) *Acta Mat.*, 55:2137-2148.
- [50] M. Kazeminezhad, A. Karimi Taheri, A. Kiet Tieu, A study on the cross-sectional profile of flat rolled wire, (2008) *J. Mat Proc. Tech.*, 200:325-330.
- [51] M. Kazeminezhad, A. Karimi Taheri, The prediction of macroscopic shear bands in flat rolled wire using the finite and slab element method, (2006) *Materials Letters* 60:3265–3268.
- [52] M. Kazeminezhad, A. Karimi Taheri, The effect of 3D and 2D deformations on flattened wires, (2008) *J. Mat. Proc. Tech.*, 202:553-558.
- [53] FD Fischer, H Clemens, T Schaden and F Appel, Compressive deformation of lamellar microstructures – a short review, (2007) *Int. J. Mat. Research*, Vol. 98, 11:1041-1046.
- [54] R. Lebensohn, J. Signorelli and H. Uhlenhut, Multiscale modelling of lamellar structures: Applications to g-TiAl-based alloys, In: *19th. RISO International Symposium on Materials Science: Modelling of Structure and Mechanics of Materials*

- from Microscale to Product, (1998) Proc. of Modelling of Structure and Mechanics of Materials from Microscale to Product, 331-337.
- [55] H. Tresca, Mémoire sur l'écoulement des solides, (1868), Vol. 18, 733-799, In French.
- [56] R. Von Mises, Mechanik der plastischen Formmnderung von Kristallen, (1928) Z. Angew Math. Mech. 8:161-185.
- [57] A.V. Hershey, The plasticity of an isotropic aggregate of anisotropic face centred cubic crystals, (1954) J. Appl. Mech., 21:241–249.
- [58] W.F. Hosford, A generalized isotropic yield criterion, (1972) J. Appl. Mech. Trans. ASME 39:607–609.
- [59] W.F. Hosford, On the crystallographic basis of yield criteria, (1996) Textures Microstruct. 26-27:479-493.
- [60] M.H. Yu, Advances in strength theories for materials under complex stress state in the 20th Century, (2002) Appl. Mech. Rev. 55:169–218.
- [61] R. Hill, A theory of the yielding and plastic flow of anisotropic metals, (1948) In Proc. Royal Soc. Of London, A193:281-297.
- [62] R. Hill, Theoretical plasticity of textured aggregates, (1979) Math. Proc. Camb. Phil. Soc., 85(1):179–191.
- [63] W.F. Hosford, On yield loci of anisotropic cubic metals, (1979) In: Proc. of the 7th north American metalworking conference, Dearborn, MI: SME; 191-7
- [64] K. Mattiasson and M. Sigvant, An evaluation of some yield criteria for industrial simulations of sheet forming processes, (2007) Int. J. Mech. Sci., 50:774-787.
- [65] M. Ben Tahar, Contribution à l'étude et la simulation du procédé d'hydroformage, (2005) Thesis report, CEMEF –MinesParistech, In French.
- [66] F. Barlat, O. Cazacu, M. Zyczkowski, D. Banabic, J.W. Yoon, Yield surface plasticity and anisotropy, (2004) In: Raabe D, et al., editors, Continuum scale simulation of engineering materials: fundamentals microstructure-process applications. Berlin: Wiley-VCH., 145–85.
- [67] W. Hu, A novel quadratic yield model to describe the feature of multi-yield-surface of rolled sheet metals, (2007) Int. J. Plast. 23 :2004-2028.
- [68] F. Barlat, J. Lian, Plastic behavior and stretchability of sheet metals-part I: a yield function for orthotropic sheets under plane stress conditions, (1989) Int. J. Plasticity, 5:51–66.
- [69] A.P. Karafillis, M.C. Boyce, A general anisotropic yield criterion using bounds and a transformation weighting tensor, (1993) J. Mech. Phys. Solids, 41:1859–86.

- [70] M. Darrieulat and F. Montheillet, A texture based continuum approach for predicting the plastic behaviour of rolled sheet, (2003) *Int. J. Plasticity*, 19 :517-546.
- [71] F. Bron and J. Besson, A yield function for anisotropic materials application to aluminium alloys, (2004) *Int. J. Plasticity*, 20 :356-364.
- [72] D. Banabic, H. Aretz, D.S. Comsa, L. Paraianu, An improved analytical description of orthotropy in metallic sheets, (2005) *Int. J. Plasticity*, 21:493–512.
- [73] O. Cazacu, B. Plunkett, F. Barlat, Orthotropic yield criterion for hexagonal closed pack metals, (2006) *Int. J. Plasticity*, 22:1171-1194.
- [74] F. Barlat, J.W. Yoon, O. Cazacu, (2007) On linear transformations of stress tensors for the description of plastic anisotropy, *Int. J. Plasticity*, 23:876–96.
- [75] M. Kuroda and V. Tvergaard, Forming limit diagrams for anisotropic metal sheets with different yield criteria, (2000) *Int. J. Solids Struct.*, 37:5037-5059.
- [76] H. Vegter, Y. An, H.H. Pijlman, J. Huetink, Advanced mechanical testing on aluminium alloys and low carbon steels for sheet forming, (1999) In: Gelin JC, Picart P, editors. *Proceedings of NUMISHEET'99*, Besancon, France, 3–8.
- [77] H. Vegter, Y. An, H.H. Pijlman, J. Huetink, Different approaches to describe the plastic material behaviour of steel and aluminium-alloys in sheet forming, (1999) In: Covas JA, editor, *Proceedings of the 2nd ESAFORM conference on material forming*, Guimaraes, Portugal, 127–32.
- [78] H. Vegter, A.H. van den Boogaard, A plane stress yield function for anisotropic sheet material by interpolation of biaxial stress states, (2006) *Int. J. Plasticity*, 22:557–80.
- [79] W. Tong, H. Tao, X. Jiang, Modeling the rotation of orthotropic axes of sheet metals subjected to off-axis uniaxial tension, (2004) *J. Appl. Mech.* 71:521–31.
- [80] W. Tong, A plane stress anisotropic plastic flow theory for orthotropic sheet metals, (2006) *Int. J. Plasticity*, 22:497–535.
- [81] F. Montheillet, L. Briottet, Endommagement et ductilité en mise en forme, (1998) *Techniques de l'Ingenieur*, In French, Article M601.
- [82] P.O. Bouchard, L. Tollier, Modélisation numérique du procédé de rivetage autopoinçonneur, (2005) *Techniques de l'Ingénieur*, In French, Article BM7860.
- [83] J.F. Mariage, Simulation numérique de l'endommagement ductile en formage de pièces massives, (2003) PhD report, Université Technologique de Troyes, In French.
- [84] C. Dumont, Endommagement de métaux à matrice ductile en traction quasistatique et dynamique, (1991) PhD report, Centre de Mise En Forme des Matériaux (CEMEF), In French.

- [85] F.A. McClintock, A criterion for ductile fracture by growth of holes, (1968) *J. Applied Mech.*, 363-371.
- [86] J.R Rice and D.M. Tracey, On the ductile enlargement of voids in triaxial stress fields, (1969), *J. Mech. Phys Solids*, 17:201-217.
- [87] B. Budiansky, J.W. Hutchinson and S. Slutsky, Void growth and collapse in viscous solid, (1982) *The Rodney Hill 60th anniversary volume*, Ed. Hopkins H.G., Sewell M.J., 13-34.
- [88] Y. Bao, T. Wierzbicki, A comparative study on various ductile crack formation criteria, (2004) *J. Eng. Mat. Tech.*, 126:314-324.
- [89] L. M. Kachanov, On the time to rupture under creep conditions, (1958) *Izv. Acad. Nauk SSSR, OTN*, 8:26-31.
- [90] J. Lemaître, How to use damage mechanics, (1984) *Nuclear Engineering and Design* 80:233-245.
- [91] J. Lemaitre and R. Desmorat, *Engineering Damage Mechanics: Ductile, Creep, Fatigue and Brittle Failures*, (2005), Springer, Berlin.
- [92] J. Lemaître, (1971) *Proc. Int. conf. Materials*, n°1, Kyoto, p.540.
- [93] J. Lemaître, J.L. Chaboche, (1978) *J. Mech. Appl.* 2:317.
- [94] J. Lemaître, D. Baptiste, *NSF workshop on mechanics of damage and fracture* (1982), p.101.
- [95] J. Lemaître, (1984) *J. Eng. Mat. Tech. ASME* 27, 83.
- [96] J. Lemaître, J.L. Chaboche, *Mécanique des matériaux solides 2ème édition*, (1996) Edition Dunod, In French, 390-403.
- [97] Y. Bao, T. Wierzbicki, On fracture locus in the equivalent strain and stress triaxiality space, (2004) *Int. J. Mech. Sci.*, 46:81– 98.
- [98] P. Ladevèze and J. Lemaitre, *Damage Effective Stress in Quasi-Unilateral Material Conditions*, (1984) In: *Proc. of the 16th International Congress of Theoretical and Applied Mechanics*, Lyngby, Denmark.
- [99] C. Comi, U. Perego, Fracture energy based bi-dissipative damage model for concrete, (2001) *Int. J. Solids. Struct.*, 38:6427-6454.
- [100] Y. Bao, T. Wierzbicki, On the cut-off value of negative triaxiality for fracture, (2005) *Eng. Fract. Mech.* 72:1049–1069.
- [101] R. De Boer, *Theory of porous media – Past and present*, (1998) *Z. Angew. Math. Mech.*, 78, 7:441-466.

- [102] A.L. Gurson, Continuum theory of ductile rupture by void nucleation and growth: Part I – Yield criteria and flow rules for porous ductile media, (1977) *J. Eng. Mat. Tech.*, 99:2-15.
- [103] V. Tvergaard, A. Needleman, Analysis of the cup-cone fracture in a round tensile bar, (1984) *Acta Met.*, 32:157–169.
- [104] M. Bernacki, Y. Chastel, H. Dignonnet, H. Resk, T. Coupeuz and R. E. Logé, Development of numerical tools for the multiscale modelling of recrystallisation in metals, based on a digital material framework, (2007) *Comput. Met. Mat. Sci.*, Vol. 7, N°1.
- [105] T. Balan, Parameter identification of steel behaviour laws through the simulation of wire drawing, (2005) *Proc. of the International Conference on Drawing, Zakopane*. P.
- [106] J. Kubié, Le test de bipoinçonnement: étude théorique—application à l'étude du transfert de matière dans un contact frottant, Ph.D Thesis, École des Mines de Paris, 1980, In French.
- [107] F. Delamare, M. de Vathaire, J. Kubié, An evaluation of the plain strain compression test. Experimental study of the friction test. II. Role of transfer layers in boundary lubrication, (1982) *J. Lubric. Tech.*, 104:545–551.
- [108] P. Montmitonnet, R. Gratacos, J. Ducloux, (1995) *Mat. Process. Technol.*, 53 (3-4), 662-683.
- [109] W.F. Hosford, R.M. Caddell, *Metal Forming – Mechanics and Metallurgy*, 2nd ed. (1993) Prentice Hall Inc., USA.
- [110] R.W. Logan, D.J. Meuleman, W.F. Hosford, (1986) *Proc. TMS–AIME Conf.*, 159–173.
- [111] F. Barlat, (1987) *Mater. Sci. Engg.* Vol. 91, 55-72.
- [112] G. Proust, C.N. Tomé, G.C. Kaschner. *Acta Mat.* 55 (2007) 2137-2148.
- [113] F.D. Fischer, H. Clemens, T. Schaden and F. Appel. *Int. J. Mat. Res.* 98, 11 (2007) 1041-1046.
- [114] S. Fayolle, Modélisation numérique du rivetage autopoinçonneur, (2008) PhD report Mines ParisTech, Sophia Antipolis, In French.
- [115] N. Soyris, Modélisation tridimensionnelle du couplage thermique en forgeage à chaud, (1990) PhD report, Mines Paristech, Sophia Antipolis, In French.
- [116] T. Coupeuz, Grandes déformations et remaillage automatique, (1991) PhD report, Mines Paristech, Sophia Antipolis, In French.

- [117] T. Coupez, A mesh improvement method for 3D automatic remeshing, (1994) 4th International Conference of Numerical Grid Generation in Computational Fluid Dynamics and Related Fields, Swansea, Wales.
- [118] B. Rey, Methodes Multigrilles pour les grandes déformations et simulation numérique du procédé de roulage, (2007) PhD report, Mines Paristech, Sophia-Antipolis, In French.
- [119] K. Mocellin, Contribution à la simulation numérique tridimensionnelle du forgeage à chaud: étude du contact et calcul multigrille, (1999) PhD report, Mines Paristech, Sophia-Antipolis, In French.
- [120] E. Perchat, MINI-Élément et factorisations incomplètes pour la parallélisation d'un solveur de Stokes 2D. Application au forgeage, (2000) PhD report, Mines Paristech, Sophia Antipolis, In French.
- [121] S. Marie, Un modèle de parallélisation S.P.M.D. pour la simulation numérique de procédés de mise en forme de matériaux, (1997) PhD report, Mines Paristech, Sophia Antipolis, In French.
- [122] Pokorny and J. Pokorny, Inclusions non métalliques dans l'acier, Techniques de l'Ingénieur, M220, In French.
- [123] M.H.A. Bonte, Optimisation Strategies for Metal Forming Processes, (2007) Thesis report, university of Twente.
- [124] D. Vieilledent, Optimisation des Outils en Forgeage à Chaud par Simulation Eléments Finis et Méthode Inverse. Applications à des Problèmes Industriels, (1999) Thesis report, Centre de Mise En Forme des Matériaux (CEMEF), In French.
- [125] D. Montgomery, Design and analysis of experiments, 5<sup>th</sup> ed. John Wiley and Sons, Inc., NY, USA, 2001.
- [126] R. Myers, D. Montgomery, Response Surface Methodology: Process and Product Optimization Usind Design Experiments, (2002) 2nd Ed. John Wiley and Sons, Inc., New York, USA.
- [127] S. Byon and S. Hwang, FEM-based process optimal design in steady-state metal forming considering strain-hardening, (2001) Computers and Structures, 79, 14: 1363:1375.
- [128] Z. Lin, X. Juchen, W. Xinjun and H. Guoan, Optimization of die profile for improving die life in the hot extrusion process, (2003) J. Mat. Proc. Tech., 142, 3:659-664.

- [129] A. Mihelic and B. Stok, Optimization of single and multistep wire drawing processes with respect to minimization of the forming energy, (1996) *Structural Optimization*, 12:120-126.
- [130] C. Lemaréchal, Méthodes numériques d'optimisation, (1989) Collection didactique - Institut national de recherche en informatique et en automatique, Vol. 6, 84p, In French.
- [131] T. T. Do, Optimisation de Formes en Forgeage 3D, (2006) Thesis report, Centre de Mise En Forme des Matériaux (CEMEF), In French.
- [132] E. S. kundu, A. Osyczka, The Effect of Genetic Algorithm Selection Mechanisms on Multicriteria Optimization Using the distance Method, (1996) In: Proceedings of the Fifth International Conference on Intelligent Systems, Reno, Nevada, 1996; *Int. Soc. Comput. Appl. (ISCA)*, 164-168.
- [133] E. Zitzler, L. Thiele, Multiobjective Evolutionary Algorithms: a Comparative Case Study and The Strength Pareto Approach, (1999) *IEEE Trans. Evolut. Comput.*, 3:257-271.
- [134] S. Kukkonen, L. Lampinen, (2004) In: European Congress on Computational Methods to Applied Science and Engineering (ECCOMAS 2004), P. Neittaanmäki, T. Rossi, S. Korotov, E. Onáte, J. Périaux, D. Knörzer (editors), Jyväskylä, Finlande, 24-28.
- [135] N. Chakraborti, B. Siva Kumar, V Satish Babu, S. Moitra, A. Mukhopadhyay, A New Multi-objective Genetic Algorithm Applied to Hot Rolling Process, (2008) *Appl. Math. Mod.*, Vol.32, 9:1781-1789.
- [136] R. Nandan, R. Rai, R. Jayakanth, S. Moitra, N. Chakraborti, A. Mukhopadhyay, Regulating Crown and Flatness during Hot Rolling: A Multiobjective Optimization Study using Genetic Algorithms, (2005) *Mat. Man. Proc.*, 20:459-478.
- [137] N. Chakraborti, B. Siva Kumar, V. Satish Babu, S. Moitra, A. Mukhopadhyay, Optimizing surface profiles during Hot Rolling: A Genetic Algorithm based on Multi-objective Optimization, (2006) *Comput. Mat. Sci.*, 37:159-165.
- [138] N. Chakraborti, S. Moitra, A. Mitra, A. Mukhopadhyay, Evolutionary and Genetic Algorithms applied to Hot Rolling: A Multi-objective Rolling Schedule Studied using Particle Swarn Algorithm, (2006) *Trans. Indian Inst. Met.*, Vol. 59, 5:681-688.
- [139] K. Deb, Multi-objective Optimization using Evolutionary Algorithms, (2001) Jon Wiley, Chichester.

- [140] C. A. Coello, D. A. Van Veldhuizen, G. B. Lamont, *Evolutionary Algorithms for Solving Multi-objective Problems*, (2002) Klumer Academic/Plenum Publishers, New York.
- [141] J. Kleijnen, R. Sargent, *A Methodology for Fitting and Validating Metamodels in Simulation*, (2000) *Europ. J. Operat. Res.*, 120 :14-29.
- [142] Engineering Mechanics Graduate School, *Engineering Optimization Course*, (2003) Course Readings.
- [143] D.J. Kim, Y.C. Kim, B.M. Kim, *Optimization of the Irregular Shape Rolling Process with an Artificial Neural Network*, (2001) *J. Mat. Proc. Tech.*, 113:131-135.
- [144] L. Oulladji, A. Janka, J.A. Désidéri, A. Dervieux, *Optimisation Aérodynamique par Algorithmes Génétiques Hybrides : Application à la Réduction d'un Critère de Bang Sonique*, (2003) Rapport de recherche de l'INRIA, In French.
- [145] Y. Jin, M. Olhofer, B. Sendhoff, *On Evolutionary Optimisation with Approximate Fitness Functions*, (2000) In: *Proceedings of the Genetic and Evolutionary Computation Conference GECCO*, Las Vegas, Nevada, 786-793.
- [146] Y. Jin, M. Olhofer, B. Sendhoff, *Managing Approximate Models in Evolutionary Aerodynamic Design Optimization*, (2001) In: *Proceedings of IEEE Congress on Evolutionary Computation*, Seoul, Corée, 1:592-599.
- [147] T. Do, L. Fourment, M. Laroussi, *Sensitivity analysis and optimization algorithms for 3D forging process design*, (2004) In *Proc. of NUMIFORM*, Columbus OH, USA.
- [148] L. Fourment, T. Do, A. Habbal, M. Bouzaiane, *Gradient, non-gradient and hybrid algorithms for optimizing 2D and 3D forging sequences*, (2005) In *Proc. of ESAFORM*, Cluj-Napoca, Romania.
- [149] L. Fourment, T. Do, A. Habbal, M. Bouzaiane, *Optimization of forging sequences using gradient, non-gradient and hybrid algorithms*, (2005) In *Proc. of APOMAT*, Morschach, Switzerland.
- [150] M.H.A. Bonte, L. Fourment, T.T. Do, A.H. Van den Boogaard, J. Huétink, *Optimization of metal forming processes using Finite Element simulations*, *Structural and Multidisciplinary Optimization*, submitted.
- [151] L. Fourment, T. Massé, S. Marie, R. Ducloux, M. Ejday, C. Bobadilla, P. Montmitonnet, *Optimization of a range of 2D and 3D bulk forming processes by a meta-model assisted evolution strategy*, (2009) *Proc. of the 12<sup>th</sup> International ESAFORM Conference on material forming*, Twente, The Netherlands.

- [152] J.G. Wistreich, Investigation of the mechanics of wire drawing, (1955) Proc. Instn. Mecjh. Engrs, 169:654-678.
- [153] B. Avitzur, Analysis of wire drawing and extrusion through conical dies of small cone angle, (1963) J. Eng. Ind. 89.
- [154] M. Ejday, L. Fourment, Meta-model assisted Multi-Objective Optimization – Application to non-steady 3D metal forming processes, (2009) 8th World Congress on Structural and Multidisciplinary Optimization (WCSMO-8), Lisboa, Portugal.
- [155] M. Ejday, L. Fourment, Optimisation multi-objectifs à base de méta-modèle pour les problèmes de mise en forme, (2009) 9e Colloque National en Calcul Des Structures, Giens (Var)
- [156] M. Ejday, L. Fourment, Meta-model assisted Multi-Objective Optimization for non-steady 3D metal forming processes, (2009) AIP, proceedings of the 12th ESAFORM conference on material forming. Enschede.
- [157] P. Ladevèze, On an anisotropic damage theory, (1983) In Proc. CNRS Int. Coll. 351 Villars-de-Lans, Failure criteria of structured media, J. P. Boehler ed. 1993, 355–363.
- [158] M. Gologanu, J.B. Leblond, J. Devaux, Approximate models for ductile metals containing nonspherical voids—case of axisymmetric prolate ellipsoidal cavities, (2001) J. Mech. Phys. Solids 41, 1723–1754.
- [159] Gologanu, M., Leblond, J.B., Devaux, J., Approximate models for ductile metals containing nonspherical voids—case of axisymmetric oblate ellipsoidal cavities, (1994) J. Eng. Mater. Tech. 116, 290–297.
- [160] Gologanu, M., Leblond, J.B., Perrin, G., Devaux, J., Recent extensions of Gurson’s model for porous ductile metals, (1995) In: Suquet, P. (Ed.), Continuum Micromechanics, Springer-Verlag, Berlin.
- [161] Gologanu, M., Leblond, J.B., Perrin, G., Devaux, J., Theoretical models for void coalescence in porous ductile solids I. Coalescence “in layers”, (2001) Int. J. Solids Struct. 38, 5581–5594.
- [162] J. Kim & X. Gao, A generalized approach to formulate the consistent tangent stiffness in plasticity with application to the GLD porous material model, (2005) Int. J. Solids Struct., 42, 103-122.
- [163] P. Croix, F. Lauro, J. Oudin and J. Christlein, Improvement of damage prediction by anisotropy of microvoids, (2003) J. Mat. Proc. Tech., 134-144, 202-208.

- [164] K. Siruguet, J.-B. Leblond, Effect of void locking by inclusions upon the plastic behavior of porous ductile solids – part I: theoretical modelling and numerical study of void growth, (2004) *Int. J. Plast.*, 20:225-268.

## Etude et optimisation d'une gamme de mise en forme à froid en acier haut carbone

**RESUME :** Cette thèse porte sur la modélisation par éléments finis des procédés de mises en forme à froid, que sont le tréfilage et le laminage. Tout d'abord le comportement mécanique des aciers haut carbone a été mesuré grâce à une large campagne d'essais expérimentaux tout au long de cette gamme de mise en forme et une progressive anisotropie mécanique a été observée au cours du tréfilage. Puis, la simulation numérique du tréfilage et du laminage a été réalisée à l'aide de FORGE2005®. Le résultat principal concerne la prédiction de l'élargissement en fin de laminage qui est très imprécise avec une loi isotrope (sous estimation de la largeur de 10%). Cette sous-estimation passe à 5% avec une loi de comportement anisotrope. Ensuite, une troisième partie a porté sur l'étude microstructurale couplée à une analyse des mécanismes d'endommagement des aciers perlitiques au cours du tréfilage et du laminage. L'anisotropie mécanique provient de l'alignement des colonies de perlite au tréfilage et par l'apparition d'une orientation cristallographique préférentielle. Trois mécanismes d'endommagement ont pu être identifiés au cours du tréfilage. Lors du passage au laminage, les cinétiques de propagation de l'endommagement sont modifiées. La simulation a permis d'apporter des informations supplémentaires et de valider les observations expérimentales. Enfin, des calculs d'optimisation du tréfilage ont été effectués et ont permis d'étudier la sensibilité des fonctions objectifs (endommagement et force de tréfilage) aux paramètres d'optimisation (géométrie de filière). De plus, cette étude a mis en évidence que les solutions optimales diffèrent en fonction du choix de la fonction coût et qu'il est possible de diminuer l'endommagement sans trop augmenter la force de tréfilage et le risque de rupture.

**Mots clés :** acier perlitique, tréfilage, laminage, éléments finis, anisotropie, élargissement, endommagement, optimisation

## Study and optimization of a high carbon steel flat wires

**ABSTRACT:** This thesis deals with the numerical simulation of cold forming processes, i.e. wire drawing and rolling. First, high carbon steel mechanical behaviour was measured from experiments throughout this range of steel forming and a progressive mechanical anisotropy has been observed during drawing. Secondly, numerical simulations, with FORGE2005®, have been run to simulate the material behaviour during wire drawing and rolling. The main results show that the widening prediction, with an isotropic behaviour law, is not accurate with an underestimation of 10% on the total width. This underestimation is only 5% when an anisotropic behaviour is used. Then, a microstructural study coupled with an analysis of damage mechanisms was done on high carbon pearlitic steels during wire drawing and rolling. The mechanical anisotropy comes from the orientation of the pearlitic colonies in the drawing, and by the emergence of a preferential crystallographic texture. Three damage mechanisms have been identified during drawing. During rolling, damage expansion kinetics are changed because of heterogeneous strain. Simulation enabled to bring further information and to validate previous experimental observations. Finally, drawing optimization calculations have been performed and enabled to study the sensitivity of the cost functions (damage and drawing force) to optimization parameters (drawing die geometry). Moreover this study highlighted that optimal solution depends on the choice of the cost function and identified an opportunity to reduce damage by reducing the die angle without increasing the axial stresses and the fracture risk.

**Keywords:** pearlitic steel, drawing, rolling, finite elements, anisotropy, widening, damage, optimization.